

MATER. TEHNOL.	LETNIK VOLUME	50	ŠTEV. NO.	1	STR. P.	1–162	LJUBLJANA SLOVENIJA	JAN.–FEB. 2016
-------------------	------------------	----	--------------	---	------------	-------	------------------------	-------------------

VSEBINA – CONTENTS

IZVIRNI ZNANSTVENI ČLANKI – ORIGINAL SCIENTIFIC ARTICLES

Improvement of the casting of special steel with a wide solid-liquid interface

Izboljšanje ulivanja posebnega jekla s širokim intervalom trdno-tekoče

T. Mauder, J. Stetina 3

Non-traditional non-destructive testing of the alkali-activated slag mortar during the hardening

Netradicionalno neporušno preizkušanje z alkalijami aktivirane malte med strjevanjem

L. Topolář, P. Rypák, K. Timčáková-Šamárková, L. Pazdera, P. Rovnaník 7

Multi-walled carbon nanotubes effect in polypropylene nanocomposites

Vpliv večstenskih ogljikovih nanocevk v nanokompozitih iz polipropilena

C. E. Ban, A. Stefan, I. Dinca, G. Pelin, A. Ficai, E. Andronescu, O. Oprea, G. Voicu 11

Experimental and numerical study of hot-steel-plate flatness

Eksperimentalni in numerični študij ravnosti vročih plošč iz jekla

J. Hrabovský, M. Pohanka, P. J. Lee, J. H. Kang 17

Investigation of hole effects on the critical buckling load of laminated composite plates

Preiskava vpliva luknje na kritično upogibno obremenitev laminiranih kompozitnih plošč

A. Kurşun, E. Topal 23

Corrosion of the refractory zirconia metering nozzle due to molten steel and slag

Korozija ognjeodporne cirkonske dozirne šobe s staljenim jeklom in žlindro

K. Wiśniewska, D. Madej, J. Szczerba 29

Effects of an epoxy-resin-fiber substrate for a Ω -shaped microstrip antennaVpliv z vlakni ojačane epoksi podlage pri Ω -obliki mikrotrakaste antene

Md. M. Islam, M. R. I. Faruque, M. Tariqul Islam, H. Arshad 33

X-ray radiography of AISI 4340-2205 steels welded by friction welding

Rentgenski pregled jekel AISI 4340-2205, varjenih s trenjem

U. Caligulu, M. Yalcinoz, M. Turkmen, S. Mercan 39

Thermodynamic properties and microstructures of different shape-memory alloys

Termodinamične lastnosti in mikrostruktura različnih zlitin z oblikovnim spominom

L. Gomidželović, E. Požega, A. Kostov, N. Vuković, D. Živković, D. Manasijević 47

The relationship between thermal treatment of serpentine and its reactivity

Ovisnost med toplotno obdelavo serpentina in njegovo aktivnostjo

G. Sučik, A. Szabóová, L. Popović, D. Hršak 55

Deformations and velocities during the cold rolling of aluminium alloys

Deformacija in hitrosti pri hladnem valjanju aluminijevih zlitin

M. Mišović, N. Tadić, M. Jaćimović, M. Janjić 59

Prediction of the chemical non-homogeneity of 30MnVS6 billets with genetic programming

Napovedovanje nehomogenosti kemijske sestave pri gredicah 30MnVS6 s pomočjo genetskega programiranja

M. Kovačič, D. Novak 69

Effect of the TiBN coating on a HSS drill when drilling the MA8M Mg alloy

Vpliv TiBN prevleke na HSS svodru pri vrtanju MA8M Mg zlitine

F. Karaca, B. Aksakal 75

Application of the Taguchi method to select the optimum cutting parameters for tangential cylindrical grinding of AISI D3 tool steel

Uporaba Taguchi metode za izbiro optimalnih parametrov odrezavanja pri tangencialnem cilindričnem brušenju orodnega jekla AISI D3

C. Ozay, H. Ballıkaya, V. Savas 81

Effects of friction-welding parameters on the morphological properties of an Al/Cu bimetallic joint

Vpliv parametrov tornega varjenja na morfološke lastnosti Al/Cu bimetalnega spoja

V. D. Milašinović, R. V. Radovanović, M. D. Milašinović, B. R. Gligorićević 89

Characterisation of the mechanical and corrosive properties of newly developed glass-steel composites

- Karakterizacija mehanskih in korozijskih lastnosti novo razvitih kompozitov steklo-jeklo
O. Lyubimova, E. Gridasova, A. Gridasov, G. Frieling, M. Klein, F. Walther 95

Phase analysis of the slag after submerged-arc welding

- Analiza faz v žlindri pri obločnem varjenju pod praškom
M. Prijanovič Tonkovič, J. Lamut 101

Optimizing the parameters for friction welding stainless steel to copper parts

- Optimiranje parametrov pri tornem varjenju nerjavnega jekla na bakrene dele
M. Sahin 109

WEDM cutting of Inconel 718 nickel-based superalloy: effects of cutting parameters on the cutting quality

- WEDM rezanje nikljeve superzlitine Inconel 718: vpliv parametrov rezanja na kvaliteto rezanja
U. Çaydaş, M. Ay 117

STROKOVNI ČLANKI – PROFESSIONAL ARTICLES**Influence of dredged sediment on the shrinkage behavior of self-compacting concrete**

- Vpliv izkopanih sedimentov na krčenje samozgoščevalnega betona
N. E. Bouhamou, F. Mostefa, A. Mebrouki, K. Bendani, N. Belas 127

Study of the properties and hygrothermal behaviour of alternative insulation materials based on natural fibres

- Študij lastnosti in higrotermalno obnašanje alternativnih izolacijskih materialov na osnovi naravnih vlaken
J. Zach, M. Reif, J. Hroudová 137

Prediction of the elastic moduli of chicken-feather-reinforced PLA and a comparison with experimental results

- Napovedovanje modulov elastičnosti PLA, ojačanega s piščančjim perjem in primerjava z eksperimentalnimi rezultati
U. Özmen, B. Okutan Baba 141

Composites based on inorganic matrices for extreme exposure conditions

- Kompoziti z anorgansko osnovo za izpostavitve ekstremnim razmeram
A. Dufka, T. Melichar 147

The effect of EO and steam sterilization on the mechanical and electrochemical properties of titanium Grade 4

- Vpliv EO in sterilizacije s paro na mehanske in elektrokemijske lastnosti titana Grade 4
M. Basiaga, W. Walke, Z. Paszenda, A. Kajzer 153

Influence of the carbide-particle spheroidisation process on the microstructure after the quenching and annealing of 100CrMnSi6-4 bearing steel

- Vpliv procesa sferoidizacije karbidnih delcev na mikrostrukturo jekla 100CrMnSi6-4 za ležaje po kaljenju in popuščanju
J. Dlouhy, D. Hauserova, Z. Novy 159

IMPROVEMENT OF THE CASTING OF SPECIAL STEEL WITH A WIDE SOLID-LIQUID INTERFACE

IZBOLJŠANJE ULIVANJA POSEBNEGA JEKLA S ŠIROKIM INTERVALOM TRDNO-TEKOČE

Tomas Mauder, Josef Stetina

Brno University of Technology, Faculty of Mechanical Engineering, Technická 2, 616 69 Brno, Czech Republic
mauder@fme.vutbr.cz, stetina@fme.vutbr.cz

Prejem rokopisa – received: 2014-07-29; sprejem za objavo – accepted for publication: 2015-03-03

doi:10.17222/mit.2014.122

In the last few years, steelmakers have been facing a significant decrease in the steel demand caused by the global economic crisis. Positive economic results have mostly been reached in the steel factories that have focused on special steel production with higher product capabilities, such as higher strength grades, steel design for acidic environments, steel for the offshore technology, etc. These steels must keep the mechanical properties, such as the resistance to rupture, compression strength, stress-strain properties, etc., within strict limits. The numerical calculations and optimization of casting parameters were provided. The results show the recommended casting parameters and differences between the examined steel and classic low-carbon steels.

Keywords: continuous casting, experimental measurement, numerical simulation, optimization

Proizvajalci jekel se zadnja leta spopadajo z zmanjševanjem povpraševanja po jeklu, kar je posledica globalne ekonomske krize. Pozitivne ekonomske rezultate so dosegle železarnice, ki so se osredinile na proizvodnjo posebnih jekel in z večjimi proizvodnimi zmogljivostmi, kot so visokotrdnostna jekla, jekla za delo v kislem okolju, jekla za naftne ploščadi itd. Ta jekla morajo v ozkih intervalih obdržati svoje mehanske lastnosti, kot so pretrg, tlačna trdnost, raztezek pri nategu itd. Izvršeni so bili izračuni in optimizacija postopka ulivanja. Rezultati kažejo predlagane parametre litja in razlike med preiskovanim jeklom in navadnim maloogljivičnim jeklom.

Ključne besede: kontinuirano litje, eksperimentalne meritve, numerična simulacija, optimizacija

1 INTRODUCTION

Continuous casting (CC) of steel, as an industrialized method of solidification processing, has a relatively short history of only about 60 years. In fact, the CC ratio in the world of steel industry now reaches more than 95 % of crude-steel output (**Figure 1**).¹⁻³ Through the years, the product quality, production efficiency, operating safety and casting of special steels and alloys have increased. Today, nearly all steel grades can be produced and productivity goals exceed by far those envisaged in the 1960s/1970s; the limits of casting-section sizes have been increased to support new steel-grade developments like thick high-strength steel plates or to realize new process routes like the direct link between the casting and rolling steps.⁴

In the early 1990s, continuous casting was an established and already matured technology. The production was focused on cost reductions through higher casting speeds, a better utilization of energy, the optimization of equipment performance and a reduction of the maintenance expenses using the equipment with a longer lifetime. The key factor, which made continuous casting the "main-stream technology", was the continuous innovation. From the metallurgical point of view, the state-of-the-art continuous casters have the features that

enable strand treatment through special cooling and soft-reduction technologies.⁵ Sophisticated process models allow an online process simulation and closed-loop control to further optimize the product quality and productivity goals.

Today, steelmakers in the European Union are facing a significantly decreasing steel demand caused by the global economic crisis. **Figure 1** shows the crude-steel production progress in the EU between 2005 and 2012

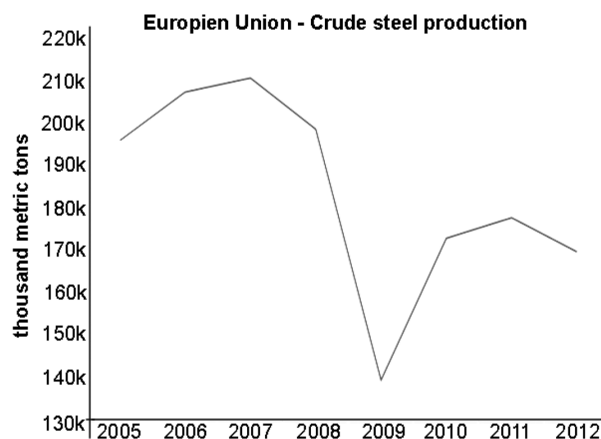


Figure 1: Crude-steel production in EU²

Slika 1: Proizvodnja surovega jekla v EU²

promulgated by The World Steel Association.² The economic crisis in 2008 caused a deep slump in the steel production in the EU. Positive economic results were mostly reached by the steel factories that focused on special steel production with higher product capabilities, such as higher-strength grades, steel plates for barrel boilers, steel design for acidic environments and steel for the offshore technology. The production of special steel is the only prospective for the EU to keep the competitiveness with the Asian market.

Steel grades for acidic environments and for the offshore technology must keep the mechanical properties, such as the resistance to rupture, compression strength, stress-strain properties and so on, within strict limits. A breakdown situation caused by a low quality of steel could have a catastrophic effect on the material and human losses. The defects of the steel for acidic environments have been known more than 50 years. Despite that, the world oil, gas and engineering companies still make huge efforts to improve the operations in acidic environments and to avoid critical situations. The mechanical properties for these grades of steel are specified by the European Standard EN 10020. Their production, unlike the classic low-carbon steel grades, requires a special treatment like the soft reduction, electromagnetic stirring, different cooling conditions, etc., to avoid crack defects.

The casting of special steel (C0.18, Ni0.04, V0.004, N0.003 w/%) was performed by the steelmaker Vitkovice Steel, a. s. A macroscopic examination (the Baumann method) shows many defects in the final quality of the steel, such as high porosity, centerline segregation and cracks.

This paper deals with the results of a numerical simulation of the temperature field and optimization of a casting process by analyzing the casting parameters and their influences on the quality of the steel.⁶

2 DATA FROM THE MACROGRAPHY

The testing set contains twenty-five samples from four heats (casting sequences). With a macroscopic test,

we evaluated the cracks in the transverse and longitudinal directions, the centerline segregation according to SMS DEMAG, the segregation index, the discontinuity and the lack of homogeneity.

The chemical composition of the steel is in **Table 1** and the macrography results are shown in **Table 2** and **Figures 2** to **5**.

Table 1: Chemical composition of the examined steel in mass fractions, w/%

Tabela 1: Kemijska sestava preiskovanega jekla v masnih deležih, w/%

C	Si	Mn	P	Cr
0.18	0.38	1.49	0.021	0.07
S	Ni	Mo	Cu	Al
0.004	0.05	0.017	0.028	0.029
Nb	Ti	V	Ca	
0.001	0.003	0.004	0.003	

Table 2: Macrostructure results

Tabela 2: Ocena makrostrukture

Heat (casting sequence)	Macrostructure						
	Surface cracks	Columnar cracks	Centerline cracks	Midway cracks	Transverse cracks	Segregation index	SMS DEMAG
26 393	6	106	23	106	5	3	2
26 394	5	107	23	107	5	2	2
26 395	6	103	23	105	5	1-2	2
26 396	5	108	22	107	5	2-3	3
occurrence of defects			Centerline segregation, cracks, local discontinuity				

From the results, it is obvious that the quality of the steel is not sufficient and has to be improved.

3 NUMERICAL SIMULATIONS

The simulation of the continuous-casting process is based on a transient numerical model of the temperature field. This model was specially modified to simulate the real casting machine operated in Vitkovice Steel, a.s. The

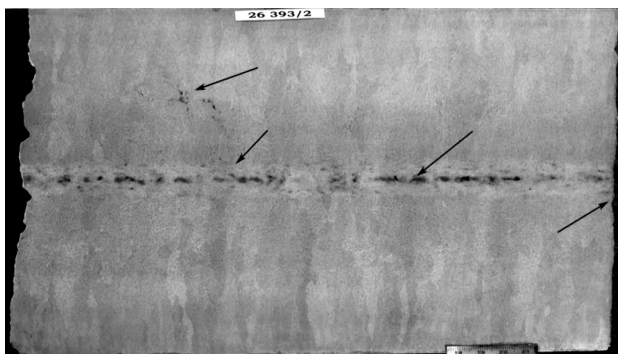


Figure 2: Steel sample from heat 26 393
Slika 2: Vzorec jekla iz taline 26 393

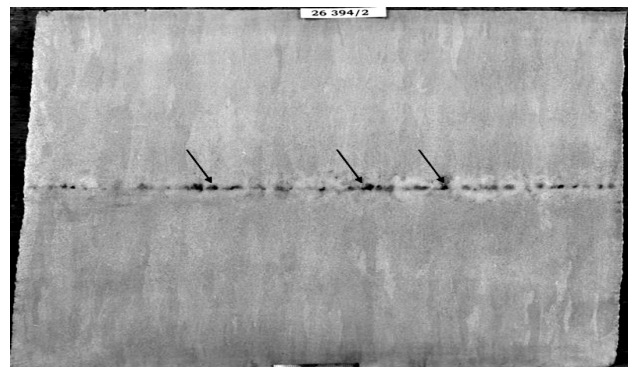


Figure 3: Steel sample from heat 26 394
Slika 3: Vzorec jekla iz taline 26 394

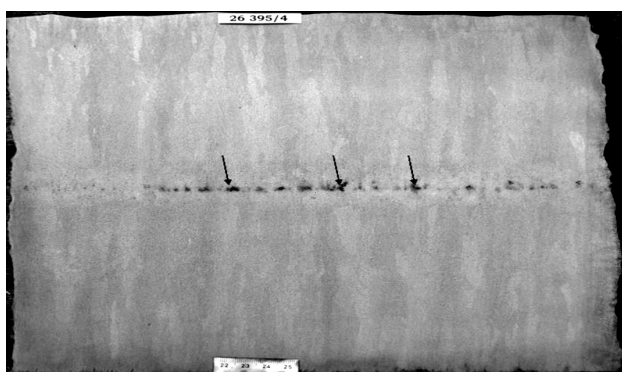


Figure 4: Steel sample from heat 26 395

Slika 4: Vzorec jekla iz taline 26 395

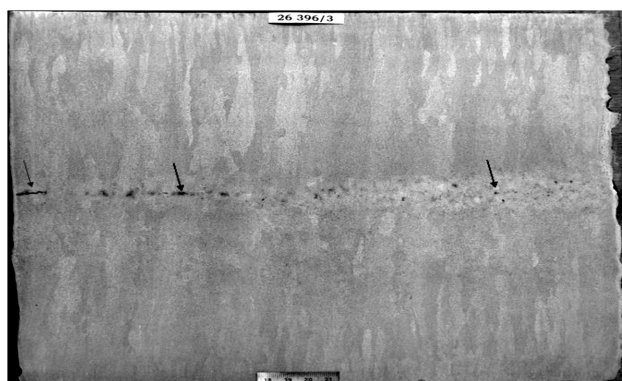


Figure 5: Steel sample from heat 26 396

Slika 5: Vzorec jekla iz taline 26 396

model represents a unique combination of numerical modeling and a large number of experimental measurements. Its results are validated with long-time measurements made during the real casting process. A detailed description of the numerical model can be found in⁷.

Thermophysical properties are calculated by the IDS solidification package. The results for the examined steel are in Figure 6.

The casting parameters, such as the casting speed, the pouring temperature, the heat removal from the mold, the cooling intensity in the secondary cooling zone, etc., for the numerical simulation were taken from the real

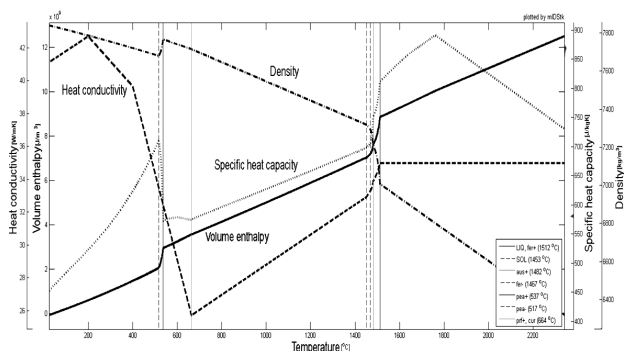


Figure 6: Thermophysical properties of the examined steel

Slika 6: Fizikalno-termične lastnosti preiskovanega jekla

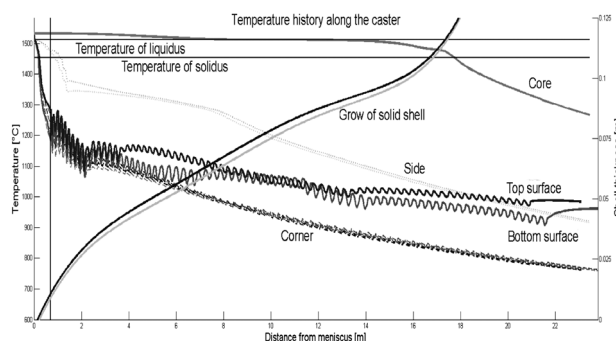


Figure 7: Temperature distribution before optimization

Slika 7: Porazdelitev temperature pred optimizacijo

measurement data for heats 26 393–26 396. The results from the simulation of heat 26 393 are in Figures 7 and 8.

The numerical simulation reveals that the examined steel is characterized by a long mushy zone in comparison with the classic low-carbon steels. The metallurgical length reaches 20.08 m and the mushy zone is almost 10 m long. For the classic low-carbon steels, the mushy zone is proximately 4–6 m long. The inner quality of steel is also influenced by the position of the metallurgical length. The steel should be fully solidified in close distance to the caster unbending point. The caster operating in Vitkovice Steel, a.s., has the unbending point located 12.6 m from the meniscus. So, the defects can also be caused by the long distance between the position of the metallurgical length and the unbending point. These rules⁸ together with the method for the optimum cooling⁹ give a set of conditions for the optimization of the casting parameters.

4 RESULTS AND DISCUSSION

According to the optimization criteria, the numerical model and fuzzy-regulation algorithm⁶ were used to calculate new casting parameters for the examined steel. In order to get the metallurgical-length position between 12–15 m, the casting speed has to decrease to 89 % of the original speed. The cooling intensity for the particular cooling circuit increases, on average, to

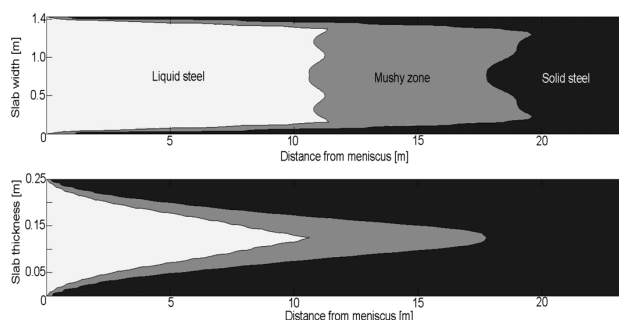


Figure 8: Distribution of liquid and solid steel

Slika 8: Porazdelitev tekočega in trdnega jekla

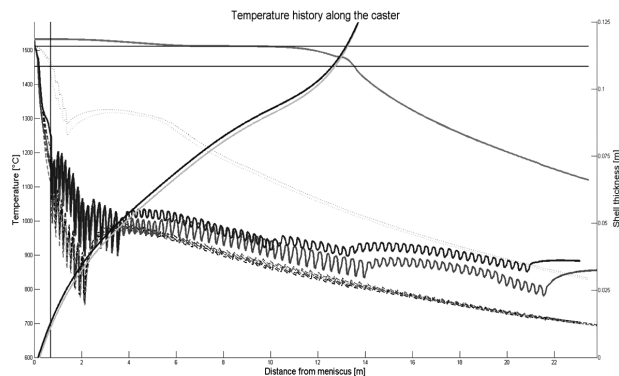


Figure 9: Temperature distribution after optimization

Slika 9: Porazdelitev temperature po optimizaciji

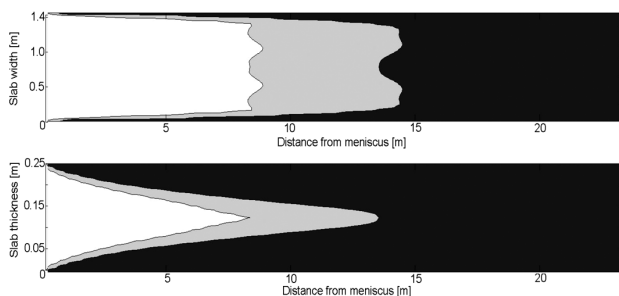


Figure 10: Distribution of liquid and solid steel

Slika 10: Porazdelitev tekočega in trdnega jekla

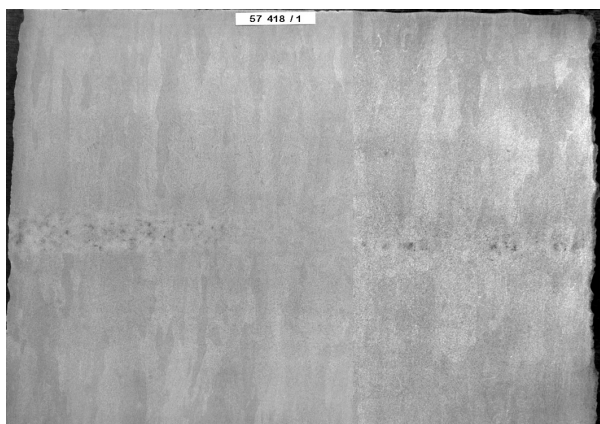


Figure 11: Steel sample from the casting after optimization

Slika 11: Vzorec litega jekla po optimizaciji

13.4 %. The results of the numerical simulation and optimization are in **Figures 9** and **10**.

The result was given to the Vitkovice Steel, a.s., as a casting recommendation for this type of steels. Despite the fact that the first macroscopic results (**Figure 11**) show a quality improvement, more experimental measurements and numerical simulations are required in order to get a general view of the behavior of the examined steel.

5 CONCLUSION

Numerical modeling and optimization will play an increasing role in the future improvements to the continuous casting of steel. A combination of the optimization algorithm based on fuzzy logic with the numerical model of the temperature field improves the casting parameters. With the optimum casting parameters, a better final quality of cast steel can be achieved. The algorithm is very general and its calculations can be used for any steel grade and caster geometry.

Acknowledgement

This work is an output of the research and scientific activities of NETME Centre, the regional R&D center built with the financial support from the Operational Programme Research and Development for Innovations within the project NETME Centre (New Technologies for Mechanical Engineering), Reg. No. CZ.1.05/2.1.00/01.0002 and, in the follow-up sustainability stage, supported through NETME CENTRE PLUS (LO1202) with the financial means from the Ministry of Education, Youth and Sports under the "National Sustainability Programme I".

6 REFERENCES

- ¹ J. P. Birat et al., The Making, Shaping and Treating of Steel: Casting Volume, 11th edition, AISE Steel Foundation, Pittsburgh, PA 2003, 1000
- ² Crude steel production, The World Steel Association [online], Brussels, Belgium 2013 [cit. 2013-03-27], <http://www.world-steel.org/>
- ³ C. A. Däcker et al., The History of Mould Slag Films Downwards the Mould and How it Affects Heat Flux and Shell Growth in Continuous Casting of Steels, Proceedings of the METEC InSteelCon 2011, Düsseldorf 2011, 8
- ⁴ A. Flick, Ch. Stoiber, Trends in Continuous Casting of Steel – Yesterday, Today and Tomorrow, Proceedings of the METEC InSteelCon 2011, Düsseldorf 2011, 8
- ⁵ Y. H. Chang et al., Development and Application of Dynamic Secondary Cooling and Dynamic Soft Reduction Control for Slab Castings, Proceedings of the METEC InSteelCon 2011, Düsseldorf 2011, 6
- ⁶ T. Mauder, C. Sandera, J. Stetina, A Fuzzy-Based Optimal Control Algorithm for a Continuous Casting Process, Mater. Tehnol., 46 (2012) 4, 325–328
- ⁷ T. Mauder, C. Sandera, J. Stetina, Optimal control algorithm for continuous casting process by using fuzzy logic, Steel Res. Int., 86 (2015) 7, 785–798, doi:10.1002/srin.201400213
- ⁸ G. S. Jansto, Steelmaking and Continuous Casting Process Metallurgy Factors Influencing Hot Ductility Behavior of Niobium Bearing Steels, Proceedings of the METAL 2013, Brno, 2013, 32–39
- ⁹ A. A. Ivanova, V. A. Kapitanov, A. V. Kuklev, Method of calculating the optimum parameters for the air-mist cooling of a continuous-cast slab, Metallurgist, 56 (2012), 173–179, doi:10.1007/s11015-012-9555-2

NON-TRADITIONAL NON-DESTRUCTIVE TESTING OF THE ALKALI-ACTIVATED SLAG MORTAR DURING THE HARDENING

NETRADICIONALNO NEPORUŠNO PREIZKUŠANJE Z ALKALIJAMI AKTIVIRANE MALTE MED STRJEVANJEM

**Libor Topolář, Peter Rypák, Kristýna Timčáková-Šamárková, Luboš Pazdera,
Pavel Rovnaník**

Brno University of Technology, Faculty of Civil Engineering, Veveri 331/95, 602 00 Brno, Czech Republic
topolar.l@fce.vutbr.cz

Prejem rokopisa – received: 2014-07-30; sprejem za objavo – accepted for publication: 2015-01-30

doi:10.17222/mit.2014.130

This paper reports the results of the measurements of alkali-activated slag mortars made during the hardening and drying of specimens. The alkali-activated slag is a material with a great potential for practical use. The main drawback of this material is its high level of autogenous and, especially, drying shrinkage, which causes a deterioration in the mechanical properties. The aim of this paper is to present the effects of the treatment method for mortars and the curing time on the microstructures of the alkali-activated slag mortars. The knowledge of the microstructure/performance relationship is the key to a true understanding of the material behaviour. The results obtained in the laboratory are useful for understanding the various stages of the micro-cracking activity during the hardening process in quasi-brittle materials such as alkali-activated slag mortars and for their extension to field applications. Non-destructive acoustic-analysis methods – the impact-echo method as a traditional method and the acoustic-emission method as a non-traditional method for civil engineering – were used for the experiment. The principle of the impact-echo method is based on analysing the response of an elastic-impulse-induced mechanical wave. Acoustic emission is the term for the noise emitted by materials and structures when they are subjected to stress. The types of stress can be mechanical, thermal or chemical. Ultrasound testing and the loss in mass were used as complementary methods for the tested samples.

Keywords: acoustic-emission method, loss in mass, impact-echo method, ultrasound testing, alkali-activated slag mortars

Članek obravnava rezultate meritev med strjevanjem in sušenjem vzorcev malt, aktiviranih z alkalijami. Z alkalijami aktivirana žindra je material, ki ima velik potencial za praktično uporabo. Glavna pomanjkljivost tega materiala je, da ima sam po sebi, še posebno pa pri sušenju, velik skrček, ki povzroči poslabšanje mehanskih lastnosti. Namen tega članka je predstavitev vpliva metode obdelave malte in časa strjevanja na mikrostrukturo z alkalijami aktivirane malte. Razumevanje odvisnosti med mikrostrukturo in zmogljivostjo je ključ za pravilno razumevanje vedenja materiala. Rezultati, dobljeni v laboratoriju, so koristni za razumevanje različnih stopenj nastajanja mikrorazpok med procesom strjevanja kvazikrhega materiala, kot je malta z žindro, aktivirano z alkalijami, in za njihov prenos na gradbišče. Neporušne analize metode z akustično emisijo in metoda udarec – odmev kot tradicionalne ter metoda akustične emisije kot netradicionalna metoda v gradbeništvu, so bile uporabljene pri preizkusu. Princip metode udarec – odmev temelji na analizi odgovora elastičnega impulznega mehanskega vala. Akustična emisija je izraz za hrup, ki ga oddajata material in zgradba, ko sta izpostavljena napetosti. Napetosti so lahko mehanske, termične ali kemijske. Preiskava z ultrazvokom in izguba mase sta bili uporabljeni kot komplementarni metodi pri preizkusnih vzorcih.

Ključne besede: metoda akustične emisije, izguba mase, metoda udarec – odmev, preiskava z ultrazvokom, malta z žindro, aktivirano z alkalijami

1 INTRODUCTION

Alkali-activated aluminosilicate materials represent an alternative to ordinary Portland-cement-based materials, reducing the impact of the building industry on the environment and exhibiting new superior properties. Alkali-activated slag (AAS) is based on granulated blast-furnace slag that can be activated by alkali hydroxides, carbonates or, most preferably, by silicates.¹ The type and dosage of the activator as well as the way of the curing have significant effects on the hydration course and final mechanical properties.² The major disadvantage of AAS is an increased shrinkage during the hardening period, caused by both the autogenous and drying shrinkage, which finally results in a volume contraction, micro-cracking and deterioration of tensile and bending properties.³

The impact-echo method (IE) is a type of the non-destructive testing method. A short-term mechanical impact, generated by tapping a hammer against the surface of a concrete structure, produces low-frequency stress waves which propagate into the structure.⁴ A wave generated in this way propagates through the specimen structure and reflects from the defects located in the volume of specimen or on its surface. Surface displacements caused by the reflected waves are recorded by a transducer located adjacent to the impact.⁵ The signal is digitized via an analogue/digital data system and transmitted to a computer's memory. This signal describes the transient local vibrations, caused by the mechanical-wave multiple reflections inside the structure. The dominant frequencies of these vibrations give an account of the condition of the structure that the waves pass through.⁶

Acoustic emission (AE) is the term for the noise emitted by materials and structures when they are subjected to stress. The types of stresses can be mechanical, thermal or chemical. This emission is caused by a rapid release of the energy within a material due to the events such as a crack formation and its subsequent extension occurring under the applied stress, generating transient elastic waves that can be detected by piezoelectric sensors. The acoustic-emission system allows us to monitor the changes in the material behaviour over a long time and without moving one of its components, i.e., sensors. This makes the technique quite unique along with the ability to detect the crack propagation occurring not only on the surface but also deep inside the material. The acoustic-emission method is considered to be a "passive" non-destructive technique, because it usually identifies defects while they develop during the test.⁷

Ultrasonic testing is the name given to the study and application of ultrasound, which is a sound too high to be detected by the human ear, i.e., of the frequencies greater than about 18 kHz. Ultrasonic waves have a wide variety of applications. For example, ultrasound with high intensity is used for cutting, cleaning and destroying a tissue in medicine. For the non-destructive testing (NDT), ultrasound with a lower intensity is used. An ultrasonic inspection can be used for a flaw detection/evaluation, dimensional measurements, a material characterization and more. Ultrasonic testing (UT) is based on the propagation of low-amplitude waves through a material, measuring the time of travel or detecting any change in the intensity over a given distance. Applications include distance gauging, flaw detection and parameter measurement (such as the elastic modulus and the grain size), all relating to the material structure.⁸

2 EXPERIMENTAL PART

2.1 Material

The mixture consisted of 450 g of fine-grained granulated blast-furnace slag Štramberk 380 (a specific

surface area of 380 m² kg⁻¹), 180 g of sodium silicate (water glass) with a modulus of 1.6, 1350 g of silica sand and 95 mL of water. The AAS slurry was poured into steel moulds (40 mm × 40 mm × 160 mm) to set and after 24 h the samples were demoulded and immersed in water for another (2, 6 and 27) d before the testing.

2.2 Experimental set-up

For the impact-echo method, a short mechanical impulse (a hammer blow) was applied to the surface of a specimen during the test and detected by means of a piezoelectric sensor (**Figure 1**). The impulse reflected from the surface and also from the micro-cracks and defects present on the specimen under investigation. The resonance frequency created in this way was determined by means of a frequency analysis. Dominant frequencies could be determined from the response signal by means of the fast Fourier transform. A MIDI piezoelectric sensor was used to pick up the response and the respective impulses were directed into the input of a TiePie engineering oscilloscope, two-channel Handyscope HS3 with a resolution of 16 bits.

The initiation of cracks during the hardening was monitored with the method of acoustic emission. AE signals were detected by measuring equipment DAKEL XEDO with four channels (**Figure 2**). The AE sensors (type IDK09) were attached to the surface with beeswax.

The change in the mass during the hardening was measured using equipment QuantumX with a Z6 bending-beam load cell for the maximum mass of 50 kg by HBM.

Measuring equipment PUNDIT (portable ultrasonic non-destructive digital indicating tester) Plus was used for the ultrasonic testing. For the testing speed of the sound through the mortar specimens, the coefficient of variation for the repeated measurements at the same location was 2 %. The accuracy of the pulse velocity was

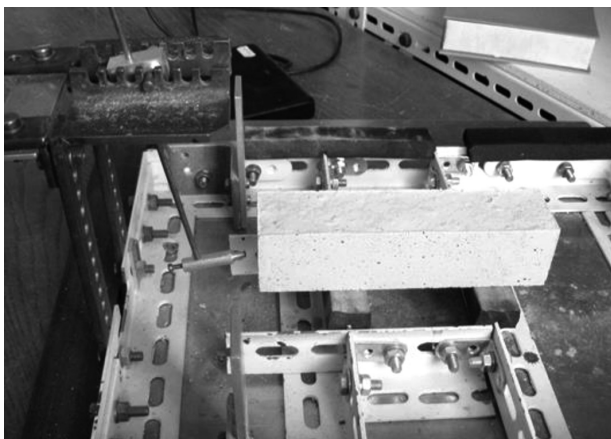


Figure 1: Photography of the impact-echo measurement
Slika 1: Posnetek meritve udarac – odmev

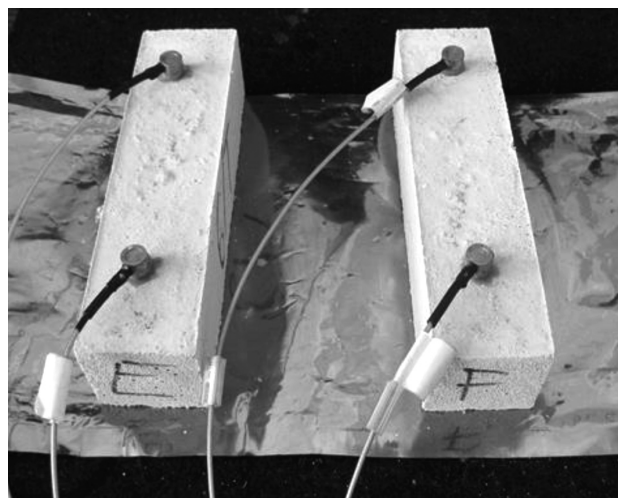


Figure 2: Photography of the acoustic-emission measurement
Slika 2: Posnetek meritve akustične emisije

a direct function of the accuracy of the measured distance between the transducer faces. The PUNDIT instruments have a transit time resolution of 0.1 s. All the measurements were carried out for 336 h (14 d) immediately after the specimens were pulled out of the immersion water.

3 RESULTS AND DISCUSSION

To evaluate the crack formation during spontaneous drying, we focused on the activity of AE with respect to the most used parameter, which is the number of signals overshooting the pre-set threshold. The diagrams in **Figures 3 to 5** show the dependence of the number of overshoots and the loss of mass versus the time of measurement. It was assumed that the number of microcracks could be inferred from the AE activity. Unfortunately, the AE signals originate not only from the crack formation but also from the process of water evaporation. However, most of the AE activity was observed within the first 24 h of spontaneous drying, which corresponds to approximately 50 % loss in mass. Therefore, at the beginning the AE signals could be attributed to both the drying process and the crack formation, whereas after 24 h of drying the observed signals corresponded mainly to the formation of microcracks. The highest number of overshoots during the remaining time of the measure-

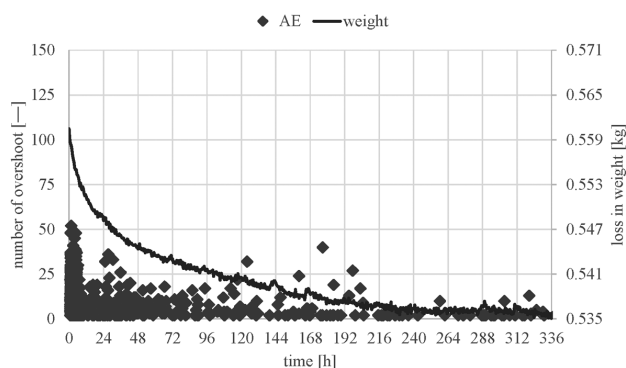


Figure 3: Results for the specimen cured in water for 2 d
Slika 3: Rezultati vzorca, ki se je 2 d utrjeval v vodi

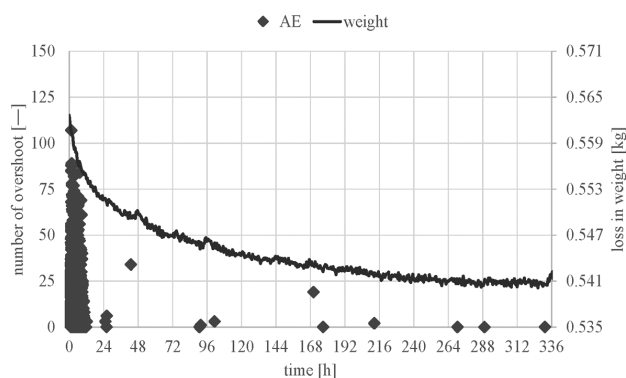


Figure 4: Results for the specimen cured in water for 6 d
Slika 4: Rezultati vzorca, ki se je 6 d utrjeval v vodi

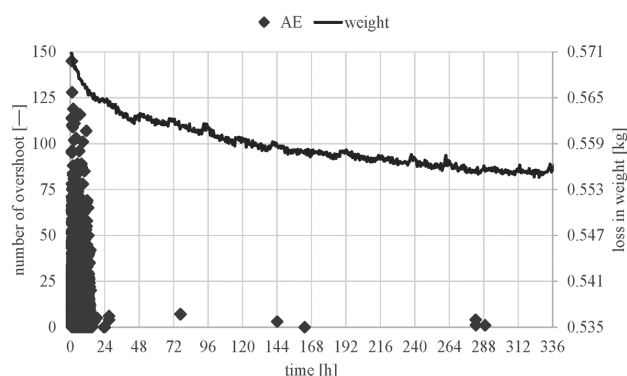


Figure 5: Results for the specimen cured in water for 27 d
Slika 5: Rezultati vzorca, ki se je 27 d utrjeval v vodi

ment was detected for the specimen that was cured in water for 2 d (**Figure 3**). The reason for such a difference in comparison with the specimens cured for 6 d and 27 d arise from a shorter hydration time. Three days after the mixing, the hydration process was still not complete and the weak basic structure was not able to bear a heavy stress; therefore, the AAS matrix was more susceptible to the cracking caused by drying shrinkage.

To evaluate the signals with the impact-echo method the fast Fourier transform was used. The modification of the dominant frequency during the drying process is displayed in **Figure 6**. The results show that the frequencies decreased from the initial values of 10.10 kHz, 10.86 kHz, 12.12 kHz to the steady values of 5.90 kHz, 7.50 kHz, 8.44 kHz, respectively, for the specimens cured in water for (2, 6 and 27) d, respectively. Similarly, the ultrasonic velocity decreased from the initial values of (3760, 3960, 4450) m s⁻¹ to the steady values of (2010, 2470, 2970) m s⁻¹, respectively, for the specimens immersed in water for (2, 6 and 27) d, respectively (**Figure 7**). The pulse cannot travel across the material/air interface, but it is able to travel from the transmitter to the receiver by diffraction at the crack edge. As the travel path is longer than the distance between the transducers, the apparent pulse velocity is lower than through the sound material.

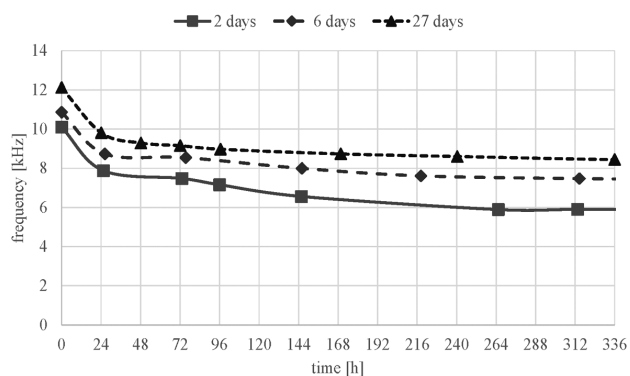


Figure 6: Change in the dominant frequency over time
Slika 6: Spreminjanje prevladujoče frekvence s časom

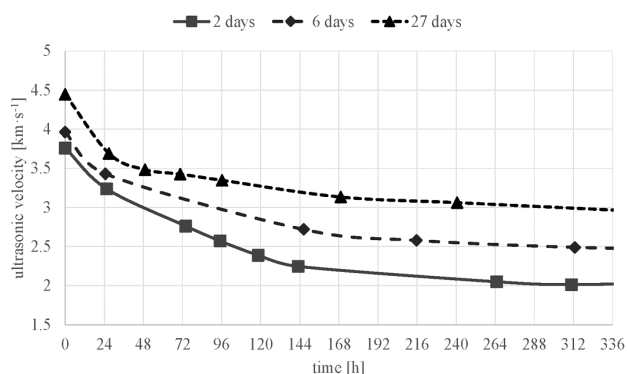


Figure 7: Change in the ultrasonic velocity over time

Slika 7: Spreminjanje hitrosti ultrazvoka s časom

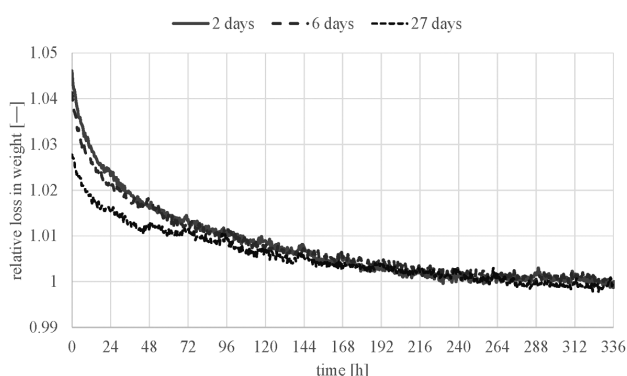


Figure 8: Change in the loss in mass in relative units over time

Slika 8: Spreminjanje izgube mase v relativnih enotah s časom

The frequencies as well as the ultrasonic velocity exhibit a decreasing trend of the values. The initial, quite steep drop corresponds to the evaporation of the water absorbed in the pore system, leaving air voids that do not transmit ultrasonic signals. The further decrease connected with the crack formation caused by drying shrinkage is bit more moderate. These results are in very good accordance with the acoustic-emission measurements. Higher absolute values of the ultrasonic velocity for the specimens cured for longer times are associated with a denser and more compact structure.

The comparison in the mass loss for variously cured specimens is given in **Figure 8**. The loss in mass was calculated relative to the steady state after spontaneous drying. The relative mass of the steady state was set to 1. The specimens cured for 27 d in water lost only 28 % of mass, whereas the specimens immersed in the water bath for 6 d and 2 d decreased their mass by 41 % and 46 %, respectively. It can be assumed that the AAS specimens that were not completely hydrated were more porous and, hence, contained higher amounts of the evaporable water.

4 CONCLUSIONS

The paper deals with the use acoustic non-destructive methods for monitoring the alkali-activated slag mortars during the process of drying and hardening. Volume variations in the alkali-activated slag mortars are connected with autogenous and drying shrinkage. The loss in mass observed during the setting and hardening of AAS is a result of the drying process. The rate of the moisture release is in good accordance with the number of signals detected with the AE method. The changes in the dominant frequency towards lower values detected with the impact-echo method for all three specimens are visible and there is also a trend of a decrease in the ultrasonic velocity, indicating that a large number of new inhomogeneities appeared in the tested specimens during their storage in air. It is assumed that most of these changes can be attributed to the crack formation; therefore, it can be concluded that the main process leading to a deterioration of the AAS binder is the drying shrinkage.

Acknowledgement

This paper was elaborated with the financial support of the Czech Science Foundation project CSF No. 13-09518S and the Ministry of Education, Youth and Sports of the Czech Republic under the "National Sustainability Programme I" (project No. LO1408 AdMaS UP), as an activity of the regional Centre AdMaS (Advanced Materials, Structures and Technologies).

5 REFERENCES

- C. Shi, P. V. Krivenko, D. Roy, Alkali-Activated Cements and Concretes, Taylor & Francis, Oxon, UK 2006, doi:10.4324/9780203390672
- C. Shi, R. L. Day, Some factors affecting early hydration characteristics of alkali-slag cements, Cem. Concr. Res., 26 (1996), 439–447, doi:10.1016/S0008-8846(96)85031-9
- M. A. Cincotto, A. A. Melo, E. L. Repetto, Effect of different activators type and dosages and relation with autogenous shrinkage of activated blast furnace slag cement, Proceedings of the 11th International Congress on the Chemistry of Cement, Durban, South Africa, 2003, 1878–1888
- M. Sansalone, N. J. Carino, Impact-Echo: A Method for Flaw Detection in Concrete Using Transient Stress Waves, National Bureau of Standards, Gaithersburg, Maryland, 1986, NBSIR 86-3452
- I. Pišková, Z. Chobola, M. Matysík, Assessment of ceramic tile frost resistance by means of the frequency inspection method, Ceramics-Silikáty, 55 (2011) 2, 176–182
- M. T. Liang, P. J. Su, Detection of Corrosion Damage of Rebar in Concrete Using Impact-Echo Method, Cem. Concr. Res., 31 (2001), 1427–1436, doi:10.1016/S0008-8846(01)00569-5
- Ch. U. Grosse, M. Ohtsu, Acoustic Emission Testing, Springer-Verlag, Berlin 2008, doi:10.1007/978-3-540-69972-9
- J. Blitz, G. Simpson, Ultrasonic Methods of Non-Destructive Testing, Springer-Verlag, New York, LLC 1991

MULTI-WALLED CARBON NANOTUBES EFFECT IN POLYPROPYLENE NANOCOMPOSITES

VPLIV VEČSTENSKIH OGLJIKOVIH NANOCEVK V NANOKOMPOZITIH IZ POLIPROPILENA

**Cristina-Elisabeta Ban^{1,2}, Adriana Stefan¹, Ion Dinca¹, George Pelin^{1,2},
Anton Fica², Ecaterina Andronesu², Ovidiu Oprea², Georgeta Voicu²**

¹National Institute for Aerospace Research "Elie Carafoli" Bucharest, Materials Unit, 220 Iuliu Maniu Blvd, 061126 Bucharest, Romania

²University Politehnica of Bucharest, Faculty of Applied Chemistry and Materials Science, 1-7 Polizu St., 011061 Bucharest, Romania
ban.cristina@incas.ro

Prejem rokopisa – received: 2014-07-31; sprejem za objavo – accepted for publication: 2015-02-06

doi:10.17222/mit.2014.142

The paper presents a study concerning thermoplastic nanocomposites having polypropylene as the matrix and different contents of carboxyl-functionalized multi-walled carbon nanotubes as the nanofiller. The materials are obtained by melt compounding the nanofiller powder and polymer pellets through the extrusion process followed by injection molding into specific-shape specimens. The materials are evaluated in terms of mechanical properties such as the tensile and flexural strengths and moduli, the thermal stability under load (the heat deflection temperature) and the thermal-behavior properties using a TG-DSC analysis. The fracture cross-section is analyzed using FTIR spectroscopy and SEM microscopy to evaluate the bulk characteristics of the materials. The results show positive effects of the nanofiller addition to the thermoplastic polymer on the mechanical strength and modulus of the materials during flexural and tensile tests, while in the case of the thermal stability under load, the nanofiller addition has a minor influence on the heat-deflection-temperature values.

Keywords: polypropylene, melt mixing, carbon nanotubes, mechanical properties, thermal resistance

Članek predstavlja študijo termoplastičnih nanokompozitov s polipropilensko osnovo in različno vsebnostjo s karboksilom obdelanih, večstenskih ogljikovih nanocev kot nanopolnilom. Materiali so bili dobljeni iz taline, sestavljene iz prahu nanopolnila in peletov polimerov, s postopkom ekstruzije, ki mu je sledilo tlačno litje vzorcev. Materiali so ocenjeni glede mehanskih lastnosti, kot so natezna in upogibna trdnost in moduli, toplotne stabilnosti pri obremenitvi (deformacijska toplota) in toplotne značilnosti z uporabo TG-DSC analize. Za oceno značilnosti osnovnega materiala je bil analiziran prelom s pomočjo FTIR spektroskopije in SEM mikroskopije. Rezultati kažejo pozitivne učinke vpliva dodatka nanopolnila termoplastičnemu polimeru na mehansko trdnost in module materiala pri upogibnem in nateznem preizkusu, medtem ko ima dodatek nanopolnila manjši vpliv na vrednosti deformacijske toplote pri obremenitvi.

Ključne besede: polipropilen, mešanje taline, ogljikove nanocевke, mehanske lastnosti, toplotna obstojnost

1 INTRODUCTION

Polymer nanocomposites found applications in a wide variety of fields, from microelectronics to aerospace.¹ Carbon nanotube-based polymer composites combine the good processability of the matrix with the remarkable functional properties of these nanofillers. Multi-walled-carbon-nanotube (MWCNT) filled isotactic polypropylene (PP) nanocomposites can be obtained through several processing methods, such as melt mixing, solution casting and in-situ polymerization, among them, melt mixing having some major advantages as it combines high speed and simplicity with the absence of solvents and contaminants.² For the production of these nanocomposites, a double-screw extruder is a more appropriate device than a single-screw extruder.³ The formation of a filler network structure (**Figure 1**) depends on several parameters, e.g., the concentration or dispersion states of the nanotubes in the matrix. Carbon nanotubes have a tendency to form agglomerates that lead to a decrease in the surface area, consequently hindering the structure formation.⁴ The screw speed is a

strong factor that influences the dispersion of the carbon nanotubes in polypropylene; too high a speed rate can generate a mechanical degradation of the final nanocomposite as a high shear stress can affect the nanotubes structure, while too low a speed rate may be insufficient for an aggregate disentanglement.⁴

Achieving a good dispersion is influenced also by the surface optimization between the two phases. The MWCNT-matrix interfacial-adhesion enhancement can be obtained by modifying the MWCNT surface through the non-covalent functionalization that maintains the nanotube structure or the covalent functionalization, such as acid treatment creating carboxyl and hydroxyl groups on the surface, that enhances the load transfer to the matrix.⁵ There are studies showing that properties enhancements are achieved for smaller nanotubes contents and moderate acid-treatment times.^{5,6}

The study presents the characterization of isotactic polypropylene filled with carboxyl-functionalized MWCNT obtained through the simple melt-extrusion technique. The results show an improvement in the tensile and flexural strengths and moduli when adding



Figure 1: Exfoliated nanocomposite formation during the polymer-melt mixing

Slika 1: Nastanek eksplaniranega nanokompozita med mešanjem taline polimera

the nanofiller. In the case of a higher MWCNT loading ($w(\text{MWCNT}) = 4\%$), the nanocomposites present a higher stiffness, decomposition temperature and thermal stability under load, while at a lower loading ($w(\text{MWCNT}) = 2\%$) they exhibit a better mechanical strength.

2 EXPERIMENTAL SECTION

2.1 Materials

The matrix was an isotactic polypropylene (TIPP-LEN H 949 purchased from Basplast SRL) of the homopolymer type with a flow index of 45. The nanofiller was carboxyl-functionalized multi-walled carbon nanotubes of a 95 % purity (Chengdu Organic Chemicals Co. Ltd, outer diameter: 10–20 nm, COOH content: $w = 2.56\%$, length: 10–30 μm , specific surface area: 233 m^2/g , density: $\sim 2.1 \text{ g/cm}^3$).

2.2 Nanocomposites synthesis

The nanocomposite samples were obtained by direct melt compounding using a twin-screw extruder (Leistritz LSM 3034 with a 34 mm screw diameter). The polypropylene (PP) pellets and nanofiller powder were mixed at a gradual temperature increase on the ten heating areas of the extruder, with a temperature profile between 150–170 $^{\circ}\text{C}$ and at a screw speed rate of 220 min^{-1} . The filaments were cooled in water, chopped, dried and injected at 165–185 $^{\circ}\text{C}$ into the specimens with a specific shape. Samples of pure PP, 2 and 4 % of mass fractions of MWCNT (relative to the matrix) were obtained, as higher contents favor agglomeration and lead to economically non-viable materials.

2.3 Testing and characterization

The nanocomposites were subjected to a spectroscopy analysis (Thermo iN10 MX, mid-infrared FTIR microscope/ATR mode) and scanning electron microscopy (SEM – HITACHI S2600N microscope), in the fracture cross-section to highlight the nanofiller presence. Tensile and flexural tests were performed using an INSTRON 5982 machine, on a minimum of 5 specimens per test, according to SR EN ISO 527-2⁷ at a tensile rate of 50 mm/min, on 1A-type specimens and SR EN ISO

178⁸ at a test speed of 2 mm/min, for conventional deflection on rectangular specimens. The thermal-degradation behavior was followed by TG-DSC (Netzsch TG 449C STA Jupiter) heating at 10 K/min, from 25–900 $^{\circ}\text{C}$, under a dried-air flow of 10 mL/min. The HDT thermal stability under load was evaluated using Qualitest HDT1 according to SR EN ISO 75, using a 2 $^{\circ}\text{C}/\text{min}$ heating rate and the standard deflection of 0.34 mm at a flexural stress of 1.8 MPa. The density was calculated as the ratio between mass and volume; the volume was measured using the displacement method.

3 RESULTS AND DISCUSSION

3.1 FTIR spectroscopy

Figure 2 presents the spectra of the isotactic PP in comparison with the samples nanofilled with 2 and 4 % of mass fractions of MWCNT. All the spectra present the characteristic peaks of PP: $-\text{CH}_2$ and $-\text{CH}_3$ stretching vibrations (2800–2950 cm^{-1})⁹, $-\text{CH}_3$ and $-\text{CH}_2$ bending (1376, 1456 cm^{-1})^{10,11}, and $\text{C}-\text{CH}_3$ stretching (841 cm^{-1})¹⁰.

Calculating the ratio of the absorption bands at 998 and 973 cm^{-1} (A_{998}/A_{973})¹² characteristic for the pure isotactic PP, the isotacticity index for the PP used in this study was 77.8 %.

There are some differences between the MWCNT samples due to the matrix-nanofiller interaction.¹³ Between 1000–1100 cm^{-1} the signals are more intense, probably due to the $\text{C}=\text{O}$ bonding from the COOH

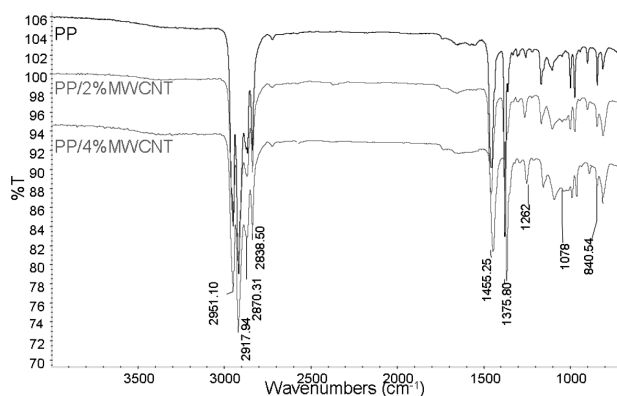


Figure 2: FTIR spectra of the polypropylene-based nanocomposites
Slika 2: FTIR-spektri nanokompozitov na osnovi polipropilena

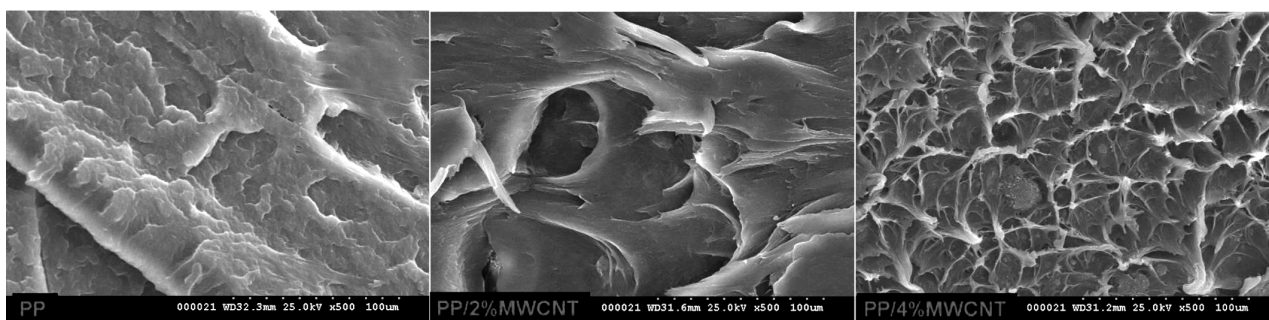


Figure 3: SEM images of PP-based nanocomposites compared to simple PP, at 500× magnification

Slika 3: SEM-posnetki nanokompozitov na osnovi PP v primerjavi z enostavnim PP, pov. 500×

functionalization.¹⁴ The increase in the signal intensity at 1078 cm^{-1} can be due to the stretching vibration of C-O.¹⁵ Minor differences appear at $1500\text{--}1750\text{ cm}^{-1}$, more visible in the 4 % of mass fractions of MWCNT-COOH samples; the weak peak at approximately 1738 cm^{-1} can be due to the C=O stretching vibration from the COOH group¹⁵ and the modifications at 1550 cm^{-1} to the OH groups in C-OH from the nanotubes treatment.¹⁶

Minor differences between the FTIR spectra can be due to the low MWCNT content or a weak connection with the polymer, probably because of the non-polar nature of the polypropylene.

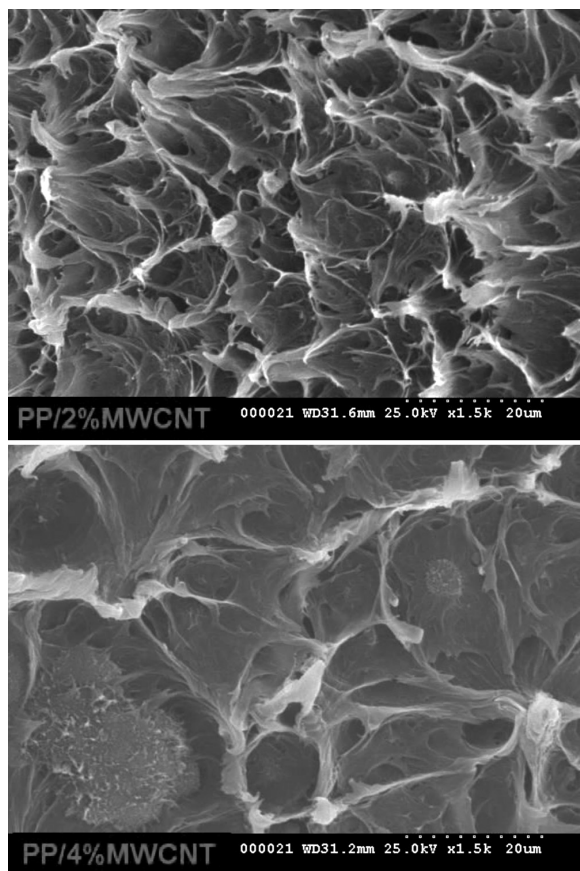


Figure 4: SEM images of PP-based nanocomposites at 1500× magnification

Slika 4: SEM-posnetka nanokompozitov na osnovi PP, pov. 1500×

3.2 SEM electronic microscopy

SEM highlights the sample morphology at different magnifications. The cross-section is strongly influenced by the nanofiller, presenting visible edges and cracks prior to the tensile-test fracture. The fracture area of the samples with $w(\text{MWCNT}) = 2\%$ is rougher, more like the simple PP than the ones with $w(\text{MWCNT}) = 4\%$, due to the lower nanofiller content. At a 500× magnification, a good dispersion of MWCNT can be noticed (**Figure 3**). In PP/2 % MWCNT there are some pores, probably as impurities from the carbon nanotubes. In the case of PP/4 % MWCNT there are no visible pores, but there are some non-uniform areas, most likely due to the higher nanofiller content that increases the agglomeration tendencies. In the case of PP/4 % MWCNT, fracture-initiation sites can be observed (**Figure 4**).

3.3 Mechanical testing

Figure 5 presents the stress-strain curves of the replicas of the mediated specimens corresponding to the samples. **Figure 6** presents the load-extension evolution, illustrating that during the flexural test the materials mainly exhibit the same behavior; in the first stage, PP/2 % MWCNT followed the PP trend, then its line was the same as the one for PP/4 % MWCNT.

Table 1 presents the summary of the mechanical and heat-deflection results. The nanocomposites exhibit

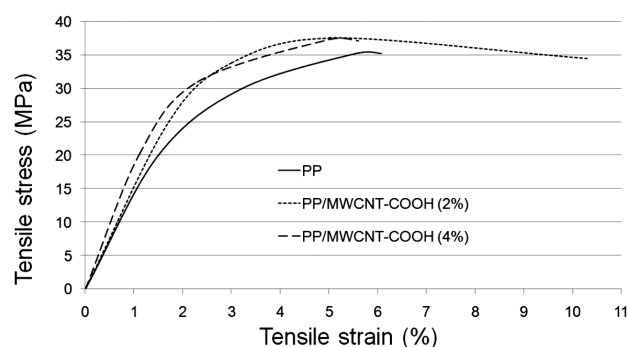


Figure 5: Stress-strain curves corresponding to PP-based nanocomposites

Slika 5: Krivulje napetost – raztezek nanokompozitov na osnovi PP

superior characteristics compared to the bare PP; the increase is more significant for the Young's modulus, while the density remains low.

Table 1: Results for mechanical and thermal stability under load tests
Tabela 1: Rezultati mehanske in toplotne stabilnosti pri obremenitvi

Sample	PP	PP/MWCNT-COOH (2 %)	PP/MWCNT-COOH (4 %)
Density, g/cm ³	0.87	0.91	0.93
Tensile stress at tensile strength, MPa	35.34	37.56	37.38
Young's modulus, MPa	2026.1	2307	2413.71
Flexure stress at tensile strength, MPa	32.51	35.42	33.59
Young's flexure strain, MPa	1439	1547.66	1575.19
HDT, °C	66.9	69.2	70.3

Adding 2 % of mass fractions of MWCNT-COOH generated an increase in the tensile modulus of about 15 % while 4 % of mass fractions of led to a 20 % increase compared to the bare PP. The flexural modulus of the $w = 4$ % sample presented an increase by 10 %, proving that adding MWCNT-COOH leads to stiffer materials.

For the tensile and flexural strengths, the increase values are in the range of 5–9 % for both the 2 and 4 % samples, with slightly higher values for the 2 % sample. This fact can be due to the higher content of the nanofiller, which favors agglomerations, an issue that was probably not overcome with the mechanical dispersion using the extrusion. At the 2 % loading, there is a significant increase in the elongation at break, while at the 4 % loading, both the strength and the elongation at break decrease compared to the 2 % loading, indicating a decrease in the ductility.¹⁷ At the higher MWCNT content filler-filler agglomerates are likely to act as stress-concentrating sites¹⁷ as observed in the SEM images,

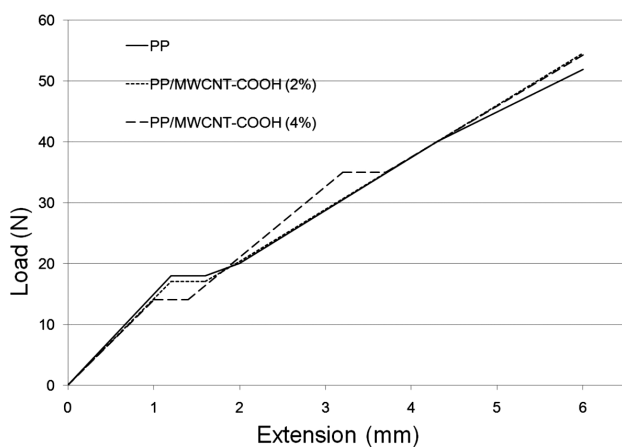


Figure 6: Load-extension evolution during the flexural testing of PP-based nanocomposites

Slika 6: Obnašanje obremenitev – raztezek med upogibnim preizkusom nanokompozitov na osnovi PP

resulting in lower strength values. The number of the stress-concentration sites increases with the nanotubes content, leading to a decrease in the elongation.¹⁸

The mechanical properties show that the composite failure is dependent on the nanofiller content.

3.4 HDT thermal stability under load

The thermal stability under load is in concordance with the other test results. There is a minor increase in HDT for the MWCNT sample, from 66.9 to 69.2 °C for the 2 % loading and 70.3 °C for the 4 % loading, which is confirmed by the DSC curves of the PP-based materials that present no change in the thermal behavior up to 200 °C.

3.5 Thermal degradation behavior

The TG curves from **Figure 7a** indicate that the materials are thermally stable up to approximately 200–220 °C; after this temperature they undergo thermal-degradation processes.

Table 2 summarizes the TG-DSC results, showing that a MWCNT-COOH addition leads to an increase in the initial temperature of the degradation process (T_{onset}) on the TG curve of approximately 65 °C. The 50 % weight loss is generally considered to be an indicator of the structural destabilization¹⁹, which occurs up to

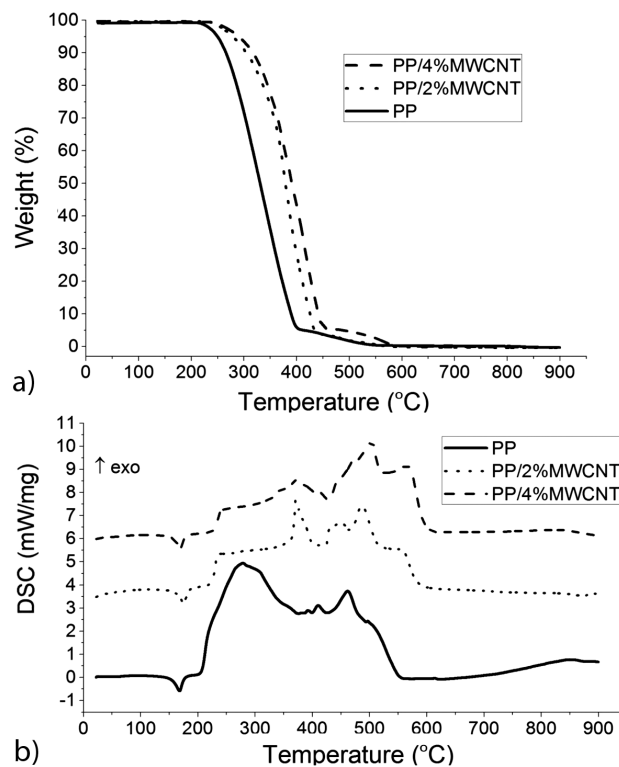


Figure 7: a) TG and b) DSC curves for PP/MWCNT nanocomposites compared to simple PP

Slika 7: a) TG- in b) DSC-krivulje za PP/MWCNT kompozite v primerjavi z enostavnim PP

approximately 330 °C for PP, up to 370 °C for PP/2 % MWCNT and 390 °C for PP/4 % MWCNT. The end of the degradation process (T_{endset}) is shifted towards higher values as the MWCNT content increases.

Table 2: TG-DSC analysis results

Tabela 2: Rezultati TG-DSC analiz

Sample	T_{onset} , °C	T_{endset} , °C	T_{melting} , °C	T_{decomp1} , °C	T_{decomp2} , °C
PP	263.3	390	167.9	279.2	410/461.5/ 496.7
PP/2 % MWCNT	326.5	408.7	166.8	362.6	441.4/487.4/ 546.4
PP/4 % MWCNT	327.2	441.2	167.3	365.2	471.4/500.9/ 561.4

In the 25–200 °C region, an endothermic effect is registered on the DSC curve (**Figure 7b**), associated with the polymer melting process. As melting is a physical process, the effect is not accompanied by the weight loss. The maximum rate of the endothermic effect is reached at approximately the same temperature (167 °C) for all the samples, showing that the MWCNT addition does not induce changes in the melting temperature, but the intensities of the corresponding peaks are lower for the MWCNT samples.

In the regions above 200 °C, exothermic effects appear, associated with the decomposition processes that occur in two main stages, mainly between 200–400 °C and 400–600 °C, divided into several secondary exothermic effects, accompanied by the weight loss. The recorded effects for the PP-based materials are similar, but because of their different compositions, the peak intensities differ.

In the 200–400 °C region, the maximum weight loss occurs for all the samples, being approximately 94 %. On the DSC curve, the peaks corresponding to the exothermic effects are shifted towards higher values; the peak for PP appears at 279 °C, for PP/2 % MWCNT it appears at 363 °C and for PP/4 % MWCNT it appears at 365 °C, but with a lower intensity for the MWCNT samples. The increase in the decomposition temperature of the MWCNT nanocomposites could be due to the barrier effect generated by the nanotubes, when they are well dispersed into the matrix, hindering oxygen diffusion and retarding the thermo-oxidative degradation of polypropylene.^{20,21} MWCNT acts as the protective agent against a thermal degradation of polypropylene.

Between 400–600 °C, the exothermic effects are accompanied by a weight change of approximately 6 % for all the samples. Also, in this region, the exothermic effects recorded on the DSC curves of PP/MWCNT appear at higher temperatures and with higher intensities, with the difference increasing with the MWCNT content. This shows that the protective effect is more pronounced at higher temperatures and higher MWCNT contents.

The residual mass is extremely low (up to $w = 0.5$ % for all the samples), proving that although the

PP/MWCNT nanocomposites burn slower than the bare PP, they burn nearly completely, indicating that the eventual flame-retardancy properties of these materials are probably due to the chemical and physical processes in the condensed phase rather than the gas phase.²²

The TG-DSC analysis results prove that the addition of MWCNT improves the decomposition temperature of the polypropylene nanocomposites and, consequently, the thermal-degradation resistance.

4 CONCLUSIONS

The study presents a characterization of an isotactic polypropylene filled with carboxyl-functionalized MWCNT prepared through the simple and quick way of the melt-extrusion technique. The results show an improvement in the mechanical strength and modulus, thermal stability under load as well as decomposition temperature when adding the nanofiller. In the case of the higher MWCNT loading ($w(\text{MWCNT}) = 4$ %), the nanocomposites exhibited higher stiffness, decomposition temperature and thermal stability under load, while in the case of the lower loading ($w(\text{MWCNT}) = 2$ %) the nanocomposites exhibited better mechanical strengths. The nanocomposites maintained their low-density advantages showing a minor increase when adding the nanofiller. The results prove that the thermoplastic polymers loaded with carbon nanotubes might be a new class of light and strong composites that could find applications in a large variety of fields.

Further compatibilization of the polypropylene matrix by grafting it with different agents such as maleic anhydride, methylstyrene²³ and copolymers based on maleic anhydride²⁴ can lead to nanocomposites with even higher mechanical and thermal properties, due to an increased matrix-filler adhesion.

Acknowledgments

This work was funded by the Romanian Ministry of Education through the PN-II-PT-PCCA-168/2012 project "Hybrid composite materials with thermoplastic matrices doped with fibres and disperse nano-fillings for materials with special purposes" and by the Sectoral Operational Programme "Human Resources Development 2007–2013" of the Ministry of European Funds through the Financial Agreement POSDRU/159/1.5/S/132397.

5 REFERENCES

- ¹ F. Hussain, M. Hojjati, M. Okamoto, R. E. Gorga, J. Compos. Mater., 40 (2006) 17, 1511–1565, doi:10.1177/0021998306067321
- ² E. Logakis, E. Pollatos, Ch. Pandis, V. Peoglos, I. Zuburtikudis, C. G. Delides, A. Vatalis, M. Gjoka, E. Syskakis, K. Viras, P. Pissis, Compos. Sci. Technol., 70 (2010) 2, 328–335, doi:10.1016/j.compscitech.2009.10.023
- ³ A. Szentes, G. Horvath, Cs. Varga, Hungarian Journal of Industrial Chemistry, 38 (2010) 1, 67–70

- ⁴ T. Y. Hwang, H. J. Kim, Y. Ahn, J. W. Lee, Korea-Australia Rheology Journal, 22 (2010) 2, 141–148
- ⁵ D. Bikiaris, A. Vassilou, K. Chrissafis, K. M. Paraskevopoulos, A. Jannakoudakis, A. Docoslis, Polym. Degrad. Stab., 93 (2008) 5, 952–967, doi:10.1016/j.polymdegradstab.2008.01.033
- ⁶ S. P. Bao, S. C. Tjong, Mater. Sci. Eng. A, 458 (2007) 1–2, 508–516, doi:10.1016/j.msea.2007.08.050
- ⁷ European Standard SR EN ISO 527-2: Determination of tensile properties of plastics, Test conditions for moulding and extrusion plastics, 2000
- ⁸ European Standard SR EN ISO 178: Plastics, Determination of flexural properties, 2003
- ⁹ F. Ozmihci, Polypropylene – Natural Zeolite Composite Films, Dissertation Thesis, Materials Science and Engineering Department, Izmir Institute of Technology, 1999, p. 48
- ¹⁰ I. Karacan, H. Benli, The use of infrared-spectroscopy technique for the structural characterization of isotactic polypropylene fibres, Journal of Textile & Apparel, 21 (2011) 2, 116–123
- ¹¹ G. Parthasarthy, M. Sevegney, R. M. Kannan, J. Polym. Sci., Part B: Polym. Phys., 40 (2002) 22, 2539–2551, doi:10.1002/polb.10304
- ¹² A. R. Horrocks, J. A. D'souza, J. Appl. Polym. Sci., 42 (1991) 1, 243–261, doi:10.1002/app.1991.070420129
- ¹³ L. V. Diyakon, O. P. Dmytrenko, N. P. Kulish, Yu. I. Prylutskiy, Yu. E. Grabovskiy, N. M. Belyy, S. A. Alekseev, A. N. Alekseev, Yu. I. Sementsov, N. A. Gavrylyuk, V. V. Shlapatskaya, L. Valkunas, R. Ritter, P. Scharff, Functional Materials, 15 (2008) 2, 169–174
- ¹⁴ V. T. Le, C. L. Ngo, Q. T. Le, T. T. Ngo, D. N. Nguyen, M. T. Vu, Adv. Nat. Sci.: Nanosci. Nanotechnol, 4 (2013) 3, 1–5, doi:10.1088/2043-6262/4/3/035017
- ¹⁵ S. C. Her, C. Y. Lai, Materials, 6 (2013) 6, 2274–2284, doi:10.3390/ma6062274
- ¹⁶ C. R. Biswal, K. Mishra, P. L. Nayak, Synthesis and Characterization of Modified Multi-Walled Carbon Nanotubes Filled Thermoplastic Natural Rubber Composite, Middle-East Journal of Scientific Research, 18 (2013) 2, 168–176, doi:10.5829/idosi.mejsr.2013.18.2.12431
- ¹⁷ S. A. Girei, S. P. Thomas, M. A. Atieh, K. Mezghani, S. K. De, S. Bandyopadhyay, A. Al-Juhani, J. Thermoplast. Compos. Mater., 25 (2012) 3, 333–350, doi:10.1177/0892705711406159
- ¹⁸ S. R. Katti, B. K. Sridhara, L. Krishnamurthy, G. L. Shekar, Mechanical Behaviour of MWCNT Filled Polypropylene Thermoplastic Composites, Indian Journal of Advances in Chemical Science, 2 (2014), 6–8
- ¹⁹ E. M. Sabri, O. Emel, Fibres & Textiles in Eastern Europe, 21 (2013) 2, 22–27
- ²⁰ F. Avalos-Belmontes, L. F. Ramos-deValle, E. Ramirez-Vargas, S. Sanchez-Valdes, J. Mendez-Nonel, R. Zitzumbo-Guzman, Journal of Nanomaterials, 2012 (2012), 1–8, doi:10.1155/2012/406214
- ²¹ N. Khelidj, X. Colin, L. Audouin, J. Verdu, C. Monchy-Leroy, V. Prunier, Polym. Degrad. and Stab., 91 (2006) 7, 1593–1597, doi:10.1016/j.polymdegradstab.2005.09.011
- ²² T. Kashiwagi, E. Grulke, J. Hilding, R. Harris, W. Awad, J. Douglas, Macromol. Rapid Commun., 23 (2002) 13, 761–765
- ²³ E. Manias, A. Touny, L. Wu, K. Strawhecker, B. Lu, T. C. Chung, Chem. Mater., 13 (2001) 10, 3516–3523, doi:10.1021/cm0110627
- ²⁴ A. Szentes, C. Varga, G. Horváth, L. Bartha, Z. Kónya, H. Haspel, J. Szél, Á. Kukovecz, EXPRESS Polymer Letters, 6 (2012) 6, 494–502, doi:10.3144/expresspolymlett.2012.52

EXPERIMENTAL AND NUMERICAL STUDY OF HOT-STEEL-PLATE FLATNESS

EKSPERIMENTALNI IN NUMERIČNI ŠTUDIJ RAVNOSTI VROČIH PLOŠČ IZ JEKLA

Jozef Hrabovský¹, Michal Pohanka¹, Pil Jong Lee², Jong Hoon Kang²

¹Heat Transfer and Fluid Flow Laboratory, Faculty of Mechanical Engineering, Brno University of Technology, Technická 2, 616 69 Brno, Czech Republic

²POSCO, Rolling Technology & Process Control Research Group, 1, Geodong-dong, Nam-gu, Pohang, Gyeongbuk 790-785, Korea
hrabovsky@fme.vutbr.cz

Prejem rokopisa – received: 2014-07-31; sprejem za objavo – accepted for publication: 2015-02-10

doi:10.17222/mit.2014.153

One aspect of the steel-product quality is the flatness of a steel plate. This is one of the reasons why it is important to describe and understand the process of steel-plate deformation during the cooling process. The temperature distribution has the largest impact on the deformation of a strip. The temperature distribution is affected by the cooling process. The cooling homogeneity or inhomogeneity is the most important factor influencing the final flatness of a cooled strip or steel plate. Inhomogeneous cooling can lead to large differences in the thermal distribution inside the material and also to high deformations. The cooling homogeneity is mainly influenced by the water distribution in the cooling section. The goal of this paper is to experimentally and numerically study and describe the deformation process of a hot steel plate during the cooling process. To meet these goals, experimental measurements of a cooled steel plate were carried out and the boundary conditions and temperature field were obtained. Based on this data, two numerical models were created. The first numerical model focused on the cooling process, the thermal-field simulation and the input-data preparation for the next step. In the next step, the second numerical model was generated using the finite-element method and an analysis of the structure and deformation of the steel plate was simulated. The description of the shape deformation of cooled steel plates should lead to an improved flatness of final products.

Keywords: cooling process, deformation, flatness, numerical simulation

Eden od vidikov kvalitete izdelka iz jekla je ravnost jeklene plošče. To je eden od razlogov, zakaj je potrebno opisati in razumeti postopek deformiranja plošče med njenim ohlajanjem. Razporeditev temperature ima glavni vpliv na deformacijo traku. Na razporeditev temperature vpliva proces ohlajanja. Homogenost ali nehomogenost hlajenja je najpomembnejši faktor, ki vpliva na končno ravnost ohlajenega traku ali plošče. Nehomogeno hlajenje lahko povzroči velike razlike v razporeditvi toplote znotraj materiala in tudi velike deformacije. Na homogenost hlajenja najbolj vpliva razporeditev vode v področju hlajenja. Namen tega članka je eksperimentalni in numerični študij ter opis procesa deformacije vroče jeklene plošče med procesom hlajenja. Za dosego namena so bile eksperimentalno izmerjene hlajene jeklene plošče in dobljeni so bili mejni pogoji in temperaturno polje. Na osnovi teh podatkov sta bila postavljena dva numerična modela. Prvi numerični model je bil osredotočen na proces hlajenja, simulacijo temperaturnega polja in pripravo vhodnih podatkov za naslednji korak. V naslednjem koraku je bil generiran drugi numerični model s pomočjo metode končnih elementov in simulirana je bila analiza strukture ter deformacije jeklene plošče. Opis deformacije oblike ohlajanih jeklenih plošč naj bi omogočil boljše ravnost končnih proizvodov.

Ključne besede: proces hlajenja, deformacija, ravnost, numerična simulacija

1 INTRODUCTION

The flatness of a hot steel plate or strip is an important issue of heat treatment in the steel industry. POSCO Korea is also dealing with this problem. The flatness of a final product has a significant impact on the quality and price of the strip. The flatness of a steel plate is mainly affected by the water distribution and cooling homogeneity during the quenching process. Two important non-homogeneous types of water distribution can occur. The first type of non-homogeneity is caused by different intensities of the cooling from the top and bottom sides of a steel plate. The second type of non-homogeneity during a cooling process is created by different water distributions in the center and corners of a steel plate. Both of these types can occur simultaneously and produce problems with regard to the flatness of a steel plate^{1,2}. Non-homogeneous cooling also affects other

aspects such as material properties, phase changes, residual stresses and so on³⁻⁵. The combination of all the aspects has a significant impact on the final quality of a steel plate and, therefore, the cooling process must be studied. The description of the cooling process can be performed using several parameters, including the cooling intensity, the distribution of the heat-transfer coefficient (*HTC*) and so on^{6,7}. Experimental measurements were carried out at defined conditions to describe the cooling process and non-homogeneity identification during the quenching. The *HTC* distribution was obtained from the results and a model of the steel-surface thermal field was prepared. The inverse problem with a sequential estimation of the time and varying boundary conditions was used to simulate the cooling process and time-dependent boundary conditions⁸. The calculated thermal field of the steel plate was used in the next numerical simulation. This numerical simulation was

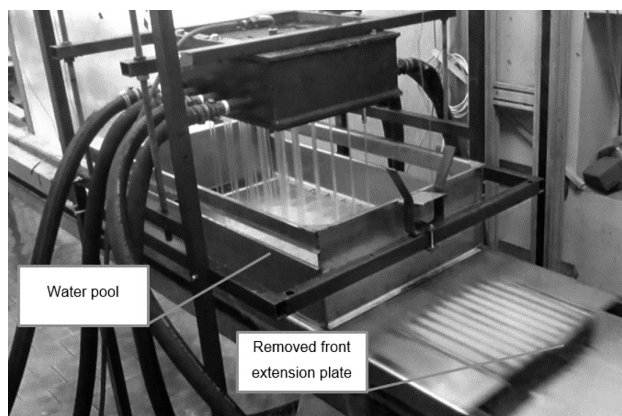


Figure 1: Experimental apparatus

Slika 1: Eksperimentalna naprava

focused on steel-plate deformations and an analysis of the flatness. The numerical simulation was based on the finite-element method in Ansys, a commercial software program.

2 EXPERIMENTAL MEASUREMENT OF COOLING HOMOGENEITY

The cooling process under defined conditions was experimentally measured using a laboratory apparatus prepared in the Heat Transfer and Fluid Flow Laboratory. The experimental apparatus is shown in **Figure 1**. The experimental measurements were focused on the study of the cooling non-homogeneity in the longitudinal and transverse directions of the test plate and also of the differences in the water distribution from the top and bottom sides.

A test plate equipped with three thermocouple sensors was used to investigate the heat transfer in the longitudinal and transverse directions. A schematic of the experimental measurement is depicted in **Figure 2**. The thermocouples recorded the temperature history during the cooling process and, using an inverse analysis, the surface temperatures and heat-transfer coefficients were computed. Both the upper and lower surfaces were investigated.

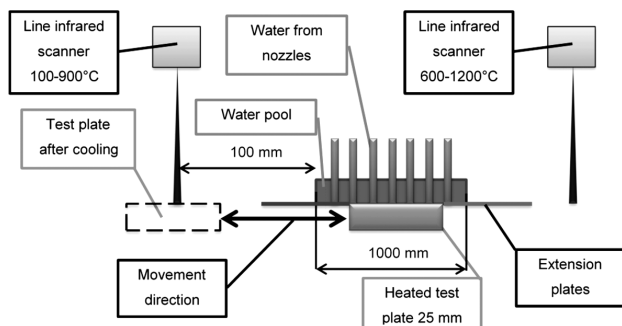


Figure 2: Schematic illustration of the experimental measurement

Slika 2: Shematičen prikaz izvedbe meritvah

The measurements were performed for several conditions. The examples of the experimental conditions are presented in **Table 1**. For the cooling from the top, a pool with an adjustable height was used to set the proper water layer.

Table 1: Examples of the measurement conditions

Tabela 1: Primeri pogojev pri meritvah

Surface	Spray distance (mm)	Flow rate (m ³ /min)	Water layer (mm)	Velocity (m/s)
Top	400	3.0	54	0.8
Top	400	4.5	65	0.8
Bottom	50	3.0	–	0.8
Bottom	50	5.3	–	0.8

The temperature history recorded during the experiment was used to compute the time-dependent boundary conditions. These boundary conditions were computed using the sequential estimation of the time-varying boundary conditions and the *HTCs* were obtained using the inverse solution of the problem for each measurement. Using the applied calculation methodology, the *HTC* distribution on the steel plate was obtained. The evaluated data for the full temperature range of the experiments performed for the upper and lower cooling are shown in **Figure 3**. These figures represent the *HTC* distribution as a function of the surface temperature and the position.

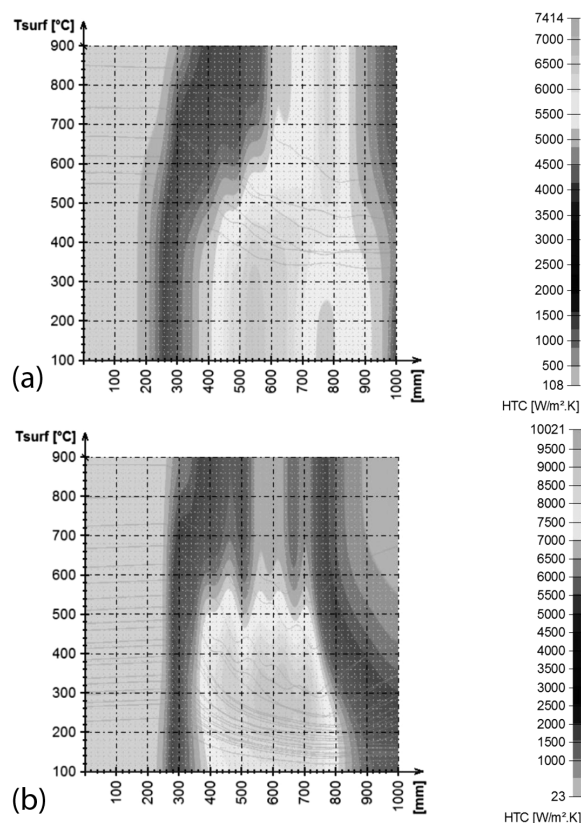


Figure 3: *HTC* distribution for: a) upper and b) bottom cooling

Slika 3: *HTC*-razporeditev za hlajenje: a) zgoraj in b) spodaj

3 NUMERICAL SIMULATION

The numerical simulation was prepared in two steps. In the first step, a numerical model of the thermal field was prepared. In this step, FDM methods were considered as the solver for the heat conduction. The second step was focused on the preparation of the numerical model for the structural analysis of the steel plate. The second numerical model was based on the FEM.

3.1 Temperature-field simulation

A cooling test plate was simulated to verify the HTC values obtained with the laboratory measurements. The selected discretization equations obtained using the FDM have a clear physical meaning – they are not simply a formal mathematical approximation. The derived equations represent the conservation principles (mainly the energy conservation) for each control volume and the resulting numerical solution correctly satisfies the conservation over the whole calculation domain. As the conductivities of the neighboring volumes may be different due to the different temperature, there may be a discontinuity of the slope (dT/dx) at the control volume boundary. Whenever there is a need to get the temperature at a control volume boundary (e.g., during the interpolation of the temperature across the control volume), a detailed equation should be used together with the temperature at the node.

When the mass density or specific heat becomes more dependent on the temperature, special care must be paid to the time integration: if the time step is too large, the latent heat of the phase change may be neglected. In the case of a phase change, the properties are highly dependent on the temperature. This problem can be eliminated by solving it using the enthalpy instead of the specific heat and the mass density. The approach that was used and overcomes this problem was inspired by the apparent-heat-capacity method.

The boundary conditions were prepared from the data presented in the previous section (Figure 3). The data was considered as a function of three variables: HTC

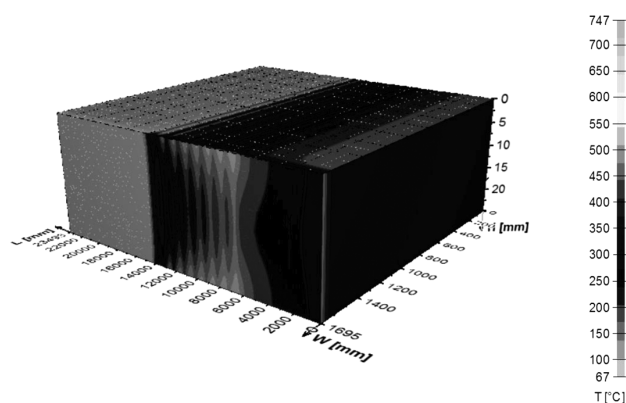


Figure 4: Temperature profile (different scales on the axes)
Slika 4: Profil temperature (različna merila po oseh)

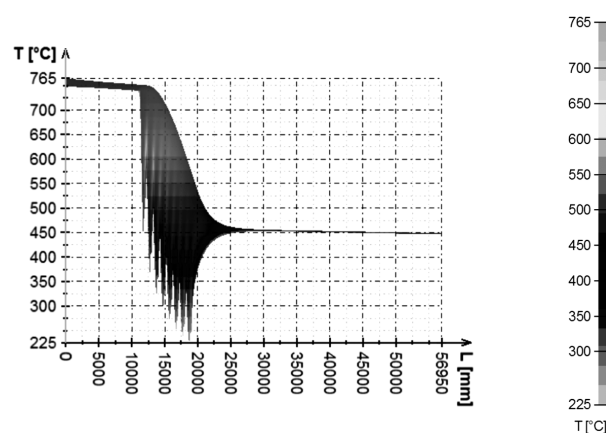


Figure 5: Center and surface temperature histories in the middle of the plane

Slika 5: Temperaturna zgodovina sredine in površine na sredini površine

(length, T_{surface} , width). An example of the applied boundary conditions at a time of 32 s for the upper cooling of the test plate is shown in Figure 4.

The computed temperature histories for the entire cooling process are shown in Figure 5. This figure indicates a large temperature difference between the surface and the center of the plate in the middle of the plate. The applied method for the temperature-field simulation agrees with the plant measurements.

3.2 Simulation of deformation

This section contains the structural analysis of the steel plate focusing on the deformations. The measured thermal loading produced by the simulated cooling process was described in the previous chapter. The purpose of this calculation was to assess the impact of the cooling process on the deformation of the steel plate produced experimentally.

The calculation methodology for the structural analysis of the FE model consists of three steps. In the first step, the 3D finite-element model was created with respect to the real dimensions and conditions. In the second step, the calculated temperature field, the structural boundary conditions and the initial conditions were applied. In the final step, the analysis of the structure and deformation of the steel plate was calculated. Two types of loads were considered for the prepared FE model: the experimentally measured thermal field as the thermal load and the mechanical loads represented by the movement of the plate. The analysis of the steel-plate deformation due to different conditions was carried out for two cases. In the first case, the specimen was tested under measured cooling conditions, and the second case was the same as the first case (the same cooling conditions) but without considering the gravity. The case without the gravity acceleration was performed to obtain the true deformation due to the cooling process.

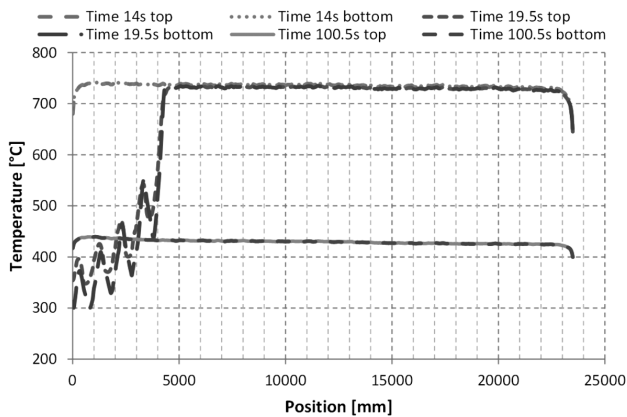


Figure 6: Evaluated temperatures through the path at defined time points

Slika 6: Ocenjene temperature skozi sredino, v določenih časovnih trenutkih

The thermal loads were FDM analyzed and applied as the body loads of the steel plate. The temperature was evaluated at the center of the steel plate along a defined path (the symmetry plane) on the top and bottom sides. The evaluation of the temperature distribution along the defined path is shown in **Figure 6**. The temperature distributions (**Figure 6**) show that at the beginning (14 s) and at the end of the cooling (100.5 s), the top and bottom temperatures are almost equal. At a time of 19.5 s it is clear that the cooling is less intense on the top and that the bottom temperatures are lower.

Different values of the temperature on both sides of the steel plate lead to different stresses and deformations. The presented thermal field was used for the structural analysis and the deformation of the steel plate was calculated. The final vertical deformation at the end of the cooling reached 2.8 mm. The maximum vertical deformation is located at the corner of the steel plate.

The deformation of the steel plate along the path at the corner and along the path at the center was evaluated (**Figure 7**). The comparison of these two locations confirmed two reasons for the maximum deformation in

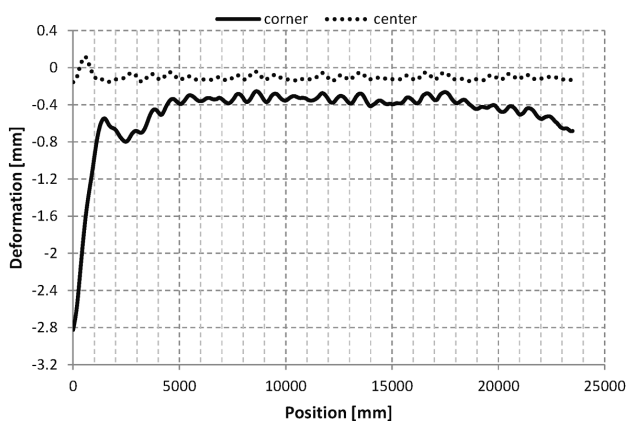


Figure 7: Evaluation of the total vertical deformation at a time of 100.5 s

Slika 7: Ocena skupne vertikalne deformacije pri času 100,5 s

the corner. The first reason is the non-homogeneous thermal field at the corner. The second reason is that the corner is free and a deformation is possible. In the center, the steel plate is constrained by the symmetry (in reality the steel plate would continue). The gravitational acceleration contributes to a decrease in the total deformation.

For the second case, the same type of cooling as for the first case was used and the gravitational acceleration was not considered. The final vertical deformation at the end of the cooling reached 596 mm. The maximum vertical deformation is located symmetrically at the beginning of the steel plate. The deformations of the steel plate in this case are mainly affected by the thermal distribution and the thermal gradients.

The presented deformation results confirm that the more intense cooling from the bottom side of the steel plate leads to the final deformation on the lower-cooling side of the steel plate (the top side). This effect can be explained with the following mechanism. On the bottom side, which is cooled more intensely, the temperature drops quickly and the stiffness (K) represented by the modulus of elasticity (E) of the bottom layer is changed to a higher value. In the middle part of the steel plate, the temperature is still high and the stiffness is low (the modulus of elasticity at a higher temperature). On the top side of the steel plate, the temperature also decreases but not as intensely as on the bottom side. The stiffness of the top layer is lower than the stiffness of the bottom layer.

The combination of the temperature and the stiffness distribution of defined layers leads to different directions of the deflection (U) in each layer. The highest deflection in the axial direction of the steel plate is in the middle layer due to the higher temperature and thermal expansion.

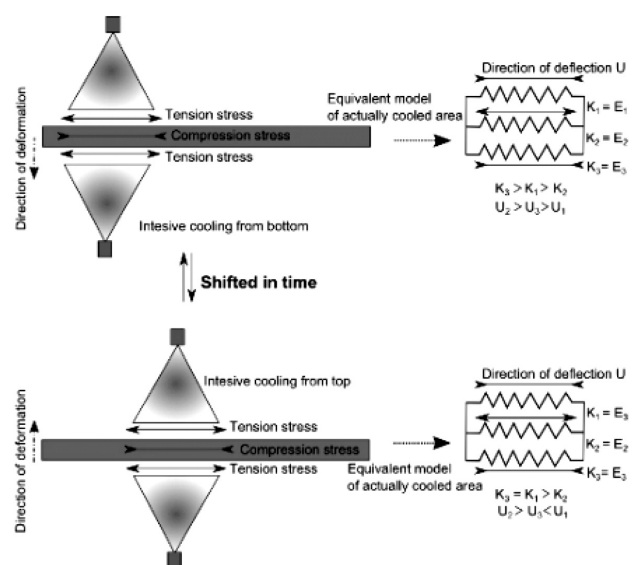


Figure 8: Schematic illustration of the steel-plate deformation mechanism

Slika 8: Shematičen prikaz mehanizma deformacije plošče iz jekla

sion. On the bottom side of the steel plate, deflection occurs in the opposite direction than in the middle layer due to intense cooling. At the top layer, the lower cooling intensity leads to a deflection in the same direction as at the bottom layer, but the deflection is lower than on the bottom side. These deflection distributions through the thickness of the steel plate generate a deformation in the intensely cooled side direction.

Non-homogeneous cooling on the bottom and top sides of the steel plate cause a time shift in the temperature distribution on both sides. The time shift in the temperatures on both sides causes a deflection inverted from the bottom and top layers, changing the final deformation of the steel plate in the direction of the actual cooled side (the top side). A schematic illustration of the deformation of the steel mechanism due to non-homogeneous cooling is depicted in **Figure 8**. The elastic-plastic material properties of steel are considered in the numerical model and, therefore, a permanent deformation occurs.

4 CONCLUSION

The analyses presented in this paper focused on the study of non-homogeneous cooling and its impact on the deformation of a steel plate. Several numerical models of steel plates were prepared. The first model computed time-dependent temperature fields. Plant measurements were simulated using this model. The results obtained from the simulation agree with data obtained during the plant measurements. The second numerical model focused on the cooling process of the steel plate and the impact of thermal fields on the final deformations of the steel plate. The FE simulation of the cooling process showed the impact of the non-homogeneity in the thermal field on the final deformations. The simulations confirmed that the plate is bent towards the side with the higher cooling intensity in the initial cooling stage; however, in the later stages, the plate is bent towards the opposite side, with the lower cooling intensity.

Acknowledgement

The paper presented was supported through project CZ.1.07/2.3.00/30.0005 of the Brno University of Technology.

This work is an output of the research and scientific activities of the NETME Centre, regional R&D center built with the financial support from the Operational Programme Research and Development for Innovations within the project NETME Centre (New Technologies for Mechanical Engineering), Reg. No. CZ.1.05/2.1.00/01.0002 and, in the follow-up sustainability stage, supported through NETME CENTRE PLUS (LO1202) by the financial means from the Ministry of Education, Youth and Sports under the National Sustainability Programme I.

5 REFERENCES

- ¹ X. Wang, Q. Yang, A. He, Calculation of thermal stress affecting strip flatness change during run-out table cooling in hot steel strip rolling, *Journal of Materials Processing Technology*, 207 (2008), 130–146, doi:10.1016/j.jmatprotec.2007.12.076
- ² Y. J. Jung, G. T. Lee, C. G. Kang, Coupled thermal deformation analysis considering strip tension and with/without strip crown in coiling process of cold rolled strip, *Journal of Materials Processing Technology*, 130–131 (2002), 195–201, doi:10.1016/S0924-0136(02)00705-7
- ³ H. N. Han, J. K. Lee, H. J. Kim, Y. S. Jin, A model for deformation, temperature and phase transformation behavior of steel on run-out table in hot strip mill, *Journal of Materials Processing Technology*, 128 (2002), 216–225, doi:10.1016/S0924-0136(02)00454-5
- ⁴ X. Wang, F. Li, Q. Yang, A. He, FEM analysis for residual stress prediction in hot rolled steel strip during the run-out table cooling, *Applied Mathematical Modelling*, 37 (2013), 586–609, doi:10.1016/j.apm.2012.02.042
- ⁵ S. Serajzadeh, Prediction of temperature distribution and phase transformation on the run-out table in the process of hot strip rolling, *Applied Mathematical Modelling*, 27 (2003), 861–875, doi:10.1016/S0307-904X(03)00085-4
- ⁶ M. Chabicovsky, M. Raudensky, Experimental Investigation of a Heat Transfer Coefficient, *Mater. Tehnol.*, 47 (2013) 3, 395–398
- ⁷ M. Raudensky, Heat Transfer Coefficient Estimation by Inverse Conduction Algorithm, *International Journal of Numerical Methods for Heat and Fluid Flow*, 3 (1993) 3, 257–266, doi:10.1108/eb017530
- ⁸ M. Pohanka, P. Kotrbacek, Design of cooling units for heat treatment, In: F. Czerwinski (Ed.), *Heat Treatment – Conventional and Novel Applications*, InTech, 2012, 1–20, doi:10.5772/50492

INVESTIGATION OF HOLE EFFECTS ON THE CRITICAL BUCKLING LOAD OF LAMINATED COMPOSITE PLATES

PREISKAVA VPLIVA LUKNJE NA KRITIČNO UPOGIBNO OBREMENITEV LAMINIRANIH KOMPOZITNIH PLOŠČ

Ali Kurşun, Ersin Topal

Department of Mechanical Engineering, Hitit University, 19030 Çorum, Turkey
alikhursun@hitit.edu.tr

Prejem rokopisa – received: 2014-08-01; sprejem za objavo – accepted for publication: 2015-03-04

doi:10.17222/mit.2014.164

In this study, the effects of the hole diameter on the buckling behavior of glass-fiber-reinforced, laminated composite rectangular plates were investigated both experimentally and numerically. As the test specimens, E-glass/epoxy symmetric-ply composites with eight layers were manufactured using the hand lay-up technique and drilled with different hole diameters ranging from 10 to 40 mm. The laminated composite plates were arranged with different symmetric orientation angles such as $[(0^\circ/90^\circ)_2]_s$, $[(-15^\circ/15^\circ)_2]_s$, $[(-30^\circ/30^\circ)_2]_s$ and $[(-45^\circ/45^\circ)_2]_s$. The experimental critical-buckling loads of the plates were found by clamping the bottom and upper edges and then these results were compared with the results obtained with the numerical analysis. The determination of the critical buckling loads for the laminated composite plates with different hole diameters was performed using the ANSYS 12.1[®] finite-element-analysis software. The numerical analysis showed good agreement with the experimental results for different hole diameters and fiber orientation angles. It was concluded that the critical buckling loads strongly depend on the diameter of the hole and fiber orientation angles.

Keywords: buckling, glass fibers, finite element method (FEM)

V tej študiji je bil eksperimentalno in numerično preiskovan vpliv premera luknje na obnašanje pri upogibu s steklenimi vlakni laminirane kompozitne štirioglate plošče. Kompozitni vzorci so bili izdelani s simetričnim polaganjem E-steklo/epoksi, z osmimi plastmi, z uporabo tehnike ročnega polaganja in vrtnja lukenj različnega premera od 10 do 40 mm. Laminirane kompozitne plošče so bile izdelane z različnimi, simetrično orientiranimi koti vlaken, $[(0^\circ/90^\circ)_2]_s$, $[(-15^\circ/15^\circ)_2]_s$, $[(-30^\circ/30^\circ)_2]_s$ in $[(-45^\circ/45^\circ)_2]_s$. Eksperimentalna kritična upogibna obremenitev plošč je bila ugotovljena z vpetjem spodnjega in zgornjega roba, rezultati pa so bili primerjani z rezultati numerične analize. Določitev kritične upogibne obremenitve za laminirane kompozitne plošče z luknjami z različnim premerom, je bila izvršena z uporabo programa za analizo končnih elementov ANSYS 12.1[®]. Numerična analiza je pokazala dobro ujemanje z rezultati preizkusov, za različne premere lukenj in orientacijske kote vlaken. Ugotovljeno je, da je kritična upogibna obremenitev močno odvisna od premera luknje in od kota orientacije vlaken.

Ključne besede: upogibanje, steklena vlakna, metoda končnih elementov (FEM)

1 INTRODUCTION

Fiber-reinforced composite plates are widely used in many types of engineering applications such as the aerospace, automotive and marine industries, as well as in medical prosthetic devices, electronic circuit boards and sports equipment because of certain properties such as high specific stiffness and strength. A plate which is subjected to an axial compressive load ought to remain stable. If, in spite of a small addition of an axial or lateral disturbance applied to a plate, it remains to be in equilibrium, then the plate is said to be stable. If a small additional disturbance results in a large response and the plate does not return to its original equilibrium configuration, the plate is said to be unstable.

The magnitude of the compressive axial load, at which the plate becomes unstable is called the critical buckling load. If the load is increased beyond this critical load, it results in a large deflection and the plate seeks another equilibrium configuration. Thus, the load at which a plate becomes unstable is of practical importance in the design of structural elements. One of the

important issues is the prediction of the critical buckling loads of composite materials. Here we determine the critical buckling loads of the laminated composite rectangular plates with a cylindrical hole using experimental and numerical methods.

The buckling behavior of symmetric cross-ply and angle-ply laminated flat composite columns was described in¹, investigating the effects of the column thickness and wideness, the orientation angles, the fillet radius and the modulus ratios on the critical buckling load with the finite-element method (FEM) based on the first-order shear-deformation theory (FSDT). Arman et al.² investigated the effect of the delamination around a single circular hole on the critical buckling load of woven-fabric-laminated composite plates. Besides the critical buckling load, they determined the critical delamination diameter. A buckling analysis of a woven-glass-polyester and boron/epoxy laminated composite plate containing a circular/elliptical hole given in^{3,4}, respectively, was done using the FEM.

Aydogdu⁵ studied the thermal-buckling behavior of cross-ply laminated beams, subjected to different boun-

dary conditions. He used the Ritz method to obtain the critical buckling temperatures. Kim and Lee⁶ developed fine-beam elements named as 2-, 3- and 4-noded isoparametric beam elements to analyze the lateral buckling of the shear-deformable laminated composites. Jung and Han⁷ presented an approach for the initial buckling behavior of laminated composite plates and shells subjected to the combined in-plane loading. Laurin et al.⁸ developed an approach for the multiscale-failure behavior for various stacking sequences. The buckling response of laminated composite structures with a delamination was investigated by Lee and Park⁹.

Matsunaga¹⁰ used the method of the power series expansion of continuous-displacement components to come up with the two-dimensional global-deformation theory for the thermal buckling of laminated composites and sandwich plates. The thermal-buckling behavior of laminated hybrid-composite plates containing a hole, subjected to a uniform temperature was studied by Şahin¹¹. The thermal-buckling mode shapes of laminated composites with varying fiber orientations, stacking sequences and E_1/E_2 ratios are studied in¹². The thermo-mechanical-buckling response of laminated composites and sandwich plates was investigated by Wu and Chen¹³.

The post- and thermal-buckling behavior of laminated composite beams with temperature-dependent material properties is given in¹⁴. Dash and Singh¹⁵ developed an isoparametric nonlinear finite-element method for the buckling and post-buckling of laminated composite plates. The buckling behavior of a composite structure based on the generalized differential quadrature rule (GDQR) and Rayleigh-Ritz (R-R) method is presented in^{16,17}. Topal and Uzman¹⁸ investigated the optimization of the critical failure mode of simply supported laminated composite plates under in-plane static loads. Shufrin et al.¹⁹ generated a semi-analytical formulation based on the total energy minimization and the iterative extended Kantorovich approach for the buckling analysis of symmetrically laminated composite plates. Malekzadeh and Shojaee²⁰ studied the buckling response of carbon-nanotube-reinforced, quadrilateral laminated plates. Özben²¹ presented the critical buckling load for laminated composite plates using the FEM and analytical methods. The effects of the hole location and diameter on the lateral-buckling response of woven-fabric-laminated composite cantilever beams were determined experimentally and numerically in²².

In this study, the effects of the hole diameter and fiber orientations on the buckling behavior of glass-fiber-reinforced, laminated composite rectangular plates were investigated experimentally and numerically under compression. Firstly, the test specimens for different fiber orientation angles were prepared with and without the holes. The test specimens made of glass/epoxy consisted of eight symmetric plies. A uniformly distributed load was applied to the upper edges of the plate specimens and critical buckling loads were determined

experimentally and numerically. The results obtained with the experimental and numerical methods were in good agreement. The results showed that the critical buckling loads strongly depend on the diameter of the hole and the fiber orientation angles.

2 MATERIALS AND METHODS

2.1 Test specimens

For the experiments, laminated composite plates consisting of eight layers of e-glass woven fabrics with various fiber orientation angles such as $[(0^\circ/90^\circ)_2]_s$, $[(-15^\circ/15^\circ)_2]_s$, $[(-30^\circ/30^\circ)_2]_s$ and $[(-45^\circ/45^\circ)_2]_s$ were manufactured. The fiber volume fraction and the nominal thickness of the composite were approximately 55 % and 2 mm, respectively. For the matrix material, the CY225 epoxy resin and hardener HY225 were used. The curing process was implemented at 120 °C for 3 h under a pressure of 0.25 MPa.²³ Then, the composite was cooled to room temperature. The prepared plates were cut to the dimensions of 100 × 100 mm and drilled in the center with different hole diameters such as 0 (without a hole), 10, 20, 30 and 40 mm respectively. **Table 1** shows the mechanical properties of the laminated composites.

Table 1: Mechanical properties of the composites plate

Tabela 1: Mehanske lastnosti kompozitnih plošč

$E_1 = E_2$ (GPa)	E_3 (GPa)	$G_{12} = G_{13} =$ G_{23} (GPa)	ν_{12}	$\nu_{13} = \nu_{23}$
28.500	17.100	7.840	0.148	0.088

2.2 Experimental procedure of the critical buckling load

The buckling tests were done in the compression mode on a Shimadzu AG-100 kN test machine. The buckling-test apparatus designed by Arman et al.² consists of two clamped edges at the bottom and top and two free edges as the boundary conditions as shown in **Figure 1**. As a result of the clamped boundary condition of the buckling-test apparatus that holds the specimen at the bottom and top edges, each having a 10 mm

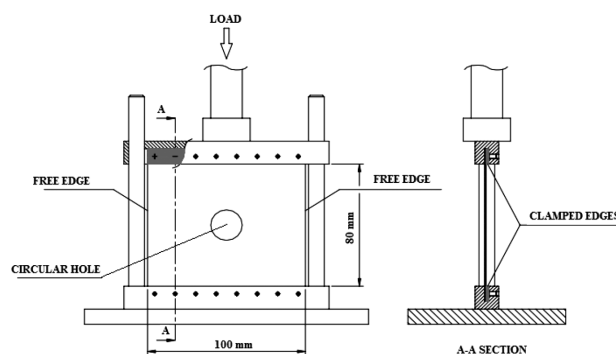


Figure 1: Buckling-test apparatus²

Slika 1: Naprava za upogibni preizkus²



Figure 2: View of the buckling-test process: a) before buckling and b) after buckling

Slika 2: Izgled upogibnega preizkusa: a) pred upogibanjem, b) po upogibanju

clamping length, the height of the test specimens were determined to be 80 mm as shown in **Figure 1**.

Three identical specimens were tested for each hole diameter and all the specimens were subjected to an axial compressive load until the first buckling mode was reached as shown in **Figure 2**. The laminated plate became unstable as the first buckling mode was reached. The magnitude of the axial compressive load, at which the plate becomes unstable, is called the critical buckling load. The other buckling modes were not studied in this paper.

The test results were taken as a text file on the data card of the test machine. Then the graphs of the load-displacement variations were created for each specimen. A MATLAB® code was written for the upheaval of the slope of the load-displacement curve. The critical buckling load was determined accordingly and shown in **Figure 3**. In this figure, P_{cr} is the critical buckling load.

2.3 Finite-element buckling model

A three-dimensional finite-element analysis of the composite plates with a single circular hole was performed using the commercial finite-element software ANSYS® 12.1. The model consists of eight layers with dimensions of $100 \times 100 \times 0.25$ mm for each layer and the 2 mm total thickness of the plate. The diameter of the hole changes from 0 (without hole) to 10, 20, 30 and 40 mm. Additionally, the fiber orientation changes from $[(0^\circ/90^\circ)_2]_s$ to $[(-15^\circ/15^\circ)_2]_s$, $[(-30^\circ/30^\circ)_2]_s$ and $[(-45^\circ/45^\circ)_2]_s$. Therefore, a total of 20 models were constructed. After the modeling of the composite plates with a circular hole, the number of layers, the element type, the material properties of the laminated composite plates, the fiber orientation angles and the thickness of each layer were introduced to the finite-element program. The element type was a SHELL layered element having six degrees of freedom at each node: the translations in the nodal x , y and z directions and the rotations about the nodal x , y and z axes. Finally, for the analysis,

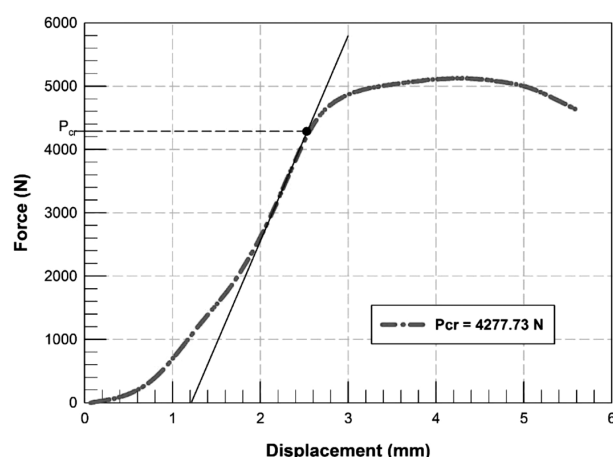


Figure 3: Determination of the experimental critical buckling load

Slika 3: Eksperimentalno določanje kritične upogibne obremenitve

the unit pressure was applied to one of the clamped edges, the model was meshed and the program was run.

3 RESULTS AND DISCUSSION

The critical-buckling-load results were obtained both experimentally and numerically for the $[(0^\circ/90^\circ)_2]_s$, $[(-15^\circ/15^\circ)_2]_s$, $[(-30^\circ/30^\circ)_2]_s$ and $[(-45^\circ/45^\circ)_2]_s$ fiber orientations for all the buckling-test specimens having 0 (without hole), 10, 20, 30 and 40 mm hole diameters, respectively. The experimental results for each hole diameter are presented in **Figure 4**. In this figure, three identical experimental graphs and their average values are shown.

It is clear that all the repeated experimental tests for each group with various hole-diameter values show a very similar buckling behavior as reported in **Figures 4a** to **4e**.

The average values of all the results obtained experimentally and numerically are given in **Table 2** in order to compare them in terms of the critical buckling load. In the same table, P_{cr}^* refers to the critical buckling load for the specimen without a hole.

Table 2: Critical buckling loads for numerical and experimental studies

Tabela 2: Kritična upogibna obremenitev pri numerični študiji in pri preizkusu

Hole diameter (mm)	Critical buckling loads (P_{cr} , P_{cr}^*) (N)							
	Fiber orientations ($^\circ$)							
	$[(0^\circ/90^\circ)_2]_s$		$[(-15^\circ/15^\circ)_2]_s$		$[(-30^\circ/30^\circ)_2]_s$		$[(-45^\circ/45^\circ)_2]_s$	
	Exp.	Num.	Exp.	Num.	Exp.	Num.	Exp.	Num.
0	4867.2	4497.0	4347.3	4296.3	4000.7	4023.0	3660.1	3853.0
10	4310.5	4261.5	4277.7	4155.4	3934.1	3891.8	3540.8	3734.4
20	4194.7	4073.5	3896.2	3970.9	3700.6	3709.1	3140.3	3355.0
30	3710.9	3758.9	3703.3	3666.9	3434.5	3424.4	2830.7	3272.2
40	3326.3	3365.3	3117.8	3279.2	3034.3	3050.5	2280.9	2905.4

In addition, the experimental and numerical results showing the variation in the critical buckling load versus the hole diameter were presented in **Figure 5**. It is clear

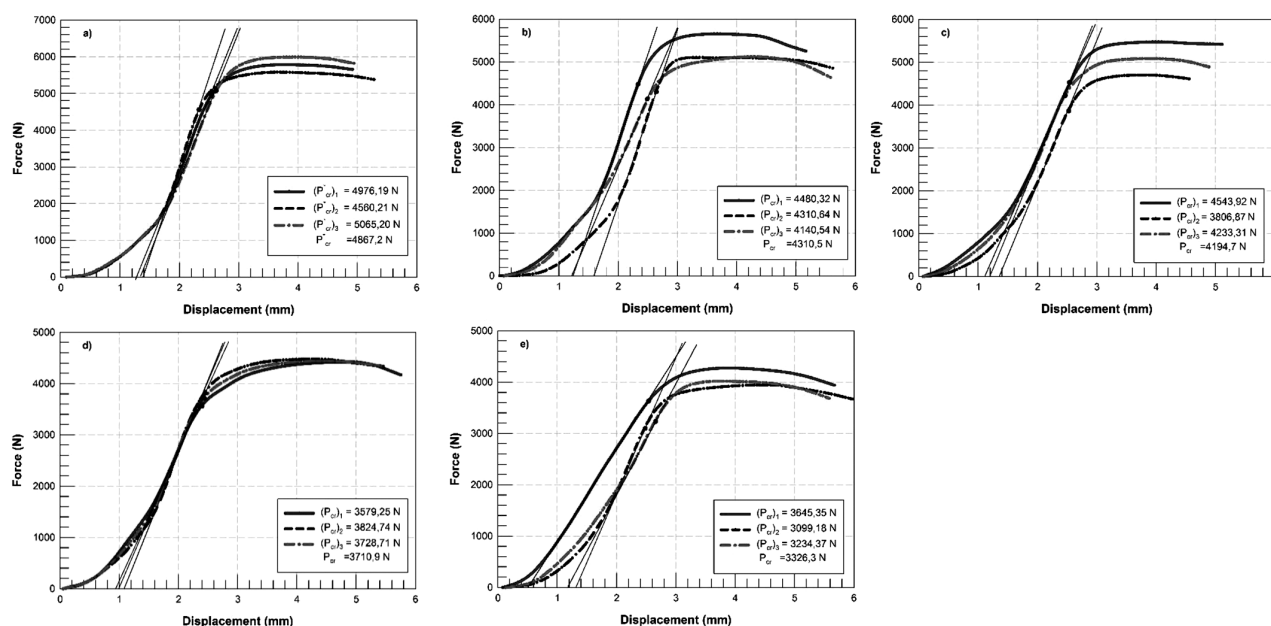


Figure 4: Experimental critical buckling loads for: a) without a hole, b) 10 mm hole diameter, c) 20 mm hole diameter, d) 30 mm hole diameter and e) 40 mm hole diameter

Slika 4: Eksperimentalne kritične upogibne obremenitve pri: a) brez luknje, b) premer luknje 10 mm, c) premer luknje 20 mm, d) premer luknje 30 mm in e) premer luknje 40 mm

from this figure that the experimental and numerical results are consistent with each other. **Figures 5 and 6** were automatically scaled starting at buckling loads of 1000 N and 2800 N, respectively, in order to clarify the difference between of the results.

From **Table 2** and **Figure 5**, it is concluded that the critical buckling load for all the types of fiber orientation angle has the highest value for the specimens without a hole and the lowest value for the specimens having a 40 mm hole diameter.

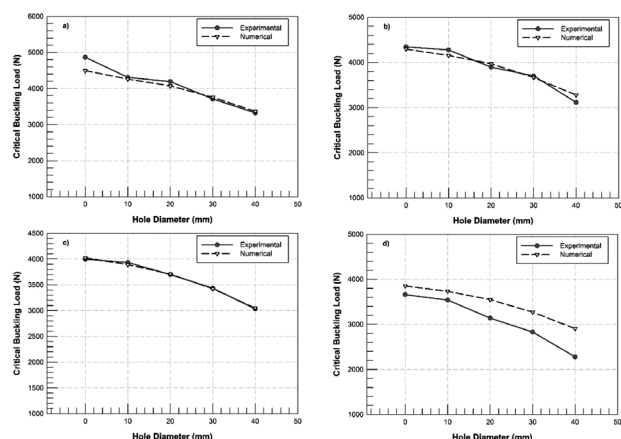


Figure 5: Comparison between the experimental and numerical results for fiber orientations: a) $[0^\circ/90^\circ]_2s$, b) $[-15^\circ/15^\circ]_2s$, c) $[-30^\circ/30^\circ]_2s$ and d) $[-45^\circ/45^\circ]_2s$

Slika 5: Primerjava rezultatov preizkusov in numeričnih rezultatov pri orientaciji vlaken: a) $[0^\circ/90^\circ]_2s$, b) $[-15^\circ/15^\circ]_2s$, c) $[-30^\circ/30^\circ]_2s$ in d) $[-45^\circ/45^\circ]_2s$

Figure 6 shows the variation in the critical buckling load versus the hole diameter in terms of fiber orientation. The critical buckling load for the same hole diameter is maximum at the orientation angle of $[(0^\circ/90^\circ)_2]_s$ and it decreases with the order of $[(-15^\circ/15^\circ)_2]_s$, $[(-30^\circ/30^\circ)_2]_s$ and $[(-45^\circ/45^\circ)_2]_s$ as reported in **Figure 6**. And also, the critical buckling load gradually decreases, while the hole diameter increases for all the types of fiber orientation.

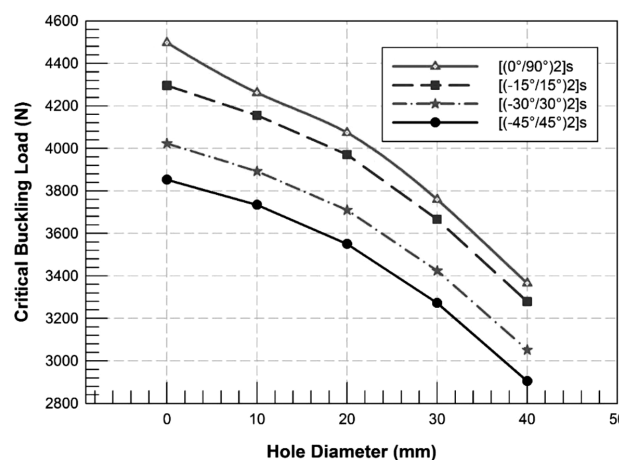


Figure 6: Numerical results for the critical buckling load versus the hole diameter for all types of fiber orientation

Slika 6: Numerični rezultati za kritično upogibno obremenitev v odvisnosti od premera luknje, pri vseh orientacijah vlaken

4 CONCLUSION

In this study, the buckling response of the composite plates with symmetric orientation angles such as $[(0^\circ/90^\circ)_2]_s$, $[(-15^\circ/15^\circ)_2]_s$, $[(-30^\circ/30^\circ)_2]_s$ and $[(-45^\circ/45^\circ)_2]_s$ with a single circular hole were examined by employing an experimental study and a numerical analysis performed with the finite-element technique. The conclusions that can be made in the contribution are as follows:

- The critical buckling loads are strongly dependent on the hole size for all the types of fiber orientation.
- The maximum values of the critical buckling load were obtained for the specimens with the $[(0^\circ/90^\circ)_2]_s$ orientation angle.
- The buckling load decreases exponentially with a decrease in the fiber orientation angle of the composite material.

5 REFERENCES

- ¹ H. Akbulut, O. Gundogdu, M. Şengül, *Finite Elements in Analysis and Design*, 46 (2010) 12, 1061–1067, doi:10.1016/j.finel.2010.07.004
- ² Y. Arman, M. Zor, S. Aksoy, *Composites Science and Technology*, 66 (2006) 15, 2945–2953, doi:10.1016/j.compscitech.2006.02.014
- ³ M. Aydin Komur, F. Sen, A. Ataş, N. Arslan, *Advances in Engineering Software*, 41 (2010) 2, 161–164, doi:10.1016/j.advengsoft.2009.09.005
- ⁴ D. Ouinas, B. Achour, *Composites Part B: Engineering*, 55 (2013), 575–579, doi:10.1016/j.compositesb.2013.07.011
- ⁵ M. Aydogdu, *Composites Science and Technology*, 67 (2007) 6, 1096–1104, doi:10.1016/j.compscitech.2006.05.021
- ⁶ N. I. Kim, J. Lee, *International Journal of Mechanical Sciences*, 68 (2013), 246–257, doi:10.1016/j.ijmecsci.2013.01.023
- ⁷ W. Y. Jung, S. C. Han, *Composite Structures*, 109 (2014), 119–129, doi:10.1016/j.compstruct.2013.10.055
- ⁸ F. Laurin, N. Carrere, J. F. Maire, *Composite Structures*, 80 (2007) 2, 172–182, doi:10.1016/j.compstruct.2006.04.074
- ⁹ S. Y. Lee, D. Y. Park, *International Journal of Solids and Structures*, 44 (2007) 24, 8006–8027, doi:10.1016/j.ijsolstr.2007.05.023
- ¹⁰ H. Matsunaga, *Composite Structures*, 68 (2005) 4, 439–454, doi:10.1016/j.compstruct.2004.04.010
- ¹¹ Ö. S. Şahin, *Composites Science and Technology*, 65 (2005) 11–12, 1780–1790, doi:10.1016/j.compscitech.2005.03.007
- ¹² L. C. Shiau, S. Y. Kuo, C. Y. Chen, *Composite Structures*, 92 (2010) 2, 508–514, doi:10.1016/j.compstruct.2009.08.035
- ¹³ Z. Wu, W. Chen, *International Journal of Mechanical Sciences*, 49 (2007) 6, 712–721, doi:10.1016/j.ijmecsci.2006.10.006
- ¹⁴ A. R. Vosoughi, P. Malekzadeh, Ma. R. Banan, Mo. R. Banan, *International Journal of Non-Linear Mechanics*, 47 (2012) 3, 96–102, doi:10.1016/j.ijnonlinmec.2011.11.009
- ¹⁵ P. Dash, B. N. Singh, *Mechanics Research Communications*, 46 (2012), 1–7, doi:10.1016/j.mechrescom.2012.08.002
- ¹⁶ M. Darvizeh, A. Darvizeh, R. Ansari, C. B. Sharma, *Composite Structures*, 63 (2004) 1, 69–74, doi:10.1016/s0263-8223(03)00133-8
- ¹⁷ Y. Tang, X. Wang, *International Journal of Mechanical Sciences*, 53 (2011) 2, 91–97, doi:10.1016/j.ijmecsci.2010.11.005
- ¹⁸ U. Topal, Ü. Uzman, *Thin-Walled Structures*, 45 (2007) 7–8, 660–669, doi:10.1016/j.tws.2007.06.002
- ¹⁹ I. Shufrin, O. Rabinovitch, M. Eisenberger, *Composite Structures*, 82 (2008) 4, 521–531, doi:10.1016/j.compstruct.2007.02.003
- ²⁰ P. Malekzadeh, M. Shojaee, *Thin-Walled Structures*, 71 (2013), 108–118, doi:10.1016/j.tws.2013.05.008
- ²¹ T. Özben, *Computational Materials Science*, 45 (2009) 4, 1006–1015, doi:10.1016/j.commatsci.2009.01.003
- ²² E. Eryiğit, M. Zor, Y. Arman, *Composites Part B: Engineering*, 40 (2009) 2, 174–179, doi:10.1016/j.compositesb.2008.07.005
- ²³ A. Kursun, M. Senel, *Experimental Techniques*, 37 (2013) 6, 41–48, doi:10.1111/j.1747-1567.2011.00738.x

CORROSION OF THE REFRACTORY ZIRCONIA METERING NOZZLE DUE TO MOLTEN STEEL AND SLAG

KOROZIJA OGNJEODPORNE CIRKONSKE DOZIRNE ŠOBE S STALJENIM JEKLOM IN ŽLINDRO

Klaudia Wiśniewska, Dominika Madej, Jacek Szczerba

AGH University of Science and Technology, Faculty of Materials Science and Ceramics, Department of Ceramics and Refractories,
Al. A. Mickiewicza 30, 30-059 Kraków, Poland
kwis@agh.edu.pl

Prejem rokopisa – received: 2014-08-08; sprejem za objavo – accepted for publication: 2015-03-03

doi:10.17222/mit.2014.188

This paper presents a study on the phase composition and microstructure changes of a sintered Mg-stabilized zirconia metering nozzle exposed to the corrosive effect of the molten steel and slag in a tundish for continuous casting for 30 h. A macroscopic observation of the corroded material showed cracks and two zones that were distinguished with respect to colour. An X-ray diffraction analysis showed that the dark layer was richer in stabilized ZrO_2 than the light layer. After the corrosion test, the nozzle had higher contents of MgO , SiO_2 , CaO , Al_2O_3 and Fe_2O_3 than the reference sample as evidenced by an X-ray fluorescence analysis. Moreover, during the corrosion process, liquid steel and slag infiltrated the zirconia material, which was confirmed with a SEM investigation. Along the hot face of the metering nozzle, the grains of zirconium oxide recrystallized with a high-temperature structure of ZrO_2 and dissolved MgO and CaO derived from the slag, stabilizing this phase.

Keywords: partially stabilized ZrO_2 , metering nozzle, corrosive effect of molten steel, refractories

Članek predstavlja študijo fazne sestave in mikrostrukturnih sprememb sintrane, z Mg stabilizirane cirkonske dozirne šobe, izpostavljene korozivnim vplivom staljenega jekla in žlindre po 30 urnem delovanju v vmesni ponovci pri postopku kontinuirnega litja. Makroskopsko opazovanje korodiranega materiala je pokazalo razpoke in dve področji, ki sta se razlikovali po barvi. Rentgenska difrakcijska analiza je pokazala, da je bilo temnejše področje bogatejše s stabiliziranim ZrO_2 , kot pa svetlejša področja. Rentgenska fluorescenčna analiza je pokazala, da ima šoba po korozivnem preizkusu, v primerjavi z referenčnim vzorcem, višjo vsebnost MgO , SiO_2 , CaO , Al_2O_3 in Fe_2O_3 . Poleg tega sta, med procesom korozije, tekoče jeklo in žlindra prodirala v cirkonijev material, kar je bilo potrjeno s SEM preiskavo. vzdolž vročega čela dozirne šobe so zrna cirkonijevega oksida rekristalizirala v visoko temperaturno strukturo ZrO_2 , raztopila MgO in CaO , ki izvirata iz žlindre in stabilizirala to fazo.

Ključne besede: delno stabiliziran ZrO_2 , dozirna šoba, korozivski vpliv staljenega jekla, ognjevarna gradiva

1 INTRODUCTION

Partially stabilized ZrO_2 (PSZ) materials are widely used as refractories owing to their high refractoriness, high corrosion resistance and good thermal-shock resistance. In the metal industry, the most popular are Mg- and Ca-stabilized zirconia and Y-stabilized zirconia, applied in the production of thermal-barrier coatings. It is commonly known that during the corrosion process of PSZ due to molten steel and slag, a cubic or tetragonal phase is destabilized and transformed into monoclinic zirconia, related to the microcrack formation¹. The destabilization process is associated with the reaction of SiO_2 from slag with CaO and MgO from the zirconia material^{2,3}. Zirconium oxide is used for metering nozzles in the continuous casting of steel^{2,4,5}. A metering nozzle is mounted to the bottom of a tundish and used to control the flow of molten steel. The working temperature of a metering nozzle is up to 1600 °C.

The main factors causing the damage of the metering nozzle are the erosion of the liquid flowing steel, the infiltration of the molten steel and slag into the refractory material, the slag composition and the rapid tem-

perature changes². The chemical composition of the slag is based on the MgO - CaO - SiO_2 - Al_2O_3 system, but the proportion between the components depends on the type of the produced steel.

In this paper the phase composition and microstructure changes of a sintered Mg-stabilized zirconia metering nozzle, exposed to the corrosive effect of the molten low-carbon steel and slag in a tundish for continuous casting for 30 h were studied.

2 EXPERIMENTAL METHOD

The procedure of this experiment included the following steps: preparing a sintered Mg-stabilized zirconia metering nozzle under industrial conditions, a corrosion test in a tundish for continuous steel casting and a post-experiment study of the zirconia metering nozzle.

The metering nozzle was exposed to a corrosive environment for 30 h. The factors influencing the corrosion of the nozzle were the molten steel and slag. After the corrosion test, the corroded nozzle (designated as CN)

was studied and compared with the reference sample (designated as RS), which was a zirconia metering nozzle before serving. For the XRF, XRD and SEM/EDS investigations, the samples were taken from the middle of the heights of the metering nozzles.

The X-ray fluorescence (XRF) method was used to determine the contents of oxides such as MgO, SiO₂, CaO, Al₂O₃ and Fe₂O₃. An Axios mAX wavelength dispersive X-ray fluorescence spectrometer from PANalytical was used for this study. The crystalline phases were identified with X-ray diffraction using Cu-K α radiation on a FPM Seifert XRD7 diffractometer with the Bragg-Brentano geometry, while the quantitative composition was determined with the Rietveld method. The dark zone (designated as CN-D) and the light zone (designated as CN-L) of the corroded nozzle were examined separately. The microstructure was observed using a scanning electron microscope (SEM) coupled with an energy-dispersive X-ray system (EDS). The ultra-high-definition NOVA NANO SEM 200 was used for this purpose.

3 RESULTS

During a macroscopic observation of the corroded material, cracks and two zones were distinguished with respect to colour. The dark zone was strongly corroded due to molten steel and slag (the hot-zone refractory material) while the light zone remain unchanged. **Figure 1** shows a photograph of the metering nozzle exposed to the corrosive effect of the molten steel.

The XRF analysis confirmed that the main component of the nozzle was zirconium oxide; the content of ZrO₂ was about 90 % in both CN and RS samples. Moreover, the XRF study revealed content changes in the oxides such as MgO, SiO₂, CaO, Al₂O₃ and Fe₂O₃. After the corrosion test, sample CN had higher contents of these oxides, which is illustrated in **Figure 2**.

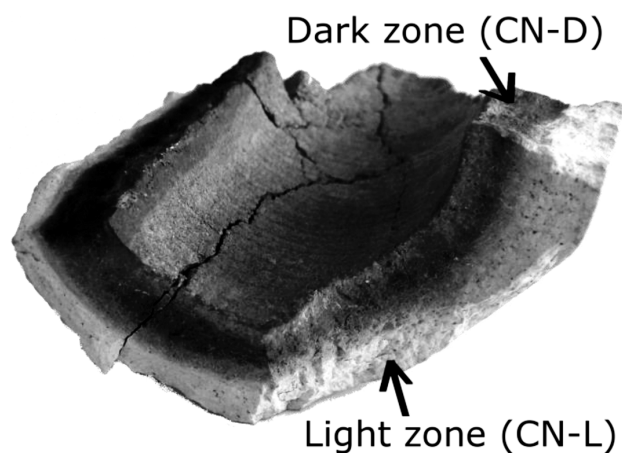


Figure 1: Refractory zirconia metering nozzle exposed to the corrosive effect of the molten steel and slag

Slika 1: Ognjevarna cirkonska dozirna šoba, izpostavljena korozivskemu vplivu staljenega jekla in žilindre

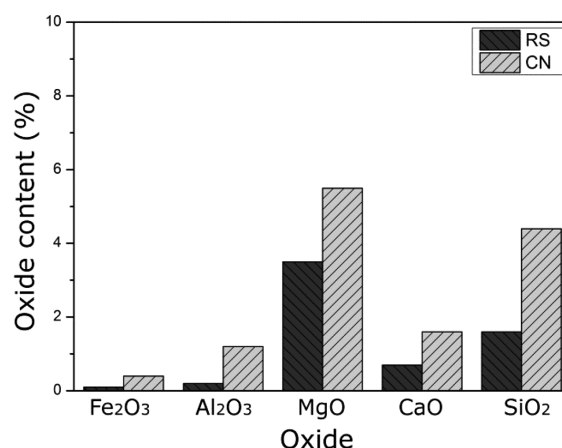


Figure 2: Contents of the secondary oxides in test samples RS and CN (XRF analysis)

Slika 2: Vsebnost sekundarnih oksidov v preizkusnih vzorcih RS in CN (XRF-analiza)

The XRD analysis with the Rietveld quantitative-phase analysis showed that the dark layer (CN-D) was richer in the stabilized ZrO₂ than the light layer (CN-L) or the RS sample. In the CN-D sample, the content of the stabilized zirconium oxide was 11.5 %, while in the

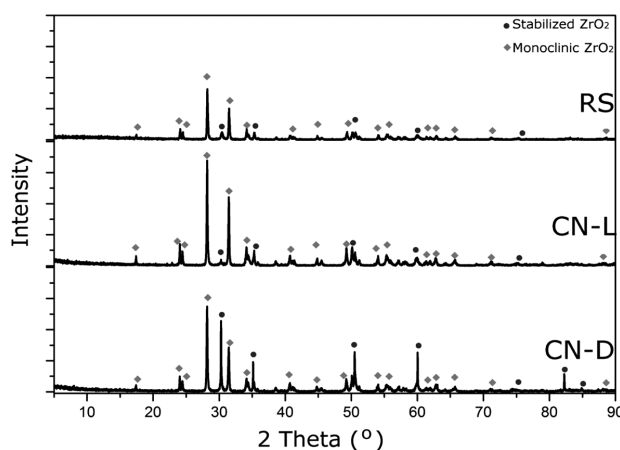


Figure 3: XRD patterns of test samples RS, CN-L and CN-D

Slika 3: Rentgenogrami preizkusnih vzorcev RS, CN-L in CN-D

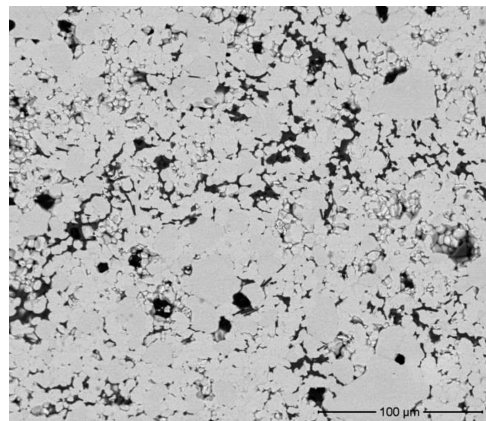


Figure 4: Microstructure of test sample RS

Slika 4: Mikrostruktura preizkusnega vzorca RS

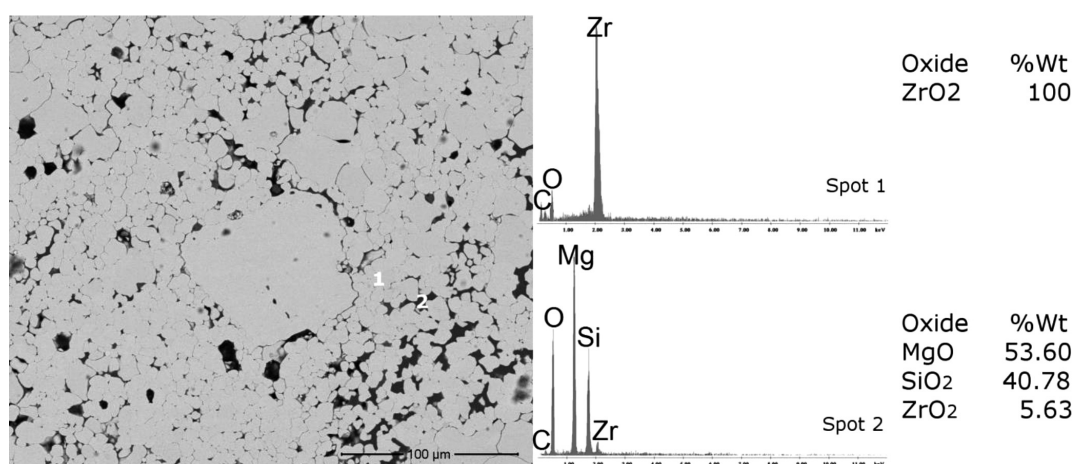


Figure 5: Microstructure of test sample CN-L obtained with the EDS analysis; Spot 1 – zirconium oxide, Spot 2 – forsterite
Slika 5: Mikrostruktura preizkusnega vzorca CN-L z EDS-analizo; točka 1 – cirkonov oksid, točka 2 – forsterit

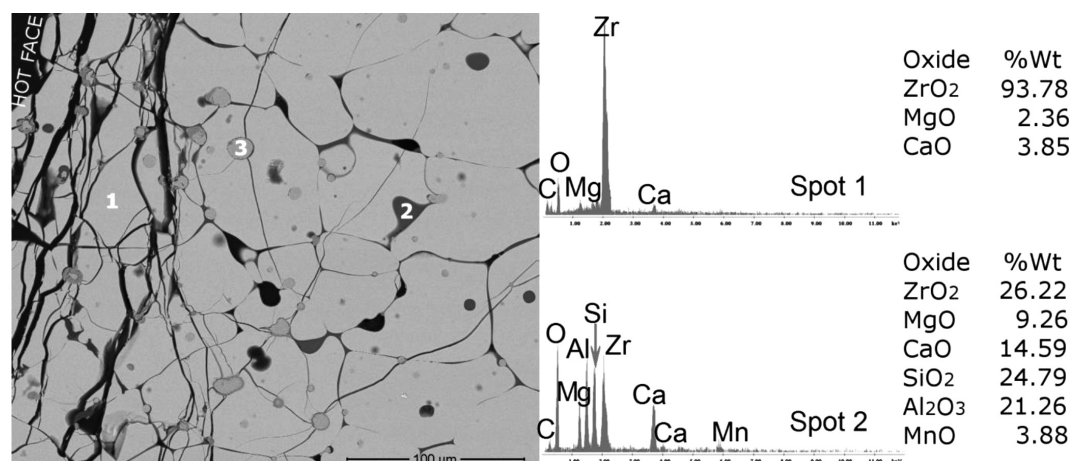


Figure 6: Microstructure of test sample CN-D obtained with the EDS analysis; Spot 1 – zirconium oxide, Spot 2 – slag, Spot 3 – iron
Slika 6: Mikrostruktura preizkusnih vzorcev CN-D z EDS-analizo; točka 1 – cirkonov oksid, točka 2 – žlindra, točka 3 – železo

CN-L sample, it was 1 % and in the RS sample, it was 3.3 %. The XRD results are shown in **Figure 3**.

Figures 4 to 6 show the microstructures of test samples RS, CN-L and CN-D, respectively. The microstructure of the CN-L sample is similar to the reference sample. The grains of zirconium oxide are surrounded by a silicate phase. The microstructure of sample CN-D shows micro-fracturing along the hot-face of the nozzle. The crystallites of zirconium oxide are bigger than in samples CD-L and RS.

4 DISCUSSION

In the reference sample, the main crystalline phases were monoclinic ZrO₂ and Mg-stabilized zirconium oxide, which were confirmed with the XRD analysis. The SEM/EDS investigation showed that the secondary phase was forsterite (Mg₂SiO₄). However, the content of forsterite was too low to be detected on the XRD pattern. After the operation, there were two zones in the nozzle, a corroded and an uncorroded zone. The XRD analysis

with the Rietveld method confirmed that test samples CN-L and RS were not significantly different in their phase composition. The biggest changes in the phase composition were found in the corroded zone (CN-D), where the content of stabilized zirconia was the highest.

The obtained results are not in agreement with the earlier results presented in^{2,3,5}. The stabilization process of zirconium oxide can be explained with the dissolution of MgO and CaO derived from the slag in zirconia at a high temperature. The XRF and SEM/EDS investigations confirmed that, at the temperature of the corrosion test, the molten slag and steel penetrated the zirconia nozzle.

As can be seen in **Figure 6**, the microstructure of CN-D was changed. The fine grains of ZrO₂ recrystallized at the corrosion-test temperature, which was observed as an increase in their dimension. The high-temperature phase of zirconium oxide was stabilized due to MgO and CaO, which dissolved in ZrO₂. The micro-fractures along the hot face of the metering nozzle and the macroscopic cracks present in the corroded nozzle could be attributed to the rapid temperature changes during the corrosion test.

5 CONCLUSION

The results of the corrosion of a refractory zirconia metering nozzle tested under industrial conditions are reported. During the service in a continuous-casting tundish, the molten steel and slag infiltrated the zirconia nozzle. A rapid change in the temperature had a significant influence on the formation of cracks and microfractures.

Along the hot face of the zirconia nozzle, the grains of ZrO_2 recrystallized with a high-temperature structure. The oxides present in the slag dissolved in zirconia and stabilized the ZrO_2 phase.

Acknowledgments

This work was supported by grant no. INNOTECH-K2/IN2/16/181920/NCBR/13 of the National Centre for Research and Development.

6 REFERENCES

- ¹ A. Sibil, T. Douillard, C. Cayron, N. Godin, M. R'mili, G. Fantozzi, Microcracking of high zirconia refractories after $t \rightarrow m$ phase transition during cooling: An EBSD study, *Journal of the European Ceramic Society*, 31 (2011), 1525–1531, doi:10.1016/j.jeurceramsoc.2011.02.033
- ² E. Volceanov, A. Abagiu, M. Becherescu, A. Volceanov, P. Nita, R. Trusca, F. Mihalache, Development of Zirconia Composite Ceramics and Study on Their Corrosion Resistance up to 1600 °C, *Key Engineering Materials*, 264–268 (2004), 1739–1742, doi:10.4028/www.scientific.net/KEM.264-268.1739
- ³ Y. Hemberger, C. Berthold, K. G. Nickel, Wetting and Corrosion of Yttria Stabilized Zirconia by Molten Slags, *Journal of the European Ceramic Society*, 32 (2012), 2859–2866, doi:10.1016/j.jeurceramsoc.2011.12.005
- ⁴ A. H. Bui, S. C. Park, I. S. Chung, H. G. Lee, Dissolution Behavior of Zirconia Refractories During Continuous Casting of Steel, *Metals and Materials International*, 12 (2006) 5, 435–440, doi:10.1007/BF03027711
- ⁵ M. O. Suk, J. H. Park, Corrosion Behaviors of Zirconia Refractory by $CaO-SiO_2-MgO-CaF_2$ Slag, *Journal of the American Ceramic Society*, 92 (2009), 717–723, doi:10.1111/j.1551-2916.2008.02905.x

EFFECTS OF AN EPOXY-RESIN-FIBER SUBSTRATE FOR A Ω -SHAPED MICROSTRIP ANTENNA

VPLIV Z VLAJNI OJAČANE EPOKSI PODLAGE PRI Ω -OBLIKI MIKROTRAKASTE ANTENE

**Md. Moinul Islam¹, Mohammad R. I. Faruque¹, Mohammad Tariqul Islam²,
Haslina Arshad³**

¹Centre for Space Science (ANGKASA), Kompleks Penyelidikan Building, Universiti Kebangsaan, Malaysia

²Department of Electrical, Electronic & Systems Engineering, Universiti Kebangsaan, Malaysia

³Centre of Artificial Intelligence Technology, Universiti Kebangsaan Malaysia, 43600 UKM, Bangi, Selangor D. E., Malaysia
mmoislam@yahoo.com; rashedgen@yahoo.com; titareq@yahoo.com; has@ftsm.ukm.my

Prejem rokopisa – received: 2014-08-18; sprejem za objavo – accepted for publication: 2015-03-09

doi:10.17222/mit.2014.206

A Ω -shaped microstrip antenna using an epoxy-resin-fibre substrate is presented. The proposed antenna consists of a circular slot and two rectangular slots printed on a dielectric resin-fibre substrate and is excited by a 50- Ω microstrip transmission line. A commercially available, high-frequency structural simulator (HFSS) based on the finite-element method (FEM) was used in this investigation. The nearly omni-directional and bidirectional radiation pattern exhibited average gains of 3.12 dBi and 5.44 dBi for the lower band and upper band, respectively. The effects of epoxy-resin-fiber are discussed through comparisons of different substrate materials.

Keywords: epoxy resin-fibre, microstrip line, Ω -shaped

Predstavljena je mikrotrakasta antena Ω -oblike na epoksi podlagi, ojačani z vlakni. Predlagana antena sestoji iz krožne reže in dveh pravokotnih rež, natisanih na dielektrični podlagi iz smole z vlakni in sta vzbujani s 50 Ω mikrotrakastim vodnikom. V tej preiskavi je bil uporabljen komercialno razpoložljiv visoko frekvenčni strukturni simulator (HFSS), ki temelji na metodi končnih elementov (FEM). V spodnjem in zgornjem pasu je vsesmerno sevanje kazalo 3,12 dBi, dvosmerno sevanje pa 5,44 dBi. Vpliv vlaken za ojačanje je bil prikazan s primerjavo različnih materialov podlage.

Ključne besede: vlakna za ojačanje epoksija, mikrotrakasta linija, Ω -oblika

1 INTRODUCTION

The microstrip patch antenna plays an important role as a harbinger in wireless communication systems and is now being used to address the changing demands of future antenna technology. The microstrip patch antenna has been extensively used in wireless communication systems, because they are conformal, have a low profile, are easy to fabricate with integrated circuits (ICs), and enable easy integration with array and electronic components. Many researchers have an interest in designing microstrip antennas and still face a major challenge to implement these applications. Currently, various types of antennas have been proposed to face the increasing requirements for a modern bearable wireless communication device that has the capability of consolidating more than one communication system into a single module.¹⁻⁶

In⁷, a rectangular slot antenna was proposed for dual-frequency operation. Su et al.⁸ presented a printed dipole antenna using U-slot arms to enable dual-band operation. Suh and Chang⁹ reported a low-cost microstrip dipole antenna for wireless communications. In¹⁰, a PIFA antenna with a U-slot was presented for dual-band operation. Lin et al.¹¹ mentioned a dual-loop antenna for

use with a 2.4/5 GHz Wireless LAN. A monopole antenna with double-T was presented in¹² for 2.4/5.2-GHz WLAN operations. A planar antenna was investigated with bandwidth enhancement for X-band applications¹³. An E-shaped patch antenna of wideband circularly polarized was presented for wireless applications¹⁴. A Compact 5.5-GHz Band-Rejected UWB Antenna was proposed using Complementary Split Ring Resonators¹⁵. A new double L-shaped multiband patch antenna was presented on a polymer resin material substrate¹⁶.

In this study, a Ω -shaped microstrip antenna was designed on a 1.6-mm-thick epoxy-resin-fibre substrate material. The downlink frequency range is from 4.74 GHz to 4.87 GHz and the uplink frequency range is from 8.42 GHz to 8.73 GHz. The results will be discussed in detail with a parametric study.

2 ANTENNA GEOMETRY AND PARAMETRIC STUDY

High-Frequency Structure Simulator (HFSS), a commercially available Ansoft package, is a powerful and efficient three-dimensional (3D) full-wave simulation software that solves EM equations through the subdivision of a large problem into easy constituent units

and then consolidating the solution as a matrix of simultaneous equations for the complete problem space, which provides a numerical solution to Maxwell's equations using the FEM. Hence, HFSS was used in this study.

The geometry of the proposed antenna is shown in **Figure 1**. The antenna comprises three conducting slots on the patch and two on the ground. A circular slot and two similar lateral rectangular slots are on the patch and two rectangular slots are on the ground of the proposed antenna. The two rectangular slots are of equal length L_p and width W_p . R is the radius of the circular slot. The design procedure begins with the radiating patch, along with the substrate, the ground plane and a feed line. The antenna was printed on a FR4 substrate with 1.6 mm in thickness that exhibits a relative permittivity of 4.60, a relative permeability of 1, and a dielectric loss tangent of 0.02. One circular slot and two rectangular slots are cut from the rectangular copper patch. Another two rectangular slots are also cut from the ground plane. In this manner, the proposed slotted circle patch antenna is produced. Two resonant frequencies of 4.51 GHz and 8.35 GHz are obtained by adjusting the length and width of the slots of the proposed antenna. Here, a microstrip line is used to feed the RF signal into the proposed antenna. The Sub Miniature version A (SMA) connector

is used at the end of antenna feeding line for the input RF signal.

Finally, the optimal dimensions were determined as follows: $L = 40$ mm, $L_p = 12$ mm, $L_g = 40$ mm, $L_s = 4$ mm, $R = 12$ mm, $W = 40$ mm, $W_p = 4$ mm, $W_g = 40$ mm, $M_l = 17$ mm, and $M_w = 6$ mm.

The epoxy-resin-fibre consists of reinforcing insulation material. There are various types of epoxy-resin-fibre material for use as an antenna substrate. In this study, we have used FR4 as the epoxy-resin-fibre substrate material that is impregnated with thermoset resin. FR4 has superior mechanical and dielectric properties, good moisture/heat resistance, stable electrical performance at high temperature, good flatness and a smooth surface. FR4 is widely used to produce printed-circuit boards (PCBs).

The length, width, VSWR, return loss of the patch antenna can be calculated from Equations (1) to (6) presented in¹⁷, where L and W are the length and width of the patch, respectively, c is the velocity of light, ϵ_r is the dielectric constant of substrate, h is the thickness of the substrate, f_0 is the target centre frequency, ϵ_e is the effective dielectric constant and ρ is the radiation coefficient:

$$W = \frac{c}{2f_0} \sqrt{\frac{\epsilon_r + 1}{2}} \quad (1)$$

$$L = \frac{c}{2f_0 \sqrt{\epsilon_r}} - 2\Delta l \quad (2)$$

$$\epsilon_e = \frac{1}{2}(\epsilon_r + 1) + \frac{1}{2}(\epsilon_r - 1) \sqrt{1 + \frac{10h}{W}} \quad (3)$$

$$\Delta l = 0.412h \frac{(\epsilon_e + 0.3)(W/h + 0.8)}{(\epsilon_e - 0.258)(W/h + 0.8)} \quad (4)$$

$$VSWR = \frac{1 + \rho}{1 - \rho} \quad (5)$$

$$\text{Return loss} = -10 \lg \left(\frac{1}{\rho^2} \right) \quad (6)$$

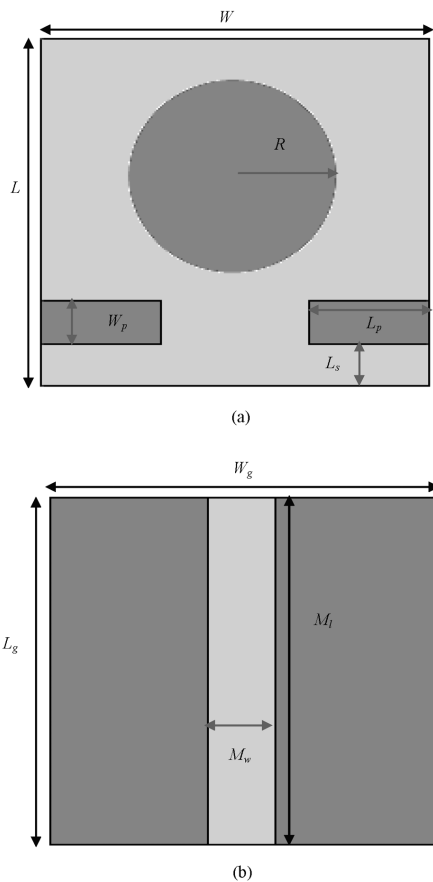


Figure 1: Proposed antenna: a) top view and b) bottom view
Slika 1: Predlagana antenna: a) pogled iz vrha in b) pogled iz dna

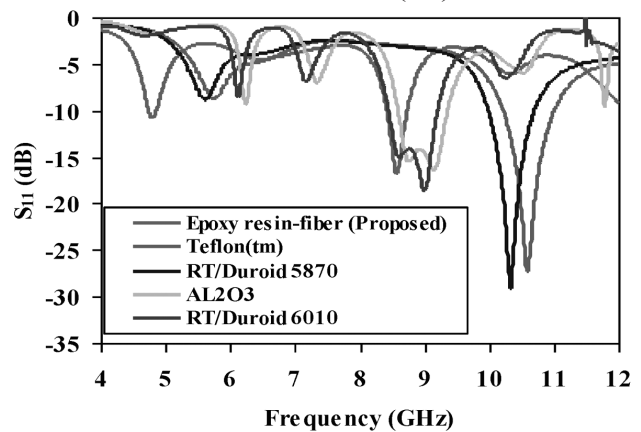


Figure 2: Return loss of simulation using different substrate materials
Slika 2: Povratne izgube pri simulaciji z uporabo različnih materialov podlage

Table 1: Dielectric properties of the different substrates**Tabela 1:** Dielektrične lastnosti različnih podlag

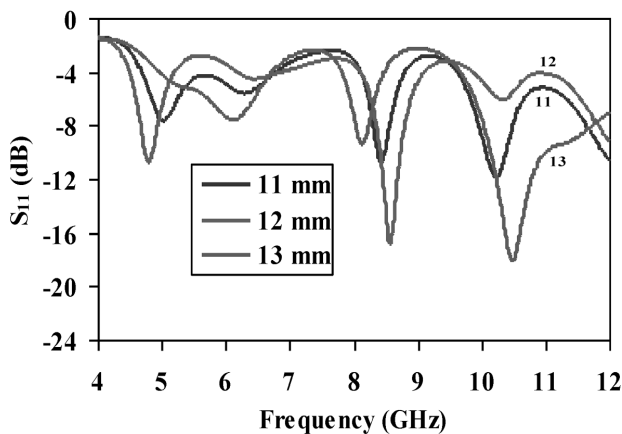
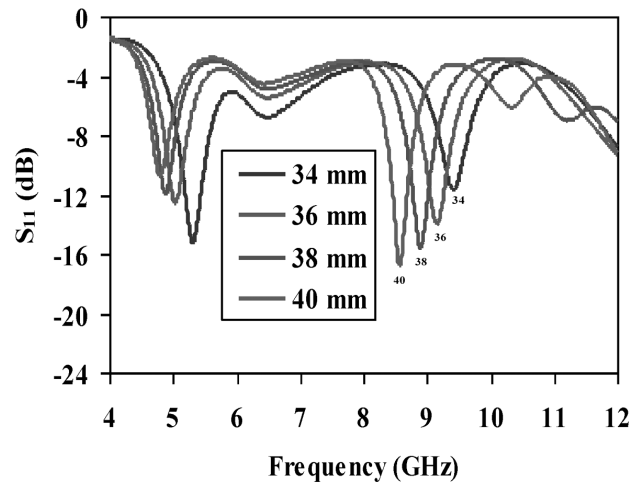
Material	Permittivity	Loss Tangent
Teflon (tm)	2.1	0.01
RT/Duroid 5870	2.33	0.0023
Epoxy resin-fiber (Proposed)	4.66	0.02
Al ₂ O ₃	9.8	0.0009
RT/Duroid 6010	10.2	0.0023

The return losses determined by the simulation using different substrate materials are shown in **Figure 2**. No resonance was found on the lower band when we used the high-permittivity materials of Duroid 6010, and Al₂O₃ ceramic and the low permittivity materials of Duroid 5870, and Teflon as a substrate. Finally, FR4 was used in the proposed design as the epoxy-resin-fiber substrate material and two strong resonances were achieved, with the desired bandwidth and high gain. The 10-dB bandwidths of 130 MHz from 4.74 GHz to 4.87 GHz and of 310 MHz from 8.42 GHz to 8.73 GHz were achieved. The dielectric properties of the materials are listed in **Table 1**.

A parametric study was performed to observe the effects of the proposed antenna parameters. In particular, the effects of the different parameters on the return loss were observed.

Figure 3 shows the return loss of the simulation for different values of R . The simulation includes $L = 40$ mm, $L_p = 12$ mm, $L_g = 40$ mm, $L_s = 4$ mm, $W = 40$ mm, $W_p = 4$ mm, $W_g = 40$ mm, $M_1 = 17$ mm, and $M_w = 6$ mm with the different values of R . The graph indicates that better coupling is obtained for the upper band using the value of radius as 11 mm and 13 mm. By using $R = 12$ mm, the desired dual-band operation was obtained, with a better coupling on both the lower and upper bands.

The return loss of the simulation for different values of M_1 is shown in **Figure 4**. The simulation includes $L = 40$ mm, $L_p = 12$ mm, $L_g = 40$ mm, $L_s = 4$ mm, $R = 12$ mm, $W = 40$ mm, $W_p = 4$ mm, $W_g = 40$ mm and $M_w = 6$

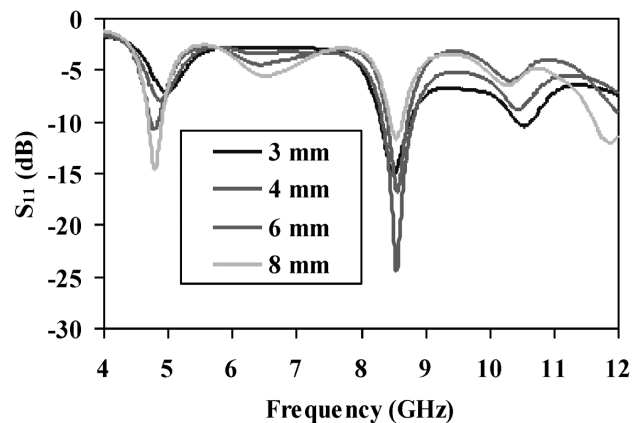
**Figure 3:** Return loss of the simulation using different values of R
Slika 3: Povratne izgube pri simulaciji z uporabo različnih vrednosti R **Figure 4:** Return loss of the simulation using different values of M_1
Slika 4: Povratne izgube pri simulaciji z uporabo različnih vrednosti M_1

mm with M_1 . The results presented in the graph clearly indicate that improved coupling was achieved at the upper band when using the value of M_1 as 40 mm. As a result, the optimized value is 40 mm.

Figure 5 shows the return loss simulation for different values of M_w . The simulation includes $L = 40$ mm, $L_p = 12$ mm, $L_g = 40$ mm, $L_s = 4$ mm, $R = 12$ mm, $W = 40$ mm, $W_p = 4$ mm, $W_g = 40$ mm, $M_1 = 17$ mm, and with the different values of M_w . The width of the microstrip line has a greater effect on the coupling for both the lower- and upper-band frequencies. This coupling can be achieved when M_w is 6 mm.

3 RESULTS AND DISCUSSION

The gain of the proposed antenna is shown in **Figure 6**. An average gain of 3.12 dBi is achieved with the first resonance of 4.80 GHz and 5.44 dBi is achieved with the second resonance of 8.57 GHz. In addition, the gain for the upper band is greater than that for the lower band. **Figure 7** shows the radiation efficiency of the proposed

**Figure 5:** Return loss of the simulation using different values of M_w
Slika 5: Povratne izgube pri simulaciji z uporabo različnih vrednosti M_w

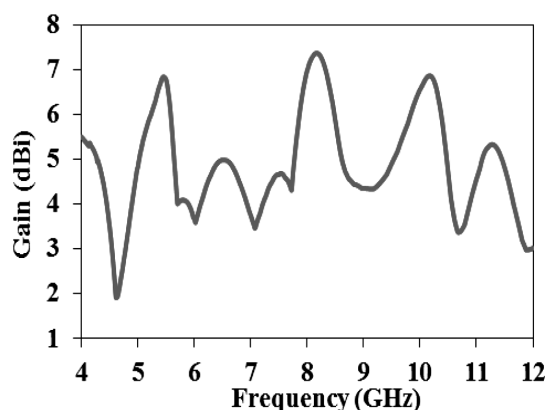


Figure 6: Gain of the proposed antenna

Slika 6: Izkoristek predlagane antene

antenna. The average lower-band efficiency is 75.18 % and the higher-band efficiency is 81.35 %, i.e., the lower-band radiation efficiency is smaller than the higher-band efficiency.

The radiation pattern of the proposed antenna is shown in Figure 8 for: a) 4.80 GHz at the E-plane, b) 4.80 GHz at the H-plane, c) 8.57 GHz at the E-plane, d) 8.57 GHz at the H-plane. The E_ϕ and E_θ fields indicate the cross-polar and co-polar components, respectively. The effect of cross-polarization in the radiation pattern is due to the lower microstrip antenna. The cross polarization effect is higher in the H-plane for both resonances. When the frequency increases, the effect increases, enabling simple interpretation from the radiation pattern. Moreover, nearly omni-directional and symmetrical radiation patterns were attained along both the E-plane and the H-plane. The same radiation pattern was found to exist over the C and X-bands. The obtained radiation patterns indicate that the proposed antenna delivers linear polarization, where the level of cross-polarization is lower than that of the co-polarization in all of the simulated radiation patterns. When the radiation pattern of a microstrip antenna is symmetric and omni-directional, it provides some reasonable benefits. One benefit is that the resonance does not shift for different directions, so a large amount

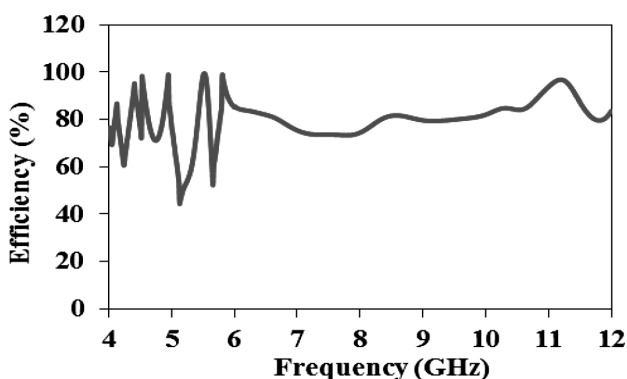


Figure 7: Radiation efficiency of the proposed antenna

Slika 7: Učinkovitost sevanja predlagane antene

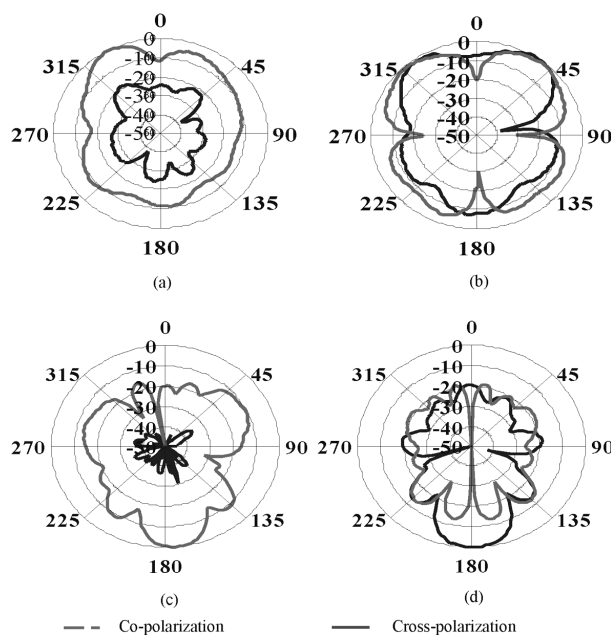


Figure 8: Radiation pattern of the proposed antenna: a) 4.80 GHz at the E-plane, b) 4.80 GHz at the H-plane, c) 8.57 GHz at the E-plane and d) 8.57 GHz at the H-plane

Slika 8: Sevalni diagram predlagane antene: a) 4,80 GHz v ravnini E, b) 4,80 GHz v ravnini H, c) 8,57 GHz v ravnini E in d) 8,57 GHz v ravnini H

of stable power is in the direction of the broadside beam. Another advantage is that the radiation pattern is more reliable on the operational bands.

Figure 9 shows the current distribution of the proposed antenna for: a) 4.51 GHz and b) 8.35 GHz. A large amount of current flows through the feeding line. The

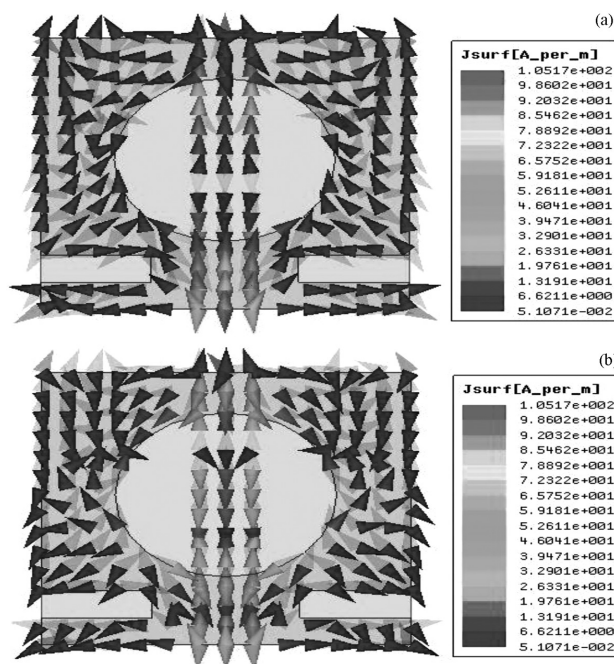


Figure 9: Current distribution at: a) 4.80 GHz and b) 8.57 GHz

Slika 9: Razporeditev toka pri: a) 4,80 GHz in b) 8,57 GHz

electric field was initiated at this point. The current distribution is more stable in the lower band than in the upper band. The creation of the electric field near the slots is reasonable. As a result, the excitation is strong over all parts of the antenna for both the lower and upper bands.

4 CONCLUSION

A Ω -shaped microstrip antenna using an epoxy-resin-fibre substrate was proposed in this paper. A simple Ω -shaped patch was proposed to miniaturize the antenna and to obtain a new operating band resonant mode. An antenna structure was designed, simulated and finally characterized. The Ω -shaped resonator, compact size, stable nearly omni-directional and directional radiation patterns, low cross-polarization, and efficiency with improved bandwidth and higher gain make the proposed Ω -shaped dual band antenna a candidate for use in C-band and X-band applications.

Acknowledgements

This work was supported by Universiti Kebangsaan Malaysia under grant, Arus Perdana, No. AP-2013-011.

5 REFERENCES

- ¹ W. C. Liu, C. M. Wu, N. C. Chu, A compact CPW-fed slotted patch antenna for dual-band operation, *IEEE Antenna Wirel. Propag. Lett.*, 9 (2010), 110–113, doi:10.1109/LAWP.2010.2044135
- ² M. M. Islam, M. R. I. Faruque, W. Hueyshin, J. S. Mandeep, T. Islam, A double inverted F-shape patch antenna for dual-band operation, *International Journal of Antennas and Propagation*, 2014 (2014), 8, doi:10.1155/2014/791521
- ³ C. P. Hsieh, T. C. Chiu, C. H. Lai, Compact dual-band slot antenna at the corner of the ground plane, *IEEE Trans. Antennas Propag.*, 57 (2009), 3423–3426, doi:10.1109/TAP.2009.2027348
- ⁴ M. M. Islam, M. T. Islam, M. R. I. Faruque, Dual-band operation of a microstrip patch antenna on a duroid 5870 substrate for Ku- and K-bands, *The Scientific World Journal*, 2013 (2013), 10, doi:10.1155/2013/378420
- ⁵ C. M. Wu, Dual-band CPW-fed cross-slot monopole antenna for WLAN operation, *IET Microw. Antennas Propag.*, 1 (2007), 542–546, doi:10.1049/iet-map:20050116
- ⁶ M. R. I. Faruque, M. T. Islam, B. Yatim, M. A. M. Ali, Analysis of the effects of metamaterials on the radio-frequency electromagnetic fields in the human head and hand, *Mater. Tehnol.*, 47 (2013) 1, 129–133
- ⁷ J. W. Wu, H. M. Hsiao, J. H. Lu, S. H. Chang, Dual broad band design of rectangular slot antenna for 2.4 and 5 GHz wireless, *Electron. Lett.*, 40 (2004), 1461–1463, doi:10.1049/el:20046873(410)
- ⁸ C. M. Su, H. T. Chen, K. L. Wong, Printed dual band dipole antenna with U-slot arms for 2.4/5.2 GHz WLAN operation, *Electr. Lett.*, 38 (2002), 1308–1309, doi:10.1049/el:20020919
- ⁹ Y. H. Suh, K. Chang, Low cost microstrip fed dual frequency printed dipole antenna for wireless communications, *Electr. Lett.*, 36 (2000), 1177–1179, doi:10.1049/el:20000880
- ¹⁰ D. Nashhat, H. A. Elsadek, H. Ghali, Dual band reduced size PIFA antenna with U-slot for blue tooth and WLAN operations, *Proc. of IEEE Antennas Propagation International Symposium*, 2 (2003), 962–965, doi:10.1109/APS.2003.1219395
- ¹¹ C. C. Lin, G. Y. Lee, K. L. Wong, Surface mount dual loop antenna for 2.4/5 GHz WLAN operations, *Electr. Lett.*, 39 (2003), 1302–1304, doi:10.1049/el:20030845
- ¹² Y. L. Kuo, K. L. Wong, Printed double-T monopole antenna for 2.4/5.2 GHz dual band WLAN operations, *IEEE Trans. Antennas Propag.*, 51 (2003), 2187–2192, doi:10.1109/TAP.2003.816391
- ¹³ M. R. I. Faruque, M. M. Islam, M. T. Islam, Investigation of a planar antenna with bandwidth enhancement for X-band applications, *Electronics World*, 120 (2014), 12–16
- ¹⁴ A. Khidre, K. F. Lee, F. Yang, A. Eisherbeni, Wideband circularly polarized E-shaped patch antenna for wireless applications, *IEEE Antennas and Propag. Magazine*, 52 (2010), 219–229, doi:10.1109/MAP.2010.5687547
- ¹⁵ M. M. Islam, M. R. I. Faruque, M. T. Islam, A Compact 5.5 GHz Band-Rejected UWB Antenna Using Complementary Split Ring Resonators, *The Scientific World Journal*, 2014 (2014), 10, doi:10.1155/2014/528489
- ¹⁶ M. H. Ullah, M. T. Islam, J. S. Mandeep, N. Misran, A new double L-shaped multiband patch antenna on a polymer resin material substrate, *Applied Physics A*, 110 (2013), 199–205, doi:10.1007/s00339-012-7114-0
- ¹⁷ I. J. Bahl, P. Bhartia, *Microstrip Antennas*, 2nd Edn., Artech House, Boston, London 1980

X-RAY RADIOGRAPHY OF AISI 4340-2205 STEELS WELDED BY FRICTION WELDING

RENTGENSKI PREGLED JEKEL AISI 4340-2205, VARJENIH S TRENJEM

Ugur Caligulu¹, Mahmut Yalcinoz², Mustafa Turkmen³, Serdar Mercan⁴

¹Firat University, Faculty of Technology, Dept. of Met. and Materials Eng., Elazig, Turkey

²Firat University, Faculty of Technical Education, Dept. of Metallurgy Education, Elazig, Turkey

³Kocaeli University, Hereke Vocational School, 41800 Kocaeli, Turkey

⁴Cumhuriyet University, Faculty of Technology, Dept. of Mechatronic Eng., Sivas, Turkey
ucaligulu@firat.edu.tr

Prejem rokopisa – received: 2014-08-25; sprejem za objavo – accepted for publication: 2015-03-04

doi:10.17222/mit.2014.211

In this study, X-ray radiographic tests of friction-welded AISI 4340-AISI 2205 steels were investigated. AISI 4340 tempered steel and AISI 2205 duplex stainless steel, each of 12 mm diameter, were used to fabricate the joints. The friction-welding tests were carried out using a direct-drive-type friction-welding machine for different parameters. After this process, the radiographic tests of the welded joints were examined by X-ray diffraction. The experimental results indicated that the AISI 4340 tempered steel could be joined to the AISI 2205 duplex stainless steel using the friction-welding technique and for achieving a weld with sufficient strength. The result of the radiographic tests indicated that by increasing the rotation speed, the friction pressure and the forging pressure, the amount of flash increased for all the specimens. In contrast, when increasing the friction time the amount of flash decreased. The best properties for steels AISI 4340-2205 were observed for the specimens welded at a rotation speed of 2200 min⁻¹, a friction pressure of 40 MPa, a forging pressure of 80 MPa, a friction time of 6 s and a forging time of 3 s.

Keywords: AISI 4340, AISI 2205, friction welding, radiographic test

V tej študiji so bili rentgensko pregledani spoji jekel AISI 4340-AISI 2205, zvarjeni s trenjem. Spoji so bili izdelani s popuščenim AISI 4340 jeklom in AISI 2205 dupleks nerjavnim jeklom, vsako premera 12 mm. Preizkus varjenja s trenjem je bil izvršen z uporabo neposredno gnanega stroja za varjenje s trenjem, pri različnih parametrih. Po tem postopku so bili zvarjeni spoji pregledani z rentgenom. Rezultati preizkusov so pokazali, da je z varjenjem s trenjem mogoče spojit AISI 4340 popuščeno jeklo in AISI 2205 dupleks nerjavno jeklo in da je mogoče dobiti zvar z zadostno trdnostjo. Rezultati rentgenskih preiskav so pokazali, da pri naraščajoči hitrosti vrtenja, tornega tlaka in tlaka pri kovanju delež zmehčanega roba narašča pri vseh vzorcih. Nasprotno pa se pri podaljšanju časa trenja zmanjša količina zmehčanega roba. Najboljše lastnosti pri jeklih AISI 4340-2205 so bile opažene pri vzorcih, varjenih z rotacijo 2200 min⁻¹, tornim tlakom 40 MPa, kovaškim tlakom 80 MPa, časom trenja 6 s in časom kovanja 3 s.

Ključne besede: AISI 4340, AISI 2205, varjenje s trenjem, rentgensko testiranje

1 INTRODUCTION

Duplex stainless steel (DSS) is well known for its excellent strength and corrosion resistance. However, joining DSS plates by fusion welding causes a significant reduction in the mechanical properties, because of microstructure changes during weld solidification. It is essential to maintain the characteristics of the weld zone to use DSS in servicing highly critical environments, such as ocean-mining machinery, oil and gas pipe lines, desalination plants and chemical tankers of ships, etc. DSS has ferrite (α) and austenite (γ) in approximately equal proportions, which possess body centered cubic (BCC) and face centered cubic structure (FCC), respectively.¹ During the controlled alloying process of the DSS, under equilibrium conditions, ferrite-promoting elements (Cr, Mo, Mn, W, Nb, Si, Ti and V) will concentrate by diffusing in the ferrite. At the same time, austenite-promoting elements (Ni, C, N, Co and Cu) will concentrate by diffusing in the austenite phases. This gives the formation of a dual-phase microstructure.^{2,3} But

the welding of DSS forces the microstructure to remain in an excessive ferritic nature, because of the higher amounts of ferrite promoting elements in its chemical composition, and also due to a faster cooling rate. Austenite usually nucleates in the temperature range 1200–900 °C. During cooling, the weld zone remains in this temperature range for a very short period of time, i.e., from 4 s to 15 s. Thus, the arc energy and filler metal composition play a major role in the microstructural stability after welding.⁴

Tempered types of steel are machinery manufactured steels with and without alloy, whose chemical compositions, especially in terms of carbon content, are suitable for hardening and which show high toughness under a specific tensile strength at the end of the tempering process. Tempered types of steel, due to their superior mechanical properties, acquired at the end of the tempering process, are used in a wide range of areas, including the manufacture of parts such as various machine and engine parts, forging parts, various screws, nuts and stud

bolts, crank shafts, shafts, control and drive components, piston rods, various shafts, gears. For this reason, tempered steels are the type of steel used and produced at the highest rate after unalloyed steels and construction steels. These steels constitute the most important part of the machinery-manufacturing steels. Generally, such steels are used for the production of fitting, axle shaft, the shaft and the gear.⁵⁻⁹

Friction welding is a solid-state joining process that can be used to join a number of different metals. The process involves making welds in which one component is moved relative to, and in pressure contact with, the mating component to produce heat at the faying surfaces. Softened material begins to extrude in response to the applied pressure, creating an annular upset. Heat is conducted away from the interfacial area for forging to take place. The weld is completed by the application of a forge force during or after the cessation of the relative motion. The joint undergoes hot working to form a homogenous, full surface, high-integrity weld. Friction welding is the only viable method in this field to overcome the difficulties encountered in the joining of dissimilar materials with a wide variety of physical characteristics. The advantages of this process are, among others, no melting, high reproducibility, short production time and a low energy input.¹⁰⁻¹⁹

Welding technology is commonly used in many areas. Because it is aimed to provide high and constant quality in manufacturing sector and in products, the importance of non-destructive is the testing methods in quality-control strategies. Accordingly, the non-destructive testing of welded joints has become a part of the total quality system.^{20,21} Being one of the most important parts of quality control, non-destructive material testing method is the complementary part of the manufacturing. The non-destructive method is the common name for testing methods through which the static and dynamic information about the materials are obtained by testing the materials without damaging them. Thanks to the non-destructive testing method, defects such as cracks occurred during manufacturing or after used for a while,

space in internal structure, edge reduction, etc., are detected (**Table 1**).

The methods applied in non-destructive testing are visual testing, liquid-penetrant testing, eddy-current testing, magnetic particle inspection, ultrasonic inspection and radiographic inspection.²²

High-energy electromagnetic waves may penetrate into many materials. The radiation penetrating a specific material may affect the radiation-sensitive films that are put on the other side of the material. After the development of the films, the image of the inside of the material is seen. This image occurs because of the spaces in the material or thickness/density changes. This method is called radiographic testing, which is one of the oldest methods of nondestructive testing and has been in use for approximately five decades. Among the advantages of this method, compared to other methods, such as ultrasound tests, is the formation of an internal 'photograph' of the material, which no other method is able to achieve. Various radiation sources may be used in radiographic testing. The radiographic testing of weld bead or casting pieces using X-rays or gamma source is one of the most important uses for this inspection method. The energy gap of the X-ray used in industrial radiography is generally between 50 kV and 350 kV. The beam energy varies according to the type and thickness of the material. In order to get precise results from the testing, it has to be done in accordance with the standards. These standards are determined by considering the type of the material and/or the type of product. There are also application standards together with the standards according to which the acceptance levels are determined. The testing is done by determining the standards suitable for the features of the product. Radiographic testing is generally applied according to the EN 1435 or EN 12517 standards.²³⁻²⁵ The radiography method is applied to ferromagnetic, non-ferromagnetic metals and other all materials. Because X-ray provides the opportunity to analyze the microstructure of the materials without making any damage, it is widely used in non-destructive testing. Via X-ray or gamma ray, thickness changes, structural

Table 1: Non-destructive testing experiments in industrial areas³⁷

Tabela 1: Neporušne preiskave na području industrijskih preiskav³⁷

Practice Area	Function	Application Examples
Research and Development	Structural evaluation of materials, Comparison of production and assembly methods and evaluation findings.	Examination of fatigue and microstructure of metals and the detection of cracks in the welding seam.
Production Control Method	Determination of the variable production method and to control.	Radiographic and ultrasonic thickness measuring method and determination of the manufacturing parameters.
Quality Control	Defective parts and the detection of abnormalities, Manufacturing assembly defects, place and method of evaluation.	Poor adhesion, cracking in welding, metal in the non-uniform pores and the determination of material defects.
During the service evaluation	Wear and use during the early identification of abnormalities.	Corrosion in pipes and location of warehouses and detection, Variety of early-warning systems in vehicles.

Table 2: Chemical compositions of test materials**Tabela 2:** Kemijska sestava preizkusnih materialov

Materials	Alloy Elements (w/%)									
	C	Mn	Si	P	S	Cr	Mo	Ni	N	Cu
AISI 4340	0.4	0.8	0.3	0.035	0.040	0.9	0.3	2.00	-	-
AISI 2205	0.018	1.686	0.309	0.026	0.003	22.333	3.379	4.932	0.191	0.097

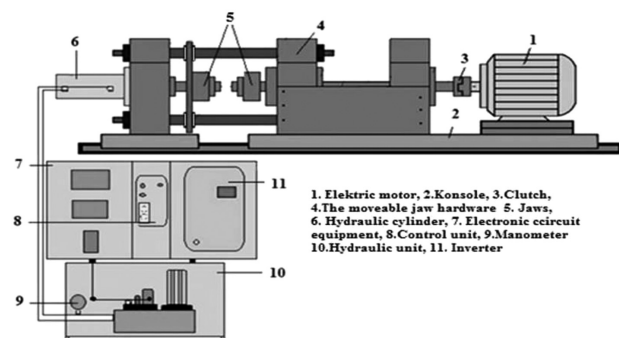
Table 3: Mechanical properties of copper and low carbon steel**Tabela 3:** Mehanske lastnosti bakra in malo ogljičnega jekla

Materials	Tensile Strength (MPa)	Yield Strength 0.2 % (MPa)	Elongation (%)	Microhardness (HV)
AISI 4340	659	400	20.98	201
AISI 2205	956	620	20	328

changes, inner defects, montage details can be determined.^{26–30}

The conventional method of inspection requires that the radiographic images are first-rate and are consequently controlled by international standards. However, radiographic inspection by inspectors is done subjectively and requires great experience, keenness of vision and knowledge of the techniques employed, and yet even when done adequately, interpretation errors occur whether it be the non-detection of a defect present or the incorrect classification of a detected defect.^{25,31–33} The advantages of the radiography method may be seen as follows, the result is shown with an image, permanent records that may be seen outside of the test area can be obtained, the sensitivity is shown on every film and it may be applied to any kind of material. As for the disadvantages, they may be sorted as follows, it is not suitable for thick pieces, may be harmful to health, direct calorise is needed for two-dimensional faults, the film needs posing and showing, is not suitable for automation, surface defects, and it does not give information about the depth of the defect under the surface. The equipment that is used is rather expensive in comparison with other methods and at most it needs careful work concerning the radiation safety.³⁴

In the present paper, X-ray radiographic testing of AISI 4340-2205 steels welded by friction welding were investigated.

**Figure 1:** Experimental set-up¹⁷**Slika 1:** Eksperimentalni sestav¹⁷

2 MATERIALS AND METHODS

AISI 4340 tempered steel and AISI 2205 duplex stainless steel of 12 mm diameter were used to fabricate the joints in this study. **Table 2** illustrates the chemical compositions of the base metals. The friction-welding tests were carried out using a direct-drive-type friction-welding machine. **Table 3** has the mechanical properties and **Table 4** has the physical properties of AISI 4340 and AISI 2205 steels. **Table 5** illustrates the experimental conditions. The experimental set-up is shown in **Figure 1**.¹⁷

Table 4: Physical properties of copper and low carbon steel**Tabela 4:** Fizikalne lastnosti bakra in malo ogljičnega jekla

Materials	α (10^{-6})	λ (W/m °C)	Ω (n Ω m)	E (GPa)
AISI 4340				
AISI 2205	14.7	19	85	200

α : Thermal Expansion Coefficient (20–800 °C)

λ : Thermal Conductive (20 °C)

Ω : Electrical Resistance (20 °C)

E : Elastic modulus (20 °C)

After the friction-welding procedure the specimens were divided into sections transversely in order to investigate the microstructural variations from the centre to the outside of the weld. Transverse sections were prepared, and then grinding and polishing with 3- μ m diamond paste were made in order to conduct a metallographic examination of the joined materials. The specimens were etched in a chemical solution for AISI 4340 2 % HNO₃ + 98 % alcohol and in a solution for AISI 2205 25 % HNO₃ + 75 % pure water to conduct the microstructural examination (7.5 V + 30 s). The microstructures of the joints were observed using light microscopy (LM), the energy-dispersive spectroscopy (EDS) and X-ray diffraction (XRD). Microhardness measurements were taken under a load of 50 g. The tensile tests were conducted at room temperature with 10⁻² mm s⁻¹ cross-head rate.

In controlling the weld seam, as the thickness is 4 mm, radiographic testing was chosen from among the

non-destructive methods and an X-ray tube was chosen as the radiation source. The principle can be seen in **Figure 2**.^{35,36}

Table 5: The process parameters used in the friction welding

Tabela 5: Parametri procesa, uporabljeni pri varjenju s trenjem

Sample no	Welding parameters						Axial shortening (mm)
	Rotating speed (min ⁻¹)	Friction pressure (MPa)	Forging pressure (MPa)	Friction time (s)	Forging time (s)		
S1	2200	30	60	6	3		4.00
S2	2200	30	60	10	5		4.37
S3	2100	30	60	6	3		3.15
S4	2100	30	60	10	5		3.41
S5	2000	30	60	6	3		2.10
S6	2000	30	60	10	5		2.80
S7	2200	40	80	6	3		4.50
S8	2200	40	80	10	5		4.78
S9	2100	40	80	6	3		3.44
S10	2100	40	80	10	5		3.96
S11	2000	40	80	6	3		2.20
S12	2000	40	80	10	5		2.60

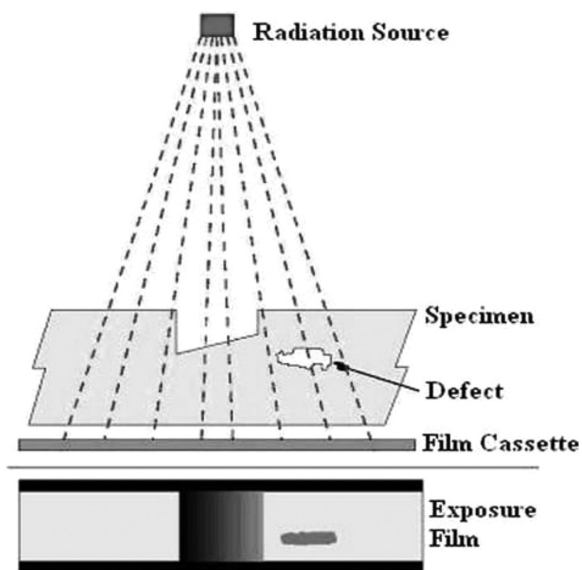


Figure 2: Working principle of radiographic test^{35,36}
Slika 2: Princip delovanja rentgenskega preizkusa^{35,36}

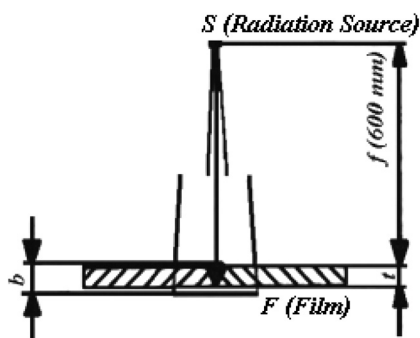


Figure 3: Test preparation for plane wall and one wall
Slika 3: Priprava preizkusa za ravno steno

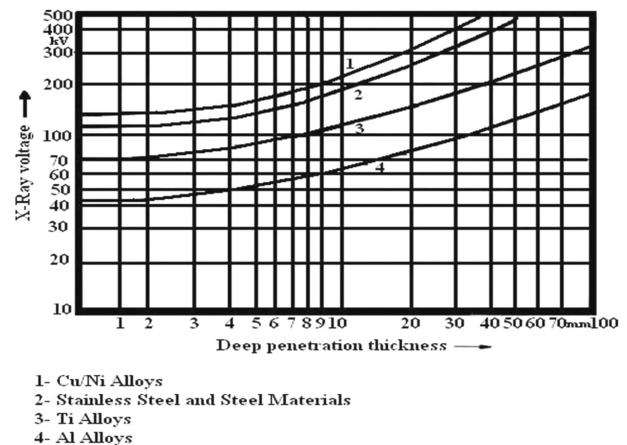


Figure 4: The deep-penetration thickness and material as a function up to 500 kV for the X-ray device and to determine the voltage plot graphic

Slika 4: Debelina globine penetracije pri materialu v odvisnosti od napetosti do 500 kV za rentgensko napravo in za določanje diagrama napetost debelina

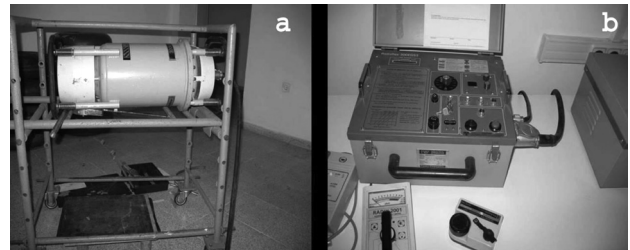


Figure 5: a) Rigaku mark Radioflex-300EGS3-type device and b) control panel

Slika 5: a) Naprava vrste Rigaku Radioflex-300EGS3 in b) kontrolna plošča

Tests TS 5127 and EN 1435 were applied, according to the standards, in class B and in a type that will cover the area affected by the weld and the heat (**Figure 3**).

The X-ray tension that was chosen according to the thickness of the material was 130 kV to image (**Figure 4**).

The X-ray device, Rigaku Radioflex-300EGS3 type, having the capacity of 300 kV was used (**Figures 5a** and **5b**).



Figure 6: Film, penetrometer, stenciling pattern and beam setting
Slika 6: Film, merilec globine penetracije, vzorec šablone, nastavitve snopa

Table 6: Definition of weld defects and radiographic image^{37,38}**Tabela 6:** Definicije napak zvarov in rentgenskih posnetkov^{37,38}

A: Gas gaps Aa: Porosity Ab: Gas bubbles	Description	* Because the captured gas bubbles are formed. * Gas channels or long gaps
	Radiographic Image	* Sharp black shadows around the circle. * Sharp black depending on the round or the long shadows of the error change.
B: Slag Ba: Slag Bb: Slag errors	Description	* Slag or other foreign materials during the welding. * Captured within gaps slag or foreign matter.
	Radiographic Image	* Dark shadows or random shapes. * Continuous dark lines parallel to the seam edge welding.
C. Insufficient Welding	Description	Between the main material source material during welding seam merger due to lack of two-dimensional error.
	Radiographic Image	Sharp-edged thin dark line.
D. Insufficient Deep Penetration	Description	Merger at the root welding of the lack of sewing filled fully with the welding or root.
	Radiographic Image	The middle of the dark seam continuous or discrete line welding.
E. Cracks Ea: Vertical Cracks Eb: Horizontal Cracks	Description	Local tensile strength of metal exceeded.
	Radiographic Image	Flat thin dark line.
F. Swelter Channel	Description	Welding material on the surface along the seam formed channel or groove.
	Radiographic Image	Weldings are spread wide and dark line along the seam.

C4 type, 100 × 240 mm² Kodak film was used. Front and back lead screens with a thickness of 0.125 mm were used. The weld seam applied to the material with the thickness of 4 mm was filmed by sending the beam to the pose diagram for 48 s. The distance between the X-ray device and film was 600 mm. The placement of the film is shown in **Figure 6**.^{37,38}

3 RESULTS AND DISCUSSION

The flash obtained was symmetric, which indicated plastic deformation on both the rotating and upsetting (reciprocating) side. The integrity of the joints was evaluated for the friction-welded joints. The friction-processed joints were sectioned perpendicular to the bond line and observed through an optical microscope. It is clear that there were no cracks and voids in the weld

interface. From the microstructural observations, the microstructures formed in the interface zone during or after FW processes, there are three distinct zones across the specimens identified as unaffected zone (UZ), deformed zone (DZ) and transformed and recrystallized fully plastic deformed zone (FPDZ).³⁹ Typical grain refinement occurred in the DZ region by the combined effect of the thermal and mechanical stresses (**Figure 7**). A typical micrograph showing the different morphologies of the microstructure at different zones of the friction-processed joint is shown in **Figure 7**.

According to the International Institute of Welding, welding defects and the explanations of the radiographic images were defined as in **Table 6**.^{37,38} The films are placed into the viewer shown in **Figure 8** and the image is evaluated according to **Table 6**. It was determined that the most common welding defects shown in **Table 6** have a lack of penetration according to the definitions of welding defects and the radiographic images (D) (S2). In other samples the defects were not shown.

In **Figure 9** the radiographic testing images of all the samples are shown. The experimental results indicated that AISI 4340 tempered steel could be joined to AISI 2205 duplex stainless steel using the friction-welding technique and for achieving a weld with sufficient strength. The result of the radiographic tests indicated that by increasing the rotation speed, friction pressure and forging pressure the amount of flash increased in all the specimens. In contrast, when increasing the friction time the amount of flash decreased. The best properties of the AISI 4340-2205 steels were observed for the specimens welded at a rotation speed of 2200 min⁻¹, a friction pressure of 40 MPa, a forging pressure of 80

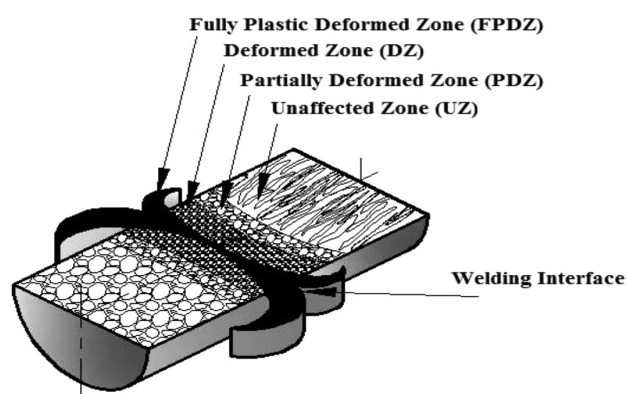


Figure 7: Regions in which occurred microstructural changes³⁹
Slika 7: Področja, kjer se pojavijo spremembe v mikrostrukturi³⁹



Figure 8: Film-examination device (Viewer)

Slika 8: Naprava za pregled filma

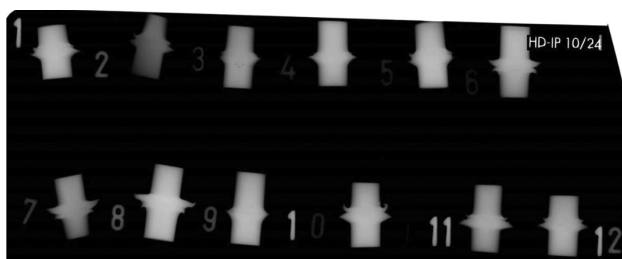


Figure 9: Radiographic test photographs of samples (S1 – S12)

Slika 9: Rentgenski posnetki vzorcev (S1 – S12)

MPa, a friction time of 6 s and a forging time of 3 s (Figure 9).

4 CONCLUSIONS

In this study, X-ray radiographic testing of AISI 4340 tempered steel and AISI 2205 duplex stainless steel welded with friction welding were investigated. The following results were obtained.

- Friction-welding experiments were carried out using a direct-drive-type friction-welding machine according to Table 5. This study concluded that the AISI 4340 tempered steel could be joined successfully to AISI 2205 duplex stainless steel using the friction-welding technique. The best joining was seen in number S7. It was clear that the joining decreased in the other samples.
- Comprehensive microstructural investigations for the AISI 4340-2205 steels' friction-welded joints revealed that there were different regions at the welding interface, the wideness of fully plasticized deformed zone (FPDZ) decreases when rotational speed and friction pressure increase.
- The larger microstructural changes take place in the HAZs. An increase in the contraction of the samples was observed after increasing the friction-welding rotation speeds. The width of the HAZ is mainly affected by the friction time and rotation speed. This infers that the width and formation of HAZs that occurred as a result of the reactions taking place at the welding interface have an adverse effect on the

mechanical strength and, consequently, the quality of the friction-welded joints.

- It has been determined that the most common welding defects shown in Table 6 have a lack of penetration according to the definitions of welding defects and the radiographic images (D) (Sample No: 2). In other samples there were no defects. The result of the radiographic tests indicated that by increasing the rotation speed, the friction pressure and the forging pressure the amount of flash increased in all the specimens. In contrast, when increasing the friction time the amount of flash decreased. The best properties of were AISI 4340-2205 steels observed for the specimens welded at a rotation speed of 2200 min⁻¹, a friction pressure of 40 MPa, a forging pressure of 80 MPa, a friction time of 6 s and a forging time of 3 s (Figure 9).
- The highest deformation was always for the AISI 4340 tempered steel side and in all samples the original structure was preserved in the undeformed region.

5 REFERENCES

- ¹ ASM Handbook on welding, vol. 6, ASM International Publisher, 1993, 471–481
- ² J. Charles, Duplex stainless steel, A Review, Proc. 7th Duplex Int. Conf. & Expo, Grado, Italy, 2007
- ³ J. C. Lippold, D. J. Kotecki, Welding metallurgy and weldability of stainless steels, Wiley-Interscience, 2005
- ⁴ A. V. Jebaraj, L. Ajaykumar, Microstructure analysis and the influence of shot peening on stress corrosion cracking resistance of duplex stainless steel welded joints, Indian Journal of Engineering & Materials Sciences, 21 (2014), 155–167
- ⁵ S. D. Meshram, T. Mohandas, R. G. Madhusudhan, Friction welding of dissimilar pure metals, Journal of Materials Processing Technology, 184 (2008), 330–337, doi:10.1016/j.jmatprotec.2006.11.123
- ⁶ P. Sathiyar, S. Aravindan, A. Noorul Haq, Some experimental investigations on friction welded stainless steel joints, Materials and Design, 29 (2008), 1099–1109, doi:10.1016/j.matdes.2007.06.006
- ⁷ S. Celik, I. Ersozlu, Investigation of the mechanical properties and microstructure of friction welded joints between AISI 4140 and AISI 1050 steels, Mater. Design, 30 (2009), 970–976, doi:10.1016/j.matdes.2008.06.070
- ⁸ <http://www.celmercelik.com>.
- ⁹ M. Sahin, H. E. Akata, An experimental study on friction welding of medium carbon and austenitic stainless steel components, Indust. Lubricat. Tribol., 56 (2004) 2, 122–129, doi:10.1108/00368790410524074
- ¹⁰ M. Sahin, Evaluation of the joint interface properties of austenitic-stainless steels (AISI 304) joined by friction welding, Materials and Design, 28 (2007), 2244–2250, doi:10.1016/j.matdes.2006.05.031
- ¹¹ I. Kirik, N. Ozdemir, Weldability and joining characteristics of AISI 420/AISI 1020 steels using friction welding, International Journal of Materials Research, 104 (2013) 8, 769–775, doi:10.3139/146.110917
- ¹² N. Ozdemir, F. Sarsilmaz, A. Hascalik, Effect of rotational speed on the interface properties of friction-welded AISI 304L to 4340 steel, Mater. Des., 28 (2007), 301–307, doi:10.1016/j.matdes.2005.06.011
- ¹³ Welding handbook, Welding Processes, Volume 2, Eighth edition, American Welding Society Inc., Miami 1997, 739–761
- ¹⁴ R. E. Chalmers, The Friction Welding Advantage, Manufacturing Engineering, 126 (2001), 64–65

- ¹⁵ N. Ozdemir, Investigation of the mechanical properties of friction-welded joints between AISI 304L and AISI 4340 steel as a function rotational speed, *Materials Letters*, 55 (2005), 2504–2509, doi:10.1016/j.matlet.2005.03.034
- ¹⁶ D. E. Spindler, What Industry Needs to Know about Friction Welding, *Welding Journal*, (1994), 37–42
- ¹⁷ I. Kirik, N. Ozdemir, U. Caligulu, Effect of particle size and volume fraction of the reinforcement on the microstructure and mechanical properties of friction welded MMC to AA 6061 aluminum alloy, *Kovove Mater.*, 51 (2013) 4, 221–227, doi:10.4149/km_2013_4_221
- ¹⁸ I. Kirik, N. Ozdemir, F. Sarsilmaz, Microstructure and Mechanical Behaviour of Friction Welded AISI 2205/AISI 1040 Steel Joints, *Materials Testing*, 54 (2012) 10, 683–687, doi:10.3139/120.110379
- ¹⁹ M. B. Uday, M. N. Ahmad Fauzi, H. Zuhailawati, A. B. Ismail, Advances in friction welding process: a review, *Science and Technology of Welding and Joining*, 15 (2010) 7, 534–558, doi:10.1179/136217110X12785889550064
- ²⁰ M. Taskin, U. Caligulu, M. Türkmen, X-Ray Tests of AISI 430 and 304 Stainless Steels and AISI 1010 Low Carbon Steel Welded by CO₂ Laser Beam Welding, *Materials Testing*, 53 (2011) 11–12, 741–747, doi:10.3139/120.110283
- ²¹ H. Dikbas, U. Caligulu, M. Taskin, M. Türkmen, X-Ray Radiography of Ti6Al4V Welded by Plasma Tungsten Arc (PTA) Welding, *Materials Testing*, 55 (2013) 3, 197–202, doi:10.3139/120.110426
- ²² http://makina.ktu.edu.tr/static/lab_foy/lab21.doc
- ²³ <http://www.wtndt.metu.edu.tr/ndt/tr/node/8>
- ²⁴ <http://asalmakina.com/anasayfam.asp?sid=6&pid=4>
- ²⁵ R. R. da Silva, L. P. Calôba, M. H. S. Siqueira, J. M. A. Rebello, Pattern recognition of weld defects detected by radiographic test, *NDT&E International*, 37 (2004) 6, 461–470, doi:10.1016/j.ndteint.2003.12.004
- ²⁶ T. Tekiz, The Non-destructive Testings, ITU Faculty of Mechanical Engineering, Istanbul, 1984
- ²⁷ M. Albayrak, The Control and Inspection of the Welding Seams, IGDAS, 1997
- ²⁸ <http://www.ndt-ed.org>
- ²⁹ <http://www.wtndt.metu.edu.tr>
- ³⁰ TS EN 444, TS EN 462 Standards, 1994
- ³¹ K. Aoki, Y. Suga, Intelligent image processing for abstraction and discrimination of defect image in radiographic film, *Proceedings of the Seventh International Offshore and Polar Engineering Conference*, Honolulu, USA, 1997, 527
- ³² A. Kehoe, G. A. Parker, Image processing for industrial radiographic inspection: image enhancement, *Br J NDT*, 32 (1990) 4, 183–190
- ³³ Y. Cherfa, Y. Kabir, R. Drai, X-rays image segmentation for NDT of welding defects, *7th European Conference on Non Destructive Testing*, Copenhagen, 1998, 2782
- ³⁴ C. R. Clayton, K. G. Martin, *Conf. Proceedings High Nitrogen Steels*, The Institute of Metals, Lille, 1989, 256
- ³⁵ S. Ekinici, The Evaluation of the Welding Seam Errors with Digital Radiographic Methods, The Atom Energy Foundation of Turkey, Istanbul
- ³⁶ The Certificate of Material Testing Knowledge, Ereğli Iron and Steel Plants T.A.S
- ³⁷ N. Ozakin, H. Baycik, The Radiographic Inspection of the Welding Seam of the Body of Ship, The 4th Iron–Steel Congress, Karabük, 2007, 289
- ³⁸ A. Topuz, The Non-destructive Inspections, YTU, Istanbul, 1993
- ³⁹ S. Mercan, N. Ozdemir, A Couple of AISI 2205/AISI 1020 Material Combination with Friction Welding Method, *NWSA-Technological Applied Sciences*, 2A0080, 8 (2013) 2, 18–34, doi:10.12739/NWSA.2013.8.2.2A0080

THERMODYNAMIC PROPERTIES AND MICROSTRUCTURES OF DIFFERENT SHAPE-MEMORY ALLOYS

TERMODINAMIČNE LASTNOSTI IN MIKROSTRUKTURA RAZLIČNIH ZLITIN Z OBLIKOVNIM SPOMINOM

**Lidija Gomidželović¹, Emina Požega¹, Ana Kostov¹, Nikola Vuković²,
Dragana Živković³, Dragan Manasijević³**

¹Mining and Metallurgy Institute, Zeleni bulevar 35, 19210 Bor, Serbia

²University of Belgrade, Faculty of Mining and Geology, Dušina 7, 11000 Belgrade, Serbia

³University of Belgrade, Technical Faculty, VJ 12, 19210 Bor, Serbia

lgomidzelovic@yahoo.com

Prejem rokopisa – received: 2014-08-26; sprejem za objavo – accepted for publication: 2015-02-06

doi:10.17222/mit.2014.212

The results of a thermodynamic-properties calculation conducted using a general solution model (GSM) and an experimental investigation of the microstructures of different shape-memory alloys (SMAs) are presented in this paper. The investigated alloys belong to ternary systems Cu-Al-Zn and Cu-Mn-Ni and to quaternary system Ni-Cu-Fe-Mn. The examinations were conducted using light microscopy (LM) and scanning electron microscopy with energy-dispersive X-ray spectrometry (SEM-EDX).

Keywords: thermodynamics, shape-memory alloys, microstructure, LM, SEM-EDX

V tem članku so predstavljeni rezultati termodinamičnih izračunov lastnosti, ki so bili izvršeni z uporabo splošnega modela rešitev (GSM) in eksperimentalne preiskave mikrostrukture različnih zlitin z oblikovnim spominom (SMAs). Preiskovane zlitine pripadajo ternarnim sistemom Cu-Al-Zn in Cu-Mn-Ni in kvaternarnem sistemu Ni-Cu-Fe-Mn. Preiskave so bile izvedene s pomočjo svetlobne mikroskopije (LM), z vrstično elektronsko mikroskopijo (SEM) in z rentgensko energijsko disperzijsko spektrometrijo (EDX).

Ključne besede: termodinamika, zlitine z oblikovnim spominom, mikrostruktura, LM, SEM-EDX

1 INTRODUCTION

Shape-memory materials are able to recover their original shape after being distorted, at the presence of the right stimulus. These materials include: a) shape-memory alloys, b) shape-memory polymers, c) shape-memory composites and newly developed d) shape-memory hybrids¹.

The shape-memory effect was first discovered for a gold-cadmium alloy in the 1930s, but this type of behavior of materials did not attract the attention of the researchers until 1960s, when a significant recoverable strain was observed for a Ni-Ti alloy, enabling commercial applications.

Shape-memory alloys (SMAs) are characterized by unique properties (pseudoelasticity and shape-memory effect), which enable them to "remember" their original shapes. These alloys are used as activators, changing their shapes, positions and other mechanical characteristics in a response to a variation in the temperature and electromagnetic field.

SMAs can be classified, in accordance with the alloying metals, into:

1. Alloys based on nickel (Ti-Ni, Ni-Mn-Ga)
2. Alloys based on copper (Cu-Zn-Al, Cu-Zn-Si, Cu-Zn-Sn, Cu-Zn-Ga, Cu-Zn-Mn, Cu-Zn-Al-Ni, Cu-Zn-Al-Mn, Cu-Al-Ni, Cu-Al-Be, Cu-Al-Mn)

3. Alloys based on iron (Fe-Mn, Fe-Ni-C, Fe-Mn-Cr, Fe-Mn-Si, Fe-Ni-Nb, Fe-Co-Ni-Ti)
4. Alloys based on noble metals (Au-Cd, Au-Ag, Pt-Al, Pt-Ga, Pt-Ti, Pt-Cr)
5. Exotic alloys (In-Te, In-Cd, V-Nb)².

The interest in SMAs is continuously increasing as new areas of application are discovered. Today, SMAs are used in different areas such as civil engineering^{3,4}, the production of microsystems⁵, medicine⁶⁻⁸, earthquake technologies⁹⁻¹¹ and robotics^{12,13}.

The first copper-based SMA to be commercially exploited was the Cu-Al-Zn alloy and the shape-memory alloys from this ternary system typically contain mass fractions of $w(\text{Zn}) = 15\text{--}30\%$ and $w(\text{Al}) = 3\text{--}7\%$.

Cu-Mn-Ni shape-memory alloys are magnetic, but some of their properties (like the brittleness) limit their applications, so the alloying elements like gallium, iron or aluminum are added to an alloy in order to achieve satisfying characteristics.

The objective of this work is to provide some new information about the thermodynamics and microstructures of selected shape-memory alloys.

Table 1: Composition, shape and production method of investigated samples**Tabela 1:** Sestava, oblika in način izdelave preiskanih vzorcev

Sample	Alloy	Composition (w/%)						Shape	Production method
		Al	Cu	Zn	Mn	Ni	Fe		
A1	NiCuFeMn	/	32	/	1.5	65	1.5	rod, R 1.27 cm	casting
A2	CuMnNi	/	84	/	12	4	/	wire, R 1 mm	casting, extraction
A3	CuAlZn	4.54	68.14	27.31	/	/	/	wire, R 3.5 mm	casting
A4	CuAlZn	5.7	68.27	26.03	/	/	/	rod, R 8 cm	casting

2 EXPERIMENTAL WORK

The characterization of the selected shape-memory alloys was done using light microscopy and a SEM-EDX analysis. The samples were obtained from the industrial production. The composition, shape and production method of the investigated samples are given in **Table 1**. The samples were used as prepared (no annealing).

The microstructural analysis of the investigated samples was performed with light microscopy (LM), using a Reichert MeF2 microscope (a magnification of up to 500 \times) and a SEM-EDX analysis performed on a JEOL JSM-6610LV scanning electron microscope (a magnification of up to 300000 \times) coupled with an Oxford Instruments, X-Max 20 mm² SDD, energy-dispersive X-ray spectrometer (an accelerating voltage of 20 kV and a beam current of 1.25 nA). Prior to the metallographic analysis, the surfaces of the polished samples were etched with an appropriate etching solution (**Table 2**) in order to reveal the structures of the investigated alloys.

Table 2: Solutions used for sample etching**Tabela 2:** Raztopine, uporabljene za jedkanje vzorca

Sample	Etching solution
A1	HCl+H ₂ O ₂ +H ₂ O
A2	FeCl ₃ +HCl+H ₂ O
A3	FeCl ₃ +HCl+H ₂ O
A4	FeCl ₃ +HCl+H ₂ O

3 THEORETICAL FUNDAMENTALS

Among many available methods for calculating the thermodynamic properties of a ternary system based on the information about the constitutive binary systems, Chou's general solution model (GSM)^{14,15} proved to be the most reasonable in all respects, overcoming the inherent defects of the traditional symmetrical and asymmetrical geometric models. This model breaks down the boundaries between symmetrical and asymmetrical systems and generalizes various situations; the accuracy of the calculation was also proven with practical examples^{16,17}.

Recently, a new, improved version of the general solution model based on the Redlich-Kister parameters was presented by Zhang and Chou¹⁸. As the older version of GSM required a series of integration processes, which

significantly complicated the calculation, and a large number of real systems can be approximately fit using a Redlich-Kister polynomial, a new formalism, based on the binary Redlich-Kister-type parameters, was presented.

Therefore, this new GSM version is utilized for calculating the thermodynamic properties of the Cu-Al-Zn and Cu-Mn-Ni ternary systems.

The basic equation of the general solution model for a ternary system is:

$$\begin{aligned} \Delta G^E = & x_1 x_2 \sum_{i=0}^n L_{12}^i (x_1 - x_2 + (2\xi_{12} - 1)x_3)^i + \\ & + x_2 x_3 \sum_{i=0}^n L_{23}^i (x_2 - x_3 + (2\xi_{23} - 1)x_1)^i + \\ & + x_3 x_1 \sum_{k=0}^n L_{31}^k (x_3 - x_1 + (2\xi_{31} - 1)x_2)^i \end{aligned} \quad (1)$$

Similarity coefficient ξ is defined as:

$$\xi_{12} = \eta_I / (\eta_I + \eta_{II}) \quad (2)$$

$$\xi_{23} = \eta_{II} / (\eta_{II} + \eta_{III}) \quad (3)$$

$$\xi_{31} = \eta_{III} / (\eta_{III} + \eta_I) \quad (4)$$

and the deviation sum of squares can be calculated using:

$$\begin{aligned} \eta_I = & \sum_{i=0}^n \frac{1}{2(2i+1)(2i+3)(2i+5)} (L_{12}^i - L_{13}^i)^2 + \\ & + \sum_{j=0}^n \sum_{k>j}^m \frac{1}{(j+k+1)(j+k+3)(j+k+5)} (L_{12}^i - L_{13}^i)(L_{12}^j - L_{13}^j) \end{aligned} \quad (5)$$

$$\begin{aligned} \eta_{II} = & \sum_{i=0}^n \frac{1}{2(2i+1)(2i+3)(2i+5)} (L_{21}^i - L_{23}^i)^2 + \\ & + \sum_{j=0}^n \sum_{k>j}^m \frac{1}{(j+k+1)(j+k+3)(j+k+5)} (L_{21}^i - L_{23}^i)(L_{21}^j - L_{23}^j) \end{aligned} \quad (6)$$

$$\begin{aligned} \eta_{III} = & \sum_{i=0}^n \frac{1}{2(2i+1)(2i+3)(2i+5)} (L_{31}^i - L_{32}^i)^2 + \\ & + \sum_{j=0}^n \sum_{k>j}^m \frac{1}{(j+k+1)(j+k+3)(j+k+5)} (L_{31}^i - L_{32}^i)(L_{31}^j - L_{32}^j) \end{aligned} \quad (7)$$

The basic equation of the general solution model for a quaternary system¹⁹ is:

$$\begin{aligned} \Delta G^E = & x_1 x_2 \sum_{k=0}^n L_{12}^k (2X_{1(12)} - 1)^k + x_1 x_3 \sum_{k=0}^n L_{13}^k (2X_{1(13)} - 1)^k + \\ & + x_1 x_4 \sum_{k=0}^n L_{14}^k (2X_{1(14)} - 1)^k + x_2 x_3 \sum_{k=0}^n L_{23}^k (2X_{2(23)} - 1)^k + \\ & + x_2 x_4 \sum_{k=0}^n L_{24}^k (2X_{2(24)} - 1)^k + x_3 x_4 \sum_{k=0}^n L_{34}^k (2X_{3(34)} - 1)^k \end{aligned} \quad (8)$$

with

$$X_{i(ij)} = x_i + \sum_{\substack{k=1 \\ k \neq i, j}}^4 \xi_{i(ij)}^k x_k \quad (9)$$

$$\xi_{i(ij)}^k = \eta_{(ij,ik)} / (\eta_{(ij,ik)} + \eta_{(ji,jk)}) \quad (10)$$

and

$$\begin{aligned} \eta_{(ij,ik)} = & \sum_{l=0}^n \frac{1}{2(2l+1)(2l+3)(2l+5)} (L_{ij}^l - L_{ik}^l)^2 + \\ & + \sum_{l=0}^n \sum_{m>l}^m \frac{1}{(l+m+1)(l+m+3)(l+m+5)} (L_{ij}^l - L_{ik}^l)(L_{ij}^m - L_{ik}^m) \end{aligned} \quad (11)$$

In Equation (11) the second part is different from zero only if the sum of m and n is an even number, and it applies to all the L_{ij} parameters that $L_{ij}^k = (-1)^k L_{ij}^k$. In all the equations given, L_{ij}^k is the Redlich-Kister parameter for the binary system ij , independent of the composition and only dependent on the temperature; ΔG^E is the integral molar excess Gibbs energy for the ternary or quaternary system and x_i is the mole fraction of component i .

Partial thermodynamic quantities are calculated according to the equations:

$$G_i^E = G^E + (1-x_i)(\partial G^E / \partial x_i) = RT \ln \gamma_i \quad (12)$$

and:

$$a_i = x_i \gamma_i \quad (13)$$

4 RESULTS AND DISCUSSION

The basic thermodynamic data on the constituent binary subsystems, needed for the calculation of the thermodynamic properties of the investigated systems, were taken from the available literature data^{20–28} and presented in the form of Redlich-Kister parameters in **Table 3**.

The results for the integral molar excess Gibbs energies of the investigated sections at the corresponding temperatures, obtained with the general solution model, are given analytically in polynomial forms (**Table 4**).

The general solution model and Equations (12) and (13) were used for the calculation of the copper activities in the selected sections of ternary systems Cu-Al-Zn and Cu-Mn-Ni and for the calculation of the nickel activity in the selected cross-section of quaternary system Ni-Cu-Fe-Mn. The results of these calculations are presented in a graphic form (**Figures 1 to 3**). The thermodynamic

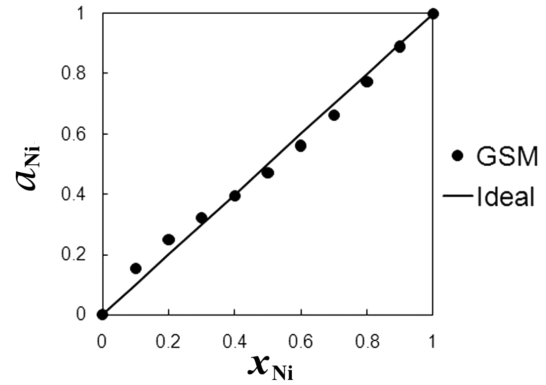


Figure 1: Dependence of nickel activity on the composition, for cross-section Cu : Fe : Mn = 20 : 1 : 1 from quaternary Ni-Cu-Fe-Mn system, calculated with GSM, at 1873 K

Slika 1: Odvisnost aktivnosti niklja od sestave, za presek Cu : Fe : Mn = 20 : 1 : 1 v kvaternarnem sistemu Ni-Cu-Fe-Mn, izračunana z uporabo GSM, pri 1873 K

Table 3: Redlich-Kister parameters for constitutive binary systems

Tabela 3: Redlich-Kister parametri za konstitutivne binarne sisteme

System ij	$L_{ij}^0(T)$	$L_{ij}^1(T)$	$L_{ij}^2(T)$	$L_{ij}^3(T)$
Al-Cu ²⁰	$-67094 + 8.555 \cdot T$	$32148 - 7.118 \cdot T$	$5915 - 5.889 \cdot T$	$-8175 + 6.049 \cdot T$
Cu-Zn ²¹	$-40695.54 + 12.65269 \cdot T$	$4402.72 - 6.55425 \cdot T$	$7818.1 - 3.25416 \cdot T$	0
Al-Zn ²²	$10465.55 - 3.39259 \cdot T$	0	0	0
Cu-Mn ²³	$1118.55 - 5.6225 \cdot T$	-10915.375	0	0
Cu-Ni ²⁴	$11760 + 1.084 \cdot T$	-1672	0	0
Mn-Ni ²⁵	$-85853 + 22.715 \cdot T$	$-1620 + 4.902 \cdot T$	0	0
Fe-Ni ²⁶	$-18782 + 3.7011 \cdot T$	$12308 - 2.7599 \cdot T$	$4457 - 4.1536 \cdot T$	0
Cu-Fe ²⁷	$+35625.8 - 2.19045 \cdot T$	$-1529.8 + 1.15291 \cdot T$	$+12714.4 - 5.18624 \cdot T$	$+1177.1$
Fe-Mn ²⁸	$-3950 + 0.489 \cdot T$	$+1145$	0	0

Table 4: Polynomial form of integral molar excess Gibbs energies calculated using general solution model

Tabela 4: Oblika polinoma integralnih molskih odvečnih Gibbsovih energij, izračunanih z uporabo splošnega modela rešitev

System	Cross-section	T/K	$\Delta G^E / J \text{ mol}^{-1}$	R^2
Ni-Cu-Fe-Mn	Cu:Fe:Mn=20:1:1	1873	$-2180.5 \cdot x_{\text{Ni}}^3 - 6229 \cdot x_{\text{Ni}}^2 + 7760.2 \cdot x_{\text{Ni}} + 643.38$	1
Cu-Mn-Ni	Mn:Ni=3:1	1773	$13831 \cdot x_{\text{Cu}}^3 - 24352 \cdot x_{\text{Cu}}^2 + 18408 \cdot x_{\text{Cu}} - 7883.2$	1
Cu-Al-Zn	Al:Zn=1:2	1373	$11751 \cdot x_{\text{Cu}}^2 - 7231 \cdot x_{\text{Cu}} - 5241.8$	0.9895

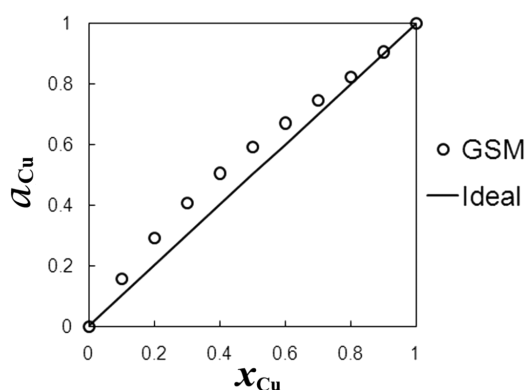


Figure 2: Dependence of copper activity on the composition, for cross-section Mn : Ni = 3 : 1 from ternary Cu-Mn-Ni system, calculated with GSM, at 1773 K

Slika 2: Odvisnost aktivnosti bakra od sestave, za presek Mn : Ni = 3 : 1 v ternarnem sistemu Cu-Mn-Ni, izračunana z uporabo GSM, pri 1773 K

properties calculated with the general solution model are related to the liquid phase of the system, so the temperature, at which the calculation was carried out, was selected according to that rule, taking into account the melting points of all the metals in the investigated system.

From **Figure 1**, it can be seen that the nickel activity in section Cu : Fe : Mn = 20 : 1 : 1 and at $T = 1873$ K shows a variable character of the deviation from Raoult's law, where up to $x_{Ni} = 0.4$ the deviation is positive, but with a higher content of nickel in the alloy the deviation becomes negative, indicating that a higher amount of nickel in the alloy leads to a better miscibility of the alloy components.

The copper activity in cross-section Mn : Ni = 3 : 1 and at $T = 1773$ K (**Figure 2**) shows a clear positive deviation from Raoult's law, which can even result in an occurrence of layering.

The copper activity in cross-section Al : Zn = 1 : 2 and at $T = 1373$ K (**Figure 3**) exhibits an apparent negative deviation from Raoult's law, indicating that the

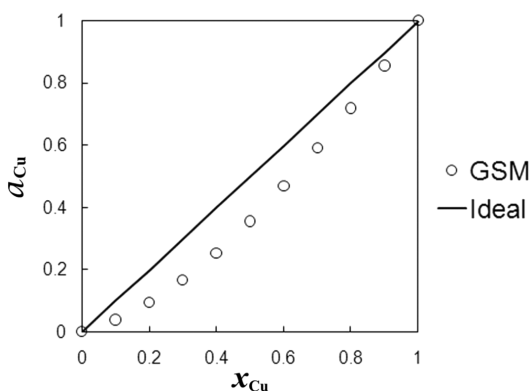


Figure 3: Dependence of copper activity on the composition, for cross-section Al : Zn = 1 : 2 from ternary Cu-Al-Zn system, calculated with GSM, at 1373 K

Slika 3: Odvisnost aktivnosti bakra od sestave, za presek Al : Zn = 1 : 2 v ternarnem sistemu Cu-Al-Zn, izračunana z uporabo GSM, pri 1373 K

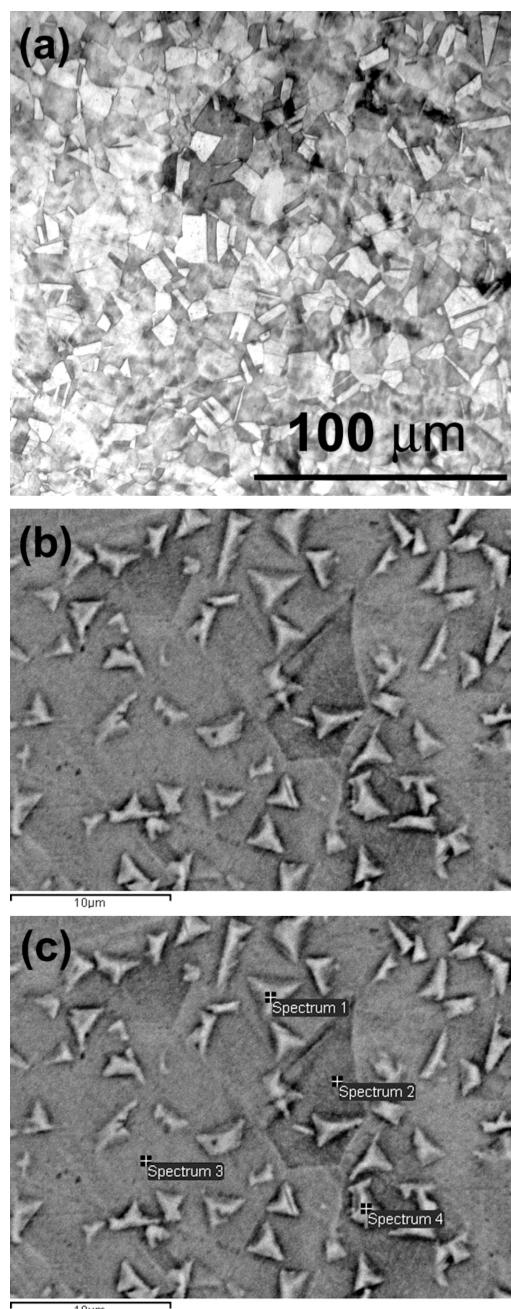


Figure 4: Microstructure of sample A1: a) LM (magnification of 500 \times), b) SEM (magnification of 4000 \times) and c) positions of EDX analysis

Slika 4: Mikrostruktura vzorca A1: a) LM (povečava 500 \times), b) SEM (povečava 4000 \times) in c) položaj EDX-analiz

Table 5: Results of EDX analysis of sample A1 in amount fractions, (x/%)

Tabela 5: Rezultati EDX-analiz vzorca A1 v množinskih deležih, (x/%)

Position	A1			
	Mn	Fe	Ni	Cu
Spectrum 1	1.23	1.52	65.49	31.75
Spectrum 2	1.20	1.69	66.63	30.48
Spectrum 3	1.26	1.67	67.95	29.12
Spectrum 4	1.31	1.27	64.97	32.46

miscibility of the metals in the ternary Cu-Al-Zn system is quite good.

The results of the microstructural analysis with light optical microscopy and SEM-EDX for sample A1 are given in **Figure 4**, with the chemical composition determined with EDX presented in **Table 5**.

The microphotograph obtained with LM (**Figure 4a**) shows that the alloy structure consists of sharp-edged polygonal grains.

The SEM image on **Figure 4b** reveals the structure of sample A1 as a gray matrix with imbedded triangular grains, but the EDX analysis shows that the grains and the matrix have almost identical chemical compositions. These findings are in agreement with the fact that copper and nickel, two components that together account for

over 90 % of the alloy's mass, form a continuous series of solid solutions²⁹.

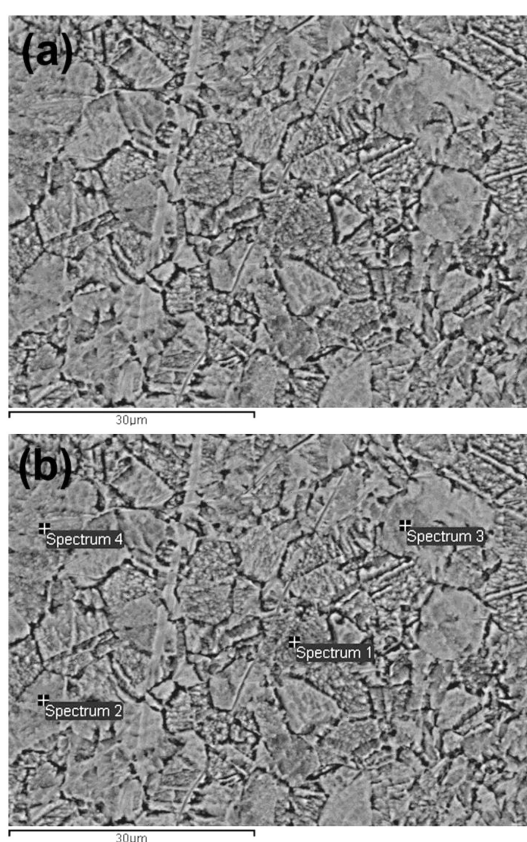


Figure 5: Microstructure of sample A2: a) SEM (magnification of 2000×) and b) positions of EDX analysis

Slika 5: Mikrostruktura vzorca A2: a) SEM (povečava 2000×) in b) položaj EDX-analiz

Table 6: Results of EDX analysis of sample A2 in amount fractions, (x/%)

Tabela 6: Rezultati EDX-analiz vzorca A2 v množinskih deležih, (x/%)

Position	A2		
	Mn	Ni	Cu
Spectrum 1	15.04	4.70	80.25
Spectrum 2	14.92	4.50	80.58
Spectrum 3	15.11	4.48	80.41
Spectrum 4	15.35	4.41	80.24

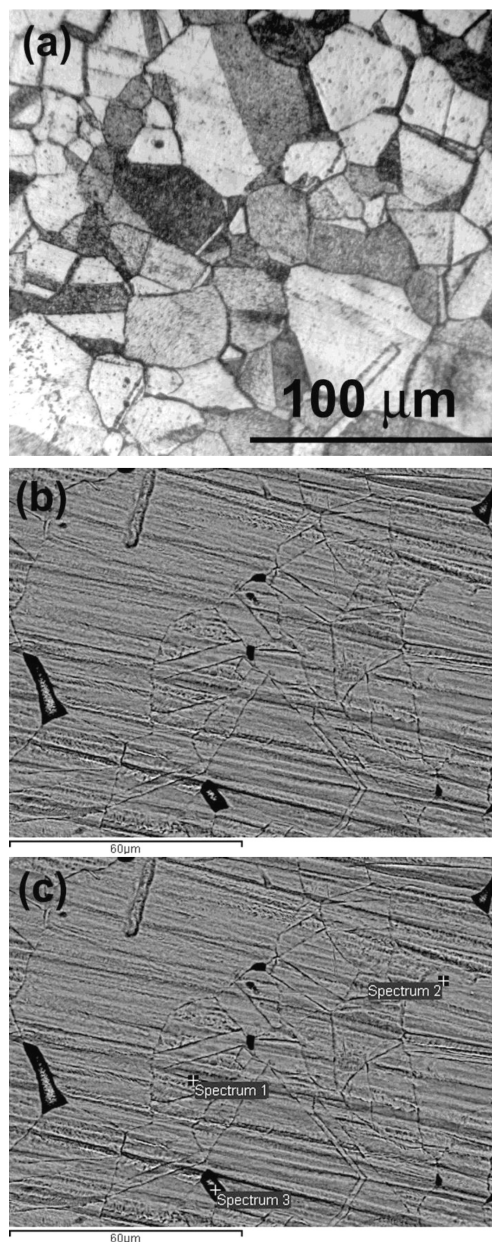


Figure 6: Microstructure of sample A3: a) LM (magnification of 500×), b) SEM-EDX (magnification of 1000×) and c) positions of EDX analysis

Slika 6: Mikrostruktura vzorca A3: a) LM (povečava 500×), b) SEM-EDX (povečava 1000×) in c) položaj EDX-analiz

Table 7: Results of EDX analysis of sample A3 in amount fractions, (x/%)

Tabela 7: Rezultati EDX-analiz vzorca A3 v množinskih deležih, (x/%)

Position	A3		
	Al	Cu	Zn
Spectrum 1	8.83	69.75	21.42
Spectrum 2	7.93	71.11	20.96
Spectrum 3	1.11	78.03	20.87

The results of the microstructural analysis with light microscopy and SEM for sample A2 are given in **Figure 5**

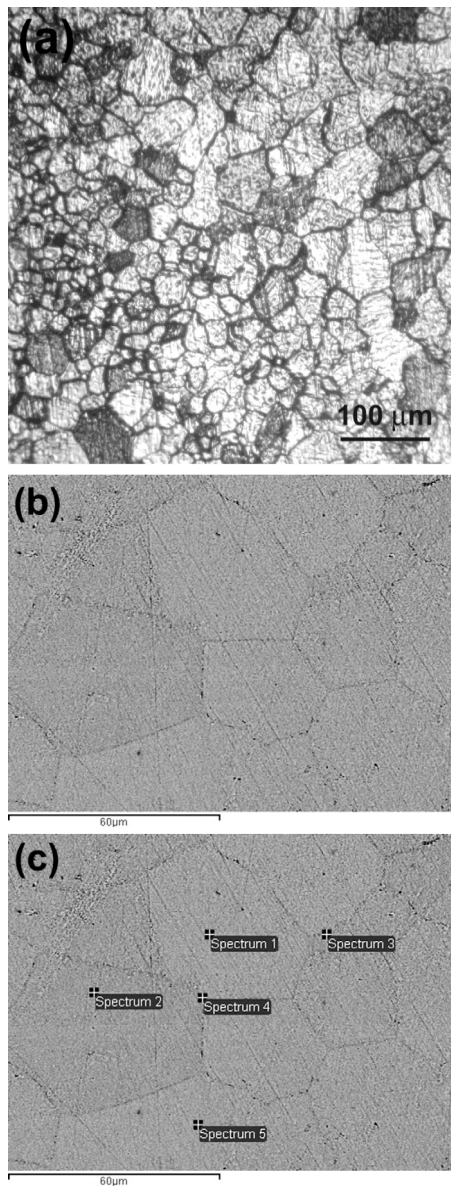


Figure 7: Microstructure of sample A4: a) LM (magnification of 80 \times), b) SEM-EDX (magnification of 1000 \times) and c) positions of EDX analysis

Slika 7: Mikrostruktura vzorca A4: a) LM (povećava 80 \times), b) SEM-EDX (povećava 1000 \times) in c) položaj EDX-analiz

Table 8: Results of EDX analysis of sample A4 in amount fractions, (x/%)

Tabela 8: Rezultati EDX-analiz vzorca A4 v množinskih deležih, (x/%)

Position	A4		
	Al	Cu	Zn
Spectrum 1	12.14	63.45	24.41
Spectrum 2	11.95	64.22	23.83
Spectrum 3	12.03	63.60	24.37
Spectrum 4	12.09	63.66	24.25
Spectrum 5	12.10	63.15	24.76

5 and the chemical compositions determined with the EDX analysis are presented in **Table 6**.

Technical difficulties like the fact that the maximal magnification of the LM apparatus is just 500 \times and a very small diameter (1 mm) of sample A2 prevented us from getting a LM photograph.

The microstructure of sample A2 (**Figure 5b**) is characterized by the grains irregular in the shape and size, and the results of the EDX analysis presented in **Table 6** are consistent with the fact that copper forms solid solutions with nickel and manganese²⁹.

The results of the microstructural analysis with light optical microscopy and SEM for sample A3 are given in **Figure 6**, with the chemical compositions determined with the EDX analysis presented in **Table 7**.

The microstructure of alloy A3, obtained with a LM microphotograph (**Figure 6a**), consists of polygonal grains with a significant variation in size.

The results of the microstructural analysis with light optical microscopy and SEM-EDX for sample A4 are given in **Figure 7** and the chemical compositions determined with the EDX analysis are presented in **Table 8**. The microstructure of sample A4 consists of polygonal grains, which vary in size.

According to the phase diagram of the binary Cu-Zn and Cu-Al systems²⁹, the solid solubility of aluminum in copper is approximately 18 % of amount fractions, and for zinc it goes up to 30 % of amount fractions. Considering that the base material for samples A3 and A4 is copper ($\approx w(\text{Cu}) = 68 \%$), it is reasonable to expect that aluminum and zinc will dissolve in copper, creating solid solutions. This was confirmed with the results of the EDX analysis presented in **Tables 7** and **8**. In addition, the EDX results indicate that the homogeneity of sample A4 is quite good because there is no significant difference in the chemical composition analyzed at various measuring points.

5 CONCLUSION

Different shape-memory alloys belonging to ternary systems Cu-Al-Zn and Cu-Mn-Ni and to quaternary system Ni-Cu-Fe-Mn were investigated. The thermodynamic properties of these alloys were investigated analytically, using the general solution model (GSM) and the known Redlich-Kister parameters for the constitutive binary systems. The thermodynamic analysis showed that the alloys with high copper amounts from systems Cu-Al-Zn and Ni-Cu-Fe-Mn display a good miscibility, while the alloys from the Cu-Mn-Ni system tend to display positive deviations from Raoult's law, which can even lead to layering.

The microstructures of the selected alloys were investigated experimentally by means of light optic microscopy (LM) and scanning electron microscopy with energy-dispersive X-ray spectrometry (SEM-EDX). The microstructure analysis of the investigated alloy samples

revealed that the microstructure is built of polygonal grains that can significantly vary in size. The EDX analysis results provided the information about the alloy chemical compositions and were, overall, in agreement with the known facts about the investigated systems. The results presented in this paper contribute to a better understanding of the thermodynamic properties and microstructures of the investigated shape-memory alloys.

Acknowledgement

The authors are grateful to the Ministry of Education, Science and Technological Development of the Republic of Serbia for the financial support provided through Projects 34005 "Development of ecological knowledge-based advanced materials and technologies for multifunctional application" and 172037 "Modern multi-component metal systems and nanostructured materials with different functional properties".

6 REFERENCES

- W. M. Huang, Z. Ding, C. C. Wang, J. Wei, Y. Zhao, H. Purnawali, Shape memory materials, *Materials Today*, 13 (2010) 7–8, 54–61, doi:10.1016/S1369-7021(10)70128-0
- D. Achitei, P. Vizureanu, N. Cimpoesu, D. Dana, Thermo-mechanical fatigue of Cu-Al-Zn shape memory alloys, *Proc. of 44th International October Conference on Mining and Metallurgy*, Bor, 2012, 401–404
- L. Janke, C. Czaderski, M. Motavalli, J. Ruth, Applications of shape memory alloys in civil engineering structures - Overview, limits and new ideas, *Materials and Structures*, 38 (2005), 578–592, doi:10.1007/BF02479550
- K. K. Jee, J. H. Han, W. Y. Jang, A method of pipe joining using shape memory alloys, *Materials Science and Engineering A*, 438–440 (2006), 1110–1112, doi:10.1016/j.msea.2006.02.094
- Y. Bellouard, Shape memory alloys for microsystems: A review from a material research perspective, *Materials Science and Engineering A*, 481–482 (2008), 582–589, doi:10.1016/j.msea.2007.02.166
- D. Mantovani, Shape Memory Alloys: Properties and Biomedical Applications, *Journal of the Minerals Metals and Materials Society*, 10 (2000), 36–44, doi:10.1007/s11837-000-0082-4
- A. Melzer, D. Stöckel, Using shape-memory alloys, *Medical Device Technology*, 6 (1995) 4, 16–23
- Y. Luo, M. Higa, S. Amae, T. Yambe, T. Okuyama, T. Takagi, H. Matsuki, The possibility of muscle tissue reconstruction using shape memory alloys, *Organogenesis*, 2 (2005) 1, 2–5, doi:10.4161/org.2.1.1757
- M. Dolce, D. Cardone, R. Marnetto, Implementation and testing of passive control devices based on shape memory alloys, *Earthquake Engineering and Structural Dynamics*, 29 (2000), 945–968, doi:10.1002/1096-9845(200007)29:7<945::AID-EQE958>3.0.CO;2-#
- S. Saadat, J. Salichs, M. Noori, Z. Hou, H. Davoodi, I. Bar-On, Y. Suzuki, A. Masuda, An overview of vibration and seismic applications of NiTi shape memory alloy, *Smart Materials and Structures*, 11 (2002), 218–229, doi:10.1088/0964-1726/11/2/305
- R. DesRoches, B. Smith, Shape memory alloys in seismic resistant design and retrofit: a critical review of their potential and limitations, *Journal of Earthquake Engineering*, 8 (2004) 3, 415–429, doi:10.1080/13632460409350495
- B. Kim, M. G. Lee, Y. P. Lee, Y. I. Kim, G. H. Lee, An earthworm-like micro robot using shape memory alloy actuator, *Sensors and Actuators A: Physical*, 125 (2006), 429–437, doi:10.1016/j.sna.2005.05.004
- R. B. Gorbet, R. A. Russell, A novel differential shape memory alloy actuator for position control, *Robotica*, 13 (1995), 423–430, doi:10.1017/S0263574700018853
- K. C. Chou, A general solution model for predicting ternary thermodynamic properties, *Calphad*, 19 (1995), 315–325, doi:10.1016/0364-5916(95)00029-E
- K. C. Chou, S. K. Wei, A new generation solution model for predicting thermodynamic properties of a multicomponent system from binaries, *Metallurgical and Materials Transactions B*, 28 (1997), 439–445, doi:10.1007/s11663-997-0110-7
- Lj. Balanović, D. Živković, A. Mitovski, D. Manasijević, Ž. Živković, Calorimetric investigations and thermodynamic calculation of Zn-Al-Ga system, *Journal of Thermal Analysis and Calorimetry*, 103 (2011) 3, 1055–1061, doi:10.1007/s10973-010-1070-8
- L. Gomidželović, I. Mihajlović, A. Kostov, D. Živković, Cu–Al–Zn System: Calculation of thermodynamic properties in liquid phase, *Hemijska Industrija*, 67 (2013) 1, 157–164, doi:10.2298/HEMIND.120306041G
- G. H. Zhang, K. C. Chou, General formalism for new generation geometrical model: application to the thermodynamics of liquid mixtures, *Journal of Solution Chemistry*, 39 (2010), 1200–1212, doi:10.1007/s10953-010-9570-5
- G. H. Zhang, L. J. Wang, K. C. Chou, A comparison of different geometrical models in calculating physicochemical properties of quaternary systems, *Calphad*, 34 (2010) 4, 504–509, doi:10.1016/j.calphad.2010.10.004
- V. T. Witusiewicz, U. Hecht, S. G. Fries, S. Rex, The Ag–Al–Cu system: Part I: Reassessment of the constituent binaries on the basis of new experimental data, *Journal of Alloys and Compounds*, 385 (2004), 133–143, doi:10.1016/j.jallcom.2004.04.126
- A. T. Dinsdale, A. Kroupa, J. Vizdal, J. Vrestal, A. Watson, A. Zemanova, COST Action MP0602, Version 1.0, Thermodynamic Database, Brno, Czech Republic, 2009 (http://www.cost.eu/COST_Actions/mpns/Actions/MP0602)
- S. Mey, Re-evaluation of the Al-Zn system, *International Journal of Materials Research*, 84 (1993) 7, 451–455
- C. He, Y. Du, H. L. Chen, S. Liu, H. Xu, Y. Ouyang, Z. K. Liu, Thermodynamic modeling of the Cu–Mn system supported by key experiments, *Journal of Alloys and Compounds*, 457 (2008), 233–238, doi:10.1016/j.jallcom.2007.03.041
- J. Miettinen, Thermodynamic description of the Cu–Mn–Ni system at the Cu–Ni side, *Calphad*, 27 (2003) 2, 147–152, doi:10.1016/j.calphad.2003.08.003
- J. Miettinen, Thermodynamic solution phase data for binary Mn-based systems, *Calphad*, 25 (2001) 1, 43–58, doi:10.1016/S0364-5916(01)00029-3
- G. Cacciamani, A. Dinsdale, M. Palumbo, A. Pasturel, The Fe–Ni system: Thermodynamic modelling assisted by atomistic calculations, *Intermetallics*, 18 (2010), 1148–1162, doi:10.1016/j.intermet.2010.02.026
- Q. Chen, Z. P. Jin, The Fe–Cu system: A thermodynamic evaluation, *Metallurgical and Materials Transactions A*, 26 (1995) 2, 417–426, doi:10.1007/BF02664678
- W. Huang, An Assessment of the Fe–Mn system, *Calphad*, 13 (1989) 3, 243–252, doi:10.1016/0364-5916(89)90004-7
- http://www.crct.polymtl.ca/fact/documentation/sgte/sgte_figs.htm

THE RELATIONSHIP BETWEEN THERMAL TREATMENT OF SERPENTINE AND ITS REACTIVITY

ODVISNOST MED TOPLOTNO OBDELAVO SERPENTINA IN NJEHOVO AKTIVNOSTJO

Gabriel Sučík¹, Adriana Szabóová¹, Ľuboš Popovič¹, Damir Hršak²

¹Technical University of Kosice, Faculty of Metallurgy, Department of Ceramics, Park Komenského 3, 04200 Kosice, Slovakia

²University of Zagreb, Faculty of Metallurgy, Aleja narodnih heroja, 44103 Sisak, Croatia
gabriel.sucik@tuke.sk

Prejem rokopisa – received: 2014-09-09; sprejem za objavo – accepted for publication: 2015-02-04

doi:10.17222/mit.2014.222

In this research the effect of the thermal treatment of chrysotile serpentine on the increase in the reactivity during the process of its leaching in a diluted hydrochloric acid was investigated. Measurements were made on samples of 5 g taken from the heap by selecting the fractions of 3–5 mm. The calcination in air of individual samples, required for the analysis, was carried out in an electric muffle furnace at temperatures from 500 to 1100 °C at intervals of 50 °C. The specific surface areas of the calcined samples were measured with the multipoint B.E.T. method and the relative density with a mercury high-pressure porosimeter. The results were related with the yield of Mg^{2+} in an extract of 1 g of a ground serpentine fraction from 0 to 315 μm in 250 cm^3 of 0.25 M HCl, taken after 5 min from a reactor stirred at 500 min^{-1} and at 20 °C. The strong relation between the temperature of the serpentine calcination and the rate of leaching was confirmed. The specific surface area of the examined serpentine rose from 16.2 $m^2 g^{-1}$ at a calcination temperature of 600 °C to the maximum value of 45.2 $m^2 g^{-1}$ at a calcination temperature of 700 °C. At this temperature, the degree of dehydroxylation was 82 % and, at the same time, the maximum rate of dissolution of Mg^{2+} was reached. Above this temperature, the specific surface area decreased and, at a temperature of 1100 °C, it fell to a value of 2 $m^2 g^{-1}$, which also resulted in a reduction of the yield of Mg^{2+} .

Keywords: serpentine, calcination, specific surface area, apparent porosity, leaching rate, crystallinity

V tem članku je bil preiskovan vpliv toplotne obdelave krizotil serpentina na povečanje reaktivnosti pri procesu izločanja iz raztopine solne kisline. Meritve so bile izvršene na 5 g vzorcih, vzeti na odlagališču, z ločitvijo frakcije 3–5 mm. Kalcinacija na zraku, posameznih vzorcev za analizo, je bila izvršena v električni retortni peči pri temperaturah od 500 °C do 1100 °C, v intervalih po 50 °C. Specifična površina kalciniranih vzorcev je bila izmerjena z večtočkovno B.E.T. metodo, relativna gostota pa z živo-srebrnim visoko-tlačnim porozimetrom. Rezultati so bili primerjani z izkoristkom Mg^{2+} pri ekstrakciji iz 1 g osnovne frakcije serpentina z zrnatostjo 0 do 315 μm v 250 cm^3 0,25 M HCl, vzeti po 5 min iz reaktorja s hitrostjo mešanja 500 min^{-1} pri 20 °C. Potrjena je bila močna odvisnost med temperaturo kalcinacije serpentina in hitrostjo izločanja. Specifična površina preiskovanega serpentina je narasla iz 16,2 $m^2 g^{-1}$ pri temperaturi kalcinacije 600 °C na največjo vrednost 45,2 $m^2 g^{-1}$ pri temperaturi kalcinacije 700 °C. Pri tej temperaturi je bila stopnja dehidroksilacije 82 % in istočasno je bila dosežena tudi največja hitrost raztapljanja Mg^{2+} . Nad to temperaturo se je specifična površina zmanjšala in pri temperaturi 1100 °C padla na 2 $m^2 g^{-1}$, kar je vplivalo tudi na zmanjšanje izkoristka Mg^{2+} .

Ključne besede: serpentin, kalcinacija, specifična površina, navidezna poroznost, hitrost izločanja, kristaliničnost

1 INTRODUCTION

The economic efficacy of chemical technologies is closely related with the production speed. The raw material, the subject of this paper and also of earlier papers, is the waste micro-chrysotile material from the Dobšiná area (Slovakia). The aim of the chemical treatment is the production of chemically pure magnesium compounds¹, silica^{2–4} and ferric hydroxide⁵. In the previous papers^{6–8}, the following leaching agents were tested: hydrochloric acid, acetic acid and ammonium chloride. The effect of the leaching-agent concentration and the temperature on the kinetics of the leaching of crude serpentine was monitored.

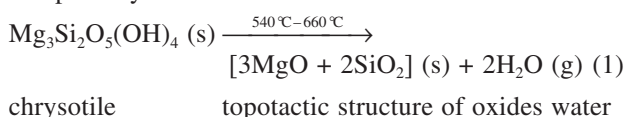
The impacts of the thermal-treatment calcination, where the key parameters were the degree of conversion and the temperature of the dehydroxylation of serpentine, were examined in previous papers^{9–14}. According to these papers, the calcination of serpentine of up to 80 %

resulted in an up to 30-time acceleration of the transfer of Mg^{2+} in the solution compared to the leaching of crude serpentine. The rapidity is attributed to the destruction of the layers of magnesium octahedron and the release of internal links. In addition, there are also changes in the specific surface area and bulk density, relating to the porosity¹⁵. These parameters are directly measurable and, in contrast to the qualitative parameter change in the crystallinity, they may be related to the kinetic parameters of the chemical reactions of the solidus-liquidus type, where the control process is the reaction at the phase interface.

2 EXPERIMENTAL WORK

The measurements of the specific-surface-area and density criteria were implemented on fractions of 3–5 mm. The apparent/open porosity was measured on sam-

ples with a cube shape and a volume of 0.2–0.5 cm³. For the chemical and thermal analysis, the samples were ground in a Mn-steel spherical vibrating chamber. The chemical composition of serpentine was analyzed with ICP OES iCAP6300 and the results are summarized in **Table 1**. By heating the crude serpentine, the thermal dissociation to the origin of the so-called topotactic structure¹⁶ of serpentine anhydride¹⁷ (Equation (1)) occurs in a temperature range of 540–660 °C, which is characterized by a low chemical stability and is accompanied by an increase in the specific surface area and porosity:



By heating them to above 700 °C, the MgO and SiO₂ oxides react with each other on a stable forsterite and amorphous silica¹⁷, stabilizing the structure and increasing the resistance to acids. The chemical reaction is expressed with Equation (2):

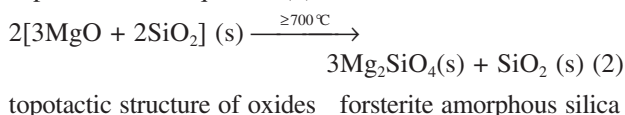


Table 1: Chemical composition of SED serpentine

Tabela 1: Kemijska sestava SED serpentina

MgO	SiO ₂	Al ₂ O ₃	CaO	Fe ₂ O ₃	NiO	L.O.I.
47.8	28.6	2.4	0.9	5.9	0.3	12.57

The thermochemical processes are identified with a differential thermal analysis and a NETZSCH STA 449F3 Jupiter thermogravimetric instrument, and evaluated in the NETZSCH Proteus program. A graphic recording with characteristic temperature points is shown in **Figure 1** and used for setting the experimental conditions of the calcination.

The calcination in air of 5 g samples of coarse fractions of 3–5 mm was carried out under controlled conditions in an electric muffle furnace at 500–1100 °C, with

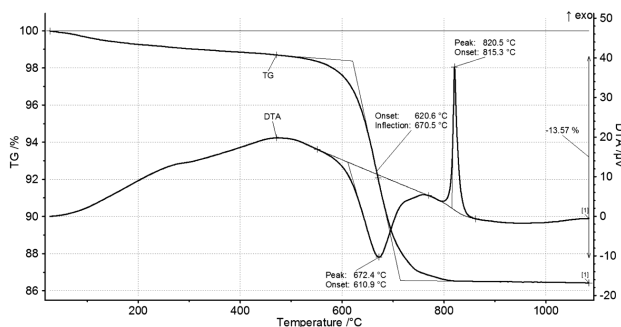


Figure 1: Differential thermal and thermogravimetric analysis of crude serpentine

Slika 1: Diferenčna termična in termogravimetrična analiza surovega serpentina

increments of 50 °C and a dwell time at a particular temperature of 180 min. The samples were inserted into the cold furnace and heated at a rate of 15 °C per minute. With this procedure, 13 samples (SED500– SED1100) were prepared. After the annealing procedure, the residual loss due to annealing (the degree of conversion) and dimensional changes were determined. In the first step of the analysis, the weight and moisture content of each sample were determined on a KERN MLB 50-3N thermobalance, and the geometric volume of mercury was determined on an Amsler 9/593 volume meter. The pore size distribution and the open porosity of the samples were measured with the method of high-pressure mercury porosimetry using automatic Quantachrome porosimeter Poremaster 33. The specific surface areas of S_A samples were measured with a surface-and-pore analyzer through the sorption of nitrogen, with the B.E.T. method. The results were compared with the parameters of the reference sample of unannealed serpentine (SEDraw).

3 RESULTS AND DISCUSSION

The measurement of open porosity π_a of calcined samples SED500 to SED1100 did not confirm the expected correlation between the chemical reactivity in terms of the leaching rate of Mg^{2+} and π_a . It can be claimed that the maximum π_a of almost 20 % was measured on the samples exposed to the temperatures of the forsterite formation with the maximum rate of around 900 °C, with the increase from the temperature of 700 °C in accordance with the forsterite formation¹⁷. On the contrary, at the temperatures in the area of dehydroxylation, $\pi_a = 1.5$ % at the level of raw serpentinite (SEDraw). Intragranular pores had the major proportion, up to 2/3 π_a , as shown in **Figure 2**.

The only noticeable consistency between π_a and specific surface area S_A is the local minimum of 1.5 % and 16 m² g⁻¹ at 600 °C, which could be explained with the closing of the pores due to the impact of the ox-

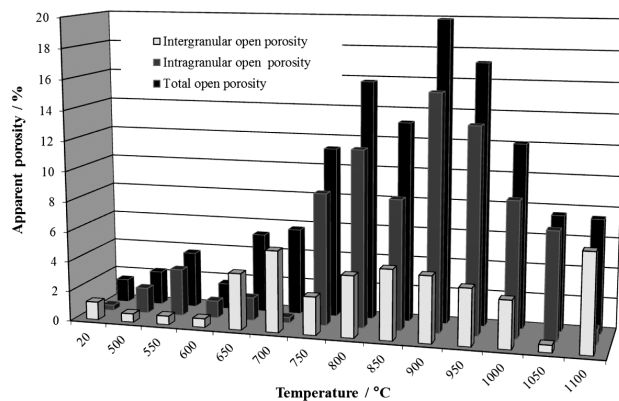


Figure 2: Open porosity and pore character depending on the calcination temperature of SED

Slika 2: Odprta poroznost in značilnost por v odvisnosti od temperature kalcinacije SED

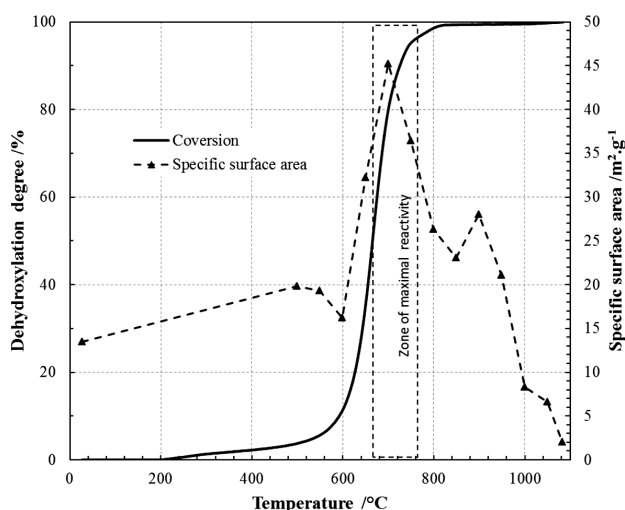


Figure 3: Change in the specific surface of SED depending on the calcination temperature

Slika 3: Spreminjanje specifične površine SED, v odvisnosti od temperature kalcinacije

dizing reactions of $\text{Fe}^{2+} \rightarrow \text{Fe}^{3+}$. Strong correlations between the degree of conversion α and S_A can be found in **Figure 3**. The maximum S_A of $45.2 \text{ m}^2 \text{ g}^{-1}$ was measured for sample SED700 with $\alpha = 82 \%$. Increasing the temperature over the recrystallization temperature causes sintering, which is shown as a decrease in π_a and S_A over the value of $2 \text{ m}^2 \text{ g}^{-1}$.

The reactivity of ground calcinate was tested for fractions of $0\text{--}315 \mu\text{m}$. **Figure 4** shows a graphical representation of the function of the yield of Mg^{2+} $\alpha_{\text{Mg}} = f(\alpha, T)$ in intervals of (10, 20 and 60) min. From this dependence it follows that for the maximum efficiency

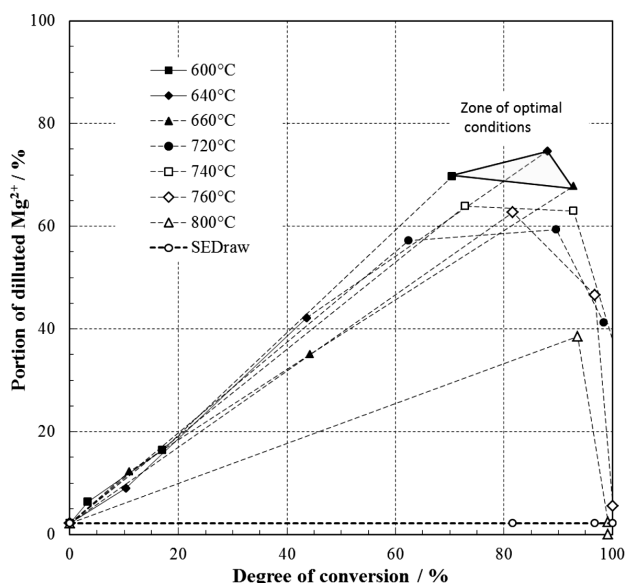


Figure 4: Dependence of the dissolution efficiency of magnesium depending on the calcination condition for serpentine (SED)

Slika 4: Odvisnost učinkovitosti raztapljanja magnezija od pogojev pri kalcinaciji serpentina (SED)

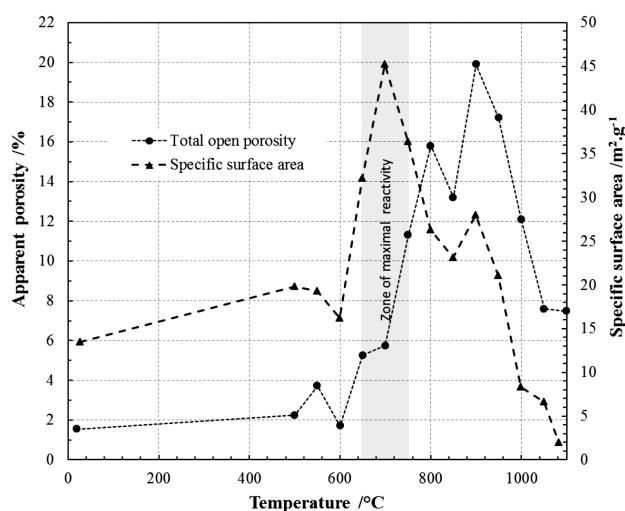


Figure 5: Comparison of the total open porosity and specific surface area as the function of temperature

Slika 5: Primerjava skupne odprte poroznosti in specifične površine v odvisnosti od temperature

of leaching, it is necessary to calcine serpentine so that a conversion of about 80 % is achieved and the calcination temperature is in a range from 600 to 700 °C. This will also guarantee the maximum surface area, which is an important parameter affecting the kinetics of the leaching. On the other hand, a porosity increase does not indicate a leaching improvement because of the structure stabilization due to the transformation to forsterite as shown in **Figure 5**.

4 CONCLUSION

The chemical reactivity of calcined serpentine depends primarily on the degree of structural crystallinity. The leaching rate of the forsterite-crystal phase is similar to the leaching rate of crude serpentine. It makes the thermal activation meaningless.

The reactive serpentine formation at temperatures of 600–700 °C does not significantly depend on the dwell time, unlike in the case of higher temperatures. At a temperature above 700 °C, a partial forsterite formation takes place.

At the temperature above 700 °C, the apparent porosity increases, but the specific surface decreases. This phenomenon is related to the recrystallization, the overall contraction of the volume and the sintering.

Acknowledgement

This work was supported by the Scientific Grant Agency of the Ministry of Education of the Slovak Republic and The Slovak Academy of Sciences – Grant VEGA 1/0378/14.

5 REFERENCES

- ¹ L. Haurie, A. I. Fernández, J. I. Velasco, J. M. Chimenos, J. M. L. Cuesta, F. Espinel, *Polymer Degradation and Stability*, 91 (2006) 9, 989–994, doi:10.1016/j.polymdegradstab.2005.08.009
- ² V. V. Velinskii, G. M. Gusev, *J. of Mining Science*, 38 (2002) 4, 402–404, doi:10.1023/A:1023324206554
- ³ A. Pietriková, M. Búgel, M. Golja, *Metalurgija*, 43 (2004) 4, 299–304
- ⁴ A. Fedoročková, B. Plešingerová, G. Sučík, P. Raschman, A. Doráková, *Int. J. of Mineral Processing*, 130 (2014), 42–47, doi:10.1016/j.minpro.2014.05.005
- ⁵ R. A. Silva, C. D. Castro, C. O. Petter, I. A. H. Schneider, *Mine Water – Managing the Challenges*, IMWA 2011, Aachen, 2011, 469–473
- ⁶ A. Fedoročková, M. Hreus, P. Raschman, G. Sučík, *Minerals Engineering*, 32 (2012), 1–4, doi:10.1016/j.mineng.2012.03.006
- ⁷ A. Fedoročková, P. Raschman, *Chemical Papers*, 100 (2006) 5, 337–347
- ⁸ W. Gao, J. Wen, Z. Li, *Industrial and Engineering Chemistry Research*, 53 (2014) 19, 7947–7955, doi:10.1021/ie4043533
- ⁹ J. N. Weber, R. T. Greer, *American Mineralogist*, 50 (1965), 450–464
- ¹⁰ A. F. Gualtieri, A. Tartaglia, *Journal of the European Ceramic Society*, 20 (2000) 9, 1409–1418, doi:10.1016/S0955-2219(99)00290-3
- ¹¹ D. Hršak, J. Malina, A. B. Hadžipašić, *Mater. Tehnol.*, 39 (2009) 6, 225–227
- ¹² C. Viti, *American Mineralogist*, 95 (2010) 4, 631–638, doi:10.2138/am.2010.3366
- ¹³ A. F. Gualtieri, C. Giacobbe, C. Viti, *American Mineralogist*, 97 (2012) 4, 666–680, doi:10.2138/am.2012.3952
- ¹⁴ P. Raschman, A. Fedoročková, G. Sučík, *Hydrometallurgy*, 139 (2013), 149–153, doi:10.1016/j.hydromet.2013.08.010
- ¹⁵ B. Plešingerová, K. K. Tkáčová, L. Turčániová, *Transactions of the Technical University of Kosice*, 4 (1994) 1, 79
- ¹⁶ J. R. Günter, H. R. Oswald, *Bulletin of the Institute for Chemical Research, Kyoto University*, 53 (1975) 2, 249–255, [cited 2014-08-22], available from World Wide Web: <http://hdl.handle.net/2433/76601>
- ¹⁷ G. W. Brindley, R. Hayami, *Mineral Magazine, Pennsylvania*, 35 (1965), 189–195

DEFORMATIONS AND VELOCITIES DURING THE COLD ROLLING OF ALUMINIUM ALLOYS

DEFORMACIJA IN HITROSTI PRI HLADNEM VALJANJU ALUMINIJEVIH ZLITIN

Mitar Mišović¹, Nebojša Tadić¹, Milojica Jaćimović², Mileta Janjić³

¹University of Montenegro, Faculty of Metallurgy and Technology, Džordža Vašingtona bb, 81000 Podgorica, Montenegro

²University of Montenegro, Faculty of Natural Sciences and Mathematics, Džordža Vašingtona bb, 81000 Podgorica, Montenegro

³University of Montenegro, Faculty of Mechanical Engineering, Džordža Vašingtona bb, 81000 Podgorica, Montenegro
mitarm@ac.me

Prejem rokopisa – received: 2014-10-02; sprejem za objavo – accepted for publication: 2015-01-20

doi:10.17222/mit.2014.250

This paper presents the analysis results of investigations on the deformations and velocities during the cold rolling of strips of aluminium alloys AW2024 and AW5083 obtained with an application of the finite-element method (FEM) and the conventional rolling theory. The results of the simulation obtained using the FEM software DEFORM-2D were analysed for the displacements, effective strain and velocity of rolling. The diagrams of the changes in these values along the deformation zone were presented together with the identified characteristics of the trajectories of the surface and axis as the boundary surfaces for simulating the cold rolling of the strips. The finite effective strains were compared with the degree of reduction of the strip thickness, and equations were derived for the dependence of their ratio on the starting thickness of a strip. The equations for the dependence of the velocity of a strip and the roll ratio on the degree of reduction due to the control of forward and backward slips were also derived. The reliability of the obtained results and derived equations was tested with experimental tests, theoretical relationships for plane strain and the results for the forward slip published in the literature.

Keywords: cold rolling, FEM, displacements, effective strain, forward slip

Članek predstavlja analizo rezultatov preiskav deformacije in hitrosti pri hladnem valjanju trakov aluminijevih zlitin AW2024 in AW5083, dobljenih z uporabo metode končnih elementov (FEM) in konvencionalne teorije valjanja. Analizirani so bili rezultati simulacije, dobljene s FEM programsko opremo DEFORM-2D, za raztezek, efektivno obremenitev in hitrost valjanja. Predstavljeni so diagrami sprememb teh vrednosti vzdolž deformacijske cone, skupaj z identifikacijo značilnosti trajektorij površine in osi, kot mejnih površin za simulacijo hladnega valjanja trakov. Končne efektivne obremenitve so bile primerjane s stopnjo redukcije debeline trakov in razvite so bile enačbe za odvisnost njihovega razmerja od začetne debeline traku. Razvite so tudi enačbe za odvisnost hitrosti traku in razmerja valjev na stopnjo redukcije zaradi kontrole prehitevanja in zaostajanja traku. Zanesljivost dobljenih rezultatov in razvitih enačb je bila preizkušena s preizkusom, s teoretičnimi odvisnostmi za ravninsko napetost in za rezultate prehitevanja, objavljenega v literaturi.

Ključne besede: hladno valjanje, FEM, raztezek, efektivna obremenitev, prednji zdrs

1 INTRODUCTION

Cold rolling is the primary technological process for the preparation of strips, thin strips and foils of aluminium and its alloys. This process is applied for strips with thicknesses of up to 4 mm, although strips with larger thicknesses can be rolled as well.

The cold-rolling technology has been constantly developed and improved with the intent to establish reliable quality and high productivity^{1,2}. Regardless of the continuous development in all the areas, theoretical models of the process are still the subjects of a comprehensive research^{3,4}. The understanding and control of deformation, kinematics and stress states are particularly complex due to the conditions for a reliable planning and control of the process⁵⁻⁷. The conventional theory of rolling^{8,9}, the experimental procedures for tracing the measurement weights¹⁰⁻¹² and the procedures for the FEM simulation^{4,13,14} were used in the research.

This paper reports experimental results for cold strip rolling and characteristic results for deformations and

velocities obtained via FEM. A connection and comparison of the results obtained from different research procedures are discussed as well.

Strips made of alloys AW2024 and AW5083 with thicknesses from 4 to 0.6 mm were chosen for this research. These two alloys are widely used in all areas of metal material application and are also characterised by a wide range of final mechanical properties.

The analysis of the cold rolling of strips, thin strips and foils is based on the condition that it is a process with plane strain. In this manner, the geometry of the deformation zone and the change in the velocity of a strip and roll can be described using the scheme shown in **Figure 1**.

For the plane strain, the change in the width can be neglected ($b_0 = b_1$), and thus the deformations and geometric criteria for the dimensions of a strip and deformation zone can be described with the relationships:

$$\varphi_h = \ln(h_0/h_1), \varphi_l = \ln(l_1/l_0), \varphi_b = \ln(b_1/b_0) = 0; \\ \varphi_h = -\varphi_l; b_0/h_0 \geq 10; (l_d/h_m)_{\min} = 2 - 3 \quad (1)$$

The length of the deformation zone (l_d) for absolutely solid rolls is calculated using the following equation:

$$l_d = \sqrt{R\Delta h - (\Delta h / 2)^2} \approx \sqrt{R\Delta h} \quad (2)$$

However, a high value of the contact stress (the roll pressure) for cold rolling causes an elastic deformation of the roll with a radial compression (roll flattening). Thus, the length of the deformation zone increases (**Figure 1**) and can be calculated using the following equation:

$$l_{de} = x_0 + x_1 = x_0 + \sqrt{R\Delta h + x_0^2} \quad (3)$$

The value of x_0 is determined using the Hertz equation:

$$x_0 = \frac{8(1-\nu^2)}{\pi \cdot E} RP_a \quad (4)$$

where ν – Poisson's ratio, E – the modulus of elasticity of the roll material, and P_a – the average roll pressure.

The movements of a strip at the entrance of the roll gap occur under the action of an active tangential friction force between the rolls and the strip. The horizontal velocity of the strip (V_{sx}) is determined using the horizontal velocity of the roll (V_{rx}). These velocities are

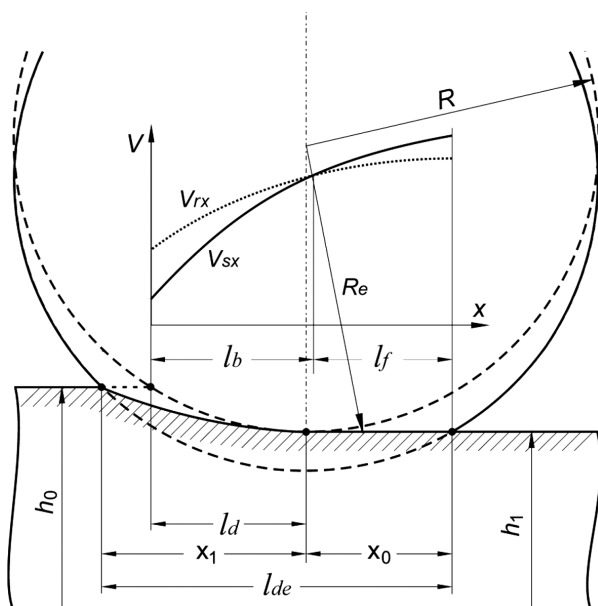


Figure 1: Deformation-zone geometry with and without an elastic deformation of rolls: h_0 , b_0 , l_0 / h_1 , b_1 , l_1 – thickness, width and length of the initial/rolled strip, respectively; l_d , l_{de} – length of deformation zone (contact between strip and roll) with and without an elastic deformation of rolls; l_b , l_f – length of backward and forward slip zones; R – roll radius; R_e – radius of an elastically deformed roll; $\Delta h = h_0 - h_1$ – absolute strip thickness reduction; h_m – mean strip thickness, i.e., $(h_0 + h_1)/2$; V_{sx} , V_{rx} – horizontal velocities of strip and roll

Slika 1: Geometrija područja deformacije z in brez elastične deformacije valjev: h_0 , b_0 , l_0 / h_1 , b_1 , l_1 – debljina, širina in dolžina začetnega oziroma valjanega traku; l_d , l_{de} – dolžina područja deformacije (stik med trakom in valjem) z in brez elastične deformacije valjev; l_b , l_f – dolžina područja zaostajanja in prehitevanja; R – premer valja; R_e – premer elastično deformiranega valja; $\Delta h = h_0 - h_1$ – absolutno zmanjšanje debljine traku; h_m – povprečna debljina traku, to je $(h_0 + h_1)/2$; V_{sx} , V_{rx} – horizontalna hitrost traku in valja

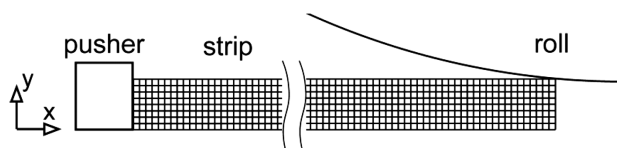


Figure 2: Scheme of 2D-FEM simulation of the rolling process
Slika 2: Shema 2D-FEM simulacije postopka valjanja

altered along the deformation zone, thus creating a zone of the backward slip (l_b) in which the friction force is active and the relationship of the velocities is described as $V_{sx} < V_{rx}$, and a forward-slip zone (l_f) in which the friction force is reactive and the relationship of the velocities is described as $V_{sx} > V_{rx}$ (**Figure 1**). The relative difference in the velocity $(V_{sx} - V_{rx})/V_{rx}$ in zone l_b is known as the backward slip, and in zone l_f , it is known as the forward slip. The forward and backward slips of a strip represent significant and carefully researched weights of the kinematics of the rolling process^{4,15–17}.

A simulation of the rolling process for plane strain can be accomplished using the 2D method of finite elements. The scheme of the process simulation is presented in **Figure 2**.

As cold rolling is symmetrical to the longitudinal x -axis, it is sufficient to present the top half of a strip thickness and the top roll for a 2D simulation. The lower symmetrical portion of the strip and the lower roll can be neglected by setting the boundary condition in such a way that the displacement velocity in the y -axis direction is equal to zero on the longitudinal x -axis. In addition, when the friction force cannot accomplish the grasping of a strip by the rolls, it is necessary to use pushers, keeping in mind that the active friction force has a limited value and the pushing force is also limited. The movement velocity of a pusher is smaller than the velocity of the movement of a strip ($0.1 V_{sx}$) and, therefore this force acts only while the rolls grasp the strip.

2 EXPERIMENTAL DETAILS AND THE FEM SIMULATION

2.1 Rolling process

The laboratory rolling of this work was carried out to assess the plane strain, the tolerance of dimensions, and the strain hardening of the alloys. Alloys AW2024 and AW5083 were examined. The final properties of the alloys can be obtained via different processes of thermal treatment (T conditions) and mechanical treatment (H conditions). Alloy AW2024 can be thermally hardened so that its final mechanical properties are obtained through the thermal precipitation, whereas alloy AW5083 cannot be thermally hardened and its final mechanical properties are accomplished through strain hardening or annealing.

The initial 2024-alloy strips for the experimental rolling were industrially rolled to a thickness of 5 ± 0.01 mm and, subsequently, soft annealed (the T0 condition) and rolled. The modes of rolling and annealing for the

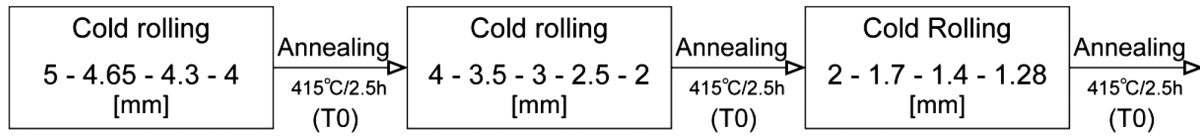


Figure 3: Modes of cold rolling/annealing of alloy-2024 strips

Slika 3: Načini hladnega valjanja/žarjenja trakov iz zlitine 2024

preparation of strips with thicknesses of 4, 2 and 1.28 mm are shown in **Figure 3**. The initial thickness of the 5083-T0 alloy strips is 1.28 ± 0.01 mm. The choice of dimensions and reductions was intended to ensure the conditions corresponding to the plane strain. The highest values of the reduction for all the strip thicknesses correspond to the conditions of the maximum bite on the laboratory rolling mill.

The rolling was completed on a laboratory duo rolling mill having rolls with a diameter of 125 mm and a peripheral velocity of $V_r = 173.4$ mm/s. The lubrication of the strip and rolls was carried out with hydraulic oil. All the testing processes were completed without the use of tension on the strips.

The annealing was completed in a laboratory furnace with a temperature regulation accuracy of ± 2 °C.

2.2 FEM simulation of the rolling process

2.2.1 Software and mathematical formulation of tasks

The commercial DEFORM-2D software was chosen for the simulation of the planned program of cold strip rolling under the conditions of plane strain. The DEFORM formulation of FEM for the mechanics of a rigid-plastic body is based on the known principle of the minimum virtual work expressed via the functional balance between the external and internal forces^{18,19}:

$$\pi = \int_V \bar{\sigma} \dot{\bar{\epsilon}} dV + \int_V \lambda \dot{\epsilon}_v dV - \int_S F_i v_i dS \quad (5)$$

where $\bar{\sigma}$ – the equivalent or effective stress (equal to yield stress K_f), $\dot{\bar{\epsilon}}$ – the equivalent or effective strain rate (determined on the basis of the components of the velocity of deformation for the plane strain), λ – the Lagrange multiplier (equal to the mean stress), $\dot{\epsilon}_v$ – the volumetric strain rate, F_i – the surface traction (for the processes with slip friction, this represents the friction force at the strip/roll contact determined with the normal rolling force and the friction coefficient) and v_i – the velocity (the slipping velocity of a strip on the roll surface).

The first term in Equation (5) refers to the deformational work, the second term expresses the condition of incompressibility and the third term refers to the impact of the friction forces on the strip/roll contact surface.

The Newton-Raphson iterative method is used by DEFORM to find solutions. This method is recommended for the majority of problems because it usually converges, using fewer iterations than the other methods¹⁹. All the simulations were completed with a strip as a rigid-plastic, deformable body hardened by the

deformation, based on experimentally determined equations and with the rolls elastically deformed to a diameter determined with the Hitchcock formula.

2.2.2 Choice of the finite-element mesh

The finite-element mesh provides important baseline data for the analysis of strains, kinematics, and stress values. The choice of the shape and number of finite elements influences the calculation and the accuracy of the solutions for the analysed values. Square isoparametric finite elements represent a simple shape and are adequate for a simulation of the plane-strain process^{18,20}. For cold rolling of strips, the geometry of the deformation zone takes on a simple shape. If square elements are chosen in a manner proportional to the strip thickness, the results for the strips with different thicknesses and under different conditions of reductions can be easily compared. The square isoparametric shape was chosen for these reasons.

The choice of the number of elements, i.e., the mesh density, should enable the required accuracy and convergence of the solutions. Based on the recommendations for the number of finite elements relative to the thickness, the checks for a mesh of 4 to 20 elements on half of a strip thickness were carried out for the simulation of plane strain in thin elements¹⁹. The changes in the shape of the displacement along the x and y axes were analysed depending on the number of finite elements. The displacements represent particularly important values because the strains, velocities and stresses are calculated on the basis of these values. For the sake of clarity, the displacement diagram was considered in a simplified form with two characteristic lines (trajectories) of nodes corresponding to the boundary surfaces of a strip: the line of contact between the metal and roll (the strip surface) and the horizontal centreline (the longitudinal axis of the strip). Since the characteristics of the displacement diagrams change slightly if the number of finite elements (FE) increases above 8, the complete further analysis was carried out with a mesh of eight finite elements on a half strip thickness (the shape of the displacement diagram is analysed in additional detail in Section 3.3.1).

2.2.3 Choice of the coefficient of friction

The choice of the contact-friction condition holds special importance for the cold-rolling process. A quantitative indicator of the friction conditions in plastomechanics is the contact-friction coefficient (f). A functional analysis of the friction conditions is thus considered with respect to the change in the value of this coefficient. The simulation and analysis of the process

can be carried out on the basis of a constant value for the friction coefficient. In this research, the simulation was carried out with an adopted value for the friction coefficient based on Coulomb's law. The coefficient of friction was varied in a range of $f = 0.06\text{--}0.2$ for the purpose of performing this check^{4,21}. In the choice of the values of the friction coefficient, an analysis of the displacement diagrams was carried out in a manner similar to that of the choice of the finite-element mesh. The changes in the diagrams of displacements for different values of the friction coefficient from the extracted interval are evident and expected, but these values are not expressed to the extent of a reliable quantification along the complete deformation zone. Therefore, for further research on deformations and velocities, the presented results are given for the friction-coefficient value of $f = 0.1$, which is often used for simulating similar rolling conditions^{22,23}.

3 RESULTS AND DISCUSSION

3.1 Dimensions and deformation coefficients of rolled strips

The dimensions of the strips, the thickness reductions, the thickness tolerances ($\pm\delta h$) and the spread (ε_b) of the experimental rolling were determined. The thickness tolerances of the rolled strips ($\pm\delta h$) met the production standards for the given thicknesses and reductions of the tested alloys²⁴.

The experimentally verified value of the spread (ε_b) was less than 2 %, which satisfied the condition for plane strain^{25,26}.

3.2 Strain hardening of the alloys

The strain hardening of the alloys was examined via tensile testing of standard specimens. The values of the yield stress (K_f), which depend on the degree of deformation by elongation (φ_l) and the coefficient (K) and the index (n) of strain hardening were determined according to Hollomon's equation $K_f = K \varphi_l^n$. Hollomon's equation was chosen because it describes the area of plastic deformation with a satisfactory accuracy. The beginning of the interval corresponds to the conventional yield strength ($R_{p0.2}$). The boundary values of the uniform deformation intervals of the method of the tensile testing by elongation are limited.

In the area of high deformation degree, the data can be extrapolated but cannot be experimentally verified using the tensile-testing method. For this reason, the strain-hardening testing was carried out within the strip-rolling process. The strips with the same initial dimensions in the thermal state (T0) were rolled with different thickness reductions. After the rolling, specimens for the tensile testing were prepared from the strips, and the yield strength $R_{p0.2}$ was determined. The degree of deformation for the rolled strips was calculated on the basis of the strip thickness change (φ_h in Equation (1)). The results for the standard deviation prove that Hollomon's

equation $K_f = f(\varphi_h)$ fully applies to the strain hardening in the area of high deformation degrees.

Thus, for the FEM simulation of rolling, the chosen alloys are considered as the rigid-plastic materials that can be hardened in the deformational sense according to Hollomon's equation.

3.3 Deformations

3.3.1 Displacements

Displacement diagrams (Δx and Δy) for a 4-mm-thick strip and the singled-out trajectories of the surface and axes of the strip are presented in **Figure 4**. The points at the entrance and exit of the deformation zone were chosen according to the positions that are located outside the boundary values of the displacements. The displacements relative to the geometrical length of the deformation zone determined by Equation (3) are also traced in this analysis.

The change in the horizontal Δx -displacements shows the presence of characteristic areas and different mutual relationships of the boundary surfaces (**Figure 4a**). Area I is located at the entrance of the roll gap. The deformation begins on the surface, before the geometric entrance into the roll gap. The deformation is non-uni-

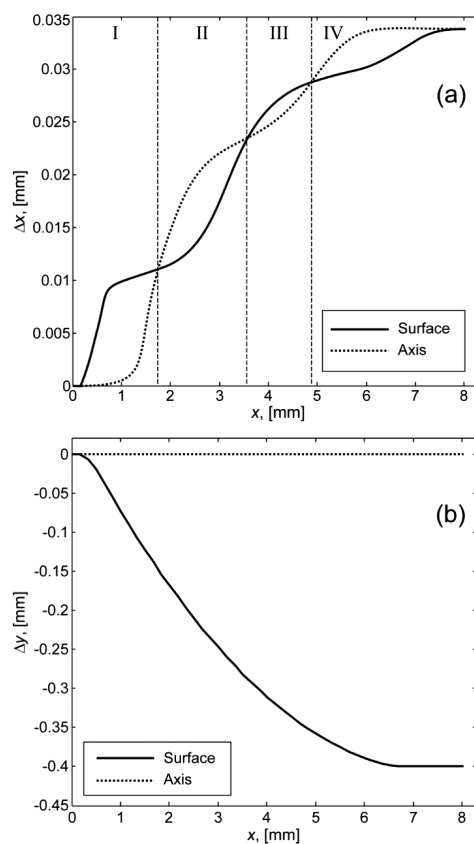


Figure 4: Displacements of mesh nodes in the directions of: a) x-axis and b) y-axis for reduction $\varepsilon = 20\%$ (alloy 2024, $h_0 = 4$ mm, 8 FE, $f = 0.1$)

Slika 4: Premiki vozlišč v mreži v smeri: a) x-osi in b) y-osi pri redukciji $\varepsilon = 20\%$ (zlitina 2024, $h_0 = 4$ mm, 8 FE, $f = 0.1$)

form over the cross-section so that the differences between the surface and axis are apparent. The other trajectories between the surface and axis have the same shape and are distributed inside this area at mutually uniform distances. Area I ends near the vertical cross-section with the same displacements. Area II is observed after Area I inside the deformation zone. The same characteristics are visible, but the positions of the curves for the surface and axis are changed. Area III displays the same characteristics of the trajectories as Area I, but the inhomogeneity is lower. Area IV covers the exit from the roll gap, and the relationship of the values along the trajectories is same as in Area II. At the exit from the roll gap, the balance between the surface and axis is re-established.

The vertical displacements Δy on the surface show a monotonic flow that follows the roll geometry in the roll gap. Because of the rolling symmetry, the vertical displacement on the axis is zero (**Figure 4b**). The other trajectories have the same shape as the trajectories of the surface and are regularly distributed (the same distances on average).

The diagrams of the horizontal and vertical displacements shown in **Figure 4** retain the characteristic shapes for all the tested conditions depending on the number of finite elements and the friction coefficient.

3.3.2 Reduction of the strip thickness and indicators of deformation

The reduction of thickness ε_h (often referred to as the deformation degree) in cold rolling is a particularly important, influential process parameter. The production processes for rolling aluminium and its alloys are predominantly carried out in an interval of $\varepsilon_h = 20\text{--}50\%$. The same interval was used for the experimental rolling and simulation. The results obtained with the simulation also show that the thickness reduction significantly influences the components of deformation. In accordance with the goal of the work, the effective strain (ε_{ef}) was particularly singled out because the value and boundary states (yield stress, stresses and forces) primarily depend on ε_{ef} . **Figure 5** presents FEM diagrams of the ε_{ef} change along the deformation zone for a strip with the starting thickness of 4 mm that was rolled with reductions of 20 and 50 %.

The first reduction (**Figure 5a**) exhibits an obvious correlation with the diagrams of the Δx displacements. The difference between the lengths of the trajectories on the surface and axis, conditioned by the shape of the deformation zone, causes large differences in the values of ε_{ef} on these trajectories. Indeed, the same areas as for the Δx displacements can be extracted from the diagram of ε_{ef} . However, the finite values of ε_{ef} differ between the surface and axis, and thus the final strain over the cross-section of a strip is non-uniform. The strain relationships show that the deformation zone ends with a localisation of the plastic deformation in the surface layer. The localisation of the plastic deformation, i.e., the elastic

area around the axis and the plastic area in the surface zone, causes phenomena that follow the inhomogeneous deformation of the vertical cross-section. One of these phenomena is the residual stress²⁷.

The increase in the strip thickness reduction to 50 % was followed by changes in ε_{ef} , so that an inhomogeneous deformation (differences between the values for the surface and axis) was formed at the entrance of the roll gap and retained along the entire deformation zone (**Figure 5b**).

3.3.3 Relationships of the strip thickness and the effective strain

Final values φ_h and ε_{ef} for the trajectories of the surface and the axis, and the average values on the vertical cross-section of the strip with $h_0 = 4$ mm were found (for the strips with $h_0 = 2$ mm and 1.28 mm analogous results were obtained). Because φ_h and ε_{ef} are integral values, the differences between their values are apparent. The condition of plane strain obtained with the FEM simulation can be checked by comparing these two indicators of deformation. Specifically, for plane strain with components $d\varepsilon_1$, $d\varepsilon_2$, and $d\varepsilon_3$ and defined relationships $d\varepsilon_2 = 0$ and $d\varepsilon_1/d\varepsilon_3 = -1$, the following equation applies for

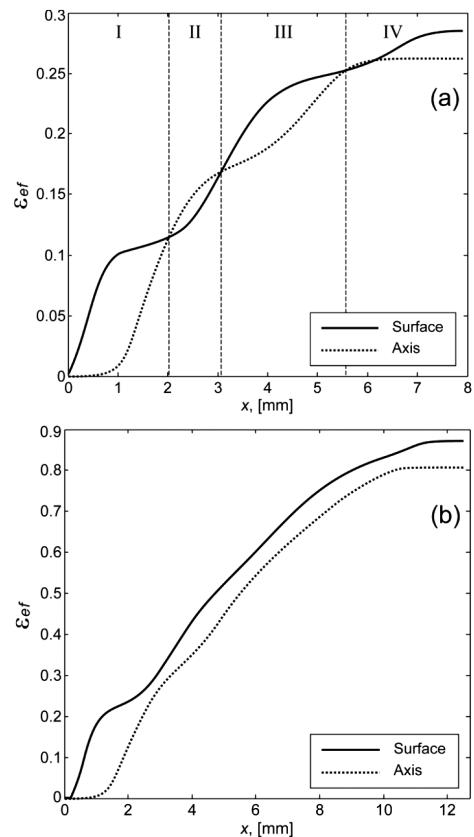


Figure 5: Effective strain on the surface and axis of a strip rolled with thickness reductions of: a) 20 % and b) 50 %. Parameters of the simulation are as listed in **Figure 4**.

Slika 5: Efektivna napetost na površini i v osi traku, valjanega z redukcijo debeline: a) 20 % in b) 50 %. Parametri simulacije so navedeni na sliki 4.

the effective strain: $d\varepsilon_{ef} = (2/\sqrt{3})d\varepsilon_1$, i.e., $\varepsilon_{ef} = 1.155 \varepsilon_1$.²⁸ According to Equation (1) $\varepsilon_1 = \varphi_h$ and, therefore, the previous equation can be rewritten as follows:

$$\varepsilon_{ef} = 1.155\varphi_h, \varepsilon_{ef}/\varphi_h = 1.155 \text{ and } (\varepsilon_{ef2}/\varphi_{h2})/(\varepsilon_{ef1}/\varphi_{h1}) = 1 \quad (6)$$

The values for relationships $\varphi_{h2}/\varphi_{h1}$ and $\varepsilon_{ef2}/\varepsilon_{ef1}$ slightly differ for the same rolling program. Therefore, the compatibility of the results obtained with the simulation using Equation (6) can be found with a sufficient accuracy. These results present an opportunity for a simple correlation of the change in the dimensions and the effective strain obtained with FEM.

The correlation of relationships $\varepsilon_{ef}/\varphi_h$ and the change in the dimensions were assessed. The change in $\varepsilon_{ef}/\varphi_h$ depending on the thickness reduction is similar for all the starting thicknesses. The area of change is limited, but all the values differ from 1.155. Therefore, the mean values of $\varepsilon_{ef}/\varphi_h$ for each initial thickness were calculated. The results were determined with a 95 % confidence interval. The confidence interval in all the cases entirely covers the area of the changes in the values, indicating that the mean values can be reliably used.

It is obvious that the relationship $\varepsilon_{ef}/\varphi_h$ indicates a regular change on the surface and axis and that it depends on the starting thickness of the strip. Thus, the results of $\varepsilon_{ef}/\varphi_h = f(h_0)$ were analytically processed, and the equations used to approximate them were determined with a satisfactory accuracy. According to the limited number of data, the analytical processing of the results was completed using the STATEGRAPH program for all the equations checked with this software program package²⁹. The linear equations were chosen.

The derived equations of dependence $\varepsilon_{ef}/\varphi_h = f(h_0)$ were additionally checked for the cold rolling of the strips with starting thicknesses of 6, 0.6 and 0.012 mm. The thickness of 6 mm is the largest starting thickness for cold rolling, 0.6 mm is the largest starting thickness for rolling thin strips, and 0.012 mm is the thickness for rolling the thinnest foils (aluminium foils with a thickness of 6 μm are produced by doubling two 12- μm foils prior to the rolling and separation after the rolling).

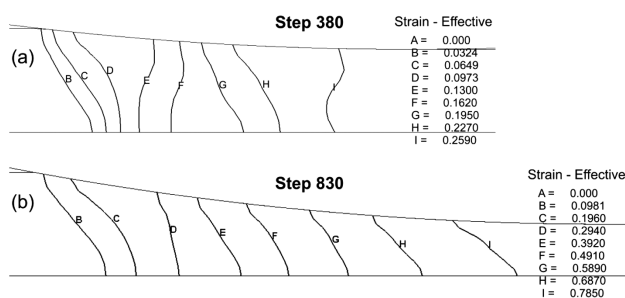


Figure 6: Isolines of ε_{ef} for rolling a strip with a thickness of 4 mm with reductions of: a) 20 % and b) 50 % (simulation parameters as listed in Figure 4)

Slika 6: Izolinije ε_{ef} pri valjanju 4 mm debelega traku, z redukcijom: a) 20 % in b) 50 %. Parametri simulacije so navedeni na sliki 4.

The lowest value of the ratio $\varepsilon_{ef}/\varphi_h$ was obtained for the axis of a 12- μm foil and it is 1.160. This value also differs from the theoretical value of 1.155, although only slightly. For the axis of the 6-mm strip, the difference is approximately 2 %, which represents an allowed deflection from the condition of proportionality for the plane strain. Therefore, the linear equations for the transition of the thickness reduction into effective strains depending on the starting thicknesses of the strips are quite reliable.

3.3.4 Deformation zone

The results in Figure 6 show the positions of the isolines for ε_{ef} in the deformation zone during the rolling of a strip with a thickness of 4 mm. The DEFORM program gives the possibility of presenting the deformation zone as isolines that divide the zone into eight intervals with a constant increment of $\varepsilon_{ef}/8$. The shapes of isolines as well as the areas between two consecutive isolines show a non-uniform deformation of the cross-section, and thus the theory of a homogeneous deformation over the

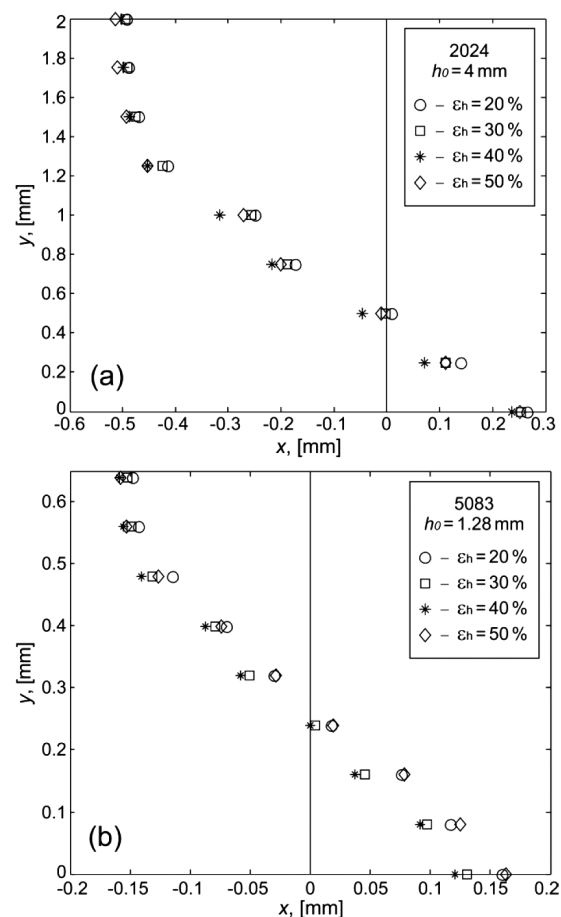


Figure 7: Isolines of the beginning of the plastic deformation zone ($\varepsilon_{ef} = 0.002$) for: a) alloy 2024, strip with $h_0 = 4$ mm and b) alloy 5083, strip with $h_0 = 1.28$ mm ($y = h/2$; simulation parameters as listed in Figure 4)

Slika 7: Izolinije začetka področja plastične deformacije ($\varepsilon_{ef} = 0.002$) za: a) zlitine 2024, trak $h_0 = 4$ mm in b) zlitine 5083, trak debeline $h_0 = 1,28$ mm ($y = h/2$; parametri simulacije so navedeni na sliki 4)

cross-section adopted for the conventional-rolling theory cannot be applied.

The positions of the isolines on the boundary of plasticity $\varepsilon_{ef} = 0.002$ were chosen at the beginning. The results for the chosen conditions are given in **Figure 7**. The vertical line corresponding to the first point of the contact between the strip and the roll is presented as the "0" position at the start of the zone. The deformation on the cross-section begins non-uniformly (similarly to isoline B in **Figure 6**), first on the surface and prior to the initial contact of the strip and the rolls. This "out-of-contact" deformation is a consequence of the strain gradient, which causes the pulling of the external region of the strip and has been known and considered in numerous works in the area of rolling^{21,25,30}. It causes a significant difference between different reductions of the strip at the cross-section so that these cannot be reliably quantified.

The end of the deformation zone on the vertical cross-section is also non-homogeneous (isoline I in **Figure 6**). However, these lines represent the boundary of the plastic area of the complete vertical cross-section. A detailed examination showed that the plastic deformation continues (after isoline I) but it is localised on the

surface layer. Thus, the actual shape of the boundary of the plastic deformation is elastic-plastic (an approximate mirror image of the beginning of the plastic deformation). Such boundaries are completely in accordance with the experimental results²⁸ and schemes used for the analysis of the process parameters (e.g., for use of "a slab analysis")³¹.

3.4 Velocities

The kinematics of cold rolling are determined by the velocities of the strip and roll in the deformation zone, i.e., by the horizontal (V_{sx} , V_{rx}) and vertical (V_{sy} , V_{ry}) velocities. In the conventional theory of rolling, the horizontal velocities are predominantly considered (**Figure 1**). Because they can be directly (immediately) measured, this situation offers an opportunity to include the control of the process in the results of the analysis.

In reality, no adequate data are available for the vertical velocity of strips for cold rolling in the conventional theory. The FEM simulation ensures that these data can also be obtained in the deformation zone.

3.4.1 Horizontal velocity

Figure 8a shows the relationship of the horizontal velocity of a strip and the velocity of the rolls (V_{sx}/V_{rx}) for surface and axis trajectories. The velocity for a con-

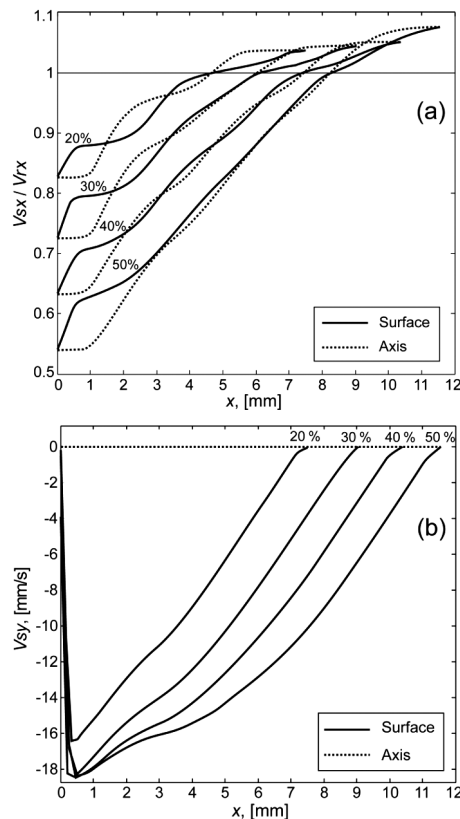


Figure 8: Diagrams of relationship changes of: a) V_{sx}/V_{rx} and b) V_{sy} on the surface and on the axis along the deformation zone. Alloy 2024, $h_0 = 4$ mm, simulation parameters as listed in **Figure 4**.

Slika 8: Diagram sprememb odvisnosti: a) V_{sx}/V_{rx} in b) V_{sy} na površini in vzdolž osi področja deformacije. Zlitina 2024, $h_0 = 4$ mm, parametri simulacije so navedeni na **sliki 4**.

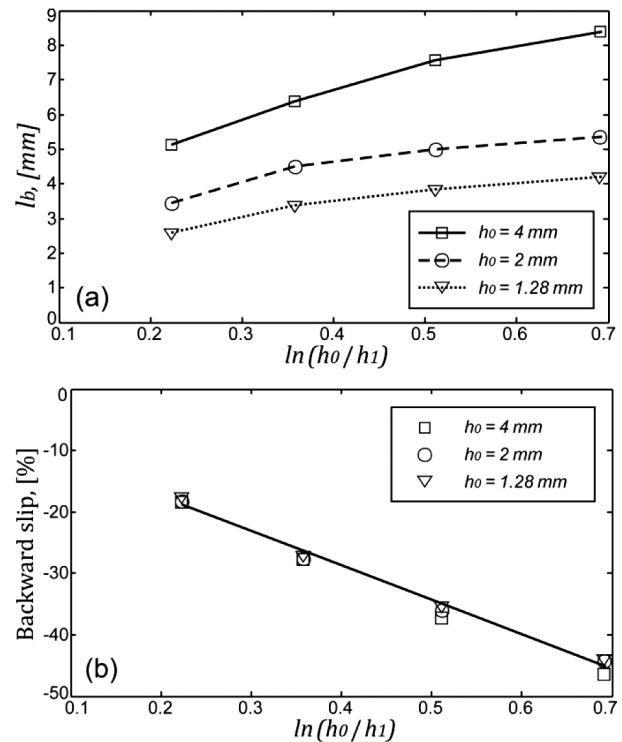


Figure 9: Results for the backward slip depending on the reduction degree obtained with the FEM simulation: a) length of the backward-slip zone and b) backward slip for the simulation parameters as listed in **Figure 4**.

Slika 9: Rezultati za zaostajanje v odvisnosti od stopnje redukcije, dobljene s FEM-simulacijo: a) dolžina področja zaostajanja in b) zaostajanja za simulacijske parametre, navedene na **sliki 4**.

stant time interval ($\Delta\tau$) is determined by the displacement itself ($V_{sx} = \Delta x / \Delta\tau$). As the roll velocity (V_{rx}) also changes slightly, it is expected that the diagrams for V_{sx}/V_{rx} in **Figure 8a** completely correspond to the diagrams of the Δx displacement shown in **Figure 4a**.

Significant data for the backward slip are shown in **Figure 9**. The zone of the backward slip (l_b), i.e., its length, covers an important portion of the deformation zone and increases with an increase in the initial thickness and the degree of reduction (**Figure 9a**). The lowest l_b/l_d relationship is $>2/3$ of the total deformation zone. The highest l_b/l_d relationship is $>3/4$ of the total deformation zone, which means that for a neutral cross-section, $V_{sx}/V_{rx} = 1$, it is necessary to obtain an adequate increment of the displacement and its homogenous distribution on the cross-section of the strip. Both of these factors require a certain length of the zone but also depend on the initial strip thickness and the reduction degree.

Diagrams of the backward slip depending on the initial strip thickness and reduction degree are shown in **Figure 9b**. A linear increase in the backward slip can be observed with an increase in the reduction degree and a slight difference in the tested strip thicknesses. As the shape of the backward-slip diagram is notably close to a straight line, the results are approximated using straight-line equations. The scale for the backward slip expressed in percentages is convenient for the approximation. However, the results for relationship V_{sx}/V_{rx} are selected for the equation because of a simple tracing of the values relative to the roll velocity and the connections with the forward slip. The derived equations are obtained and the correlation coefficients for the equations have high values. The other indicators also confirm their significance.

The diagrams of the backward slip and the free term in the equations of the V_{sx}/V_{rx} relationship show that the backward slip is unavoidable (for $\varphi_h = 0$ $V_{sx}/V_{rx} > 0$). In a physical sense, the condition for the unavoidable backward slip is completely justifiable, but it is not realistic that it differs from zero if the reduction is equal to zero. The equations should thus be accepted to show how the backward slip increases from zero to certain values, which are already in the area of small reduction degrees.

The forward slip changes in the interval of 2.4 to 12.5 %. According to the continuity equation, the forward slip has a significantly lower value than the backward slip (a smaller length of the zone causes a smaller total displacement).

The check of the simulation results for the backward and forward slips can be carried out on the basis of the continuity equation. All the results of the simulations satisfy this condition with a high level of accuracy. Therefore, the forward slip can be determined on the basis of the roll velocity, the backward slip and the reduction level.

The forward and backward slips were thoroughly tested and experimentally determined. Thus, the calculated values of the backward and forward slips provided in¹⁵ amount to 19.2 and 4.1 %, respectively. The results for the forward slip, which depends on the coefficient of friction, given in⁴ are 4 to 6 %. The forward slip depending on the velocity of the rolls and the reduction given in¹⁶ reaches up to 4 %, and in^{4,17} this value is as high as 10 %. All these results highly coincide with the results presented in this work.

3.4.2 Vertical velocity

The diagrams in **Figure 8b** show the change in the vertical velocity on the surface of a strip with a thickness of 4 mm. These changes are characterised by the maximum values at the beginning of the deformation zone. The maximum value of velocity V_{sy} is almost one order of magnitude lower than the horizontal velocity. The influence of this velocity on the total velocity/kinematics of rolling is thereby symbolic.

4 CONCLUSIONS

This paper presents the results and analysis of the deformations and kinematics during the cold rolling of aluminium alloy strips. The relevant experimental rolling was completed on a laboratory rolling stand using strips with thicknesses ranging from 4 to 1.28 mm.

The FEM simulation of the process was completed using the DEFORM-2D program with a mesh of eight finite elements on a half thickness of a strip and a constant friction coefficient of $f = 0.1$. The choice and analysis of deformations and velocities were carried out with the aim of comparison with the results from the conventional rolling theory. The following results were established:

The horizontal displacement diagram, presented with the chosen trajectories, has four characteristic areas with clear differences between the changes on the surface and axis. The shape of the changes is also reflected in the other strain components and velocities of cold rolling;

The relationship of the reduction degree and the effective strain based on the derived equations ensures a simple and reliable calculation of these indicators, through which other dependencies can also be quantified in the analysis of the rolling process;

With use of the FEM, the boundaries of the start and end of the deformation zone can be reliably identified as well as the out-of-contact deformation at the entrance and exit of the deformation zone;

The values of the backward slip amount to 18–46 % and linearly depend on the strip thickness reduction. The forward slip lies in the interval of 2.4–12.5 % and can be quantified on the basis of the dependence of these two kinematic parameters of the cold-rolling process.

5 REFERENCES

- ¹ P. Montmitonnet, P. Buessler, *ISIJ International*, 31 (1991), 525–538, doi:10.2355/isijinternational.31.525
- ² SIROLL ALU, Simens AG, Linz, 2012, 1–28, available from World Wide Web: www.industry.siemens.com/verticals/metals-industry/en/metals/aluminum-rolling/Pages/home.aspx
- ³ I. Yarita, M. Katahama, K. Kenmochi, *Kawasaki Steel Technical Report*, 41 (1999), 20–24
- ⁴ J. G. Lenard, *Primer on Flat Rolling*, 2nd ed., Elsevier, London 2014, doi:10.1016/B978-0-08-099418-5.00005-6
- ⁵ X. Liu, *J Iron Steel Res Int.*, 18 (2011) 1, 1–7, doi:10.1016/S1006-706X(11)60001-0
- ⁶ A. Kroll, A. Vollmer, *ABB Review*, 4 (2004), 44–49
- ⁷ P. Hartley, C. E. N. Sturges, C. Liu, G. W. Rowe, *Int. Mater. Rev.*, 34 (1989), 19–34, doi:10.1179/imr.1989.34.1.19
- ⁸ I. Y. A. Tarnovskii, A. A. Pozdeyev, V. B. Lyashkov, *Deformation of Metals During Rolling*, Pergamon Press, Oxford 2013, 200–259, doi:10.1016/B978-0-08-010223-8.50010-4
- ⁹ H. Changqing, D. Hua, C. Jie, H. U. Xinghua, Y. Shuangcheng, *Proc. Eng.*, 16 (2011), 745–754, doi:10.1016/j.proeng.2011.08.1150
- ¹⁰ F. E. Dolzhenkov, *Metall. Min. Ind.*, 1 (2009) 1, 33–37
- ¹¹ D. Pérez, F. J. Garcia-Fernandez, I. Diaz, A. A. Cuadrado, D. G. Ordonez, A. B. Diez, M. Dominguez, *Eng. Appl. Artif. Intel.*, 26 (2013) 8, 1865–1871, doi:10.1016/j.engappai.2013.05.009
- ¹² S. Zhang, B. Song, X. Wang, D. Zhao, *Appl Math Model*, 38 (2014), 3485–3494, doi:10.1016/j.apm.2013.11.061
- ¹³ R. Mei, L. Changsheng, X. Liu, *Finite Elem Anal Des*, 61 (2012), 44–49, doi:10.1016/j.finel.2012.06.006
- ¹⁴ S. H. Zhang, G. L. Zhang, J. S. Liu, C. S. Li, R. B. Mei, *Finite Elem Anal Des*, 46 (2010), 1146–1154, doi:10.1016/j.finel.2010.08.005
- ¹⁵ E. B. Li, A. K. Tieu, W. Y. D. Yuen, *Opt Laser Eng*, 39 (2003), 479–488, doi:10.1016/S0143-8166(02)00030-1
- ¹⁶ E. B. Li, A. K. Tieu, W. Y. D. Yuen, *J Mater Process Tech*, 133 (2003), 348–352, doi:10.1016/S0924-0136(02)01049-X
- ¹⁷ A. K. Tieu, Y. J. Liu, *Tribol. Int.*, 37 (2004), 77–183, doi:10.1016/S0301-679X(03)00048-3
- ¹⁸ P. Hartley, I. Pillinger, C. Sturges, *Numerical Modelling of Material Deformation Processes: Research, Development and Application*, Springer-Verlag, London 1992, doi:10.1007/978-1-4471-1745-2
- ¹⁹ J. Fluhrer, *DEFORMTM 2D-User's Manual*, Scientific Forming Technologies Corp., Ohio, 2004
- ²⁰ R. S. Prakash, P. M. Dixit, G. K. Lal, *J Mater Process Tech*, 52 (1995), 338–358, doi:10.1016/0924-0136(94)01728-J
- ²¹ Y. M. Hwang, H. H. Hsu, *J Mater Process Tech*, 88 (1999), 97–104, doi:10.1016/S0924-0136(98)00390-2
- ²² J. G. Lenard, S. Zhang, *J Mater Process Tech*, 72 (1997), 293–301, doi:10.1016/S0924-0136(97)00183-0
- ²³ Y. J. Liu, A. K. Tieu, D. D. Wang, W. Y. D. Yuen, *J Mater Process Tech*, 111 (2001), 142–145, doi:10.1016/S0924-0136(01)00541-6
- ²⁴ *Aluminium Alloy-EN Standards for Rolled Aluminium*, Aalco Metals Ltd, 2014, available from World Wide Web: www.aalco.co.uk/datasheets/Aluminium-Alloy-EN-Standards-for-Rolled-Aluminium_51.ashx
- ²⁵ P. F. Thomson, J. H. Brown, *Int J Mech Sci*, 24 (1982), 559–576, doi:10.1016/0020-7403(82)90048-0
- ²⁶ A. B. Richelsen, V. Tvergaard, *Int J Mech Sci*, 46 (2004), 653–671, doi:10.1016/j.ijmecsci.2004.05.013
- ²⁷ N. Tadić, *PhD Thesis*, University of Montenegro, Podgorica, 2011
- ²⁸ W. A. Backofen, *Deformation processing*, Addison-Wesley Pub. Co., 1975
- ²⁹ *STATGRAPHICS Centurion XVI – trial version*, 2014, available from World Wide Web: www.statgraphics.com
- ³⁰ H. R. Le, M. P. F. Sutcliffe, *Int J Mech Sci*, 43 (2001), 1405–1419, doi:10.1016/S0020-7403(00)00092-8
- ³¹ W. F. Hosford, R. M. Cadell, *Metal Forming-Mechanics and Metallurgy*, 4th ed., Cambridge University Press, Cambridge 2014

PREDICTION OF THE CHEMICAL NON-HOMOGENEITY OF 30MnVS6 BILLETS WITH GENETIC PROGRAMMING

NAPOVEDOVANJE NEHOMOGENOSTI KEMIJSKE SESTAVE PRI GREDICAH 30MnVS6 S POMOČJO GENETSKEGA PROGRAMIRANJA

Miha Kovačič, Damir Novak

Štore Steel d.o.o., Železarska cesta 3, 3220 Štore, Slovenia
miha.kovacic@store-steel.si

Prejem rokopisa – received: 2014-11-13; sprejem za objavo – accepted for publication: 2015-02-18

doi:10.17222/mit.2014.280

Štore Steel Ltd. is a small and flexible steel plant. The plant also produces the 30MnVS6 steel grade, which is used for crack connection rods in the automotive industry. The chemical elements are not uniformly distributed over the billet cross-sections, consequently influencing the final product properties. The chemical distribution depends mainly on the casting parameters. The article presents an attempt at predicting the chemical non-homogeneity of 30MnVS6 billets. With respect to the chemical-element distribution (% C, % Si, % Mn, % V, % S) over the billet cross-sections and the casting parameters (casting speed, casting temperature, meniscus level), several models for the chemical non-homogeneity prediction were developed by means of the genetic-programming method. The results show that the most influential parameter is the casting speed. The results of modeling can be practically implemented in order to reduce the chemical non-homogeneity of the billets.

Keywords: steel, casting, billets, chemical composition, non-homogeneity, modelling, genetic programming

Štore Steel je majhna, a prilagodljiva jeklarna. Proizvajajo tudi jeklo 30MnVS6, ki se uporablja za ojnice, ki se izdelujejo z lomljenjem, za avtomobilsko industrijo. Kemijski elementi niso enakomerno porazdeljeni po prerezu gredice, kar posledično vpliva na lastnosti končnega izdelka. Razporeditev kemijskih elementov je najbolj odvisna od parametrov vlivanja. V članku je predstavljen poskus napovedovanja kemijske nehomogenosti gredic jekla 30MnVS6. Glede na razporeditve kemijskih elementov (% C, % Si, % Mn, % V, % S) po prerezu gredice in parametre vlivanja (hitrost vlivanja, temperatura vlivanja, nivo taline), se je izdelalo več modelov, za napovedovanje kemijske nehomogenosti gredic, s pomočjo metode genetskega programiranja. Rezultati kažejo, da je najvplivnejši parameter hitrost vlivanja. Rezultati modeliranja se lahko uporabijo v praksi z namenom zmanjšanja kemijske nehomogenosti gredic.

Ključne besede: jeklo, litje, gredice, kemijska sestava, nehomogenost, modeliranje, genetsko programiranje

1 INTRODUCTION

Due to a gradual solidification during the continuous casting of steel, chemical-composition variations occur, which influence the cast and, consequently, the processed-material properties; therefore, their optimization is essential.¹

In the previous research², the chemical composition of the cross-section of a high-grade pipeline slab was measured point by point. The results indicated that a negative segregation inside the central line is more severe than that outside the central line, and that the highest positive segregation of the elements appears close to the inner sides of the negative segregation strips. In addition, the segregation of the elements in the central area is higher than that in the outer and inner arc areas.

Article³ discusses the manufacturing of bearing steels of low distortion potential. The 100Cr6 steel billets were spray formed to achieve metallurgical homogeneity. The microstructures and properties of the billets produced under different thermal conditions were studied and evaluated. A heat-transfer model for a growing billet was established in order to investigate the thermal profiles of the billets during spray forming. An apparent correlation

between the cooling and solidification conditions of the deposit and its metallurgical properties was revealed by means of a numerical simulation and an experiment.

Gheorghies et al.⁴ developed a theoretical model that was adapted for studying the steel continuous-casting technology. The model is based on the system theory, considering input/output, command and control parameters. It can be used to describe the physicochemical processes, thermal processes, chemical processes and the characteristics of the cast material on the basis of the above-mentioned stages.

In the research described in⁵ LIBS scanning measurements were performed on samples displaying segregation. The resulting quantified elemental maps correlated very well with the data obtained with the conventional methods.

In research⁶ an artificial-intelligence analyzer of the mechanical properties of rolled steel bars was proposed using neural networks. The complex correlation among the steel bar properties, the billet compositions and the control parameters of manufacturing was developed. The developed analyzer could be used in practice in order to improve the steel quality.

Hwang et al.⁷ tried to minimize the center segregation with the help of a developed coupled temperature/displacement finite-element model. The center segregation, center porosity, homogeneity of elements and equiaxed crystal zone were improved.

This paper discusses the use of the genetic-programming method for predicting the chemical non-homogeneity of the 30MnVS6 billets, used in rolled conditions, for forging crack connection rods in the automotive industry. Genetic programming is an evolutionary computation-based methodology of artificial intelligence (AI); it is similar to the genetic algorithm (GA).⁸ Genetic programming (GP) is capable of solving many different problems in industry; however, it uses different natural phenomena in comparison to many other AI-based approaches, such as artificial neural networks (ANN), swarm intelligence (SI) and gravitational search algorithm (GSA). For a comparison of the practical uses of the above-mentioned methods in industrial applications see reference literature, for example.^{9–12}

The problem is stated in section 2. In the subsequent section the experimental background and, afterwards, the essence of the chemical non-homogeneity prediction are presented. The analysis of the modelling results are presented in section 4 and, finally, the main contributions of the research and the guidelines for further research are given in the last section.

2 EXPERIMENTAL BACKGROUND

Steelmaking begins with scrap melting in an electric-arc furnace. The melting bath, which is heated up to the tapping temperature required for the further treatment procedure, is discharged into a casting ladle.

After achieving the proper melt temperature in the melting bath, the billets are continuously cast. The melt flows through a sliding-gate system and ladle shroud towards a tundish.

After filling up the tundish with the help of the mold-filling system with tundish stoppers and submerged pouring tubes, the casting is established. The billets, with a square section of 180 mm, are cast. After reaching a certain melting-bath level, the potentiometer starts the flattening system, which drags the billet out of

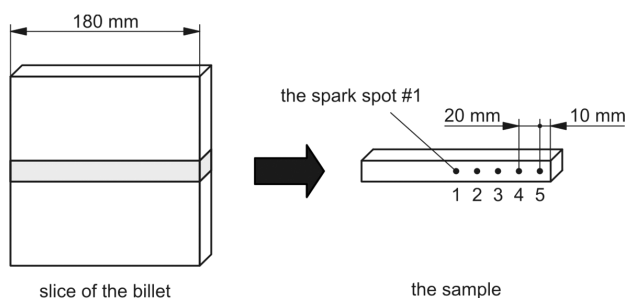


Figure 1: Sample from the billet slice with the spark spots
Slika 1: Vzorec iz rezine, odrezane iz gredice, s točkami obžiga

the mold. In this way, the continuous casting is established. Each billet goes through the cooling zone toward the gas cutters, where it is cut and laid off onto the cooling bed.

The data for the analysis was collected on the basis of 30 consecutively cast batches of the 30MnVS6 steel in Štore Steel Ltd. (**Table 1**) from May to September 2011. The data was taken from the technological documentation of the cast batches and from the chemical archive. The goal was to get as wide a range of influential parameters as possible, namely:

- the contents of C, Si, Mn, S and V in the tundish (w/%)
- the average melt temperature in the tundish (°C)
- the average meniscus level (mm)
- the average casting speed (m/min)
- the average strand temperature in the cooling zone (°C).

From each of the selected 30 batches, a billet was taken from the middle of the casting and a slice was cut out. For the chemical analysis, optical emission spectroscopy was used (instrument SPECTRO LAVMC12A). Five spark spots were used for determining the chemical non-homogeneity (**Figure 1**).

For example, the carbon content obtained from five spark spots on the sample from batch number 1 is presented in **Figure 2**.

The carbon non-homogeneity C_{n-h} can be easily calculated:

$$C_{n-h} = \frac{\sum_{i=1}^5 C_i}{\bar{C}} \quad (1)$$

where i is the individual spot size and \bar{C} is the average of all five carbon-content values for each spot:

$$\bar{C} = \frac{\sum_{i=1}^5 C_i}{5} \quad (2)$$

Similarly, the non-homogeneity for each individual chemical element can be calculated.

The experimental data and the non-homogeneities for individual chemical elements are presented in **Table 1**.

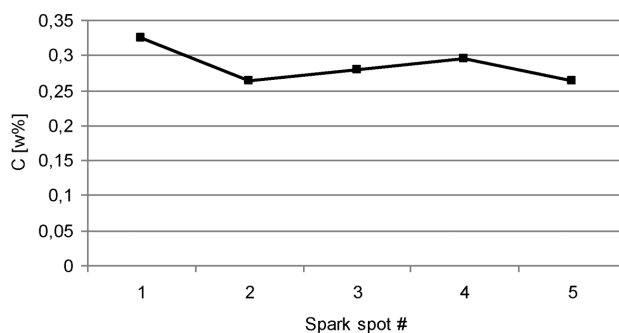


Figure 2: Carbon content at each spark spot
Slika 2: Vsebnost ogljika na posamičnem mestu obžiga

3 MODELLING OF CHEMICAL NON-HOMOGENEITY WITH GENETIC PROGRAMMING

Genetic programming is probably the most general evolutionary optimization method⁸ and it has already been found useful for several different applications in Štore Steel Ltd.^{13–17}. The organisms that undergo an adaptation are in fact mathematical expressions (models) for chemical non-homogeneity, consisting of the available function genes (i.e., basic arithmetical functions) and terminal genes (i.e., independent input parameters and random floating-point constants). In our case, the models consist of the function genes of addition (+), subtraction (−), multiplication (*) and division (/), while terminal genes include:

- the contents of C (*C*), Si (*SI*), Mn (*MN*), S (*S*) and V (*V*) in the tundish
- the average melt temperature in the tundish (*TM*)
- the average meniscus level (*ML*)
- the average casting speed (*SPEED*) and
- the average strand temperature in the cooling zone (*TC*).

Random computer programs of various forms and lengths are generated by means of selected genes at the beginning of the simulated evolution. Afterwards, the varying of the computer programs during several iterations, known as generations, is performed by means of genetic operations. For the progress of the population, only the reproduction and crossover are sufficient. A new generation is obtained after the completion of various

Table 1: Experimental data

Tabela 1: Eksperimentalni podatki

Batch	C (w/%)	Si (w/%)	Mn (w/%)	S (w/%)	V (w/%)	Average melt temperature in tundish (°C)	Average meniscus level (mm)	Average casting speed (m/min)	Average strand temperature in the cooling zone (°C)	C non-homogeneity (w/%)	Si non-homogeneity (w/%)	Mn non-homogeneity (w/%)	S non-homogeneity (w/%)	V non-homogeneity (w/%)	Sum of C, Si, Mn, S and V chemical non-homogeneity (w/%)
1	0.29	0.55	1.43	0.05	0.09	1543	74.53453	1.135516	1092.7	35.28	34.30	34.17	31.52	33.57	168.83
2	0.29	0.58	1.44	0.058	0.1	1548	76.11422	1.128306	1091.669	5.61	1.77	2.19	10.81	2.41	22.79
3	0.28	0.59	1.43	0.05	0.09	1543	74.34058	1.114705	1093.121	10.32	6.98	7.49	19.51	6.71	51.01
4	0.3	0.6	1.43	0.051	0.1	1542	74.38523	1.148343	1110.401	22.01	23.24	24.73	22.12	24.72	116.82
5	0.29	0.59	1.46	0.052	0.1	1545	74.55143	1.143362	1100.045	40.36	39.00	38.98	27.54	36.84	182.72
6	0.29	0.57	1.45	0.051	0.11	1544	74.62807	1.144693	1100.519	33.73	34.43	35.10	38.21	34.41	175.89
7	0.29	0.58	1.47	0.05	0.1	1551	74.61523	1.115993	1092.786	33.68	38.06	38.73	36.24	40.04	186.76
8	0.3	0.57	1.43	0.058	0.1	1530	74.5125	1.136773	1123.988	32.08	35.08	33.65	26.26	33.60	160.68
9	0.29	0.58	1.45	0.05	0.1	1548	74.49432	1.136511	1123.195	22.17	22.17	20.65	23.32	20.46	108.76
10	0.3	0.57	1.45	0.059	0.1	1536	74.46816	1.139951	1121.601	5.64	5.86	6.76	22.05	8.12	48.43
11	0.3	0.63	1.44	0.059	0.11	1538	74.54645	1.142406	1121.38	33.94	33.88	31.97	27.54	33.80	161.13
12	0.29	0.58	1.43	0.06	0.1	1553	74.59237	1.116969	1116.805	40.13	40.46	39.14	36.08	38.92	194.72
13	0.29	0.58	1.43	0.055	0.1	1549	74.52381	1.117879	1111.379	24.40	28.32	26.53	42.90	29.29	151.43
14	0.3	0.55	1.43	0.045	0.09	1544	74.4881	1.133849	1105.889	25.87	26.01	25.05	23.44	23.03	123.41
15	0.29	0.61	1.45	0.052	0.1	1549	74.32708	1.126732	1108.002	19.93	23.92	23.15	23.20	24.09	114.29
16	0.28	0.6	1.42	0.053	0.1	1541	74.39798	1.150479	1118.254	32.04	33.77	32.41	26.27	33.59	158.09
17	0.28	0.57	1.46	0.06	0.1	1548	74.36111	1.133132	1120.187	21.63	22.42	20.75	24.63	20.04	109.46
18	0.28	0.58	1.44	0.058	0.1	1543	74.37007	1.165916	1119.613	32.89	33.99	33.22	30.33	33.84	164.27
19	0.28	0.59	1.45	0.05	0.11	1547	74.39048	1.130368	1123.507	35.47	39.57	38.79	39.55	39.49	192.87
20	0.29	0.6	1.45	0.058	0.1	1546	74.49107	1.134441	1115.035	12.77	7.91	6.69	12.62	6.95	46.94
21	0.29	0.63	1.48	0.06	0.1	1545	74.50678	1.139199	1119.22	23.28	23.68	23.88	14.81	23.63	109.29
22	0.29	0.6	1.45	0.059	0.1	1542	74.49815	1.144132	1127.137	39.29	40.28	39.51	38.89	38.91	196.88
23	0.29	0.6	1.42	0.052	0.1	1547	74.3956	1.110585	1126.187	7.69	6.32	6.86	15.46	5.16	41.48
24	0.29	0.58	1.42	0.056	0.1	1558	74.46951	1.092817	1124.571	9.03	8.00	7.44	21.41	7.21	53.10
25	0.29	0.61	1.43	0.06	0.1	1555	74.32818	1.082388	1120.363	23.68	20.73	21.52	25.79	22.54	114.26
26	0.28	0.61	1.46	0.052	0.11	1543	74.47059	1.125766	1132.468	3.85	0.88	1.50	6.82	0.92	13.97
27	0.29	0.59	1.44	0.052	0.1	1557	74.41155	1.103096	1116.793	21.61	23.94	23.45	17.61	22.57	109.19
28	0.28	0.58	1.44	0.055	0.1	1546	74.31526	1.132103	1133.436	23.16	21.12	21.20	26.43	20.55	112.46
29	0.29	0.58	1.44	0.055	0.1	1556	74.43371	1.101385	1128.988	32.11	37.68	39.59	42.06	38.09	189.53
30	0.29	0.62	1.45	0.052	0.1	1548	74.42917	1.09335	1126.615	21.81	23.84	23.54	17.37	22.90	109.47

computer programs and this generation is then evaluated and compared with the experimental data.

The process of changing and evaluating organisms is repeated until the termination criterion of the process is fulfilled. This was the prescribed maximum number of generations.

For the process of simulated evolutions, the following evolutionary parameters were selected: the size of the population of organisms – 500; the greatest number in a generation – 100; the reproduction probability – 0.4; the crossover probability – 0.6; the greatest permissible depth of population (6); the greatest permissible depth, after the operation, of the crossover of two organisms – 10; and the smallest permissible depth of organisms when generating new organisms – 2. Genetic operations of reproduction and crossover were used. For the selection of the organisms, the tournament method with tournament size 7 was used. For the model, the fitness average relative deviation from the monitored data was selected. It is defined as:

$$\Delta = \frac{\sum_{i=1}^n \frac{|E_i - P_i|}{E_i}}{n} \quad (3)$$

where n is the size of the monitored data, E_i and P_i are the actual (experimental) and predicted sums of the C, Si, Mn, S and V chemical non-homogeneity, respectively.

We have developed 100 independent civilizations of mathematical models for the chemical non-homogeneity prediction. Each civilization had its most successful organism – mathematical model. The most successful organism of all the civilizations is presented here:

$$C + \left(\frac{-1 + \text{SPEED}}{S} + \frac{1}{\text{SPEED}} - \text{SPEED} + \frac{V^2}{(-1 + \text{SPEED})\text{SPEED}} - \frac{-1 + \text{SPEED}}{\left(\text{SPEED} - \frac{V}{(\text{SPEED} - \frac{1}{V})(1 + \text{SPEED} - \frac{V}{S})} \right) \left(C + \frac{1 + \text{SPEED} - \frac{V}{S}}{C \left(\frac{2(-1 + \text{SPEED})}{\text{SPEED}} + \text{SPEED} \right)} \right) \left(\text{SPEED} - \frac{1 + \text{SPEED} - \frac{V}{S}}{V} \right)} \right) \frac{\text{SPEED} - \frac{V}{S} + \frac{C(1 + \text{SPEED} - \frac{V}{S})}{V}}{\text{SPEED} - \frac{C(1 + \text{SPEED} - \frac{V}{S})}{\frac{C}{\text{SPEED}} + \text{SPEED}} - \left(-\frac{1}{\text{SPEED}} + \text{SPEED} \right) \left(-\frac{1 + \text{SPEED}}{S} + \text{SPEED} + \frac{C(1 + \text{SPEED} - \frac{V}{S})}{V} \right)} \frac{V}{\left(\frac{1}{\text{SPEED}} - \frac{V}{S} + \frac{1 + \text{SPEED} - \frac{V}{S}}{C} \right) \left(2 \text{SPEED} - \frac{V}{\text{SPEED} - \frac{C}{V}} - \frac{V}{C + \left(\text{SPEED} - \frac{V}{S} \right) (1 + \text{SPEED} - \frac{V}{S})} \right)} \left(2 \text{SPEED} - \frac{V}{S} - \frac{V}{\text{SPEED} - \frac{V}{\text{SPEED} - \frac{C}{V}} - \frac{V}{C + \left(\text{SPEED} - \frac{V}{S} \right) (1 + \text{SPEED} - \frac{V}{S})}} \right) \quad (4)$$

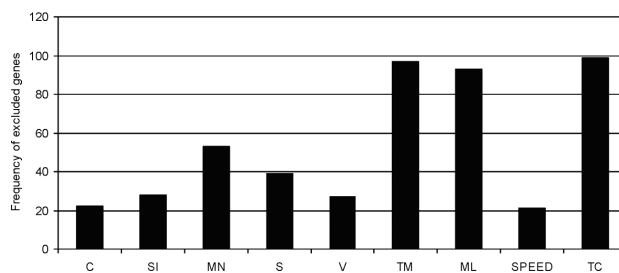


Figure 3: Frequency of genes excluded from the best 100 mathematical models for chemical non-homogeneity prediction

Slika 3: Frekvenca izločenih genov na podlagi najboljših 100-ih matematičnih modelov za napovedovanje kemijske nehomogenosti

with an average relative deviation of 27.82 %. It is obvious that only *C* (the content of C in the tundish), *S* (the content of S in the tundish), *V* (the content of V in the tundish) and *SPEED* (the average casting speed) are included in the model.

4 ANALYSIS OF THE RESULTS

A randomly driven process builds the fittest and the most complex models from generation to generation and uses the ingredients that are the most suitable for an experimental environment adaptation. For curiosity's sake, the analysis of the genes (parameters) excluded from the models is presented in the next figure (**Figure 3**).

Based on the number of the genes excluded from 100 mathematical models, we may make assumptions about the influence of the parameters on the chemical non-homogeneity. It is clear from the figure that out of 100 genetically obtained mathematical models only 21 models do not include the parameter of the average casting speed (*SPEED*) and fewer than 30 out of 100 models do not have the parameter of the contents of C (*C*), Si (*SI*), and V (*V*) included in the tundish. We can, therefore, speculate that they are probably the most important parameters influencing the chemical non-homogeneity.

Figure 4 shows the calculated influences of individual parameters on the chemical non-homogeneity using

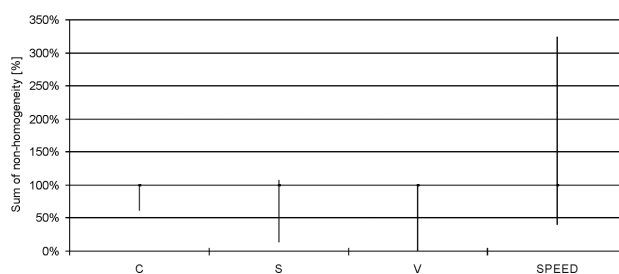


Figure 4: Calculated influences of individual parameters on chemical non-homogeneity while separately changing them within the range from **Table 1**

Slika 4: Izračunani vplivi posamičnih parametrov na kemijsko nehomogenost pri le-njihovem spreminjanju znotraj območja, navedenega v **tabeli 1**

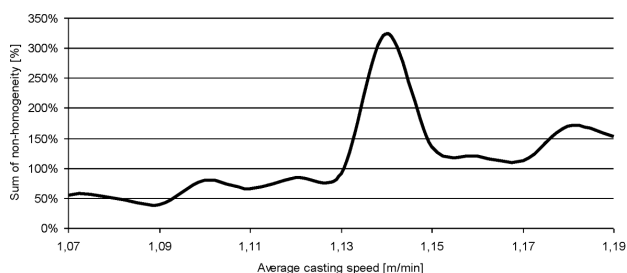


Figure 5: Calculated correlation between the casting speed and chemical non-homogeneity while separately changing the average casting speed

Slika 5: Izračunana korelacija med livno hitrostjo in kemijsko nehomogenostjo pri spreminjanju povprečne livne hitrosti

the developed model (Equation (4)) while separately changing the individual parameters within the range from **Table 1**. The dashes at individual total decarburization ranges represent the calculated average chemical non-homogeneity of all 30 collected samples, which is 98.88 %. The average chemical non-homogeneity value of the collected data is 122.96 %.

Figure 5 shows the calculated correlation between the casting speed and the chemical non-homogeneity while separately changing the average casting speed. This can be calculated and, consequently, used for individual influential parameters as a tool for selecting the optimal casting speed. It should be noted that the average value of the average casting speed for all 30 cases is 1.127 m/min (a standard deviation of 0.0191 m/min).

5 CONCLUSION

The purpose of this research was to predict the chemical non-homogeneity of 30MnVS6 steel grade billets. The data for the analysis was collected on the basis of 30 consecutively cast batches. The distribution of the chemical elements (% C, % Si, % Mn, % V, % S) over the billet cross-sections and the casting parameters (casting speed, casting temperature, meniscus level) were gathered. On the basis of the gathered data, several models for predicting the chemical non-homogeneity were developed by means of the genetic-programming method. There were 100 different models developed and only the best one was used for the chemical non-homogeneity prediction. The relative average deviation between the actual and the predicted scrap was 27.82 %. In addition, the frequencies of the genes excluded from the best 100 mathematical models for the chemical non-homogeneity prediction were analyzed. The results show that the parameters influencing the chemical non-homogeneity the most are the casting speed and the contents of C, Si and V in the melt. Also, the influences of individual parameters on the chemical non-homogeneity were calculated while separately changing individual parameters, using the best genetically developed model. The calculation shows that the variation in the speed

changes the chemical non-homogeneity from 39 to 324 %, while the calculated average chemical non-homogeneity of all 30 collected samples is 98.88 %. Finally, the correlation between the casting speed and the chemical non-homogeneity was calculated while separately changing the average casting speed. The results of the research can be used as a tool for selecting the optimum casting speed. In the future, a larger sample size will be used and a methodology for the other steel grades will be implemented.

6 REFERENCES

- W. R. Irving, Continuous casting of steel, Institute of Materials, London 1993
- J. Liu, Y. Bao, X. Dong, T. Li, Y. Ren, S. Zhang, Distribution and segregation of dissolved elements in pipeline slab, Journal of University of Science and Technology Beijing, Mineral, Metallurgy, Material, 14 (2007) 3, 212–218, doi:10.1016/S1005-8850(07)60041-3
- C. Cui, U. Fritsching, A. Schulz, R. Tinscher, K. Bauckhage, P. Mayr, Spray forming of homogeneous 100Cr6 bearing steel billets, Journal of Materials Processing Technology, 186 (2005) 3, 496–504, doi:10.1016/j.jmatprotec.2005.02.250
- C. Gheorghies, I. Crudu, C. Teletin, C. Spanu, Theoretical Model of Steel Continuous Casting Technology, Journal of Iron and Steel Research, 16 (2009) 1, 12–16, doi:10.1016/S1006-706X(09)60003-0
- F. Boué-Bigne, Laser-induced breakdown spectroscopy applications in the steel industry: Rapid analysis of segregation and decarburization, Spectrochimica Acta Part B: Atomic Spectroscopy, 63 (2008) 10, 1122–1129, doi:10.1016/j.sab.2008.08.014
- W. Wang, X. Hu, L. Ning, R. Bülte, W. Bleck, Improvement of center segregation in high-carbon steel billets using soft reduction, Journal of University of Science and Technology Beijing, Mineral, Metallurgy, Material, 13 (2006) 6, 490–496, doi:10.1016/S1005-8850(06)60100-X
- R. C. Hwang, Y. J. Chen, H. C. Huang, Artificial intelligent analyzer for mechanical properties of rolled steel bar by using neural networks, Expert Systems with Applications, 37 (2010) 4, 3136–3139, doi:10.1016/j.eswa.2009.09.069
- J. R. Koza, Genetic programming III, Morgan Kaufmann, San Francisco 1999
- M. Hrelja, S. Klancnik, T. Irgolic, M. Paulic, Z. Jurkovic, J. Balic, M. Brezocnik, Particle swarm optimization approach for modelling a turning process, Advances in Production Engineering & Management, 9 (2014) 1, 21–30, doi:10.14743/apem2014.1.173
- M. Hrelja, S. Klancnik, J. Balic, M. Brezocnik, Modelling of a turning process using the gravitational search algorithm, International Journal of Simulation Modelling, 13 (2014) 1, 30–41, doi:10.2507/IJSIMM13(1)3.248
- M. Chandrasekaran, D. Devarasiddappa, Artificial neural network modeling for surface roughness prediction in cylindrical grinding of Al-SiCp metal matrix composites and ANOVA analysis, Advances in Production Engineering & Management, 9 (2014) 2, 59–70, doi:10.14743/apem2014.2.176
- N. Senthilkumar, T. Tamizharasan, V. Anandkrishnan, An ANN approach for predicting the cutting inserts performances of different geometries in hard turning, Advances in Production Engineering & Management, 8 (2013) 4, 231–241, doi:10.14743/apem2013.4.170
- M. Kovačič, B. Šarler, Genetic programming prediction of the natural gas consumption in a steel plant, Energy, 66 (2014) 1, 273–284, doi:10.1016/j.energy.2014.02.001
- M. Kovačič, B. Jurjovec, L. Krajnc, Ladle nozzle opening and genetic programming, Mater. Tehnol., 48 (2014) 1, 23–26

- ¹⁵ M. Kovačič, S. Senčič, Modeling of PM10 emission with genetic programming, *Mater. Tehnol.*, 46 (2012) 5, 453–457
- ¹⁶ M. Kovačič, B. Šarler, Application of the genetic programming for increasing the soft annealing productivity in steel industry, *Materials and Manufacturing Processes*, 24 (2009) 3, 369–374, doi:10.1080/10426910802679634
- ¹⁷ M. Kovačič, Genetic programming and Jominy test modeling, *Materials and Manufacturing Processes*, 24 (2009) 7, 806–808, doi:10.1080/10426910902841050

EFFECT OF THE TiBN COATING ON A HSS DRILL WHEN DRILLING THE MA8M Mg ALLOY

VPLIV TiBN PREVLEKE NA HSS SVEDRU PRI VRTANJU MA8M Mg ZLITINE

Faruk Karaca¹, Bünyamin Aksakal²

¹Firat University, Technology Faculty, Dept. Mech. Eng., Elazig, Turkey

²Yildiz Technical University, Faculty of Chemical and Metallurgy, Dept. Metallurgy and Mater. Eng., Istanbul, Turkey
fkaraca@firat.edu.tr

Prejem rokopisa – received: 2014-11-30; sprejem za objavo – accepted for publication: 2015-01-28

doi:10.17222/mit.2014.290

Mg alloy MA8M is used in the aerospace and food industries and in biomedical applications due to its lightness and biocompatibility. This paper presents the drilling performance of the standard HSS and TiBN-coated drill bits during the machining of the MA8M Mg alloy at various drill rotational speeds and feed rates. After the experiments, the surface roughness, topography and chip formation were analyzed. Atomic-force microscopy (AFM) and surface profilometer were used for this purpose. It was observed that higher drilling feed rates and drill rotational speeds lead to lower surface-roughness values. TiBN-coated drill bits exhibited undesired surface qualities.

Keywords: MA8M Mg alloy, TiBN coating, twist drills, surface quality, multiple regression analysis, chip formation

Mg zlitina MA8M se uporablja v letalstvu, prehrabeni industriji in v biomedicini, ker je lahka in biokompatibilna. Članek predstavlja obnašanje pri vrtanju z normalnimi HSS in s svedri s TiBN prevleko na konici, pri obdelavi Mg zlitine MA8M pri različnih vrtiljajih svedra in hitrostih podajanja. Po eksperimentih je bila analizirana hrapavost površine, topografija in nastanek ostružka. V ta namen sta bila uporabljena mikroskop na atomsko silo (AFM) in profilometer površine. Ugotovljeno je, da večja hitrost podajanja in vrtenja svedra povzroči manjšo hrapavost površine. S TiBN prevlečeni svedri so povzročali neustrezno kvaliteto površine.

Ključne besede: MA8M Mg zlitina, TiBN prevleka, vijaki svedri, kvaliteta površine, multipla regresijska analiza, nastanek ostružka

1 INTRODUCTION

Nowadays, reducing the energy consumption and providing a better surface quality in several manufacturing industries are vital for economic production cycles. Many manufacturing industries substituted the materials, e.g., steel was replaced with light metals or plastics to decrease the energy consumption and/or increase the strength/weight ratio. Although light metals such as aluminum or magnesium are easier to machine, the magnesium alloys have a higher specific strength and stiffness than aluminum alloys.¹⁻³ Metallic implants made of stainless steel, titanium or cobalt-chromium alloys are used for stress shielding and revision surgeries, improving the quality of life and the healthcare system. On the other hand, due to their low density and compatibility, magnesium alloys are also very promising as orthopedic biomaterials compared to the other metallic alloys such as stainless steel and titanium alloys.⁴ However, the unsatisfactory corrosion resistance of magnesium alloys limit their application to a great extent.⁵

To overcome these undesired problems, in some studies, the microstructures and mechanical properties of magnesium alloys were processed with cyclic closed-die forging. Using this method under various processing conditions resulted in the desired grain size, microstruc-

tural parameters and growth mechanical properties.³ The surface integrity of a machined magnesium alloy used for biomedical implants could have a critical impact on its corrosion resistance. The influence of the cutting edge radius and the cooling method on the surface integrity was investigated. Cryogenic machining using a large edge-radius tool led to a thicker grain-refinement layer that remarkably enhanced the corrosion performance of the magnesium alloy.⁵ During another surface-integrity treatment, synergistic dry cutting/finish burnishing of magnesium-calcium implants resulted in a good surface finish, high compressive hook-shaped, low-residual stress profile and extended strain hardening of the sub-surface with little change in the grain size.⁴

The high-speed dry-machining process investigated with a finite-element model predicts that the most hazardous outcome, the chip ignition during machining magnesium alloys, does not occur during high-speed dry cutting with sharp PCD (polycrystalline diamond) tools.⁶ The effect of coated drills on the minimum-quantity-lubrication drilling of magnesium alloys was experimentally investigated using a carbon-coated HSS drill and the AZ91 magnesium alloy. Such a coating and the minimum-quantity-lubrication condition limited the temperature to below the hazardous level and, hence,

both the drill wear and the magnesium adhesion were successively reduced.⁷ On the other hand, the machining of the AZ91 magnesium alloy with both the TiN-coated and PCD tools was conducted to find the influence of tool coatings in the machining of magnesium. It showed an excessive tool wear of the TiN carbides even at low cutting speeds, while the PCD coatings showed better results at low film thicknesses.¹

A limited number of the investigations were performed in the field of machinability of magnesium alloys. In this study, experimental drilling of the MA8M magnesium-alloy sheet was conducted. The effects of the drilling parameters such as the drill speed, the diameter, the feed rate and the TiBN coating on the hole-surface quality were analyzed with respect to the surface roughness, the burr and chip formation and the hole accuracy. After these evaluations, the optimum surface quality was determined. I was also found that an increased drill feed rate increased the roughness, an increased drill speed decreased the roughness and the TiBN coating increased the surface roughness. The present study could be referenced to similar studies.

2 EXPERIMENTAL WORK

In this study, MA8M Mg-alloy sheets having dimensions of $100 \times 100 \times 8$ mm³ were used. Two different kinds of the cutting-tool material, namely HSS and TiBN-coated HSS twist drills were used to compare their effects on the surface roughness of the machined holes and the chip formation. Some pilot experiments were performed. Since the best results were obtained with a 6-mm drill diameter of the HSS tools, the TiBN coating was considered only with this diameter and the others were ignored. The tool diameter, feed rate and rotational speed of the cutting tool were changed to explore their effects. A full factorial experimentation was applied

using the parameters. In order to statistically identify the correlation between the applied parameters and the surface roughness, the multiple-regression-analysis method with a confidence interval of $p = 0.05$ was used. The drill-bit coating parameter variation of the regression was analyzed separately. The surface-roughness measurements were performed with a Mitutoyo SJ 210 profilometer with a 0.5 mm/s measuring speed and 0.25×4 mm length in line with the ISO 1997 standard. The average surface roughness R_a (μm) was used to evaluate the hole-surface roughness after the measurements were repeated three times. Furthermore, an atomic force microscope (AFM) was used to determine the 3D surface topography with a scanning area of 40×40 μm^2 and a rate of 0.15 Hz (Park System XE-100).

3 RESULTS AND DISCUSSION

The surface roughness, surface topography, chip formations and drill-bit coating were under consideration when evaluating the machinability characteristics of the MA8M Mg alloy. The measured values are discussed in the following sections.

3.1 Average surface roughness (R_a)

The surface integrity is an important parameter in machinability and is directly related to the surface roughness.^{4,5} The effects of all the experimental parameters including the drill diameter, the feed rate, the drill speed and the drill coating on the hole-surface roughness, analyzed in a body with contour graphics, are given in **Figure 1**. In order to plot these contour graphics, the weighted least square method was used. As seen in **Figure 1**, the surface roughness of the machined holes has a tendency to decrease with an increase in the feed rate for all drill types. When three drill diameters were evaluated, the maximum surface roughness was obtained at a 4-mm drill diameter, while 6-mm and 8-mm drills presented similar values. The roughness reached the highest values at 1710 min^{-1} when the 4-mm-diameter drill bit was used and then became reduced at 2730 min^{-1} , as shown in **Figure 1**.

On the other hand, the TiBN-coated HSS drill bit enhanced the surface roughness to the highest rates (**Figure 1**) compared to the other three drill bits. There was a significant difference in the roughness between the holes drilled with the TiBN-coated and uncoated 6-mm drill bits. On the other hand, the roughness was reduced with the increased drill diameter when the contour graphics were analyzed. However, a drill speed of 1080 min^{-1} caused the lowest roughness as the TiBN coating had an inverse effect on the surface roughness during the drilling of the MA8M alloy. Although the increased drill speed caused a decrease in the surface roughness at all three feed rates and with the 6-mm and 8-mm drills, the surface roughness increased with the TiBN coating as shown in **Figure 1**.

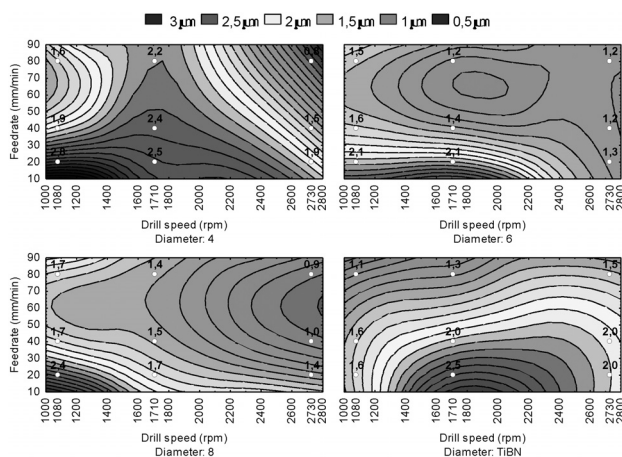


Figure 1: Variation in surface roughness with feed rate, drill speed, drill diameter, in comparison with TiBN-coated drill bits

Slika 1: Spreminjanje hrapavosti površine s podajanjem, hitrostjo vrtenja svadra, premerom svadra, v primerjavi s svadrom s TiBN prevleko

The drill speed of 1710 min^{-1} led to the peak roughness from among the three drill speeds when using the TiBN-coated drill. This speed was suggested as a switch point aspect for the surface roughness (**Figure 1**). Especially the rates of 80 mm/min and 40 mm/min exhibited similar roughnesses with all three drill speeds. The peak value of the surface roughness ($2.84 \mu\text{m}$) occurred at the speed of 1080 min^{-1} , the feed rate of 20 mm/min and the diameter of 4 mm , as shown in **Figure 1**. The drill speed, feed rate and diameter were also presented as rather parallel results when statistically analyzed. The drill speed had the maximum effect on the surface roughness when partial correlation values of the three parameters were analyzed. The partial correlation values identifying the effectiveness of the drill speed, the feed rate and the diameter were $R_{\text{part}}(\text{speed}) = -0.62$, $R_{\text{part}}(\text{force}) = -0.45$ and $R_{\text{part}}(\text{dia.}) = -0.29$, respectively. Statistical results confirmed the above contour plots of the experiment. The most effective parameter was the drill speed, and the least effective parameter was the diameter of the drill bit, also resulting from multiple regressions.

It was established with the analysis that the surface roughness increased with a decreased drill diameter. When Mg alloys are machined in a dry drilling condition, a flank build-up occurs on the cutting tool and the workpiece due to the adhesion.¹ The flank build-up formation on the Mg alloys causes sufficient temperature at the tool-workpiece contact and the adhesion of the workpiece material on the cutting tool leads to an increased cutting-edge radius and to an increase in the machining forces.^{1,8} The flank build-up formation, in the current study, increased the cutting forces and, hence, the performance of the cutting tool was reduced. This suggests that the smallest drill diameter was not enough to sufficiently overcome the cutting forces and a drilling failure occurred. On the other hand, the largest drill diameter was found to be more successful at removing the chips, resulting in a lower surface roughness. In order to achieve smooth surfaces when drilling MA8M, both higher drill speed and feed rate were required.

3.2 TiBN Coating

In the present study, the surface roughness was increased to a specific value at a drill speed of 1710 min^{-1} , and then it was diminished with the increasing drill speed up to 2730 min^{-1} . The cutting energy exceeded the plastic-deformation force of the chip and a more effective drilling can be the reason for this fact. Moreover, it was reported that higher cutting temperatures obtained with higher cutting speeds cause material softening on the shear plane, easier cuts and a smoother machined surface.^{4,9,10} Hence, the maximum drill speed of 2730 min^{-1} caused a decrease in the surface roughness after the peak value reached at 1710 min^{-1} . On the contrary, for the TiBN coating, the critical level of the roughness did not distinctly differ from the uncoated drill bits. According to the general trend, a roughness decrease was

observed via the increased drill speed. On the other hand, the surface roughness was increased with a decreased feed rate under all experimental conditions.

Larger cutting forces act more effectively in closing surface cracks and pores. However, there is a limit to the positive effect of the rolling force and beyond certain levels, such a force acts as the initiating source of cracks and cold welds, deteriorating the surface.⁴ However, the TiBN coating had a minor effect on the surface-roughness increment that was also found with the statistical analysis (the partial correlation of 0.2745). On the other hand, the feed rate had an extremely strong effect (the partial correlation of -0.66) on the surface-roughness reduction when compared with the drill speed and the coating. In the present study, the TiBN coating of HSS did not have the desired effect on the surface quality because of a lower wear resistance. As the Mg alloys caused the tool wear of the TiN-coated cutting tools, as reported before,^{1,11} this approach had similar effects on the MA8M drilling operation.

3.3 Chip formation

The achievement of a successful and better drilling operation is also indicated by removed chip formations. Moreover, the chip formations can show some variations due to the workpiece material and operation parameters such as cutting speed, feed rate or depth of cut.¹² For instance, when a regular broken chip or an irregular broken chip is formed on a workpiece with elastic properties, no chip breakers should be provided. Similarly, a workpiece material with elastoplastic properties produces a continuous fragmentary chip or a continuous chip with a wedge-shaped texture, and if the workpiece has plastic properties then the result is a continuous type of chip.¹² Long chips are usually not desirable because they can tangle along the drill body and have to be removed manually.¹³ Instead, well broken chips are associated with a smooth drilling process.

The diameter slightly influenced the chip formation, and it seemed that a larger diameter provided for a better chip formation. The feed rate seemed a more effective parameter than the drill diameter. Most of the continuous and a few irregular small-particle chips were produced when the TiBN-coated drill bits were used. The analysis suggests that the TiBN coating spoiled the drilling-process performance and the hole quality, which was also confirmed by the chip formation. The chip-formation impairment was derived from an unstable material adhesion on the drill, i.e., the surface roughness was increased by the TiBN coating. Higher drill speeds caused longer chip lengths and higher radii of helical spirals caused flutes that made it hard to drill and hard to push the chips away. Small-string chips are presented in **Figure 2a** obtained with drilling at the speed of 1080 min^{-1} , the 4-mm diameter and the 40-mm/min feed rate.

By comparing **Figure 2b** with **Figure 2a** and by keeping the other parameters constant, it is seen that the

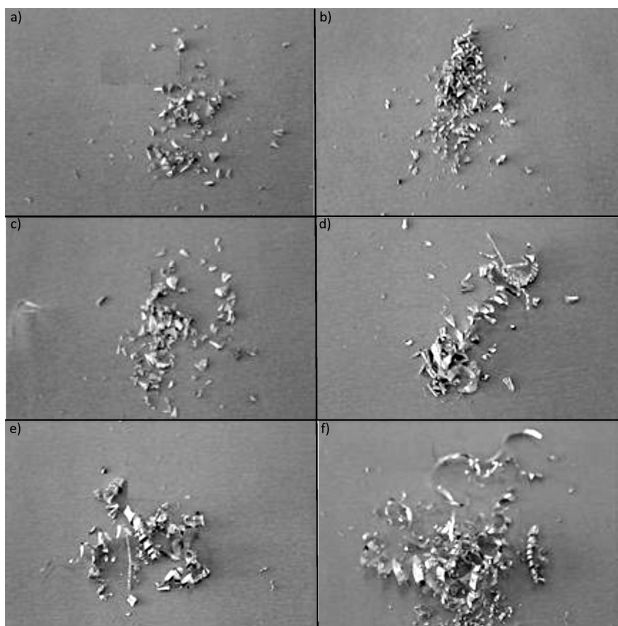


Figure 2: Chip formations for drilling conditions of: a) 1080 min⁻¹, 4 mm dia and 40 mm/min feed rate, b) 1080 min⁻¹, 6 mm dia and 40 mm/min feed rate, c) 1080 min⁻¹, 6 mm dia and 80 mm/min feed rate, d) 1080 min⁻¹, 6 mm dia, 80 mm/min feed rate by TiBN-coated drill bits, e) 1710 min⁻¹, 6 mm dia, 80 mm/min feed rate by TiBN-coated drill bits, f) 2730 min⁻¹, 6 mm dia, 80 mm/min feed rate by TiBN-coated drill bits

Slika 2: Nastanek ostružkov pri pogojih vrtanja: a) 1080 min⁻¹, 4 mm premera in hitrostjo podajanja 40 mm/min, b) 1080 min⁻¹, premer 6 mm in hitrost podajanja 40 mm/min, c) 1080 min⁻¹, premer 6 mm in hitrost podajanja 80 mm/min, d) 1080 min⁻¹, premer 6 mm in hitrost podajanja 80 mm/min pri svedru s TiBN prevleko, e) 1710 min⁻¹, premer 6 mm in hitrost podajanja 80 mm/min pri svedru s TiBN prevleko, f) 2730 min⁻¹, premer 6 mm in hitrost podajanja 80 mm/min pri svedru s TiBN prevleko

smaller and irregular chips occurred as the drill diameter changed from 4 mm to 6 mm. Since the drill diameter was changed exclusively from 4 mm to 8 mm, a slight difference was observed in the chip formation (**Figures 2a** and **2b**). An insignificant difference in the chip formation was observed when **Figures 2b** and **2c** were compared, being almost identical with **Figure 2a**. Obviously,

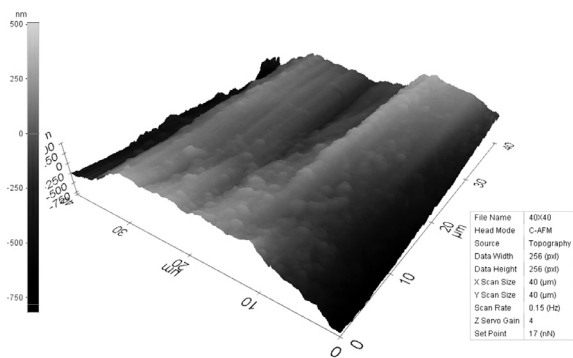


Figure 3: AFM topography of a specimen drilled at 1710 min⁻¹, 6 mm and 40 mm/min

Slika 3: AFM-topografija vzorca, vrtanega pri 1710 min⁻¹, 6 mm in 40 mm/min

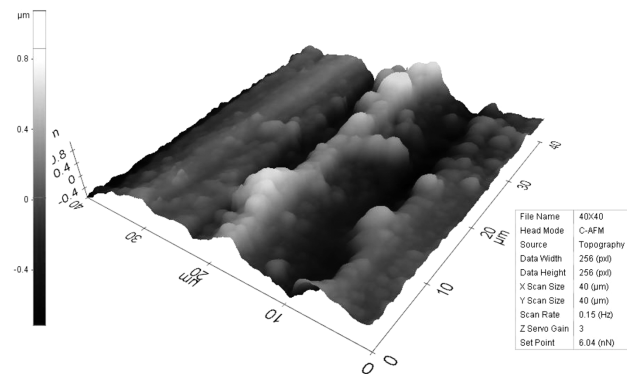


Figure 4: AFM topography of a specimen drilled at 2730 min⁻¹, 6 mm and 40 mm/min

Slika 4: AFM-topografija vzorca, vrtanega pri 2730 min⁻¹, 6 mm in 40 mm/min

no significant difference in the chip formation was observed between **Figures 2a**, **2b** and **2c**. Therefore, the chip formation was not influenced by the drill diameter and the feed rate. **Figure 2d** shows rather different chip formations formed due to the TiBN coating including a few long helical spiral chips that mostly had short strings. An increased drill speed increased the amount of the long helical spiral chips as seen from **Figures 2d**, **2e** and **2f**. Long-string chip formations were obtained especially at 2730 min⁻¹ (**Figure 2f**) though small-diameter helical chips were observed for the holes drilled at 1710 min⁻¹ (**Figure 2e**). Irregular, small chip formations presented in **Figure 2f** are also seen in **Figure 2e**. In this case, the drill speed and the TiBN coating were observed to be more effective than the feed rate in the chip formation.

3.4 Atomic-force-microscopy (AFM) observation

The maximum surface height of 500 nm was reached (**Figure 3**). The longitudinal grooves were unclear and shallow when **Figures 3** to **5** were compared. The drill-speed effect obtained at 2730 min⁻¹, the 6-mm drill diameter and the 40-mm/min feed rate was clearly observed in both **Figures 3** and **4**. The maximum height of

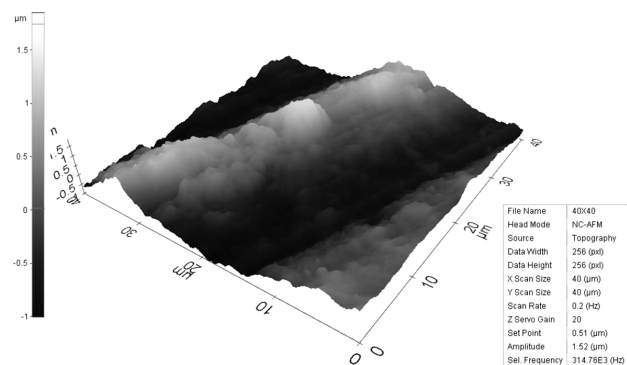


Figure 5: AFM topography of a specimen drilled at 1710 min⁻¹ and 40 mm/min with a TiBN-coated drill

Slika 5: AFM-topografija vzorca, vrtanega pri 1710 min⁻¹, s TiBN prevleko in 40 mm/min

the surface was elevated at about 1000 nm, and the longitudinal grooves are clearly seen in **Figure 4**. The TiBN-coating effect on the surface topography was observed at about 1750 nm, being measured as the maximum height and rare longitudinal grooves of the surface (**Figure 5**). The drill speed and feed rate were 1080 min⁻¹ and 20 mm/min, respectively, and the lowest level of the present experimental study led to the surface topography of **Figure 5**. When **Figures 3 to 5** are compared it is found that the drill speed and TiBN coating had an excessive negative effect on the surface topography during the drilling of the MA8M Mg alloy. On the AFM graphs, the maximum undulation was observed for the TiBN-coated drill.

4 CONCLUSION

The experimental work and the analysis showed that the MA8M alloy has a lower machinability capacity. Although the drill-speed increasing was performed rather well, the results for the roughness and chip formation were not obtained with the AFM graphs. The drill speed has a direct relationship with the cutting speed and an increase in the cutting speed resulted in smoother surfaces compared with lower cutting speeds.¹³ But the increment of the cutting speeds led to higher cutting temperatures, and the temperature increase also decreased both the cutting performance of a drill bit and the surface integrity. For this reason, the drill speed should not be performed at extremely high levels. On the other hand, the feed rate can be increased by increasing the drill speed if smooth surfaces are required. However, the feed-rate increment has a positive effect on the surface roughness, and it should be used carefully with smaller diameters of drill bits. According to the results of the experimental work, the TiBN coating was not appropriate for the MA8M drilling operation when compared with the HSS drill bit. However, the wear resistance of the TiBN-coated drilling tools should be investigated.

5 REFERENCES

- ¹ H. K. Tönshoff, J. Winkler, The influence of tool coatings in machining of magnesium, *Surface and Coatings Technology*, 94 (1997), 610–616, doi:10.1016/S0257-8972(97)00505-7
- ² H. Y. Wu, C. C. Hsu, J. B. Won, P. H. Sun, J. Y. Wang, S. Lee, C. H. Chiu, S. Torng, Effect of heat treatment on microstructure and mechanical properties of the consolidated Mg alloy AZ91D machined chips, *J. of Materials Processing Technology*, 209 (2009), 4194–4200, doi:10.1016/j.jmatprotec.2008.11.001
- ³ W. Guo, Q. Wang, B. Ye, H. Zhou, Microstructure and mechanical properties of AZ31 magnesium alloy processed by cyclic closed-die forging, *J. of Alloys and Compounds*, 558 (2013), 164–171, doi:10.1016/j.jallcom.2013.01.035
- ⁴ M. Salahshoor, Y. B. Guo, Surface integrity of magnesium-calcium implants processed by synergistic dry cutting-finish burnishing, *Procedia Engineering*, 19 (2011), 288–293, doi:10.1016/j.proeng.2011.11.114
- ⁵ Z. Pu, J. C. Outeiro, A. C. Batista, O. W. Dillon, D. A. Jr. Puleo, I. S. Jawahir, Surface integrity in dry and cryogenic machining of AZ31B Mg alloy with varying cutting edge radius tools, *Procedia Engineering*, 19 (2011), 282–287, doi:10.1016/j.proeng.2011.11.113
- ⁶ M. Salahshoor, Y. B. Guo, Cutting mechanics in high speed dry machining of bio medical magnesium-calcium alloy using internal state variable plasticity model, *Int. J. of Machine Tools and Manufacture*, 51 (2011), 579–590, doi:10.1016/j.ijmachtools.2011.04.004
- ⁷ S. Bhowmick, A. T. Alpas, The role of diamond like carbon coated drills on minimum quantity lubrication drilling of magnesium alloys, *Surface and Coatings Technology*, 205 (2011), 5302–5311, doi:10.1016/j.surfcoat.2011.05.037
- ⁸ Y. H. Celik, Investigating the effects of cutting parameters on the hole quality in drilling the Ti-6Al-4V alloy, *Mater. Tehnol.*, 48 (2014) 5, 653–659
- ⁹ A. Mavi, I. Korkut, Machinability of a Ti-6Al-4V alloy with cryogenically treated cemented carbide tools, *Mater. Tehnol.*, 48 (2014) 4, 577–580
- ¹⁰ A. Altin, The effect of the cutting speed on the cutting forces and surface finish when milling chromium 210 Cr12 steel hardfacings with uncoated cutting tools, *Mater. Tehnol.*, 48 (2014) 3, 373–378
- ¹¹ H. Çaliskan, A. Erdogan, P. Panjan, M. S. Gök, A. C. Karaoglanli, Micro-abrasion wear testing of multilayer nanocomposite TiAlSiN/TiSiN/TiAlN hard coatings deposited on the AISI H11 steel, *Mater. Tehnol.*, 47 (2013) 5, 563–568
- ¹² V. P. Astakhov, S. V. Shvets, M. O. M. Osman, Chip structure classification based on mechanics of its formation, *J. of Materials Processing Technology*, 71 (1997), 247–257, doi:10.1016/S0924-0136(97)00081-2
- ¹³ K. Feng, J. Ni, D. A. Stephenson, Continuous chip formation in drilling, *Int. J. of Machine Tools & Manufacture*, 45 (2005), 1652–1658, doi:10.1016/j.ijmachtools.2005.03.011

APPLICATION OF THE TAGUCHI METHOD TO SELECT THE OPTIMUM CUTTING PARAMETERS FOR TANGENTIAL CYLINDRICAL GRINDING OF AISI D3 TOOL STEEL

UPORABA TAGUCHI METODE ZA IZBIRO OPTIMALNIH PARAMETROV ODREZAVANJA PRI TANGENCIALNEM CILINDRIČNEM BRUŠENJU ORODNEGA JEKLA AISI D3

Cetin Ozay¹, Hasan Ballikaya², Vedat Savas¹

¹Department of Mechanical Engineering, Faculty of Technology, University of Firat, 23119 Elazig, Turkey

²Ortakoy Vocational High School, University of Aksaray, Aksaray, Turkey
cozay@firat.edu.tr, hballikaya@aksaray.edu.tr, vsavas@firat.edu.tr

Prejem rokopisa – received: 2014-12-06; sprejem za objavo – accepted for publication: 2015-02-10

doi:10.17222/mit.2014.293

The purpose of this research was an analysis of the optimum cutting conditions for the lowest surface roughness in tangential cylindrical grinding of the AISI D3 tool steel using the Taguchi method. In this experimental investigation, the surface roughness with various wheel speeds, workpiece speeds, feed rates and depths was observed. The surface roughness was investigated employing the Taguchi design of experiments and an analysis of variance (ANOVA). Significant machining parameters were identified using the signal-to-noise ratio. The results of the experiments indicate that the wheel speed and feed rate have dominating effects on the surface roughness during the cutting. The developed new grinding process can be used in the machining industries in order to determine the optimum cutting parameters for the minimum surface roughness.

Keywords: tangential cylindrical grinding, Taguchi method, surface roughness, ANOVA

Članek predstavlja analizo optimalnih pogojev rezanja s Taguchi metodo, za doseganje najmanjše hrapavosti pri tangencialnem cilindričnem brušenju orodnega jekla AISI D3. Pri teh eksperimentih je bila opazovana hrapavost površine pri različnih hitrostih kolesa, različnih hitrostih obdelovanca ter različnih hitrostih in globinah podajanja. Površinska hrapavost je bila preiskovana z uporabo Taguchi-jeve postavitve preizkusov in analize variance (ANOVA). Pomembni parametri obdelave so bili identificirani z uporabo razmerja signal – hrup. Rezultati eksperimentov kažejo, da imata hitrost kolesa in hitrost podajanja prevladujočo vlogo pri hrapavosti površine in parametrih rezanja. Razvoj novega postopka brušenja se lahko uporabi v strojni industriji za določanje optimalnih pogojev rezanja pri minimalni hrapavosti površine.

Ključne besede: tangencialno cilindrično brušenje, Taguchi metoda, hrapavost površine, ANOVA

1 INTRODUCTION

Recently, increased production quality, a reduction in the process time, an improvement in dimensional accuracy and improved workplace-safety conditions have been studied with respect to the development of production methods. The Taguchi method and ANOVA analysis used for determining the optimum values reduce the number of experimental studies while providing more accurate results.

1.1 Grinding

Grinding is a finishing process used to improve the surface finish and the abrasive materials and tighten the tolerance on flat and cylindrical surfaces by removing a small amount of the material. Grinding is an essential process for the final machining of the components requiring smooth surfaces and precise tolerances.

Grinding methods vary depending on the cutting tool and the shape, the location and the movement of the workpiece. The cylindrical grinding method is one of these methods. The cylindrical grinding method is a final

machining method, often used for processing interior and exterior surfaces of cylindrical workpieces. This method increases the surface quality of the workpieces and provides the required measurement and tolerance. Moreover, grinding is a method, which has a significant effect on the corrosion rate, the fracture strength, the abrasion and the magnetic features of a workpiece.

Large-diameter grinding wheels are used as the cutting tools for the cylindrical grinding method. They are composed of a grinding wheel, abrasive particles and sealants that join them together. Some problems occur while fixing these cutting tools to the bench and during their operation because of the errors that occurred during the manufacturing of these tools and because they are of large dimensions. The wheel is not balanced since hard particles were not homogeneously dispersed during the manufacturing of the wheel. An unbalanced wheel increases the centrifugal force while turning and cannot reach high speeds; the vibration increases, the surface quality deteriorates and the explosion risk of the wheel increases since the contact of the wheel with the workpiece is imbalanced. Such problems affect the manufacturing and manufacturer adversely.

The grinding process has an important place in highly delicate procedures performed during the manufacturing of the molds used in the molding sector. Some studies of the cylindrical grinding method have been conducted recently.

Cylindrical grinding is used to grind the external or internal diameter of a rigidly supported and rotating workpiece. Although the term cylindrical grinding may also be applied to centerless grinding, it generally refers to a workpiece that is ground in a chuck or between the supporting centers. Cylindrical grinders can be used to grind all types of hard or soft workpieces to a high degree of accuracy and very fine surface finishes¹.

Over the years, researchers focused on improving the performance of machining operations with the aim of minimizing the costs and improving the quality of manufactured products². Hassui and Diniz³ studied the effects of grinding parameters on the surface roughness and vibration and investigated the relation between the vibration and the surface roughness during the grinding of the AISI 52100 steel. Kwak⁴ stated that the geometric errors occurring during the grinding process were due to the rigidity of the grinding system and thermal effects. He also indicated that an accurate determination of the grinding parameters is of great importance for the reduction of such errors. During the cylindrical grinding of Al/SiC-metal-matrix composites, Thiagarajan et al.⁵ studied the effects of the grinding parameters on the grinding force, the surface roughness and the heat that emerges during the grinding. Fan and Miller⁶ developed a force model for grinding with segmental wheels. Both experimental and analytical results showed the average

grinding force of the wheels in comparison with the conventional wheels. Larger spaces between the segments further reduce the average force and increase the surface roughness and peak force.

Hecker and Liang⁷ theoretically examined the relationship between the thickness of a chip that was undeformed in the cylindrical grinding process and the arithmetic surface roughness. They tried to verify this relation experimentally using the cylindrical grinding method. Gavas et al.⁸ machined four different materials using the helical scan-grinding (HSG) method. They investigated the effects of the cutting parameters on the surface roughness and roundness. They stated that the helical scan-grinding method decreased the surface roughness in comparison with the conventional cylindrical grinding method. Gołabczak and Koziarski⁹ investigated the cutting capabilities of CBN grinding wheels in the grinding process. They studied the components of grinding forces, the surface roughness and the stresses on the surface layer.

A cylindrical grinder is a type of a grinding machine used to shape the outside of an object. The cylindrical grinder can work on a variety of shapes. However, the object must have the central axis of the rotation. This includes but is not limited to the shapes such as a cylinder, an ellipse, a cam or a crankshaft¹⁰. Agarwal and Venkateswara Rao¹¹ investigated the relation between the chip thickness and the surface roughness in the grinding of ceramic materials. Nguyen and Zhang¹² investigated the performance of a new, segmented, grinding-wheel system using the surface integrity of ground components as a criterion. The experimental results showed that the segmented grinding wheel had some obvious advantages in comparison with the standard wheel.

Rodrigo et al.¹³ studied the effects of tangential cutting forces on the surface roughness in the grinding process using cutting fluids flowing at different flow rates. Koshy et al.¹⁴ used the centerless-grinding-processing method by positioning the workpiece tangentially to the grinding wheel. They stated that this method creates a better surface finish than the conventional methods.

Upon the literature review, it is observed that the studies are mostly focused on the effects of the cutting parameters on the surface quality. It is determined that there is a limited number of the studies conducted on the selection of cutting tools or the location and movements of cutting tools and workpieces with respect to each other. A new approach to the cylindrical grinding method is introduced in this study. Within this new method, called the tangential cylindrical grinding, the outer surface of a cylindrical workpiece is in a tangential contact with the cutting tool and the axes of the cutting tool and the workpiece are made to be tangent to each other (**Figure 1**). This method allows us to use small grinding wheels instead of the grinding wheels with large diameters used with the conventional grinding. Moreover, the

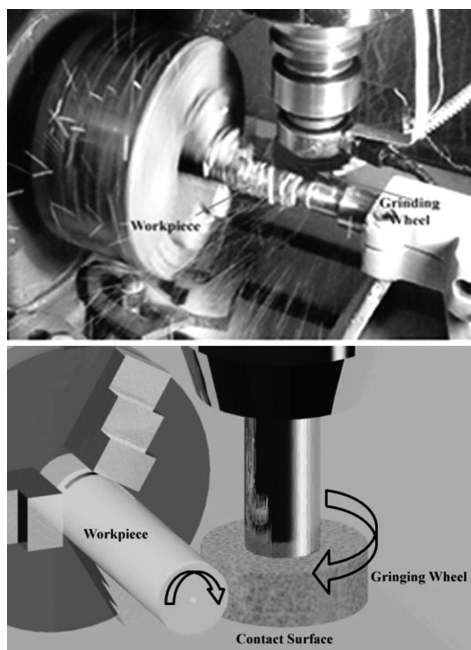


Figure 1: Position of the contact between the grinding wheel and workpiece

Slika 1: Položaj stika med brusnim kolesom in obdelovancem

negative effects that may occur during the grinding with the wheels with large diameters are eliminated.

1.2 Taguchi method and ANOVA

The Taguchi experimental-design method minimizes the number of experiments, enabling experimental studies to be conducted in a shorter and easier way. This method was first introduced by Genichi Taguchi, a Japanese engineer. This method reduces the number of experiments that would otherwise last for a long time and have high costs¹⁵.

Analysis of variance is the predominant statistical method used to interpret experimental data and make the necessary decisions on whether this method is the most objective one. The column effect is used by Taguchi as a simplified ANOVA to subjectively identify the columns that have large influences on the response¹⁵. The aim of the analysis of variance is to evaluate the significance of the cutting parameters on the surface roughness for this paper. It gives a clear picture of how much the cutting parameters affect the response and the level of significance of the factor considered. Statistically, there is a tool called an F test allowing us to see which design parameter has a significant effect on the quality characteristic. Usually, when $F > 4$, it means that the change in the design parameter has a significant effect on the quality characteristic¹⁶.

Chang and Kuo¹⁷ machined aluminium-oxide ceramics with laser machining using the Taguchi experimental-design method. They investigated the effects of the cutting parameters on the surface roughness and machining ratio in the experimental studies they conducted. Prabhu and Vinayagam¹⁸ used SAE20W40 nanocarbon-reinforced oil in the machining of the AISI D3 tool steel with the grinding method. They used the Taguchi experimental-design method in planning and evaluating their experimental studies. Kwak and Kim¹⁹ investigated the effects of machining parameters on the geometric errors that appear on the surface, during the surface grinding, using the Taguchi and surface-response methods. They also developed a secondary surface-response model for a prior detection of any geometric error. Nalbant et al.²⁰ used the Taguchi method to find the optimum cutting parameters for the surface roughness in turning. They provided experimental results to illustrate the effectiveness of this approach.

Gür²¹ alloyed the surface of medium-carbon steel using the PTA method and he investigated the wear resistance of this alloyed coating layer via the Taguchi method. He used the Taguchi design according to the L_{18} orthogonal array and experimentally evaluated the factors affecting the wear of the coating layer. The preparation of experimental study plans and an easy interpretation of the conducted experimental studies are the primary advantages of the Taguchi experimental-design method. An experimental study plan is formed following the determination of the relevant parameters to

be used and their related levels and the selection of the orthogonal arrays appropriate for their levels of freedom. It is then converted into the performance characteristic called the S/N (signal/noise) ratio for the interpretation of such experimental studies. The most commonly used performance characteristics are the smallest the best, the biggest the best and the nominal the best characteristics. The largest S/N ratio represents the value of a parameter for the optimum level¹⁵.

2 EXPERIMENTAL WORK

2.1 Experimental set-up and measurements

A VMC-850 Johnford vertical, processing, centered workbench was used for designing the experimental set-up of the tangential cylindrical grinding as a new method. The flowchart for the optimization of the cutting parameters in the tangential cylindrical grinding process is shown in **Figure 2**.

The set-up mechanism shown in **Figure 3** was installed for the workpiece to rotate around its own axis at desired rotation rates in the experimental set-up. A Micromaster 400 inverter was used for rotational adjustments. Furthermore, a grinding wheel used as the cutting tool could be easily installed on or demounted from a milling machine, acting as a milling tool. For the workpiece's rotation with no backlash, the workpiece was supported with the center on the other side.

Rotational adjustments were calibrated with an Ex-tech Instruments 461880 tachometer and a vibration-



Figure 2: Flowchart for optimizing the cutting parameters in tangential cylindrical grinding process

Slika 2: Potek optimizacije parametrov rezanja pri postopku tangencialnega cilindričnega brušenja

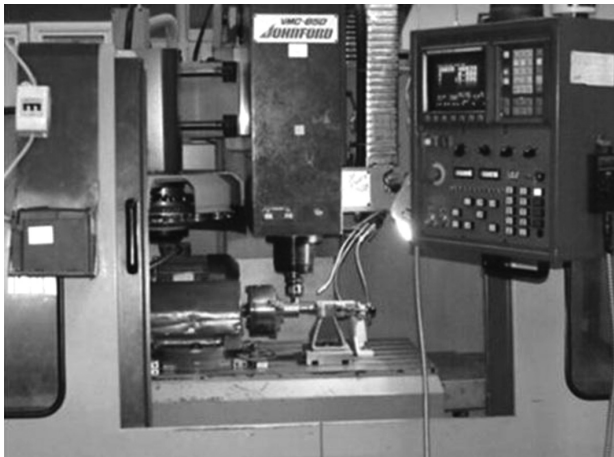


Figure 3: Tangential cylindrical grinding set-up mechanism

Slika 3: Postavitev mehanizma tangencialnega cilindričnega brušenja

measuring device. The parallelism adjustment of the workpiece was checked by means of a comparator.

Ø20 × 60 mm AISI D3 tool steel was cut using a saw to conduct tangential cylindrical grinding experiments. The length of the workpiece was determined as per $L = 2D$ ratio, where L is the length and D is the diameter of the workpiece. A center hole was opened on one side in order to enable the workpiece to be supported by the center. The machining was conducted by making the grinding wheel turn around its own axis, while being positioned tangentially to the workpiece's axis and with the feed motion providing the depth of cut.

The AISI D3 tool steel is used for manufacturing mold plates, powder-metallurgy tools, cold extrusion, punch dies, ceramic forming dies and cold punches. A 45s SIOUX 2145GP grinding wheel with a grain size of 100 µm and a diameter of $R = 44$ mm was used to conduct the tangential cylindrical grinding experiments.

The average surface-roughness values of the parts machined with the tangential cylindrical grinding method were measured using Mitutoyo Surftest S-J210. The surface-roughness measurements were taken along the cylindrical workpiece's axis and in the direction of the feed rate. The measurements were taken from four different points of the machined surfaces and the average of the measurements was calculated.

2.2 Experimental study

L_{18} orthogonal arrays were used in the machining of the AISI D3 tool steel with the tangential cylindrical grinding method in this experimental study. The number of experiments and usage levels of the parameters were specified on the Taguchi toolbar of the Minitab 15 software program. Because of conducting these experiments, the surface-roughness values obtained from the surface of the relevant workpiece were converted into the S/N ratio in the Minitab 15 software program. The following criteria were taken into consideration when determining the levels of the parameters used in the experimental studies:

- The levels of the depth of cut are generally determined as the depth of cut left for the grinding process and the values above this value.
- Relevant values were obtained from the tables according to the number of rotations of the grinding wheel, the number of rotations of the workpiece, the material features of the materials to be machined and the cutting tools to be used and the features of the workbench.
- The smallest feed rate of the workbench that was used for determining the parameters of the axial feed speed and higher feed rates were taken into consideration. **Table 1** illustrates the parameters and the related levels to be used in the experiments.

Table 1: Machining parameters

Tabela 1: Parametri obdelave

Cutting parameters	Unit	Symbol	Levels		
			Level 1	Level 2	Level 3
Depth of cut	mm	A	0.005	0.01	-
Wheel speed	min ⁻¹	B	1000	1500	2000
Workpiece speed	min ⁻¹	C	220	320	420
Table feed rate	mm/min	D	3.2	7.9	12.6

Considering the freedom degrees of these parameters, it was determined that the use of the L_{18} orthogonal array was appropriate. **Table 2** illustrates the L_{18} orthogonal array used in the experimental studies.

Table 2: L_{18} orthogonal array for the experiments

Tabela 2: L_{18} ortogonalna namestitev preizkusov

Trial No	Levels of parameters			
	Depth of cut (mm)	Wheel speed (min ⁻¹)	Workpiece speed (min ⁻¹)	Table feed rate (mm/min)
1	0.005	1000	220	3.2
2	0.005	1000	320	7.9
3	0.005	1000	420	12.6
4	0.005	1500	220	3.2
5	0.005	1500	320	7.9
6	0.005	1500	420	12.6
7	0.005	2000	220	7.9
8	0.005	2000	320	12.6
9	0.005	2000	420	3.2
10	0.01	1000	220	12.6
11	0.01	1000	320	3.2
12	0.01	1000	420	7.9
13	0.01	1500	220	7.9
14	0.01	1500	320	12.6
15	0.01	1500	420	3.2
16	0.01	2000	220	12.6
17	0.01	2000	320	3.2
18	0.01	2000	420	7.9

3 RESULTS

Table 3 illustrates the results obtained from the processing of the AISI D3 tool steel, performed with the Taguchi test-design method, and the corresponding S/N

ratio values. The average surface roughness and the cutting parameters are present in **Figures 4 to 6**.

Examining **Table 3** and **Figures 4** and **6**, it is observed that the surface roughness increases with the increase in the workpiece speed. During the grinding process, the workpiece speed is selected according to the grinding wheel and the characteristics of the workpiece material. Besides, there must be a proper ratio between the workpiece and the grinding-wheel speeds. In this study, it is found that as the workpiece speed increases, this ratio diverges from its proper value, the dynamic hardness of the grinding wheel decreases and the surface quality is reduced due to irregular abrasion. Examining **Table 3** and **Figures 4** and **5**, it is observed that the surface roughness decreases while the grinding-wheel speed increases. Since the amount of the chips that each cutting wheel removes decreases with the increase in the grinding-wheel speed, it can be asserted that the machining force per wheel decreases and the vibration is

reduced correspondingly. In consequence, it is obvious from the results that the surface quality is good.

Table 3: Experimental results obtained from the studies of the average surface roughness and S/N ratio

Tabela 3: Rezultati, dobjeni iz študija povprečne hrapavosti površine in razmerja S/N

Trial No	Levels of parameters				Surface roughness (R_a) (μm)	S/N ratio
	Depth of cut (mm)	Wheel speed (min^{-1})	Work-piece speed (min^{-1})	Table feed rate (mm/min)		
1	0.005	1000	220	3.2	0.37	8.635
2	0.005	1000	320	7.9	0.46	6.744
3	0.005	1000	420	12.6	0.59	4.582
4	0.005	1500	220	3.2	0.34	9.370
5	0.005	1500	320	7.9	0.42	7.535
6	0.005	1500	420	12.6	0.55	5.192
7	0.005	2000	220	7.9	0.35	9.118
8	0.005	2000	320	12.6	0.43	7.330
9	0.005	2000	420	3.2	0.36	8.873
10	0.01	1000	220	12.6	0.56	5.036
11	0.01	1000	320	3.2	0.46	6.744
12	0.01	1000	420	7.9	0.52	5.679
13	0.01	1500	220	7.9	0.41	7.744
14	0.01	1500	320	12.6	0.54	5.352
15	0.01	1500	420	3.2	0.41	7.744
16	0.01	2000	220	12.6	0.48	6.375
17	0.01	2000	320	3.2	0.39	8.178
18	0.01	2000	420	7.9	0.44	7.130

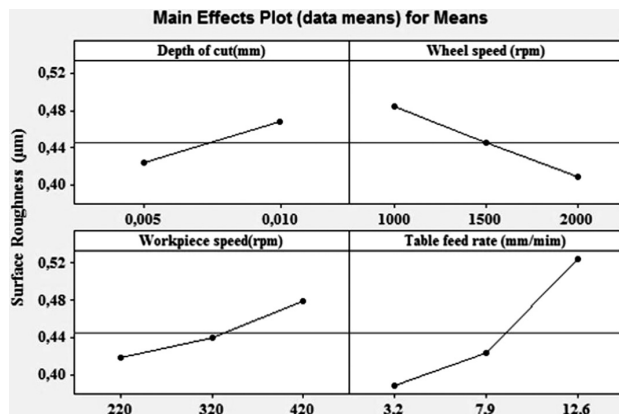


Figure 4: Effect of processing parameters on the average surface roughness of AISI D3 tool steel

Slika 4: Vpliv procesnih parametrov na povprečno hrapavost površine orodnega jekla AISI D3

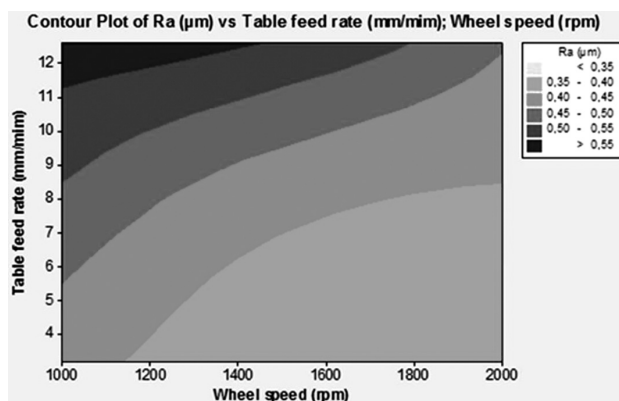


Figure 5: Effect of parameters "grinding-wheel speed" and "table feed rate" on the average surface roughness in machining of AISI D3 tool steel

Slika 5: Vpliv parametrov "hitrost brusilnega kolesa" in "hitrost podajanja mize" na povprečno hrapavost in obdelavnost orodnega jekla AISI D3

When **Table 3** and **Figures 4** to **6** are examined, it is seen that the surface roughness increases with the increase in the depth of cut and the feed rate.

The surface roughness generally increases as the feed rate increases. It can be concluded that with the increase in the depth of cut and feed rate, the cutting forces and, accordingly, the vibration increase during the processing of the AISI D3 tool steel with the tangential cylindrical grinding method. In addition, with the increasing vibration, the surface roughness increases during the machining process. In a study conducted by Demir it is stated

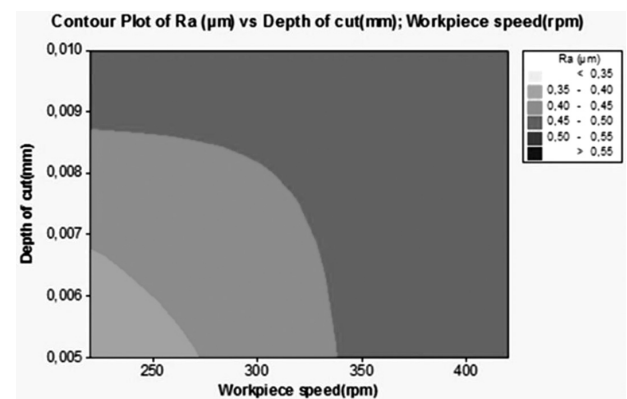


Figure 6: Effect of parameters "workpiece speed" and "depth of cut" on the average surface roughness in machining of AISI D3 tool steel

Slika 6: Vpliv parametrov "hitrost obdelovanca" in "globina reza" na povprečno hrapavost površine pri obdelavi orodnega jekla AISI D3

that the cutting section and the grinding force increase because of the increase in the depth of cut, and thus, the abrasion rate of the wheel and the average surface roughness increase^{22,23}.

Table 4 illustrates the *S/N* ratios, which correspond with the surface-roughness rates obtained according to the parameter levels during the processing of the AISI D3 tool-steel material. In this table, the optimum levels of the processing parameters are shown with (*).

Table 4: Effect of the factors at each level on the surface roughness in the machining of AISI D3 tool steel (*S/N* ratio)

Tabela 4: Vpliv faktorjev na vsakem nivoju na hrapavost površine pri obdelavi orodnega jekla AISI D3 (*S/N* razmerje)

Cutting Parameters	Symbol	Average <i>S/N</i> rate (dB)		
		Level 1	Level 2	Level 3
Depth of cut	A	7.49 ^a	6.67	–
Wheel speed	B	6.24	7.16	7.83 ^a
Workpiece speed	C	7.71 ^a	6.98	6.53
Table feed rate	D	8.26 ^a	7.33	5.64

When the results were examined, it was determined that the A1, B3, C1 and D1 levels indicated the optimum parameters in the evaluation of the effects of the cutting parameters on the average surface roughness.

In conclusion, it is evidently seen in the experimental studies conducted that the cutting parameters lead to results that are similar to those for the external surface obtained in the cylindrical grinding process with the tangential cylindrical grinding method. The study allows the grinding wheels with a smaller diameter to be used in conventional cylindrical grinding instead of the grinding wheels with a large diameter. In addition, the problems that may occur when fixing and using the grinding wheels with a large diameter are minimized. Moreover, it is possible to perform the grinding process on a turning/milling machine.

In this paper, the aim of the analysis of variance is to evaluate the effects of the cutting parameters on the average surface roughness. The analysis clearly shows how much the cutting parameters affect the response and the level of significance of the factor considered. **Table 5** shows the results of ANOVA for the average surface roughness. It can be seen from this table that the table feed rate and the wheel speed are the most significant cutting parameters affecting the surface roughness. Therefore, based on the *S/N* and ANOVA analyses, the optimum cutting parameters are the depth of cut at level 1, the wheel speed at level 3, the workpiece speed at level 1 and the feed rate at level 1. However, the most significant cutting parameter contributing the most to the quality characteristic, i.e., the average surface roughness is the table feed rate (56.27 %). The error rate of 4.56 % was found with the ANOVA.

Table 5: ANOVA analysis of the average surface roughness obtained during the processing of AISI D3 tool steel

Tabela 5: Analiza ANOVA povprečne hrapavosti površine, dobljene pri obdelavi orodnega jekla AISI D3

Cutting parameters	Degree of freedom	Sum of square	Variance	F ratio	Contribution (%)
Depth of cut (mm)	1	3.041	3.041	30.586	7.940
Wheel speed (min ⁻¹)	2	7.711	3.855	38.780	20.279
Workpiece speed (min ⁻¹)	2	4.253	2.126	21.393	10.946
Table feed rate (mm/min)	2	21.044	10.522	105.830	56.270
Error	10	0.994	0.099	–	4.562
Total		37.044	–	–	–

4 CONCLUSIONS

In this study, the AISI D3 tool steel was machined with tangential cylindrical grinding introduced as a new method. Using the variance analysis (ANOVA), the effects of different parameter levels on the average surface roughness were analyzed. The experimental studies were evaluated using the Taguchi experimental design method and ANOVA; the following results were obtained:

- It was determined that the average surface roughness increases with the increase in the workpiece speed during the processing of the AISI D3 tool-steel material with the tangential grinding method. It was observed that the best value of the average surface roughness was obtained at the first level.
- It was observed that the average surface-roughness rate increases with the increase in the depth of cut and the axial-feed rate during the processing of the AISI D3 tool-steel material. The most appropriate levels were the first levels.
- It was observed that the average surface roughness decreases with the increase in the grinding-wheel speed during the processing of the AISI D3 tool-steel material.
- The ANOVA results for all the cutting parameters affecting the average surface roughness showed that the configuration analysis has a certain effect.
- Using the Taguchi method and the *S/N* rate, parameter levels A1, B3, C1, D1 were used to obtain the optimum average surface roughness.
- The tangential cylindrical grinding process as a new method enabled us to use the grinding wheels with smaller diameters compared to the diameter of the grinding wheels used in conventional cylindrical grinding and the obtained surface quality was similar to the quality of fine grinding.

Acknowledgement

The authors would like to acknowledge the Firat University, Turkey, for the financial support (Project No. FUBAP-TEF.11.06).

5 REFERENCES

- ¹ H. A. Youssef, H. El-Hoppy, *Machining Technology, Machine Tools and Operations*, CRC Press, 2008
- ² N. H. Rafai, M. N. Islam, An investigation into dimensional accuracy and surface finish achievable in dry turning, *Machining Science and Technology*, 13 (2009) 4, 571–589, doi:10.1080/10910340903451456
- ³ A. Hassui, A. E. Diniz, Correlating surface roughness and vibration on plunge cylindrical grinding of steel, *International Journal of Machine Tools & Manufacture*, 43 (2003), 855–862, doi:10.1016/S0890-6955(03)00049-X
- ⁴ J. S. Kwak, Application of Taguchi and response surface methodologies for geometric error in surface grinding process, *International Journal of Machine Tools and Manufacture*, 45 (2005) 3, 327–334, doi:10.1016/j.ijmachtools.2004.08.007
- ⁵ C. Thiagarajan, R. Sivaramakrishnan, S. Somasundaram, Experimental evaluation of grinding forces and surface finish in cylindrical grinding of Al/SiC metal matrix composites, *Proceedings of the Institution of Mechanical Engineers, Part B: Journal of Engineering Manufacture*, 225 (2011) 9, 1606–1614, doi:10.1177/0954405411398761
- ⁶ X. Fan, M. H. Miller, Force analysis for grinding with segmental wheels, *Machining Science and Technology: An International Journal*, 10 (2006) 4, 435–455, doi:10.1080/10910340600996142
- ⁷ R. L. Hecker, S. Y. Liang, Predictive modelling of surface roughness in grinding, *International Journal of Machine Tools and Manufacture*, 43 (2003) 8, 755–761, doi:10.1016/S0890-6955(03)00055-5
- ⁸ M. Gavas, İ. Karacan, E. Kaya, A novel method to improve surface quality in cylindrical grinding, *Experimental Techniques*, 35 (2011) 1, 26–32, doi:10.1111/j.1747-1567.2009.00575.x
- ⁹ A. Gołabczak, T. Koziarski, Assessment method of cutting ability of CBN grinding wheels, *International Journal of Machine Tools and Manufacture*, 4 (2005) 11, 1256–1260, doi:10.1016/j.ijmachtools.2005.01.008
- ¹⁰ C. N. de Souza, R. E. Catai, P. R. de Aguiar, M. H. Salgado, E. C. Bianchi, Analysis of diametrical wear of grinding wheel and roundness errors in the machining of steel, *J. of the Braz. Soc. of Mech. Sci. & Eng. by ABCM*, XXVI (2004) 2, 209, doi:10.1590/S1678-58782004000200013
- ¹¹ S. Agarwal, P. Venkateswara Rao, A probabilistic approach to predict surface roughness in ceramic grinding, *International Journal of Machine Tools and Manufacture*, 45 (2005) 6, 609–616, doi:10.1016/j.ijmachtools.2004.10.005
- ¹² T. Nguyen, L. C. Zhang, Performance of a new segmented grinding wheel system, *International Journal of Machine Tools and Manufacture*, 49 (2009) 3–4, 291–296, doi:10.1016/j.ijmachtools.2008.10.015
- ¹³ D. M. Rodrigo, C. B. Eduardo, E. C. Rodrigo, R. A. Paulo, Analysis of the different forms of application and types of cutting fluid used in plunge cylindrical grinding using conventional and super abrasive CBN grinding wheels, *International Journal of Machine Tools and Manufacture*, 46 (2006) 2, 122–131, doi:10.1016/j.ijmachtools.2005.05.009
- ¹⁴ P. Koshy, Y. Zhou, C. Guo, R. Chand, Novel kinematics for cylindrical grinding of brittle materials, *Annals of CIRP*, 54 (2005), 289–292, doi:10.1016/S0007-8506(07)60105-X
- ¹⁵ P. J. Ross, *Taguchi Techniques for Quality Engineering*, McGraw-Hill, 1995
- ¹⁶ W. H. Wang, Y. S. Tarng, Design optimization of cutting parameters for turning operations based on the Taguchi method, *Journal of Materials Processing Technology*, 84 (1998), 122–129, doi:10.1016/S0924-0136(98)00079-X
- ¹⁷ C. W. Chang, C. P. Kuo, Evaluation of surface roughness in laser-assisted machining of aluminum oxide ceramics with Taguchi method, *International Journal of Machine Tools and Manufacture*, 47 (2007), 141–147, doi:10.1016/j.machtools.2006.02.009
- ¹⁸ S. Prabhu, B. K. Vinayagam, AFM investigation in grinding process with nano fluids using Taguchi analysis, *Int. J. Adv. Manuf. Technol.*, 60 (2012), 149–160, doi:10.1007/s00170-011-3599-5
- ¹⁹ J. S. Kwak, I. K. Kim, Parameter optimization of surface grinding process based on Taguchi and response surface methods, *Key Engineering Materials*, 306–308 (2006), 709–714, doi:10.4028/www.scientific.net/KEM.306-308.709
- ²⁰ M. Nalbant, H. Gokkaya, G. Sur, Application of Taguchi method in the optimization of cutting parameters for surface roughness in turning, *Materials and Design*, 28 (2007) 4, 1379–1385, doi:10.1016/j.matdes.2006.01.008
- ²¹ A. K. Gür, Investigating the wear behaviour of FeCrC/B₄C powder alloys coating produced by plasma transferred arc weld surfacing using the Taguchi method, *MP Materials Testing*, 55 (2013) 6, 462–467, doi:10.3139/120.110463
- ²² H. Demir, A. Güllü, Investigation the effects of processing parameters and wheel hardness on the surface roughness and grinding forces, *Gazi University Journal of the Faculty of Engineering and Architecture*, 3 (2008), 577–584, <http://www.mmfdergi.gazi.edu.tr/article/view/1061000403>
- ²³ C. Ozay, H. Ballikaya, V. Savas, Investigation on surface roughness of D3 tool steel using tangential cylindrical grinding method, *Proc. of the EuroTecS 2013, European Conference of Technology and Society*, Sarajevo, Bosnia and Herzegovina, 2013, 377–384

EFFECTS OF FRICTION-WELDING PARAMETERS ON THE MORPHOLOGICAL PROPERTIES OF AN Al/Cu BIMETALLIC JOINT

VPLIV PARAMETROV TORNEGA VARJENJA NA MORFOLOŠKE LASTNOSTI Al/Cu BIMETALNEGA SPOJA

Veljko D. Milašinović¹, Radovan V. Radovanović², Mijat D. Milašinović¹,
Bojan R. Gligorić³

¹University of Belgrade, Faculty of Mechanical Engineering, Kraljice Marije 16, 11120 Belgrade, Serbia

²Academy of Criminalistic and Police Studies, Cara Dušana 196, 11080 Belgrade, Serbia

³University of Belgrade, Innovation Center of Faculty of Technology and Metallurgy, Karnegijeva 4, 11120 Belgrade, Serbia
v.milasnovic@gmail.com

Prejem rokopisa – received: 2014-12-14; sprejem za objavo – accepted for publication: 2015-01-20

doi:10.17222/mit.2014.304

The objective of this research is to consider the effects of certain parameters of the friction-welding process on the morphology of an aluminum/copper joint. The effect of the following parameters was monitored: the operating time, the operating pressure, the forging time and the forging pressure. The speed was constant during the binding process and reached 1500 min⁻¹. The preparation of the welding materials was performed in accordance with the industrial production conditions. With the SEM-EDS analysis, it was found that the morphology of the Al/Cu interface slightly changes when we change the distance from the rotation axis, irrespective of the combination of the friction-welding parameters. Apart from this, the joined effects of the operating pressure of 48 MPa and the forging pressure of 160 MPa caused a morphological change of the Al/Cu interface, while the forging time at the moment of the combined pressurizing effect significantly influenced the modification of the Al/Cu interface shape within a very narrow time interval of only a few seconds.

Keywords: friction welding, bimetallic joint, interface, aluminum, copper, SEM-EDS

Cilj te raziskave je obravnava vpliva nekaterih parametrov procesa tornega varjenja na morfologijo spoja aluminij/baker. Pregledan je bil vpliv naslednjih parametrov: čas delovanja, tlak pri obratovanju, čas kovanja in tlak pri kovanju. Hitrost 1500 min⁻¹ je bila med spajanjem konstantna. Priprava materialov za varjenje je bila izvršena skladno s pogoji industrijske proizvodnje. S pomočjo SEM-EDS analiz je bilo ugotovljeno, da se morfologija spoja Al/Cu rahlo spreminja s spreminjanjem razdalje od rotirajoče osi, ne glede na kombinacijo parametrov procesa tornega varjenja. Poleg tega je skupni učinek delovnega tlaka 48 MPa in tlaka pri kovanju 160 MPa povzročil morfološke spremembe spoja Al/Cu, medtem ko čas kovanja, v trenutku kombiniranega stiskanja močno vpliva na spremembo oblike Al/Cu spoja v zelo ozkem temperaturnem intervalu samo nekaj sekund.

Ključne besede: torni varjenje, bimetalni spoj, stik, aluminij, baker, SEM-EDS

1 INTRODUCTION

In energetics, bonding elements, originally used for bonding copper and aluminum cables, were made of copper (**Figures 1a to 1c**) and a joint between aluminum (Al) and copper (Cu) (Al/Cu joint) was most frequently made by creating a mechanical contact between the two metals, e.i., by crimping them (**Figure 1a**).¹ The bonding of Al cables onto the Cu busbars in electrical substations was conducted using Cu lugs where the connection between an Al cable and a Cu lug was made by crimping (**Figure 1b**)² or by tightening a screw (**Figure 1c**)³ of the inserted Al cable. As a result of the high copper price, new and more cost-effective solutions were found, such as Al lugs with an inserted Cu ring (**Figure 1d**).⁴ However, the use of such Al/Cu joints proved to be unreliable in the long run. The reasons for this were the following: 1) the weakening of the joint during its use at higher temperatures (due to different linear Al and Cu expansion coefficients) and 2) a large transient electrical resis-

tance at the interface, which is one of the deficiencies of a joint based on the mechanical type of connection.

Further research, with the objective to find ways for achieving a tighter bond between Al and Cu, led to the discovery of Al/Cu bonding elements where the connection between Al and Cu is achieved with an inter-diffusion of the solid-state atoms. The procedure, with which such a connection is formed, is called friction welding.

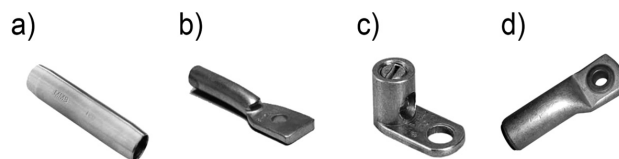


Figure 1: Cu bonding elements: a) Cu butt connector, b) Cu crimping lug, c) Cu lug with a screw, d) Al lug with the inserted Cu ring¹⁻⁴

Slika 1: Cu priključni elementi: a) Cu valjasti priključek, b) Cu priključek z zanko, c) Cu priključek z vijakom, d) Al priključek z vložnim Cu obročkom¹⁻⁴

Friction welding represents a process of bonding similar or dissimilar materials that occurs at the temperatures below the melting temperature of the base material that is the easiest to melt and are high enough to allow the optimum interdiffusion distance between the atoms of the metals, with the aim of achieving the required tensile strength.⁵ In practice, there are two methods of friction welding, different only in the method of the energy supply required for the process of welding/bonding metals. These are the continuous and inertia friction welding. In terms of continuous friction welding, the energy required for welding is supplied from a steady power source all the way to the forging phase, while the energy required for inertia friction welding is obtained from accumulated flywheel energy.⁶⁻⁸

In addition to the parameters of the welding process (time, pressure and speed), a significant impact on the quality of the achieved connection between Al and Cu is also made by the contact surfaces.^{9,10} The preparation of the bonding surfaces is of special importance since each type of surface impurities may disturb the required quality level of the joint.¹¹ Due to the tendencies of Al and Cu to oxidize under ambient conditions,¹²⁻¹⁴ it is recommended that the cleaning of the contact surfaces of these metals should be performed immediately before the welding procedure. In addition to the superficial impurities, the quality of an Al/Cu joint may be affected by the impurities present in the volumes of Al and Cu, which, apart from affecting the conductivity of the basic materials, might also induce a production of various compounds at the very joint during the welding procedure, subsequently increasing the local contact resistance upon applying the Al/Cu bonding elements.

The greatest advantages of the friction-welding procedure over the other procedures are a low power consumption and a short duration of the procedure.¹⁵ On the other hand, its greatest shortcoming is the fact that the bonding is achieved only within a narrow scope of the welding parameters. Therefore, all of these parameters may easily be exaggerated, which might lead to the occurrence of intermetallic phases affecting the joint strength and its electrical conductivity.^{9,16} The bonding elements produced during the friction-welding procedure are divided into three product families: bimetallic Al-Cu butt connectors (**Figure 2a**)¹, bimetallic Al-Cu cable lugs (**Figure 2b**)¹ and bimetallic Al-Cu bolt connectors (**Fig-**

ure 2c).⁴ These product families are different from one another in terms of the construction intended for particular types of use. The lugs are used in substations in the process of connecting Al cables to Cu busbars, the Al/Cu bolt connectors are used for cable endings, and the connectors are used for the continuation of an Al to a Cu cable and vice versa. Each of the three types of products was manufactured in several standard sizes depending on the diameter of the cable and voltage.

The objective of this paper is to evaluate the effects of the friction-welding parameters (time, pressure and speed) on the morphological properties of an Al/Cu joint, i.e., to define the parameters, at which a flat surface of the Al/Cu joint is produced. The joint is made by continuous friction welding, of the samples shaped as cylindrical bars. The samples were prepared on the basis of the standard procedure, under industrial conditions and within a serial production.

2 EXPERIMENTAL PART

The materials whose bonding was performed by friction welding were Cu and Al cylindrical bars. The Cu bars, with a 99.99 % purity and dimensions of $\varnothing 22 \times 60$ mm, were produced by cutting pieces of the Cu cathode and subsequently shaping them, with forging, on an eccentric press. After the forging, Cu bars were thermally treated for 30 min at 300 °C in the air atmosphere; then they were taken out of the furnace and cooled in the ambient air under standard conditions and at room temperature. The Al bars, with a 99.5 % purity and dimensions of $\varnothing 25 \times 90$ mm, were produced by cutting pieces from the bars of 6 m in length. These dimensions match the standard dimensions of the samples for bimetallic connectors for medium voltage (1–35 kV).

Friction-welding contact surfaces, i.e., Al/Cu cylinder bases were prepared on a lathe with the machine treatment, with the aim of eliminating the present oxides and other impurities that might have significantly impeded the quality of the bimetallic joint.⁵ Such a method of preparing friction-welding surfaces was chosen since it is most frequently applied under real industrial conditions.

Friction welding was performed on a machine, produced in the Cable Factory (FKS) in Jagodina, in the production facility producing cable accessories. This machine has two sample carriers, facing each other and controlling the process of welding. One carrier is enabled to rotate around its axis, while the other has the possibility of translation in the axial direction. As a result, during the process of friction welding, there is a possibility of a simple control of the rotational speed through the first carrier, and also the control of the operating pressure through the other carrier. In this probe, the Al rod is positioned on the rotating carrier, while the Cu rod is on the carrier allowing axial movements. The rods are brought into contact and adjusted across the

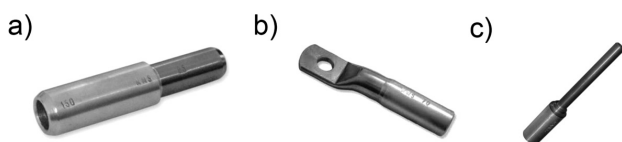


Figure 2: Examples of the Al-Cu bonding elements produced with friction welding: a) bimetal Al-Cu butt connector, b) bimetal Al-Cu cable lug, c) bimetal Al-Cu bolt connector¹

Slika 2: Vzorci spojenih Al-Cu elementov, izdanih s postopkom tornega varjenja: a) bimetalni Al-Cu valjasti priključek, b) bimetalni Al-Cu kabelski priključek, c) bimetalni Al-Cu sorniški priključek¹

cylinder axes to ensure the maximum contact of the work surfaces and achieve approximately the same quality of the joint across the entire work surface.

The procedure of friction welding was performed in two short consecutive phases. The first phase was achieved by reaching an operating pressure of $P_1 = 32\text{--}48$ MPa (depending on the sample) on the work surface of the rotating Al rod by translating the Cu rod in the axial direction. The Al rod rotated with the initial rotation speed of 1500 min^{-1} . After the first phase, during which the heat was generated due to the contact-area friction, in the second phase, an additional Cu injection to the rotating Al rod was conducted under a pressure of $P_2 = 0\text{--}160$ MPa. The first phase was executed within a period of $\Delta t_1 = 1.5$ s, whereas the other took an interval of $\Delta t_2 = 4$ s. The temperature in the zone of the material bonding was measured during the welding using a FLIR thermal imaging camera with a shooting range within a temperature interval from $0\text{--}350$ °C. Due to the reproducibility of the tests of the microstructural and morphological properties of the Al/Cu bimetallic joints, acquired in the described regimes of friction welding, at least five joints were produced with each of the four chosen regimes (**Figure 3a**).

The diameter of the sample in **Figure 3a** was reduced to $\varnothing 20$ mm along the entire sample length. The subsequent slow cutting of the basic materials (Cu and Al) was performed in the transverse direction using a water-cooled saw at a distance of approximately 10 mm from an Al/Cu bimetallic joint. The samples obtained this way were cut (halved) along the axis of the cylinder using the same procedure, with which the relevant surfaces for examining the morphology of the Al/Cu joints were obtained. For the needs of the microscopic examination, the further preparation of the relevant surfaces also included the hot mounting process, grinding and polishing (Goša Institute Ltd.). One half of each sample was mounted in bakelite with a graphite filling using the hot mounting procedure, with the face area of the relevant surface facing upwards. The hot mounting procedure lasted for 20–30 min per sample and it was performed at a temperature of $100\text{--}120$ °C and under a pressure of 5–6

bar. Grinding was performed using waterproof SiC abrasive papers P-120, P-240, P-400, P-800, P-1000, P-1500 and P-2000 with abundant amounts of water. Polishing was performed using Al_2O_3 suspensions with the average particle diameter of $1\text{ }\mu\text{m}$.

The microstructural and morphological properties of the Al/Cu bimetallic joints were examined with a scanning electron microscope (SEM). The SEM analysis was performed at the Faculty of Mining and Geology at the University of Belgrade using a JEOL JSM-6610LV microscope connected to an INCA350 energy-dispersive-spectroscopy unit for the X-ray analysis (EDS). The electron-acceleration voltage applied during the examination was 20 kV, while the electron source was a filament made of tungsten. For observing a possible presence of porosity, secondary electrons were used, while the differences in the chemical content were observed using back-scattered electrons and EDS analyzers. Prior to the SEM-EDS analysis, all of the samples were cleaned in ethanol and acetone using an ultrasonic bath, with the aim of eliminating the residual impurities from the previous phases of the sample preparation.

3 RESULTS AND DISCUSSION

In the friction-welding procedure, the bond between Al and Cu is made due to the interdiffusion of the atoms belonging to these metals through the Al/Cu border surface. In this paper, the interdiffusion was detected with the EDS analysis. It was noticed that Al and Cu do not diffuse each other to the same extent; at the same distance from the interface, the Cu concentration in the Al basis was always larger than the Al concentration in the Cu basis (**Figures 4a** and **4b**). The most probable reason for the larger concentration of Cu is the fact that the activation enthalpy of the Cu bulk diffusion in Al ($Q = 136\text{ kJ/mol}$)¹⁷ is smaller than the one required for the Al diffusion in Cu ($Q = 165\text{ kJ/mol}$).¹⁸

3.1 Effects of the speed

With an increase in the distance from the rotation axis, the speed also increases. The points at large distances from the rotation axis cross longer distances because they have longer routes than the points closer to the axis ($s = r \cdot \varphi / 2 \cdot \pi$) and thus a greater wear of the con-

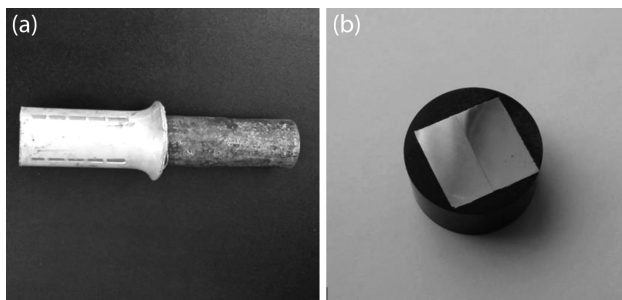


Figure 3: Representative appearance of an Al/Cu bimetallic joint immediately after: a) the friction-welding process and b) after the preparations for metallographic observations

Slika 3: Značilen izgled bimetalnoga spoja Al/Cu, takoj po: a) postopku tornega varjenja in b) po pripravi za metalografijo

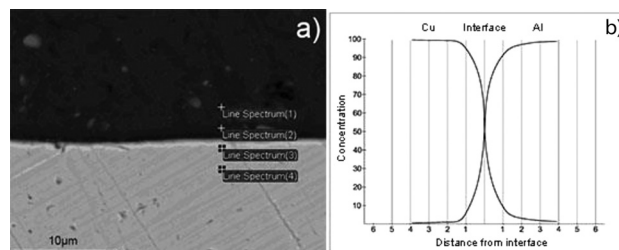


Figure 4: EDS analysis along the axis of an Al/Cu sample
Slika 4: EDS-analiza vzdolž aksialne osi vzorca Al/Cu

tact surfaces occurs at the large distances from the rotation axis. **Figures 5a to 5c** show the appearance of the Al/Cu interface of sample 1.

By comparing **Figure 5a**, where the appearance of the interface close to the rotation axis is shown, with **Figure 5b**, where the appearance of the interface at the mid-distance between the rotation axis and the sample edge is shown, and **Figure 5c**, where a joint close to the sample edge is shown, the trend of an increased wear of the surface roughness at the copper part, caused by the lathe preparation of the contact surfaces, can be clearly seen. In **Figures 5d to 5f** the appearance of the interface at the mid-distance between the axis and the sample edge and close to the edge of sample 3, produced under a different regime, is shown. For this sample, the trend of a decreasing surface roughness at the interface, from the rotation axis towards the sample edge, was noticed, proving that such a phenomenon does not depend on the

regimes of the applied friction-welding parameters, but instead, it is a typical occurrence in the friction-welding process.

3.2 Effects of the operating pressure

The aim of the operating pressure is to provide friction for producing the heat necessary for the inter-diffusion of the Al and Cu atoms as well as for realizing the Al/Cu bimetallic connection.⁵ In **Figures 6a** and **6b**, representative microstructural presentations of the Al/Cu bimetallic-joint morphologies are given for the middle and peripheral parts of sample 1, produced by the effects of the operating pressure of $P_R=32$ MPa in the period of $t_R = 1.5$ s, without the application of the forging pressure ($P_U = 0$, $t_U = 0$). **Figures 6c** and **6d** show the morphologies of the joint at the middle and peripheral parts of sample 2, respectively, produced with the operating

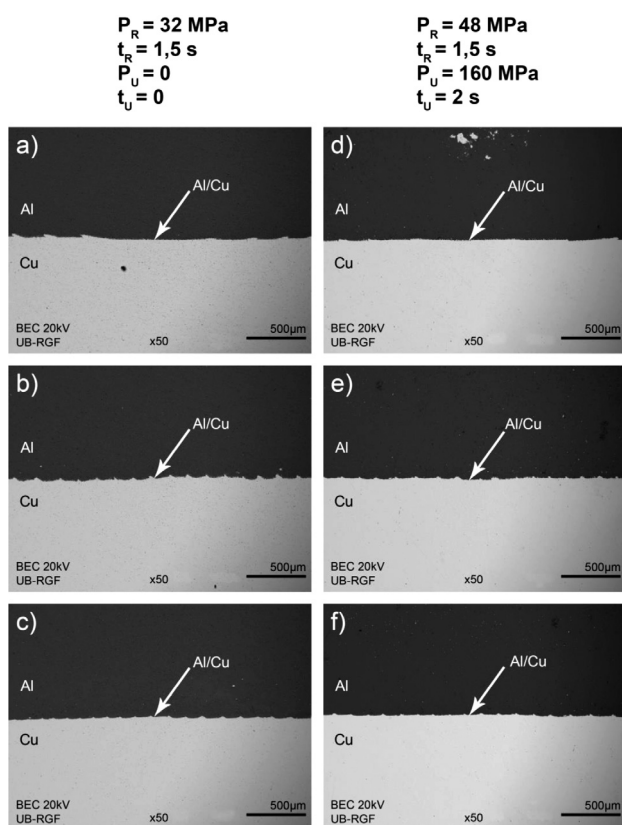


Figure 5: Appearance of the longitudinal cross-section of an Al/Cu bimetallic joint produced by friction welding: a) appearance of the joint of sample 1 close to the rotation axis, b) appearance of sample 1 at the mid-distance between the rotation axis and the sample edge, c) appearance of the sample 1 joint very close to the sample edge, d) appearance of sample 3 close to the rotation axis, e) appearance of sample 3 at the mid-distance between the rotation axis and the sample edge, f) appearance of sample 3 very close to the sample edge

Slika 5: Izgled vzdolžnoga prereza bimetalnoga spoja Al/Cu, izdela-nega s tornim varjenjem: a) izgled spoja vzorca 1, blizu osi rotacije, b) izgled vzorca 1 na sredini med rotacijsko osjo i robom vzorca, c) izgled spoja v vzorc 1, blizu roba vzorca, d) izgled vzorca 3, blizu rotacijske osi, e) izgled vzorca 3 na sredini razdalje med osjo rotacije i robom vzorca, f) izgled vzorca 3, blizu roba vzorca

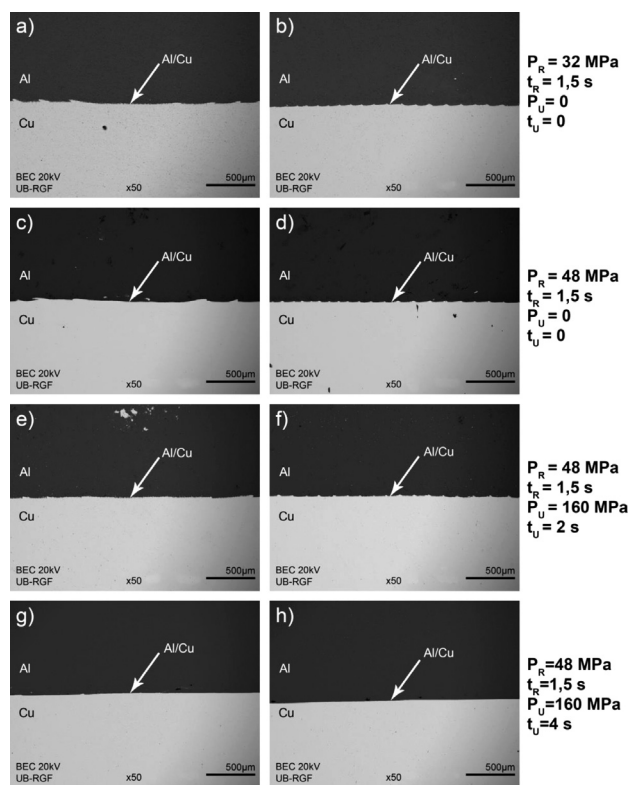


Figure 6: Appearance of the longitudinal cross-section of an Al/Cu bimetallic joint produced by friction welding: a) appearance of the joint of sample 1 close to the rotation axis, b) appearance of sample 1 very close to the sample edge, c) appearance of the sample 2 joint close to the rotation axis, d) appearance of sample 2 very close to the sample edge, e) appearance of sample 3 close to the rotation axis, f) appearance of sample 3 very close to the sample edge, g) appearance of sample 4 close to the rotation axis, h) appearance of sample 4 very close to the sample edge

Slika 6: Izgled vzdolžnoga prereza bimetalnoga spoja Al/Cu, izdela-nega s tornim varjenjem: a) izgled spoja vzorca 1, blizu rotacijske osi, b) izgled spoja vzorca 1, blizu roba vzorca, c) izgled spoja vzorca 2, blizu rotacijske osi, d) izgled spoja vzorca 2, blizu roba vzorca, e) izgled vzorca 3, blizu rotacijske osi, f) izgled vzorca 3, blizu roba vzorca, g) izgled vzorca 4, blizu rotacijske osi, h) izgled vzorca 4, blizu roba vzorca

pressure, increased by 50 % when compared to the operating pressure for sample 1.

By comparing the morphologies of the joint presented in **Figures 6a** and **6b** with the morphologies presented in **Figures 6c** and **6d**, it is noticeable that the roughness of the interface, resulting from the lathe preparation of the contact surfaces of sample 2, is slightly lower than the roughness for sample 1. This indicates that the increase in the operating pressure of up to 50 % during the rotation without forging did not significantly affect the change of the original morphology of the joint. The reason for this is the fact that the applied operating pressure was most probably lower than the pressure required for causing the deformation and change of the Al/Cu interface shape in the friction-welding process.

It should also be mentioned that the operating pressure, increased by 50 % reached 48 MPa, while the yield strength required for the deformation of pure Cu within an interval of 300–400 °C was of a similar order of magnitude (**Figure 7**).¹⁹ This means that the applied operating pressure could, in theory, deform the pure copper at the temperatures reached during the friction-welding process. However, the purity of the Al/Cu joint probably exceeds the mentioned strength of the pure Cu since the material in the vicinity of the joint most probably becomes stronger due to the dissolution in the process of friction welding.²⁰ The strengthening caused by the dissolution occurs due to the interdiffusion of the Al and Cu atoms, as proven to occur in the process (**Figure 4**).

It is known that the substitutional solid solutions with a face-centered cubic lattice, such as the solid Cu solution in Al and Al in Cu, show a prominent dependency on the strengthening by dissolution, even at increased

temperatures, since the dissolved atoms affect the thermal component of the Peierls-Nabarro stress.²⁰ Aside from this, it should be mentioned that the effect of the strengthening by dissolution also significantly depends on the atomic size, the relative size of the modulus of elasticity, as well as on the relative valence.²⁰ In **Figure 4**, it can be noticed that the amount of dissolved atoms increases towards the interface, meaning that the effect of the strengthening by dissolution was the largest precisely on the interface of the Al/Cu joint.

To define the friction-welding parameters, due to which the interface is deformed and a joint without the lathe-induced roughness is obtained, in addition to the operating pressure (P_R), further examinations also included the additional effect of the forging pressure (P_U). The additional introduction of the forging pressure P_U that is significantly larger than the pure-Cu yield strength was necessary for causing the change in the Al/Cu interface within a short interval, which is longer than in the case when friction welding is performed under the operating-pressure effects.

3.3 Effects of the forging pressure

The forging pressure during the continuous friction welding starts to apply at the moment of the termination of the rotation.¹⁰ Its role is to squeeze out all the impurities from the bonding area and to create a strong bond.

Figures 6e and **6f** show the formations of the bond of sample 3 in the center and very close to the sample edge. The production regime of sample 3 is different from the sample 2 regime: after the termination of the operating-pressure effects P_R , the forging-pressure effects of $P_U = 160$ MPa start to be effective in a duration of $t_U = 2$ s. By comparing **Figure 6e** with **6c** and **Figure 6f** with **6d**, a significant decrease in the roughness of the Al/Cu interface is noticed. Even though the operating pressure did not significantly affect the morphology of the joint, it is evident that it provides a sufficient amount of heat by friction, causing a noticeable change in the shape of the Al/Cu bimetallic joint forged under the pressure of 160 MPa.

Figures 6g and **6h** show the morphology of the sample 4 joint formed in the middle and peripheral parts relative to the rotation axis. Sample 4 was produced in a time twice as long as the time for the forging-pressure effects of $t_U = 4$ s spent for obtaining sample 3. When comparing **Figures 6g** and **6h** to **Figures 6e** and **6f**, an almost complete absence of the roughness of the Al/Cu interface is noticeable in **Figures 6g** and **6h**. This confirms the importance of the forging time as in the duration of $t_U = 4$ s a much larger deformation of the Al/Cu interface is formed than under the forging-pressure P_U effects in the duration of $t_U = 2$ s.

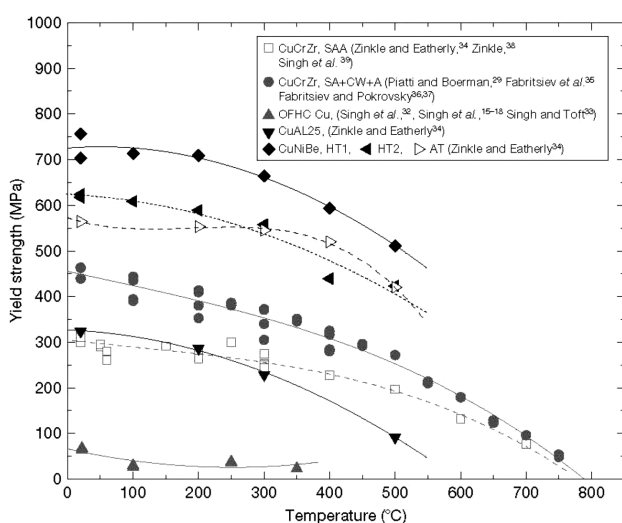


Figure 7: Changes in the yield-strength values of copper and its alloys depending on the temperature¹⁹

Slika 7: Sprememba vrednosti meje tečenja pri bakru in njegovih zlitinah, odvisno od temperature¹⁹

4 CONCLUSIONS

By increasing the distance from the rotation axis, the wear of the contact surfaces increases as well. Such an occurrence is noticed in various combinations of friction-welding parameters, thus proven to be a property of the process.

The effect of the operating pressure of 48 MPa does not significantly affect the shape of the Al/Cu interface during the first phase of bonding, but it provides a sufficient amount of heat for the interdiffusion of the atoms of the Al and Cu metals, taking place in short-term intervals of the friction-welding process.

The combined effect of the operating pressure of 48 MPa and the forging pressure of 160 MPa changes the shape of the Al/Cu interface.

The forging time for the combined effect of the pressures significantly affects the morphology of an Al/Cu joint within a very narrow time interval. After 2 s of forging, the superficial roughness caused by the lathe preparation is still obvious, but immediately after 4 s of forging, the Al/Cu interface becomes almost completely flat, i.e., without the presence of the roughness caused during the lathe preparation of the surfaces.

5 REFERENCES

- ¹ <http://www.mms-jagodina.com>
- ² <http://www.feman.net>
- ³ <http://www.elliottelectric.com>
- ⁴ <http://www.marel.rs>
- ⁵ N. Ratković, A. Sedmak, M. Jovanović, V. Lazić, R. Nikolić, B. Krstić, Quality Analysis of Al-Cu Joint Achieved by Friction Welding, *Technical Gazette*, 16 (2009) 3, 3–7
- ⁶ W. Kinley, Inertia Welding: Simple in Principle and Application, *Welding and Metal Fabrication*, (1979), 585–589
- ⁷ N. I. Fomichev, The Friction Welding of New High Speed Tool Steels to Structural Steels, *Welding Production*, (1980), 35–38
- ⁸ K. G. K. Murti, S. Sundaresan, Parameter Optimisation in Friction Welding Dissimilar Materials, *Metal Construction*, 15 (1983) 6, 331–335
- ⁹ M. Sahin, Friction Welding of Different Materials, UNITECH – International Scientific Conference, Bulgaria, Gabrovo, 2010, 131–134
- ¹⁰ M. Sahin, C. Misirli, Mechanical and Metallurgical Properties of Friction Welded Aluminium Joints, *Aluminium Alloys - New Trends in Fabrication and Applications*, InTech, Rijeka 2012, 277–300, doi:10.5772/51130
- ¹¹ R. N. Shubhvardhan, S. Surendran, Friction Welding to Join Dissimilar Metals, *International Journal of Emerging Technology and Advanced Engineering*, 2 (2012) 7, 200–210
- ¹² M. J. Freiria Gándara, Aluminium: The Metal of Choice, *Mater. Technol.*, 47 (2013) 3, 261–265
- ¹³ G. Papadimitropoulos, N. Vourdas, V. Em Vamvakas, D. Davazoglou, Deposition and Characterization of Copper Oxide Thin Films, *Journal of Physics: Conference Series*, 10 (2005), 182–185, doi:10.1088/1742-6596/10/1/045
- ¹⁴ P. Keil, D. Lützenkirchen-Hecht, R. Frahm, Investigation of Room Temperature Oxidation of Cu in Air by Yoneda-XAFS, *AIP Conference Proceedings*, 882 (2007), 490–492, doi:10.1063/1.2644569
- ¹⁵ V. I. Vill, Friction Welding of Metals, AWS, New York 1962
- ¹⁶ M. Sahin, Joining of Aluminium and Copper Materials with Friction Welding, *International Journal of Advanced Manufacturing Technology*, 49 (2010) 5–8, 527–534, doi:10.1007/s00170-009-2443-7
- ¹⁷ E. A. Brandes, G. B. Brook, *Smithells Metals Reference Book*, 7th ed., Butterworth-Heinemann, Oxford 1992, 13.16
- ¹⁸ D. R. Askeland, P. P. Fulay, *The Science and Engineering of Materials*, 5th ed., Thomson, New York 2006, 152
- ¹⁹ M. Li, S. J. Zinkle, Physical and Mechanical Properties of Copper and Copper Alloys, *Comprehensive Nuclear Materials*, 4 (2012), 667–690, doi:10.1016/B978-0-08-056033-5.00122-1
- ²⁰ Đ. Drobňak, Fizička Metalurgija – Fizika Čvrstoće i Plastičnosti 1, TMF, Beograd 1990, 207–215

CHARACTERISATION OF THE MECHANICAL AND CORROSIVE PROPERTIES OF NEWLY DEVELOPED GLASS-STEEL COMPOSITES

KARAKTERIZACIJA MEHANSKIH IN KOROZIJSKIH LASTNOSTI NOVO RAZVITIH KOMPOZITOV STEKLO-JEKLO

**Olga Lyubimova¹, Ekaterina Gridasova², Alexander Gridasov², Gerrit Frieling³,
Martin Klein³, Frank Walther³**

¹Department of Mechanics and Mathematical Modeling, Far Eastern Federal University (FEFU), Vladivostok, Russia

²Department of Welding Production, Far Eastern Federal University (FEFU), Vladivostok, Russia

³Department of Materials Test Engineering (WPT), TU Dortmund University, Dortmund, Germany
gerrit.frieling@tu-dortmund.de

Prejem rokopisa – received: 2014-12-17; sprejem za objavo – accepted for publication: 2015-02-17

doi:10.17222/mit.2014.305

This paper presents a preliminary research about a newly developed glass-steel composite created with diffusion welding of glass (C49-1) and carbon steel (St3sp). The main conclusions on the process of forming a diffusion zone during the welding of glass and steel are made. The results of quasi-static and cyclic mechanical tests and corrosion investigations are presented and interpreted on the basis of the microstructure developed during diffusion welding and described in this article.

Keywords: hardening of glass, diffusion welding, glass-steel composite material, tensile tests, cyclic tests, fatigue, corrosion, microstructure

Članek predstavlja uvodne raziskave novo razvitega kompozita steklo-jeklo, izdelanega z difuzijskim varjenjem stekla (C49-1) in ogljikovega jekla (St3sp). Postavljeni so glavni zaključki o postopku nastajanja difuzijske cone med varjenjem stekla in jekla. Na osnovi razvoja mikrostrukture pri difuzijskem varjenju so predstavljeni in razloženi rezultati kvazi statičnih, cikličnih mehanskih in korozijskih preizkusov.

Ključne besede: utrjevanje stekla, difuzijsko varjenje, steklo-jeklo kompozitni material, natezni preizkusi, ciklični preizkusi, utrujenost, korozija, mikrostruktura

1 INTRODUCTION

Glass shows a diverging behavior for different kinds of deformation. On the one hand, it has a relatively high compressive strength; however, on the other hand, it has a relatively low tensile strength. The values for the compressive strength of glass are in the range of 500–1250 MPa. So, when working in the compressive mode, glass can compete with the structural-grade carbon steel. At the same time, the tensile strength of glass is much lower: 30–50 MPa.^{1,2} This is due to the fact that the strength of glass is largely dependent on the state of its surface. The most well-known methods for the hardening of glass allow the creation of compressive stresses in the surface layers of glass (glass hardening, ion exchange, surface crystallization) and surface hardening (mechanical polishing, removal of the defective surface layer by etching the glass, application of protective coatings). It is proposed to study the methods, which allow the hardening of glass by eliminating not only the surface micro-defects but also the internal micro-defects, as well as providing insulation from the effects of the environment.^{3,4} As a result, the composite material would be larger and stronger. Diffusion welding⁵ is used widely for joining the elements of simple configuration. It finds

a wide application in electronics, aviation and other industries. However, despite the extensive study of the mechanism interaction of various materials during the diffusion welding, a general theory about the relationship between glass and metal has not yet been developed.

The aim of this study is to investigate the mechanical and corrosive properties of this newly developed glass-steel composite material. Therefore, quasi-static, cyclic and potentiodynamic polarization tests are carried out. Furthermore, light microscopic studies are performed to build the basis for microstructure-oriented assessments of the mechanical and chemical results.

2 EXPERIMENTAL METHODS

2.1 Processing of glass-metal composites

The rod was made as illustrated in **Figure 1a**. The mobile cover (3) provides holes for gas outlets and the possibility for a forward movement along the longitudinal axis of the shell (2). The movement of the cover (3) is dependent on the shrinkage of the rod (1) during the heating process.

The technological regime (pressure during diffusion bonding $p = 0.25$ MPa) is divided into six stages (**Figure**

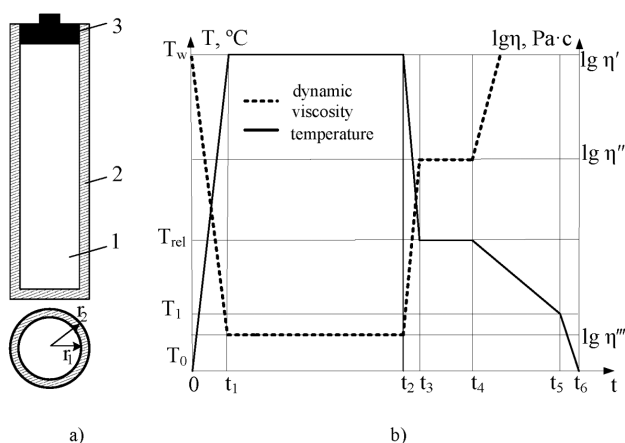


Figure 1: a) Schematic view of a composite rod: 1 – rod of glass C49-1 (3C5Na), 2 – outer shell of steel St3sp, 3 – mobile cover, b) temperature welding: T – temperature welding, $\lg \eta$ – logarithm of the dynamic viscosity of glass

Slika 1: a) Shematski prikaz kompozitne palice: 1 – palica iz stekla C49-1 (3C5Na), 2 – zunanji ovoj iz jekla St3sp, 3 – premični pokrov, b) temperaturno varjenje: T – temperaturno varjenja, $\lg \eta$ – logaritem dinamične viskoznosti stekla

1b). In the first step, which corresponds to the interval $(0, t_1)$, the composite rod is heated from $T_0 = 20^\circ\text{C}$ to the temperature of welding T_w (around 800°C). Given the limited deformation ability of glass to produce a lasting connection, $T_w = T_g$, where $T_w = (0.4 \dots 0.6) T_m$, with T_g as the temperature of glass softening and T_m as the temperature of the melting metal from which the shell (2) was made. In the interval (t_1, t_2) , T_w is maintained, providing a reliable connection between glass and steel. It is then cooled down to the temperature of annealing T_{rel} . To reduce the initial stress, the annealing is carried out in the interval (t_3, t_4) . This is a necessity at such temperatures, as the viscosity is still quite low, for example, $\eta'' = 10^{12} \text{ Pa s}$; the residual stresses are removed after 15 min and, with $\eta'' = 10^{13.5} \text{ Pa s}$, after 4 h. In the interval (t_4, t_5) , the required cooling is carried out up to T_1 , with a rate of 3–5 K/min. After $\eta' \approx 10^{15} \text{ Pa s}$, the residual stresses in the glass do not disappear so that at the last stage – the sixth stage – a more rapid cooling at 15–25 K/min is possible.

2.2 Microscopy

The microstructure of the hybrid material was investigated with light microscopy. Therefore, slices of the specimen were cut off using a cutting wheel. Before using a microscope, these slices were cold mounted, ground and polished.

2.3 Tensile and fatigue testing

The quasi-static properties with respect to the compression, tension and torsion of the glass-metal composite, consisting of chemical-laboratory glass brand C49-1 (3C-5Na) and carbon steel St3sp, were determined using a tensile testing system (Shimadzu, 1000 kN, UH-I)



Figure 2: Tensile testing system Shimadzu 1000 kN UH-I

Slika 2: Natezni preizkuševalni sistem Shimadzu 1000 kN UH-I

(**Figure 2**). Glass C49-1 has the following chemical composition: 67.5 % SiO_2 ; 20.3 % B_2O_3 ; 3.5 % Al_2O_3 ; 8.7 % Na_2O .

Carbon steel St3sp comprises the following quantities of the alloying elements: 0.14–0.22 C; 0.15–0.30 Si; 0.4–0.65 Mn; ≤ 0.05 S; ≤ 0.04 P; ≤ 0.3 Cr; ≤ 0.3 Ni; ≤ 0.3 Cu; ≤ 0.08 As; ≤ 0.01 N.

The geometries of the specimens and their dimensions are shown in **Figure 3** and **Table 1**, respectively.

Table 1: Geometrical characteristics of the specimens, in mm

Tabela 1: Geometrijske značilnosti vzorcev, v mm

d	l_0	l	D	h	r	l_g	d_g	h_g
10.0	100.0	105.0	16.0	10.0	3.0	105.0	7.5	30.0

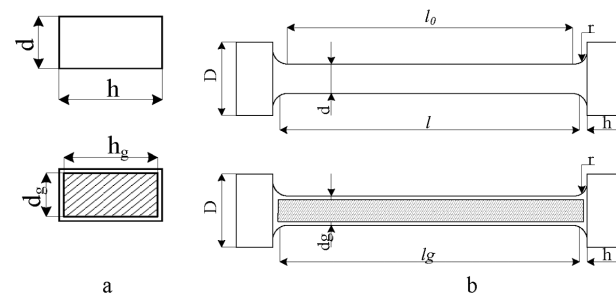


Figure 3: Geometries of the specimens for: a) compression and b) tensile tests

Slika 3: Geometrija vzorcev za: a) tlačni preizkus in b) natezni preizkus

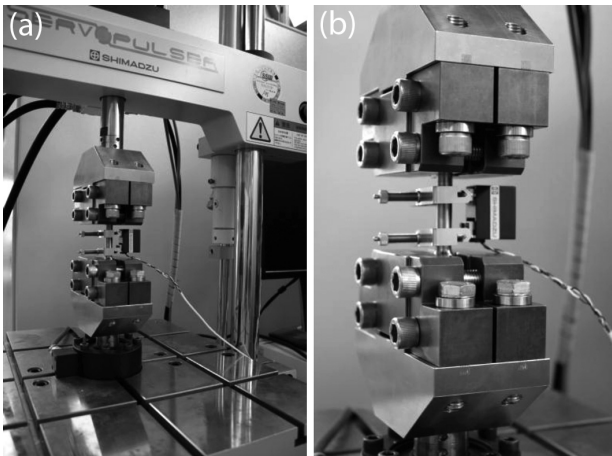


Figure 4: Fatigue testing system: a) overview and b) detail
Slika 4: Sistem za preizkušanje utrujanja: a) pregled in b) detajl

For the investigation of the fatigue behavior, load-increase tests and constant-amplitude tests were performed.^{6,7} The specimens were subjected to a stress ratio of $R = -1$ and a frequency of $f = 10$ Hz using sinusoidal load-time functions at room temperature. For the dynamic tests, the specimen geometry shown in **Figure 3b** was used. In order to measure the total strain and to determine the plastic-strain amplitude, an extensometer was attached to the specimen.

Figure 4 shows a specimen mounted onto the servo-hydraulic testing system (Shimadzu, 20 kN, EHF-LV20) with the attached extensometer. The testing system has the maximum load capacity of 20 kN and the extensometer has a range of ± 4.0 % of the total strain. The fatigue strength of the glass-metal composite rod for the ultimate number of cycles $N_{\text{limit}} = 2 \cdot 10^6$ was estimated with a stepwise load-increase test according to the

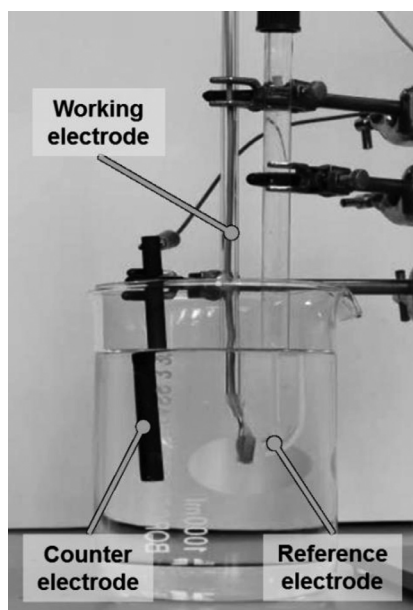


Figure 5: Potentiodynamic-polarization measurement set-up
Slika 5: Sistem za merjenje potenciodinamične polarizacije

measured material response and afterwards validated with constant-amplitude tests.

2.4 Corrosion testing

The corrosion behavior of the St3sp steel and of the hybrid interface was investigated with potentiodynamic polarization measurements in a 0.1 mol L^{-1} NaCl solution at pH7; the pH values were adjusted using a 0.1 mol L^{-1} KOH solution. A standard three-electrode system, consisting of a saturated calomel electrode (SCE) as the reference electrode and a graphite electrode as the counter electrode, was used for the measurements⁸. As the working electrodes, the St3sp steel and the cross-section of a round specimen (**Figure 3b**) for fatigue testing were used. The specimens were abraded with emery paper of $18\text{--}5 \text{ }\mu\text{m}$. Then, a copper wire was attached to the specimens and the whole specimens, except for their front sides, were embedded in the epoxy resin. Before each polarization measurement, the electrolyte was purged for 30 min with argon and afterwards the open-circuit potential was measured for 30 min. The measurements were conducted using a potentiostat (Gamry, PCI4300) at a scanning rate of 0.1 mV/s . The experimental set-up of the potentiodynamic-polarization measurements is shown in **Figure 5**.

3 RESULTS AND DISCUSSION

3.1 Microstructure

The St3sp steel was found to have a ferritic structure with around 8 % of pearlite. After polishing and analyzing the border-welding zones of the samples, there were still no visible cracks or voids. The analysis of micro-sections showed the presence of a full contact without cracks or spills in the welding zone (**Figure 6**). The microscopic examination of the welding zone clearly shows a development of the interaction at the boundary of the contact. A bright zone in the glass confirms this development. The results of the spectral analysis indicate a penetration of cations into the glass to a depth of 30 microns and more. This is in accordance with the results

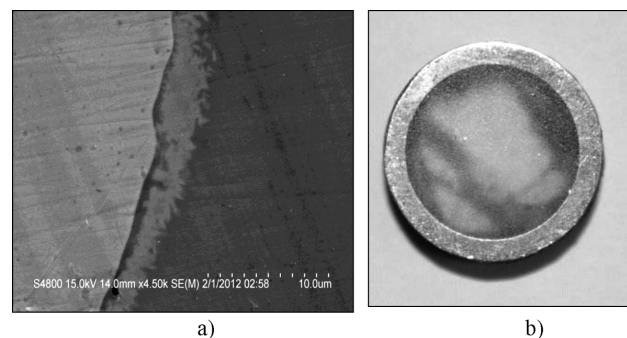


Figure 6: a) Micrograph of the welded joint between metal and glass, b) micrograph of the cross-section

Slika 6: a) Posnetek področja zvarjenega spoja med kovino in steklom, b) posnetek preseka

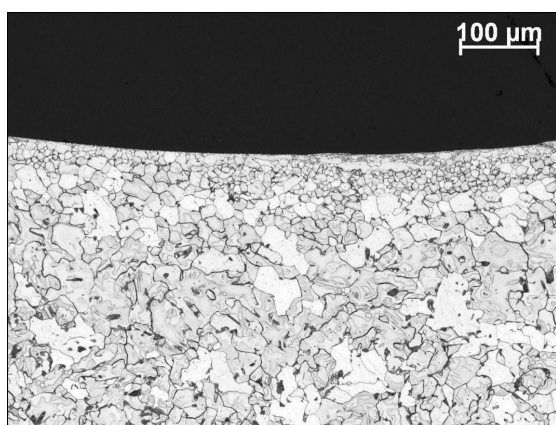


Figure 7: Micrograph of the grains in the transition area between steel and glass

Slika 7: Posnetek zrn v jeklu v prehodnem področju v steklo

of the corrosion tests, which also indicated the formation of the glass-metal phase.

Figure 7 shows the grains in the transition area between steel and glass. It is apparent that the grain size of the ferritic structure in close vicinity of the glass is smaller than at bigger distances. The explanation for this behavior has not been found yet, but it will be a topic of further investigations of this glass-steel composite material.

3.2 Deformation behavior

By performing the compression, tensile and torsional tests, the quasi-static properties of the selected glass, the steel and the glass-steel composite were determined. The stress-strain curves for compression and tension of the composite material are depicted in **Figure 8**. The results for different materials and tests are shown in **Tables 2** and **3**.

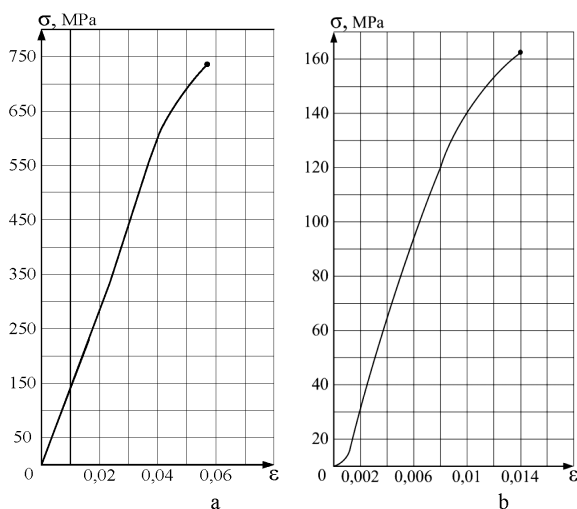


Figure 8: Stress-strain curve of the glass-metal composite for: a) compression and b) tension

Slika 8: Krivulja napetost – raztezek kompozita steklo-kovina pri: a) tlačnem in b) nateznem preizkusu

The maximum compressive stress of the composite material is more than 13 times higher than the maximum compressive stress of the C49-1 glass and it is twice as high as for the St3sp carbon steel. The maximum tensile stress of the composite sample is twice as much as that of glass and half of that of carbon steel. The Young's modulus and shear modulus of the composite have intermediate values of the modules of the base materials, glass and steel.

Table 2: Mechanical characteristics of base materials and glass-steel composite rod

Tabela 2: Mehanske značilnosti osnovnih materialov in kompozitne palice steklo-jeklo

		F_{\max}/kN	σ_{\max}/MPa
Glass (C49-1)	compressive strength	2.55	55.00
Glass (C49-1)	tensile strength	3.40	77.00
Steel (St3sp)	compressive strength	30.05	389.20
Steel (St3sp)	tensile strength	29.00	368.96
Composite glass-steel	compressive strength	58.50	745.00
Composite glass-steel	tensile strength	12.70	162.00

Table 3: Mechanical characteristics of base materials and glass-steel composite rod

Tabela 3: Mehanske značilnosti osnovnih materialov in kompozitne palice steklo-jeklo

	Glass (C49-1)	Steel (St3sp)	Composite glass-steel
Young's modulus, (MPa)	$0.73 \cdot 10^5$	$2.10 \cdot 10^5$	$1.40 \cdot 10^5$
Shear modulus, (MPa)	$0.30 \cdot 10^5$	$0.80 \cdot 10^5$	$0.56 \cdot 10^5$

3.3 Fatigue behavior

For an evaluation of the cyclic-deformation behavior and for an estimation of the fatigue strength, a stepwise load-increase test was performed with a glass-metal composite specimen as depicted in **Figure 9**. During this test, the plastic-strain amplitude was measured as the parameter of the material reaction, which characterizes the proceeding fatigue damage as the basis for the estimation of the fatigue strength.⁹ The estimation of the fatigue strength was validated with constant-amplitude tests, whose lifetimes (the number of cycles to failure) are shown with the *S-N* curve.

Starting at $\sigma_{a,\text{start}} = 6.4$ MPa, the stress amplitude was increased by 6.4 MPa each 10^4 cycles until failure. The plastic-strain amplitude $\varepsilon_{a,p}$ increases slightly within the first nine steps, but remains almost constant within each step. In the tenth step, there is a visible increase compared to the ninth step, but the plastic-strain amplitude still does not increase within the step. This is different for the eleventh step at the stress amplitude of 70.4 MPa. In the twelfth step, there is a considerable increase of the

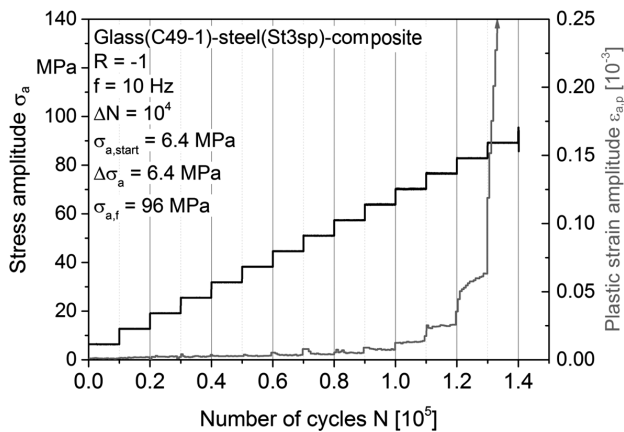


Figure 9: Stepwise load-increase test with a glass-metal composite
Slika 9: Preizkus stopničastega naraščanja obremenitve kompozita steklo-jeklo

plastic-strain amplitude and, finally, there is an exponential increase in the thirteenth step.

As the fatigue strength is linked to the first increase in the material-reaction quantity within one step,⁹ the estimate from this load-increase test for the endurance limit is 70 MPa. This estimation was validated with the constant-amplitude tests with $N_{\text{limit}} = 2 \cdot 10^6$ as the ultimate number of cycles. Ten tests with different stress amplitudes were conducted and the results are shown as an S - N curve in **Figure 10**. The highest stress amplitude used is 127 MPa, which is close to the tensile strength of 162 MPa (**Table 3**) for the glass-metal composite. The specimen with a load amplitude of 64 MPa reached the ultimate number of cycles without fracture.

For this set of specimens, the modified Basquin equation was found to be $\sigma_a = 245 \text{ MPa} (N_f)^{-0.09}$.

If the estimation of the fatigue strength from the load-increase test (70 MPa) is compared to the highest stress amplitude without failure (64 MPa), it becomes apparent that the estimation on the basis of the plastic-strain amplitude is a very suitable tool for this

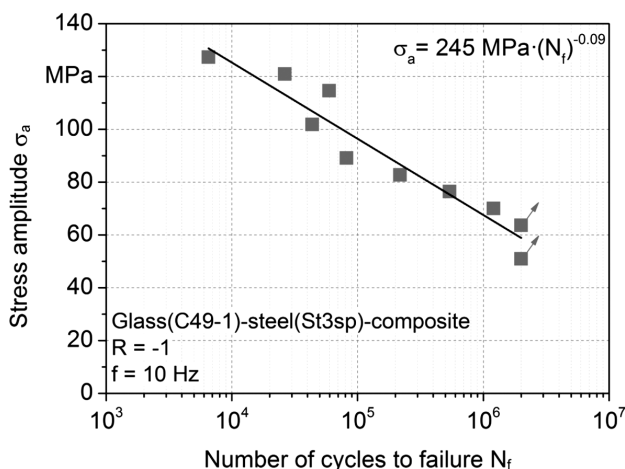


Figure 10: S - N curve for glass-steel composite
Slika 10: S - N -krivulja za kompozit steklo-jeklo

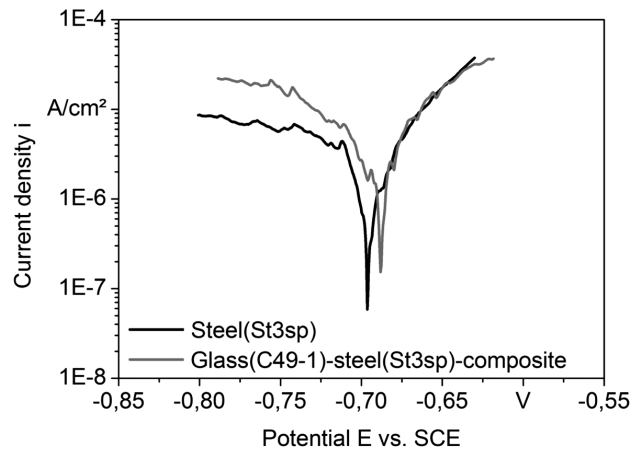


Figure 11: Tafel plots of the metal jacket and glass-steel composite
Slika 11: Taflov diagram kovinskega ovoja in kompozita steklo-jeklo

composite material, with only one specimen. The stress amplitude of the highest run-out specimen is about 40 % of the tensile strength of the composite material.

3.4 Corrosion behaviour

Figure 11 shows the Tafel plots for the steel jacket and the hybrid interface between glass and steel. The steel jacket shows a marginally less noble corrosion potential E_{corr} than the hybrid interface. However, the corrosion current density i_{corr} (i.e., the corrosion rate) of the glass-metal joint is approximately four times higher than that of the metal jacket. Consequently, the welding of glass and metal influences the corrosion resistance, suggesting that a glass-metal phase is formed through the welding process.

4 CONCLUSIONS

The formation of a glass-metal phase was determined with micrographs and corrosion tests. Furthermore, a dependency of the steel grains as a function of the distance to the transition zone was found. The newly developed glass-metal composite material has quasi-static properties, comparable to those of the St3sp steel. Using a stepwise load-increase test and constant-amplitude tests, the endurance limit of the composite was evaluated as 70 MPa. This value is about 40 % of its tensile strength. The corrosion rate of the composite material was ascertained to be four times higher than the corrosion rate of the St3sp carbon steel.

This glass-metal material has potential applications, especially for compressive loads, for example, in civil engineering. The analysis of the glass-metal phase, the examination of the grain-size distribution in the carbon steel near the transition zone as well as the mechanical investigations with a superimposed corrosive impact during the cyclic testing, i.e., corrosion-fatigue investigations, are planned as the further investigation steps.

Acknowledgements

The study was supported by the Federal Program "Nanosystems" Activity 1.2, contract № 14.575.21.0009, unique identifier ASR RFMEFI57514X0009.

5 REFERENCES

- ¹ V. P. Pukh, L. G. Baikova, M. F. Kireenko, L. V. Tikhonova, T. P. Kazannikova, A. B. Sinani, Atomic structure and strength of inorganic glasses, *Physics of the Solid State*, 47 (2005) 5, 876–881, doi:10.1134/1.1924848
- ² E. A. Gridasova, Increase of strength properties of glass as a result of metallization by diffusion welding, Ph. D. Dissertation, Vladivostok, 2013, 134
- ³ E. A. Gridasova, O. N. Lyubimova, K. N. Pestov, G. L. Kayak, Patent №2428389 RF, MPK C03C 27/02, Method of making steklo-metallokompozita – №2009149794, Zayav. 31.12.2009, Publ. 10.09.2011, Bul. № 25, 6
- ⁴ O. N. Lyubimova, E. A. Gridasova, Method of hardening during diffusion bonding of glass to the metal, *Welding and diagnostic materials*, 2010, № 6, 31–45
- ⁵ V. A. Bachin, Theory, technology and diffusion welding equipment – M: Mechanical Engineering, 1991, 352
- ⁶ F. Walther, Microstructure-oriented fatigue assessment of construction materials and joints using short-time load increase procedure, *MP Materials Testing*, 56 (2014) 7–8, 519–527, doi:10.3139/120.110592
- ⁷ F. Walther, D. Eifler, Cyclic deformation behavior of steels and light-metal alloys, *Materials Science and Engineering A*, 468–470 (2007), 259–266, doi:10.1016/j.msea.2006.06.146
- ⁸ P. Wittke, M. Klein, F. Walther, Corrosion Fatigue Behaviour of Creep-Resistant Magnesium Alloy Mg-4Al-2Ba-2Ca, *Procedia Engineering*, 74 (2014), 78–83, doi:10.1016/j.proeng.2014.06.228
- ⁹ P. Starke, F. Walther, D. Eifler, "PHYBAL": a short-time procedure for a reliable fatigue-life calculation, *Advanced Engineering Materials*, 12 (2010) 4, 276–282, doi:10.1002/adem.200900344

PHASE ANALYSIS OF THE SLAG AFTER SUBMERGED-ARC WELDING

ANALIZA FAZ V ŽLINDRI PRI OBLOČNEM VARJENJU POD PRAŠKOM

Marica Prijanovič Tonkovič¹, Jakob Lamut²

¹High Mechanical Engineering School, Šegova 112, 8000 Novo Mesto, Slovenia

²University of Ljubljana, Faculty of Natural Sciences and Engineering, Aškerčeva cesta 12, 1000 Ljubljana, Slovenia
marica.prijanovic-tonkovic@guest.arnes.si

Prejem rokopisa – received: 2015-01-16; sprejem za objavo – accepted for publication: 2015-03-04

doi:10.17222/mit.2015.014

The quality of a weld depends, to a large extent, on the filler material and type of welding. Welds and surfacing welds were produced with submerged-arc welding. The welding current was varied. The flux with a fineness of 0.2–1.8 mm was used. During the welding process, the welding flux melted and the liquid slag was formed. After the input of heat was stopped, the solidification of the slag began and different mineral phases started to precipitate. We found out that besides the basic constituents listed by the manufacturer of the welding flux, the alloying elements and deoxidizers from the flux and from the melt are also present in the slag. Based on these results, it can be concluded that in the case of reusing the welding slag for the production of welding flux, it is important to consider the composition of the welding slag.

Keywords: submerged-arc welding, welding flux, welding slag

Na kakovost zvara ima velik vpliv dodatni material ter postopek varjenja. Zvari in navari so bili izdelani po postopku varjenja pod praškom. Tok varjenja se je spreminjal. Uporabljen je bil varilni prašek, zrnatosti od 0,2 do 1,8 mm. Med varjenjem se je varilni prašek stalil in nastala je tekoča žlindra. Po končanem dovajanju toplote se je začelo strjevanje žlindre in v žlindri so se izločale različne mineralne faze. Ugotovili smo, da na mineralno sestavo žlindre vplivajo poleg osnovnih sestavin, ki jih navaja proizvajalec varilnega praška, tudi legirni elementi in dezoksidanti iz praška in iz taline. Na osnovi rezultatov preiskav sklepamo, da je pri ponovni uporabi varilne žlindre za izdelavo varilnega praška pomembno, da se upošteva tudi sestavo varilne žlindre.

Ključne besede: varjenje pod praškom, varilni prašek, žlindra po varjenju

1 INTRODUCTION

The quality of welds and surfacing welds depends on the chemical composition of the filler and base material as well as on the method of welding, determining the heat input which influences the development in the heat-affected zone and in the melt during the welding process. The slag, formed during the process of flux melting, plays an important role.¹ The slag accompanies the metal during the wire fusion and it covers the melt and protects it until it solidifies. The welding slag can be used again for the flux preparation.²

The important welding parameters are the welding current, the voltage and the speed of welding.³ If the current is too high, degassing in the weld is weak and cracks occur. Raising the current increases the depth of remelting the base material.⁴ Surfacing with a low welding current (450 A) is recommended in the case of using the alloyed agglomerated fluxes.⁵

Slag is formed during the melting of the fluxes that lead to the ionisation of the arc atmosphere and deoxidation of the melt, enable the passage of the alloying elements into the melting bath and prevent oxidation of carbon, manganese and silicon. Many types of welding fluxes are in use and they differ by the main mineral

content and the presence of metal additives.^{6–10} Recycled SAW slag can be used as a welding flux.⁸

For the investigations, the agglomerated flux labelled as FB 12.2,¹¹ suitable for reaching a high toughness in multipass welds, was used. The width of the heat-affected zone (HAZ) of steel OCR12 VM^{12,13} welded with the submerged-arc welding method depends on the welding current.¹⁴ **Figure 1a** shows the microstructure at the HAZ/weld border at a current of 470 A, and **Figure 1b** shows the effect of a current of 610 A. The mineral composition of the slag, formed during the welding process, was determined.

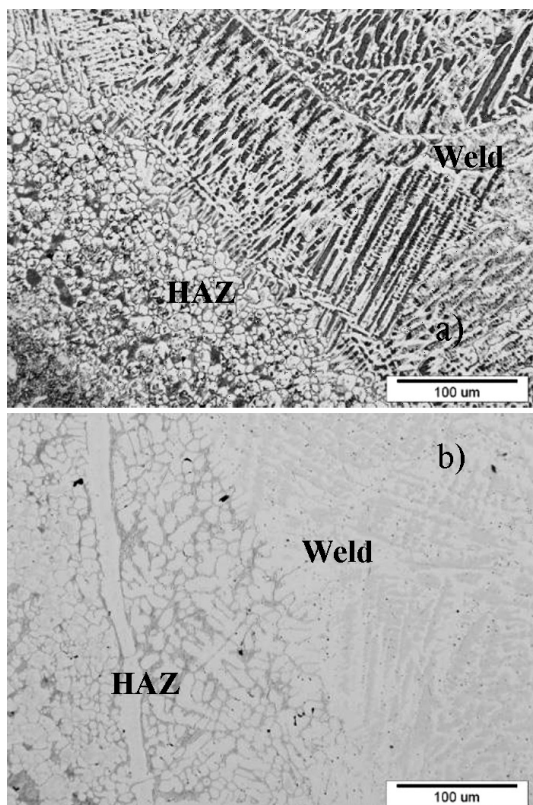
2 EXPERIMENTS

Four different welds were produced, two welds and two surfacing welds. **Figure 2a** presents a steel sample, used for welding. **Figure 2b** presents a surfacing weld. The welding was carried out on a device for submerged-arc welding made by Iskra. The chemical compositions of the welding pieces (steel OCR12 VM) and the filler material are presented in **Table 1**.

The applied basic welding flux¹¹ is used for automatic welding and surfacing of construction steels.

Table 1: Chemical composition of base steel and filler material**Tabela 1:** Kemijska sestava osnovnega jekla in dodatnega materiala

Type of material SIST EN 10027-2	Chemical composition (w/%)							
	C	Si	Mn	P	S	Cr	Mo	V
Welding piece: OCR12 VM (1.2379)	1.50	0.4	0.4	0.03	0.03	11.5	0.8	0.85
Filler material	0.08	0.35	1.4	/	0.03	5.0	0.85	/

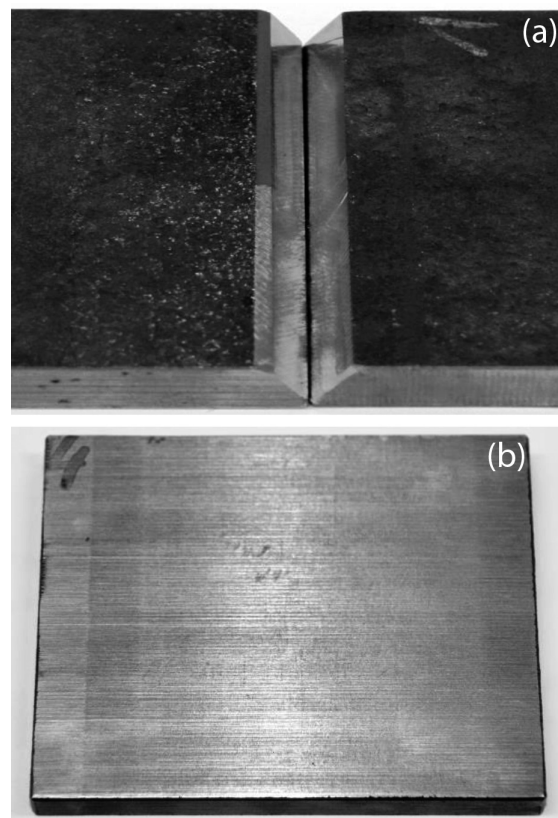
**Figure 1:** Microstructure of the weld on the HAZ/weld border with a current of: a) 470 A and b) 610 A**Slika 1:** Mikrostruktura zvara na meji CTV/zvar pri toku varjenja: a) 470 A in b) 610 A

The first joining of the welding pieces was performed with the MAG procedure. **Table 2** shows the welding parameters. The current and the voltage were varied during the welding process. The time of welding and the mass of the used welding flux were measured.

Table 2: Welding parameters**Tabela 2:** Parametri varjenja

Specimen	Wire diameter (mm)	Voltage (V)	Current (A)
Specimen 1 – weld	3.2	28	470
Specimen 2 – weld	3.2	27	610
Specimen 3 – surfacing weld	3.2	29	450
Specimen 4 – surfacing weld	3.2	28	628

The samples of the flux and slags were examined with metallography, scanning electron microscopy

**Figure 2:** Macro-shot of the welding piece for: a) weld and b) surfacing weld**Slika 2:** Makroposnetek varjenja za: a) zvar in b) navar

(SEM) of type JEOL JSM 5610 and analysed with electron dispersive spectroscopy (EDS) of type JEOL JSM 5610 and X-ray diffraction (XRD) of type PANalitical X'pert PRO.

3 WELDING-FLUX COMPOSITION

The agglomerated commercial basic welding flux of type FB 12.2 was used for the welding. The chemical composition of the welding flux (**Table 3**) and the basicity of the flux according to the Boniszewski index of 1.70 were taken from the catalogue.¹¹

For the microscopic investigation of the welding flux and welding slag, metallographic samples were prepared. After grinding and polishing, the samples were ready for the metallographic analysis. **Figure 3** shows a SEM image of a welding flux composed of non-metallic and metallic materials.

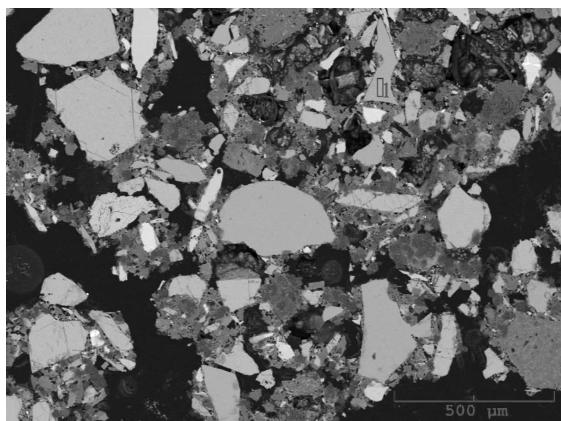


Figure 3: Microstructure of SAW flux

Slika 3: Mikrostruktura EPP praška

Table 3: Chemical composition of welding flux¹¹

Tabela 3: Kemijska sestava varilnega praška¹¹

Welding flux	Chemical composition (w/%)			
	SiO ₂ + TiO ₂	CaO + MgO	Al ₂ O ₃ + MnO	CaF ₂
FB 12.2	20	30	25	20

The distribution of the elements in the welding flux found with EDS is presented in **Figure 4**. The area where, on the EDS chart, aluminium overlaps with titanium aluminium oxide, which contains mass fractions of 1.5 % of titanium oxide, is presented.

The region where only calcium can be found indicates the presence of calcium fluorite CaF₂. Calcium overlapping with silicon is typical for calcium silicon (CaSi) and wollastonite (CaO·SiO₂). As expected, three elements – aluminium, silicon and potassium – overlap with the presence of aluminosilicate containing potassium.

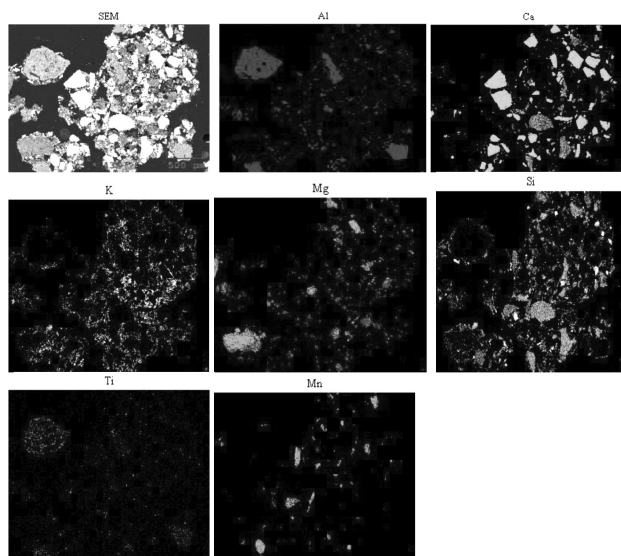


Figure 4: EDS distribution of elements; SEM; EDS

Slika 4: EDS-prikaz porazdelitve elementov; SEM; EDS

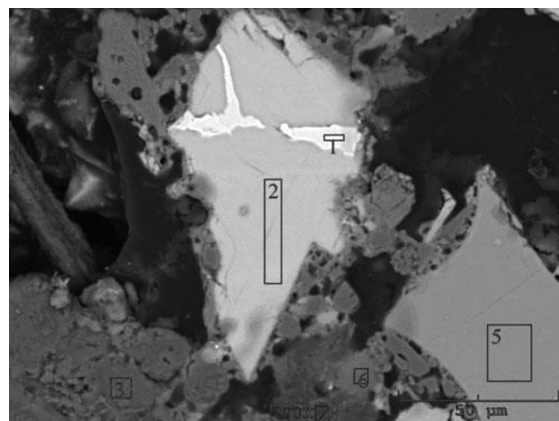


Figure 5: Microstructure of calcium silicon with a ferro-silicon inclusion

Slika 5: Mikrostruktura kalcij silicija z vključkom fero silicija

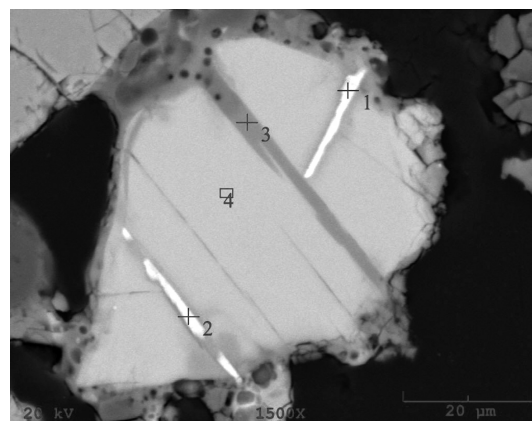


Figure 6: Microstructure of calcium silicon with included slag

Slika 6: Mikrostruktura kalcij silicija z vključkom žlindre

The presence of silico manganese (SiMn) in the welding powder indicates a distribution of manganese and silicon.

Figure 5 depicts the grains of calcium silicon (CaSi) that contain mass fractions of 46 % of calcium and mass fractions of 54 % of silicon and an inclusion of ferro-silicon with minimum amounts of $w(\text{Si}) = 45 \%$, $w(\text{Al}) = 2.7 \%$ and about $w(\text{Fe}) = 52 \%$. The calcium silicon grains have a slag inclusion from the production of calcium silicon (CaSi) (**Figure 6**).

Figure 7 presents an XRD diagram of the welding flux that shows the presence of aluminium and magnesium oxides (periclase) and calcium fluorite.

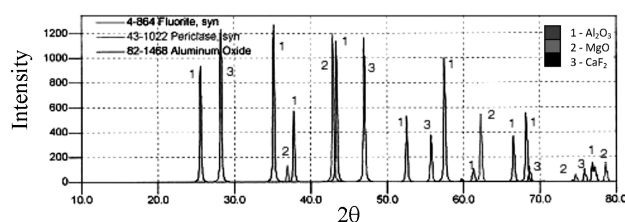


Figure 7: XRD of the welding flux FB 12.2

Slika 7: XRD-diagram varilnega praška FB 12.2

4 RESULTS AND DISCUSSION

4.1 Influence of the welding current on the welding-flux usage

During the process of welding, the welding flux melts and a liquid slag is formed. The arc is hidden in the liquid slag, which means that the welding procedure is welder friendly. The welding current influences the time of welding and the consumption of the welding flux. Different currents were applied during the welding procedures; the surfacing weld was welded at currents of 450 A and 628 A, while the weld was welded at currents of 470 A and 610 A. **Figure 8** represents the used flux in correlation with the welding current. Increasing the current power for the surfacing welds leads to a larger welding-flux consumption, while the time of the welding is decreased to a small degree.

4.2 Slag of the weld at the current of 470 A

The welding of specimen 1 was carried out at the current of 470 A. The slag was formed on the weld toe in the shape of a circular arch in the center, 2–3 cm wide and 3–5 mm thick. The weld/slag border is smooth, but some unmelted grains of the welding flux remained on its top.

Figure 9 shows the slag microstructure on the weld of steel OCR12 VM after the application of agglomerated welding flux FB 12.2. During the welding process, a liquid slag was formed, which solidified during the cooling. Aluminium and manganese oxides included in the welding flux reacted and formed a solid-solution spinel structure. The welding flux contained manganese oxide and, after the melting, it reacted with magnesium oxide which was also included in the flux.

During the welding, chromium from the base material and the welding wire is oxidized. Chromium oxide together with aluminium, magnesium and manganese oxides forms a spinel structure with a solid-solution composition $(\text{MgO}, \text{MnO}) \cdot (\text{Al}_2\text{O}_3, \text{Cr}_2\text{O}_3)$. After the welding, spinel contains mass fractions of 2.8 % MnO and mass fractions of 3.3 % Cr_2O_3 .

On the left side of **Figure 9**, there is magnesium oxide, encircled with spinel. Solid magnesium oxide

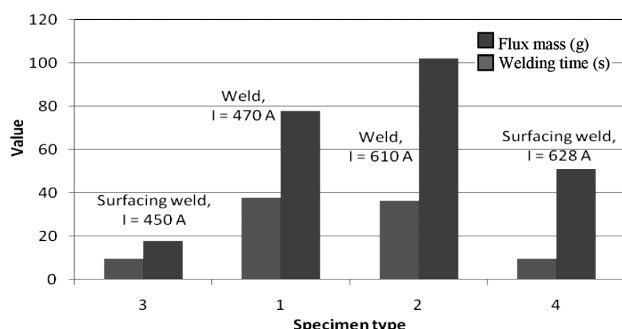


Figure 8: Welding current and flux consumption

Slika 8: Varilni tok in poraba varilnega praška

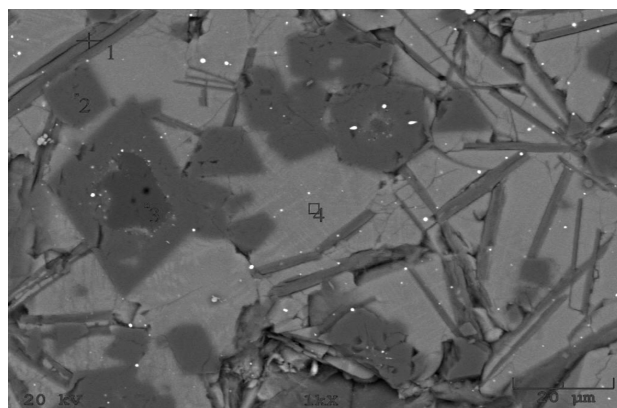


Figure 9: Microstructure of the welding slag of specimen 1

Slika 9: Mikrostruktura varilne žilindre preizkušanca 1

reacts with the liquid slag and thus spinel $(\text{MgO}, \text{MnO}) \cdot (\text{Al}_2\text{O}_3, \text{Cr}_2\text{O}_3)$ is formed on its surface. The resulting spinel prohibits a dissolution of magnesium oxide in the liquid slag.

The solidified welding slag has the following composition: magnesium oxide, spinel, a lamellar phase ($w(\text{MgO}) = 21.1\%$, $w(\text{Al}_2\text{O}_3) = 18.8\%$, $w(\text{SiO}_2) = 39.8\%$ and $w(\text{K}_2\text{O}) = 10.2\%$) and the matrix ($w(\text{CaO}) = 46.2\%$, $w(\text{MgO}) = 11.8\%$, $w(\text{SiO}_2) = 28.9\%$, $w(\text{Al}_2\text{O}_3) = 2.8\%$, $w(\text{MnO}) = 4.2\%$ and $w(\text{F}) = 4.5\%$).

Figure 10 shows an XRD diagram of the slag formed at the welding current of 470 A. The diagram shows the peaks for aluminium oxide, spinel and calcium fluorite. In the sample, the undissolved flux from the surface of the circular arch of the slag is also observed.

4.3 Slag of the weld at the current of 610 A

Figure 11 shows a SEM image of the slag formed during the welding at the current of 610 A. During the welding with a higher current, the unreacted leftovers of magnesium oxide in the welding slag are surrounded with spinel. The spinel generated during the welding with the current of 610 A contains mass fractions of 3.9 % MnO, mass fractions of 24.3 % MgO, mass fractions of 5.2 % Cr_2O_3 and mass fractions of 66.6 % Al_2O_3 . In the slag, tiny drops of metal (white particles) are located at the border between the spinel and magnesium oxide and in the lamellar phase.

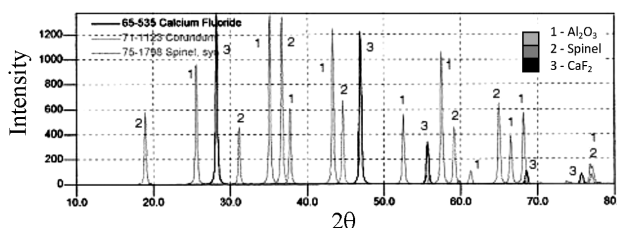


Figure 10: XRD diagram of the slag formed at the welding current of 470 A

Slika 10: Rentgenogram žilindre, nastale pri varjenju s tokom 470 A

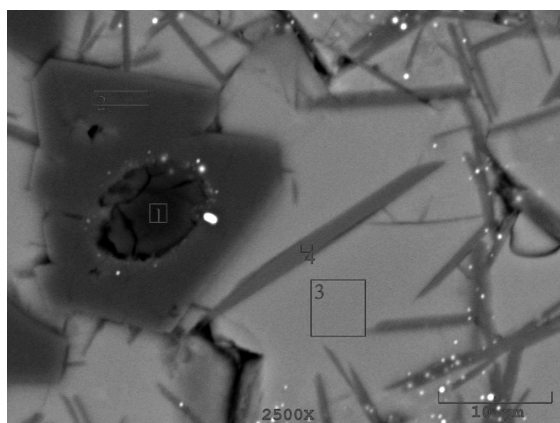


Figure 11: SEM image of welding slag; place of analysis 1
Slika 11: SEM-posnetek varilne žlindre; mesto analize 1

Figure 12 shows a SEM image of the slag, having a metallic particle with a size of 50 μm and a composition of mass fractions of 27.6 % Si, mass fractions of 4.8 % Ti, mass fractions of 4.6 % Cr, mass fractions of 33.8 % Mn (label 4), while the rest is iron. The particle was formed during the melting of silico manganese and the welding wire. Its composition is not similar to the compositions of the filler or the base material. In the slag matrix, a lamellar phase and small spinel crystals containing manganese and chromium oxides are embedded.

Welding with a higher current increases the amount of MnO by mass fractions of 1.1 % and Cr₂O₃ by mass fractions of 1.9 % in the spinel, compared to the welding with the current of 470 A.

Figure 13 presents an XRD diagram of the slag formed at the welding with current of 610 A. The diagram shows that the slag is composed of aluminium oxide, spinel, calcium fluorite and periclase (MgO).

4.4 Slag of the surfacing weld at the current of 628 A

The specimens listed under numbers 3 and 4 are the slags of the surfacing welds. **Figure 14** presents the slag formed during the surfacing with the current of 628 A. In

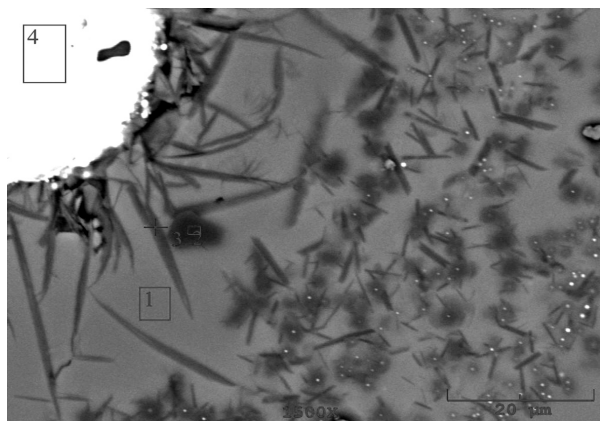


Figure 12: SEM image of welding slag; place of analysis 2
Slika 12: SEM-posnetek varilne žlindre; mesto analize 2

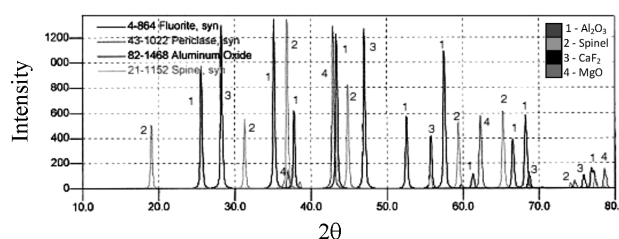


Figure 13: XRD diagram of slag formed during the welding at the current of 610 A

Slika 13: Rentgenogram žlindre, nastale pri varjenju s tokom 610 A

the base (matrix) of the slag, there are spinel, a lamellar phase and the leftovers of a free magnesium oxide. Compared to the surfacing with 450 A, during the surfacing with 628 A, the slag has more aluminium oxide and less calcium oxide. The matrix of the slag (label 2) is composed of mass fractions of 32.7 % CaO, 12.3 % MgO, 25.6 % SiO₂, 16.5 % Al₂O₃, 5.7 % MnO, 2.7 % F and 3.2 % of K₂O. In the slag, there are drops of metal and most of them are located close to the lamellar phase.

4.5 Composition of the spinel and matrix of the slag

Figure 15 gives a graphical presentation of the contents of the oxides in the slag base (the matrix), in which the phases with higher melting points are precipitated. From the diagram it is evident that specimens 1 (470 A) and 3 (450 A) were welded with lower currents and have the same contents of silicon oxide and different contents of calcium oxide and alumina. Specimens 2 and 4, welded with higher currents (610 A, 628 A), also have different contents of calcium oxide. The content of calcium oxide in a slag decreases with the increasing current, while the content of aluminium oxide increases (**Figure 15**). At lower welding currents, the slag includes phases with lower melting points, while at higher welding currents more liquid slag is formed due to the melting of the oxides with higher melting points such as aluminium and magnesium oxides as well as manganese and chromium oxides.

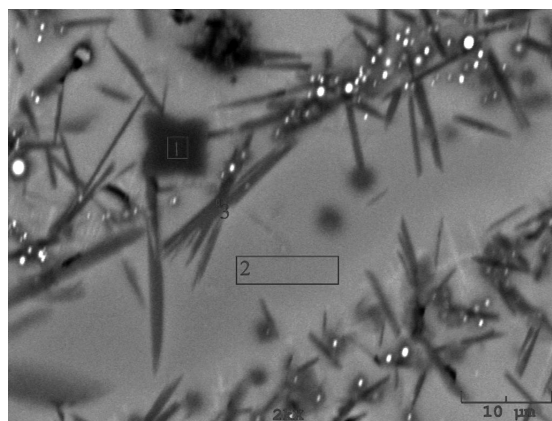


Figure 14: Micrograph of the phases in slag of specimen 4
Slika 14: Mikroposnetek faz v žlindri preizkušanca 4

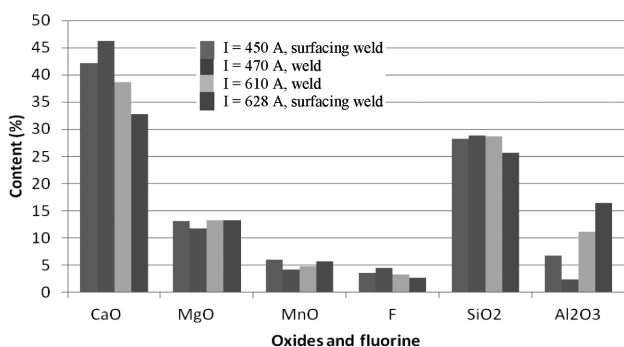


Figure 15: Relative contents of oxides and fluorine in the bases (matrices) of welding slags

Slika 15: Relativna vsebnost oksidov in fluora v osnovi (matici) varilnih žlinder

Table 4: Basicity of the base (matrix) of a slag

Tabela 4: Bazičnost osnove (matice) žlindre

Welding flux	Current (A)	Matrix basicity
Specimen 1 – weld	470	2.14
Specimen 2 – weld	610	1.68
Specimen 3 – surfacing weld	450	1.94
Specimen 4 – surfacing weld	628	1.50

The content of the formed spinel depends on the welding current. With an increase in the welding current the content of manganese oxide increases from 2.8 to 3.9 % of mass fractions and chromium oxide also increases from 3.3 to 7.3 % of mass fractions. **Figure 16** presents the change in the composition of the spinel in relation to the welding current.

We calculated the basicity¹⁵ of the main components in the slag with Equation (1):

$$B = \frac{\text{CaO} + \text{MgO} + \text{BaO} + \text{CaF}_2 + \text{Na}_2\text{O} + \text{K}_2\text{O} + 0.5 \cdot (\text{MnO} + \text{FeO})}{\text{SiO}_2 + 0.5 \cdot (\text{Al}_2\text{O}_3 + \text{TiO}_2 + \text{ZrO}_2)} \quad (1)$$

The content of the base (matrix) of a slag and its basicity also vary with respect to the welding current. The basicity is calculated with Equation (1) and it

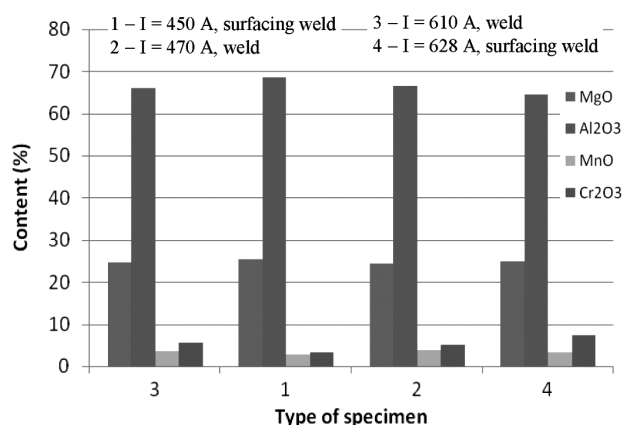


Figure 16: Composition of the spinel in relation to the welding current

Slika 16: Sestava spinela v odvisnosti od toka pri varjenju

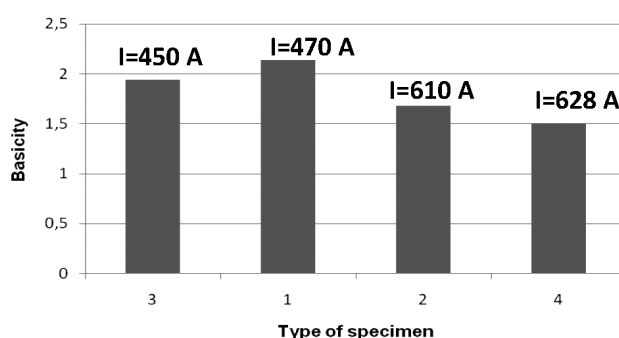


Figure 17: Basicity of the base (matrix) of the welding slag

Slika 17: Bazičnost osnove (matice) varilne žlindre

changes with the welding current, as presented in **Table 4**.

Lower welding currents also diminish the loss of the alloying elements. The calculated values of the basicity show that the basicity of the matrix of a slag is higher at lower welding currents (**Figure 17**) because of the content of Al_2O_3 in the slag melt.

5 CONCLUSIONS

During the submerged-arc welding of steel OCR 12 VM, slag solidifies above the weld in the form of a circular arch. The contact area with the slag has a smooth glassy shine. On the contrary, at the contact with the slag surface, the leftovers of undissolved welding flux are observed.

The agglomerated welding flux is in the form of pellets with a size of 0.2–1.8 mm. During the welding, the slag is liquid. The solidified weld slag contains aluminum and magnesium oxides, spinel, a lamellar phase and the matrix. The composition of the matrix is similar to that of mineral cuspidin¹⁶ ($3\text{CaO} \cdot 2\text{SiO}_2 \cdot \text{CaF}_2$) but it also contains aluminium, potassium and magnesium oxides. The magnesium oxide in the welding slag is surrounded by spinel.

Spinel¹⁶ with a complex composition ($\text{MgO} \cdot \text{MnO} \cdot (\text{Al}_2\text{O}_3, \text{Cr}_2\text{O}_3)$) is formed from magnesium and aluminium oxides, with smaller amounts of manganese and chromium oxides.

The composition of the welding-slag matrix depends on the welding current. At higher welding currents more aluminium oxide is formed.

The welding slag generated during the submerged welding can be a valuable raw material for the production of a new welding flux.

6 REFERENCES

- ¹ H. Grajon, Bases métallurgiques du soudage, Publications de la Soudure Autogène, 41, Institute de Soudure, Paris, 1989
- ² K. Singh, V. Sahni, S. Pandey, Slag Recycling in Submerged Arc Welding and its Influence on Chemistry of Weld Metal, Asian Journal of Chemistry, 21 (2009) 10, 047–051

- ³ Submerged arc welding, Copyright 1982, Muller Electric Mfg. Co., (Rev. 11/85), (http://www.millerwelds.com/pdf/spec_sheets/Submerged.pdf)
- ⁴ S. Durić, B. Sabo, M. Perović, P. Dašić, Matematični model odvisnosti oblike in dimenzij zvara od parametrov navarajanja pri postopku EPP – II. del, Varilna tehnika, 59 (2010) 3, 20–40
- ⁵ R. Kejžar, Platiranje konstrukcijskih jekel z navarjanjem, Kovine zlitine tehnologije, 28 (1994) 2, 95–100
- ⁶ R. Kejžar, B. Kejžar, Dodatni materiali na osnovi izbranih sintetičnih repromaterialov z dodatkom alkalijskih oksidov, Kovine zlitine tehnologije, 28 (1994) 3
- ⁷ A. M. Paniagua-Mecado, V. M. Lopez-Hirata, Chemical and physical properties of flux for SAW low-carbon steels, Instituto Politecnico Nacional Mexico, 2011 (www.intechopen.com)
- ⁸ J. Singh, K. Singh, J. Garg, Reuse of Slag as Flux in Submerged Arc Welding & its Effect on Chemical Composition, Bead Geometry & Microstructure of the Weld Metal, International Journal of Surface Engineering & Materials Technology, 1 (2011) 1, 24–27
- ⁹ T. Lau, G. S. Weatherly, A. McLean, Gas/Metal/Slag Reactions in Submerged Arc Welding Using CaO-Al₂O₃ Based Fluxes, Welding Journal, 65 (1986) 2, 343–347
- ¹⁰ D. Mahto, A. Kimar, Novel Methods of Productivity Improvement and Waste Reduction Through Recycling of Submerged Arc Welding Slag, Jordan Journal of Mechanical and Industrial Engineering, 4 (2010) 4, 451–466
- ¹¹ http://www.elektrode.si/html/slo/katalog/index_katalog.html
- ¹² B. Kosec, G. Kosec, M. Soković, Case of temperature field and failure analysis of die-casting die, Journal of Achievements in Materials and Manufacturing Engineering, 20 (2007) 1/2, 471–474
- ¹³ F. Legat, Orodna jekla v praksi, samozal. F. Legat, Medium, Žirovnica 2013
- ¹⁴ M. P. Tonkovič, A. Nagode, L. Kosec, Mehanizem nastanka sekundarnega ledeburita med varjenjem orodnega jekla, IRT 3000, 5 (2012), 17–21
- ¹⁵ I. Polajnar, Varjenje pod praškom I. del: Varilni procesi in oprema, Inštitut za varilstvo, Specializacija IWE/IWT, Ljubljana 2013/2014
- ¹⁶ F. Trojer, Die oxydische Kristallphasen der anorganischen Industrieerzeugnisse, E. Schweizerbart'sche Verlagsbuchhandlung, Stuttgart 1963

OPTIMIZING THE PARAMETERS FOR FRICTION WELDING STAINLESS STEEL TO COPPER PARTS

OPTIMIRANJE PARAMETROV PRI TORNEM VARJENJU NERJAVNEGA JEKLA NA BAKRENE DELE

Mumin Sahin

Department of Mechanical Engineering, Trakya University, 22180 Edirne, Turkey
mumins@trakya.edu.tr

Prejem rokopisa – received: 2015-01-25; sprejem za objavo – accepted for publication: 2015-02-13

doi:10.17222/mit.2015.023

St-Cu (stainless steel and copper) parts were friction welded with the aim to optimize the process parameters in the present study. The joints obtained with various process-parameter combinations were subjected to a tensile test. Empirical relationships were developed to predict the strength of the joints using RSM (the response-surface methodology) and the coherency of the model was tested. The tensile properties, microhardness variations, SEM, the EDS analysis and X-ray diffraction (XRD) analysis of the welded specimens were evaluated. It was found, with an ANOVA analysis, that the friction pressure/friction time relation has the largest influence on the tensile strength of the joints followed by the rotational speed. However, it was also found that the formation of intermetallics at the interface is responsible for a higher hardness and lower tensile strength of the friction-welded stainless steel-copper joints.

Keywords: friction welding, metallurgy, response-surface methodology, tensile strength

V predstavljenem delu so bili deli St-Cu (nerjavno jeklo in baker) torni varjeni z namenom optimizacije procesnih parametrov. Spoji, dobljeni z različnimi procesnimi parametri, so bili preizkušeni z nateznim preizkusom. Razvite so bile empirične odvisnosti za napovedovanje trdnosti spojev s pomočjo RSM (Metodologija odgovora površine) in izvršena je bila koherenca modela. Ocenjene so bile natezne lastnosti, spreminjanje mikrotvrdote, SEM, EDS analiza in rentgenska difrakcija (XRD) zvarjenih vzorcev. Iz ANOVA analize je bilo ugotovljeno, da ima torni tlak/čas trenja največji vpliv na natezno trdnost spojev, sledi pa mu hitrost vrtenja. Ugotovljeno je bilo, da je večja trdota in manjša natezna trdnost torni varjenih spojev posledica nastanka intermetalne zlitine na stiku nerjavno jeklo-baker.

Ključne besede: torni varjenje, metalurgija, metodologija odgovora površine, natezna trdnost

1 INTRODUCTION

Parts made of different materials are known to be cost-effective. The life cycle of the materials, especially in corrosive media, is prolonged. Many ferrous and non-ferrous alloys can be friction welded. Friction welding can be used to join metals of widely different thermal and mechanical properties. The combinations that can be friction welded cannot be joined with other welding techniques because of the formation of brittle phases that make the joint poor with respect to mechanical properties. Friction welding prevents distortion of the materials, as heat is not applied.

The welding technology is widely used in manufacturing. The development of new welding methods gained importance along with the developing technology.¹⁻⁴ Welding of different metals and their alloys is a common application in engineering solutions. Fusion welding is almost impossible in such cases due to incompatible physical characteristics and chemical compositions of different metals and alloys. As a result, friction welding was developed. Several researches worked on the heat in friction welding.⁵⁻⁷ In friction welding, heat is generated at the interface of the workpieces since mechanical energy is dissipated as heat during the rotation under

pressure. Friction welding is a solid-state welding process, using the heat generated through the mechanical friction with a moving workpiece, with an addition of an upsetting pressure to plastically displace the material. Friction welding is generally used to join the parts that are axially symmetrical and have circular cross-sections. However, it can be easily used to join parts without circular cross-sections, with the aid of automation devices and computerized control facilities.⁸ It is an energy saver since heat is not applied.

The friction time and pressure, the upset time and pressure and the speed of rotation are the principal variables in friction welding.⁹⁻¹² There are two types of friction-welding techniques: continuous-drive friction welding and inertia friction welding. Different metals have different hardness values and different melting points. Interface activity during friction welding forms brittle intermetallic phases or eutectics with low melting points. Clean welding surfaces are also of prime importance.¹³⁻¹⁵ In welded St-Cu joints, the joint strength increases with the increasing upset pressure up to the critical value. An increase in the friction time causes a lower strength of a St-Cu joint compared to the Cu base metal.¹⁶ A deformation of the material during friction welding is generally due to the diffusion involving a

migration of lattice defects, which can be influenced by an external electric field.¹⁷ Sintered powder metallurgical preforms have a low mass, high stiffness and, therefore, their natural frequency is high. Having inherent porosity, they can also be good dampeners besides possessing the latent lubricant.¹⁸ Maalekian¹⁹ found that the formation of hard interlayers, such as intermetallic phases, when joining dissimilar materials may cause a joint to become brittle. Further, Sahin et al.^{20,21} showed that the intermetallic phases formed in the interface cause a decrease in the strength of the joints.

However, based on the literature review, Murti and Sundaresan²² carried out a study about a parameter optimization using a statistical approach based on factorial-experiment-design friction welding of dissimilar materials. The response-surface methodology (RSM) is a collection of mathematical and statistical techniques that are useful for designing a set of experiments, developing a mathematical model, analyzing the optimum combination of the input parameters and graphically expressing the values.²³ To obtain the maximum strength, it is essential to have complete control over the relevant process parameters as demonstrated.²⁴

Therefore, in this work, an attempt was made to optimize the process parameters of continuous-drive friction welding to achieve the maximum tensile strength of stainless steel-copper parts using the response-surface methodology. Tensile tests were performed on the welded test parts. A microstructure analysis, EDS analysis, XRD analysis and microhardness variations were also carried out on the test parts.

2 EXPERIMENTAL WORK

In the experiments, AISI 304 austenitic stainless-steel and copper parts having a diameter of 10 mm were made

using the continuous-drive friction-welding process parameters. The chemical composition and mechanical properties of the stainless-steel and copper parts are presented in **Tables 1** and **2**, respectively, as given in²⁵.

Different combinations of the process parameters were used to carry out the trial runs. Process parameters were tested by varying one of the factors while keeping the rest of them at constant values. The working range of each process parameter was determined for a smooth appearance without any observable defects. The selected levels of the process parameters and design matrix with their units and notations are presented in **Tables 3** and **4**.

However, in order to examine the intermetallic phases formed at the interface of the joints, SEM (scanning electron microscopy) and EDS (energy-dispersive X-ray spectroscopy) were applied to the joints. Examinations were carried out with an SEM-JEOL JSM 5410 LV microscope and in the field of 200 kV. In addition, the weld zones of the joints were analyzed in this work since an XRD analysis of the phase constituents in the weld zone is of a great importance.

Then, the strength of the joints was related to the hardness variation within the HAZ. The hardness variations across the welding regions of the joints were measured using a 0.3 kg load Vickers microhardness test.

3 RESULTS AND DISCUSSION

3.1 Empirical relationships and the optimization

The responses, the tensile-strength (*TS*) values of friction-welded joints, are the functions of the friction-welding parameters such as the friction pressure per second (*F*), the forging pressure per second (*D*) and the rotational speed per second (*N*) and they can be expressed as:

Table 1: Chemical composition of austenitic stainless steel used in the experiment²⁵

Tabela 1: Kemijska sestava avstenitnega nerjavnega jekla, uporabljenega pri preizkusu²⁵

Material	% C	% P	% S	% Mn	% Si	% Cr	% Ni	Tensile strength (MPa)
AISI 304 (X5CrNi1810)	< 0.07	< 0.045	< 0.030	< 2.0	< 1.0	17–19	8.5–10.5	825

Table 2: Chemical composition of copper used in the experiment

Tabela 2: Kemijska sestava bakra, uporabljenega pri preizkusu

Copper	% Sn	% Pb	% Zn	% P	% Mn	% Fe	% Ni	% Si	% Mg	% Al	% Bi	% S	% Sb	% Cu	Tensile strength (MPa)
	0.00222	<0.0020	<0.0010	0.00137	<0.0005	0.0381	<0.0010	0.00745	0.00376	0.00500	<0.0005	0.00251	<0.0020	99.93	300

Table 3: Feasible working limits of friction-welding parameters

Tabela 3: Območje delovnih parametrov pri tornem varjenju

Parameter	Notation	Unit	Level				
			–1.68	(–1)	(0)	(+1)	+1.68
Friction pressure/Friction time	<i>F</i>	MPa/s	3.78	5.82	8.82	11.82	13.86
Upset pressure/Upset time	<i>D</i>	MPa/s	2.96	5	8	11	13.04
Rotational speed/sec	<i>N</i>	s ^{–1}	18.46	20.5	23.5	26.5	28.54

Table 4: Design matrix and the corresponding output response**Tabela 4:** Postavljena matrika in ustrezni dobljeni odgovori

Standard order	Run order	Original value			Tensile strength (MPa)
		<i>F</i>	<i>D</i>	<i>N</i>	
16	1	8.82	8	23.5	223
18	2	8.82	8	23.5	222
4	3	11.82	11	20.5	190
9	4	3.78	8	23.5	150
20	5	8.82	8	23.5	218
6	6	11.82	5	26.5	210
15	7	8.82	8	23.5	223
1	8	5.82	5	20.5	130
7	9	5.82	11	26.5	213
5	10	5.82	5	26.5	180
8	11	11.82	11	26.5	215
12	12	8.82	13.04	23.5	217
11	13	8.82	2.96	23.5	160
10	14	13.86	8	23.5	216
3	15	5.82	11	20.5	150
19	16	8.82	8	23.5	222
17	17	8.82	8	23.5	219
13	18	8.82	8	18.46	200
14	19	8.82	8	28.54	215
2	20	11.82	5	20.5	195

$$TS = f \{F, D, N\} \quad (1)$$

The second-order polynomial (regression) equation used to represent the response surface *Y* (*TS*) is as follows:

$$Y = b_0 + \sum b_{1i}x_i + \sum b_{2ij}x_i^2 + \sum b_{3ij}x_i x_j \quad (2)$$

and for three factors, the selected polynomial could be expressed as:

$$TS = b_0 + b_1(F) + b_2(D) + b_3(N) + b_{12}(FD) + b_{13}(FN) + b_{23}(DN) + b_{11}(F^2) + b_{22}(D^2) + b_{33}(N^2) \quad (3)$$

Regression coefficients are $b_1, b_2, b_3, \dots, b_{44}$ where b_0 is the average of the responses and they depend on the respective linear, interaction and squared terms of the factors as shown in^{26,27}. The significance of each coefficient was determined with a *t*-test and *p*-values, listed in **Table 5**.

The value of a coefficient was calculated using the Design-Expert software. The values of the probability > *F* of less than 0.05 indicate that the model terms are significant. In this case, *F*, *D*, *N*, *FD*, *FN*, *DN*, *F*², *D*² and *N*² are significant model terms. The values greater than 0.1 point out that the model terms are not significant. The results of multiple linear regression coefficients for the second-order response surface model are given in **Table 6**.

The final empirical relationship was obtained using only these coefficients, and the developing final empirical relationship for the tensile strength is given below:

$$TS = [221.36 + 18.16F + 10.90D + 13.05N - 6.62FD - 9.12FN + 2.88DN - 14.74F^2 - 12.80D^2 - 6.08N^2] \quad (4)$$

Table 5: ANOVA test results for the response of the tensile strength**Tabela 5:** Rezultati ANOVA preizkusa za odgovore natezne trdnosti

Source	Sum of squares	df	Mean square	<i>F</i> -value	<i>P</i> -value prob > <i>F</i>	significant
Model	14726.69	9	1636.30	13.39	0.0002	
A-F	4503.47	1	4503.47	36.85	0.0001	
B-D	1622.62	1	1622.62	13.28	0.0045	
C-N	2325.93	1	2325.93	19.03	0.0014	
AB	351.12	1	351.12	2.87	0.1209	
AC	666.12	1	666.12	5.45	0.0417	
BC	66.13	1	66.13	0.54	0.4789	
A ²	3132.15	1	3132.15	25.63	0.0005	
B ²	2360.38	1	2360.38	19.31	0.0013	
C ²	532.80	1	532.80	4.36	0.0633	
Residual	1222.11	10	122.21			
Lack of fit	1199.28	5	239.86	52.52	0.0003	
Pure error	22.83	5	4.57			
Cor. total	15948.80	19				
Std. dev.	11.05		<i>R</i> -squared		0.9234	
Mean	198.40		Adj. <i>R</i> -squared		0.8544	

Table 6: Estimated regression coefficients**Tabela 6:** Ocenjeni regresijski koeficienti

Factor	Estimated regression coefficients
	Tensile strength (MPa)
Intercept	221.36
<i>F</i> -friction force/friction time	18.16
<i>D</i> -upset force/upset time	10.90
<i>N</i> -rotational speed	13.05
<i>FD</i>	-6.62
<i>FN</i>	-9.12
<i>DN</i>	2.88
<i>F</i> ²	-14.74
<i>D</i> ²	-12.80
<i>N</i> ²	-6.08

The ANOVA (analysis of variance) technique was used to check the adequacy of the developing empirical relationship. In this investigation, the desired level of confidence was taken to be 95 %. The relationship is considered adequate if the calculated *F*-value of the model developed does not go over the standard tabulated *F*-value and the calculated *R*-value of the developed relationship exceeds the standard tabulated *R*-value for a desired level of confidence. It was found that the above model is adequate. In the same way, interactions *FD*, *FN*, *DN* had significant effects. A lack of fit was not significant though it was desired. The normal probability plot of the residuals for the tensile strength is shown in **Figure 1**. It reveals that the residuals are on a straight line, which means that the errors are distributed normally. Each predicted value matches well its experimental value, as shown in **Figure 2**. The response-surface methodology (RSM) was used to optimize the friction-welding parameters in this study. The response contours can assist in the prediction of the response for any zone in the experimental field as observed in^{24,25}.

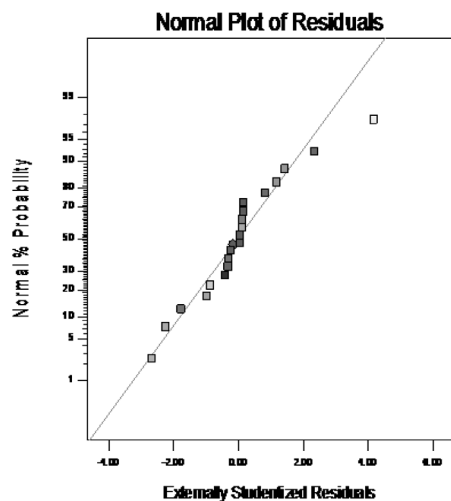


Figure 1: Normal probability plot of residuals
Slika 1: Normalna verjetnost izrisa ostankov

The end of the response plot shows the maximum achievable tensile strength. **Figures 3 and 4** show that the tensile strength increases with the increasing friction pressure/time relation and rotational speed and then it decreases.

The maximum tensile strength of the friction-welded joints was attained under the following welding conditions: a friction pressure/time relation of 8.82 MPa/s (a friction pressure of 75 MPa and a friction time of 8.5 s), an upset pressure/time relation of 8 MPa/s (an upset pressure of 160 MPa and an upset time of 20 s) and a rotational speed of and 23.5 s^{-1} , showing the accuracy of the model.

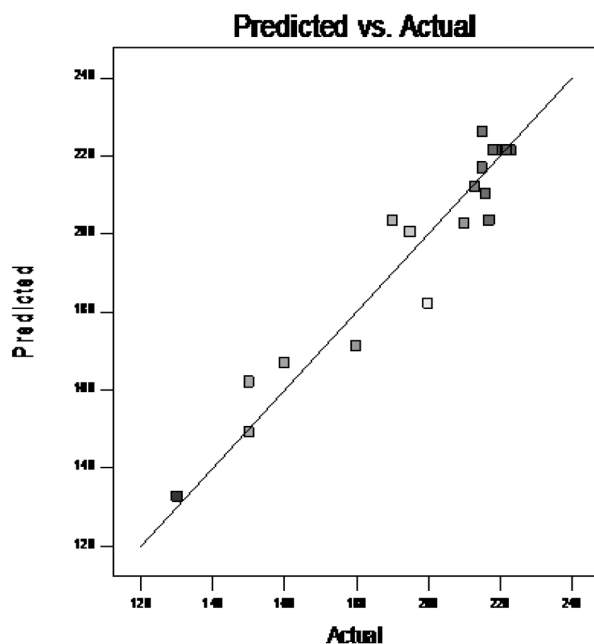


Figure 2: Correlation graph of the response
Slika 2: Prikaz korelacije odziva

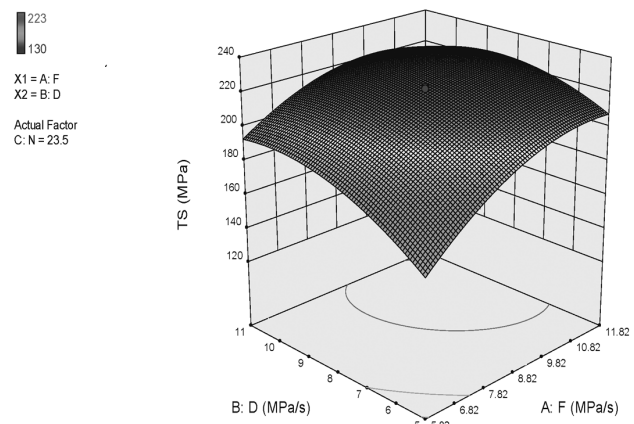


Figure 3: Response plots of the process parameters for the tensile strength

Slika 3: Prikaz odziva procesnih parametров na natezno trdnost

During the welding processes, the strength of the welds obtained with dissimilar materials strongly depends on the temperature attained by each substrate. Differences in the mechanical and thermophysical properties and behaviour of the substrates at the interface influence the quality of the joints during the welding as reported in^{20,21}.

3.2 Metallurgical analysis

The macrophotography of the joints is given in **Figure 5**. There is no evidence of cracking or other defects in the joints. Due to the variations in the strength of the materials, an appreciable variation in the width of the HAZ (heat-affected zone) region is evident from the joints. However, the microstructure of stainless steel is characterized by equiaxed grains, in the austenitic-grain structure being the natural structure of this type of steel at room temperature (**Figure 6**).

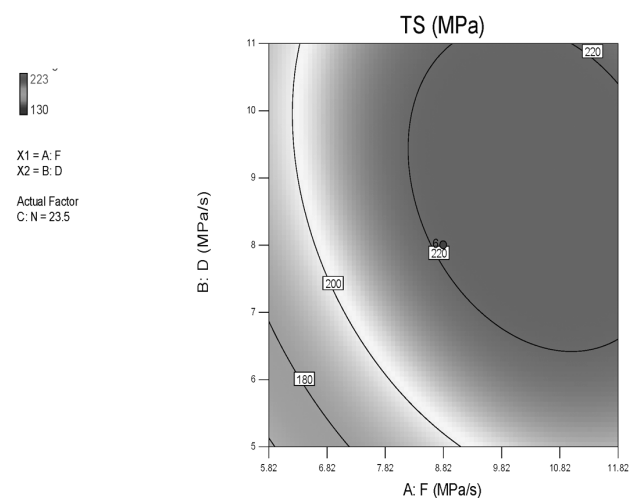


Figure 4: Contour plots of the process parameters for the tensile strength

Slika 4: Prikaz obrisov procesnih parametров na natezno trdnost

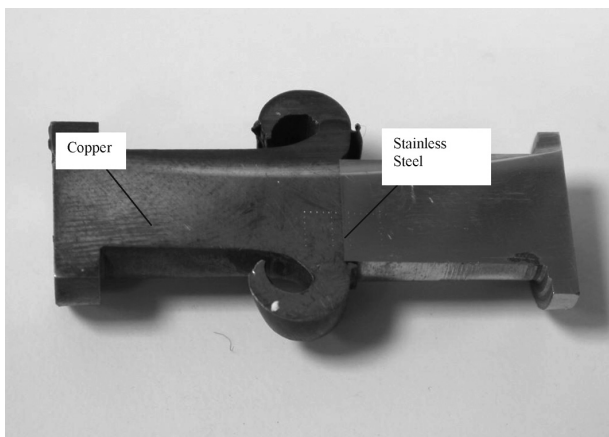


Figure 5: Macrophotography of a joint
Slika 5: Makroposnetek spoja

However, copper is formed of eutectic particles, having dark points indicating that it is a mixture of pure copper and cuprous oxide, dispersed in the ground copper (**Figure 7**). The effect of melting was minimal at the interface because the heat-affected zone (HAZ) was small (**Figure 8**).

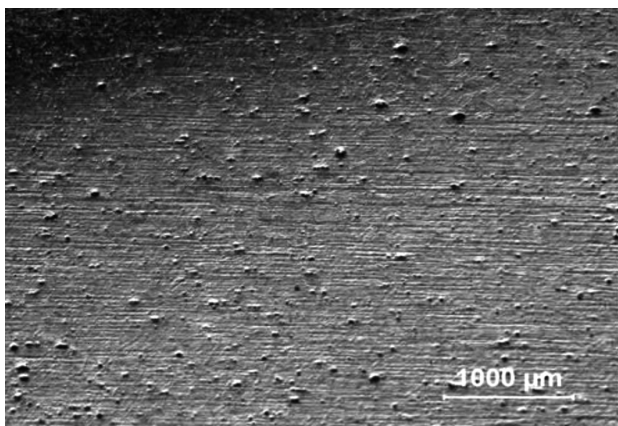


Figure 6: Microstructure of stainless steel
Slika 6: Mikrostruktura nerjavnega jekla

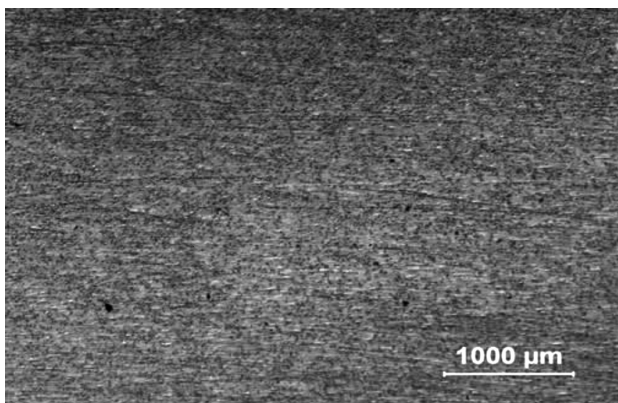


Figure 7: Microstructure of copper
Slika 7: Mikrostruktura bakra

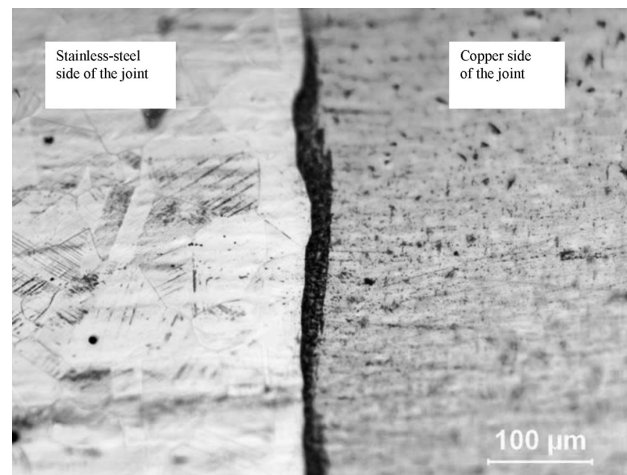


Figure 8: Image of the interface of a joint
Slika 8: Posnetek stika v spoju

It is also observed that the joints have larger deformations on the Cu side compared to the steel side (**Figure 5**). Welding flashes occur on the copper side of the interface because the melting temperature of copper is lower than the melting temperature of steel. However, stainless steel does not undergo an extensive deformation while copper undergoes an extensive melting because of the high generated and concentrated frictional heat.

Since copper has a higher thermal conductivity than steel, the heat-affected zone on the copper side is wider

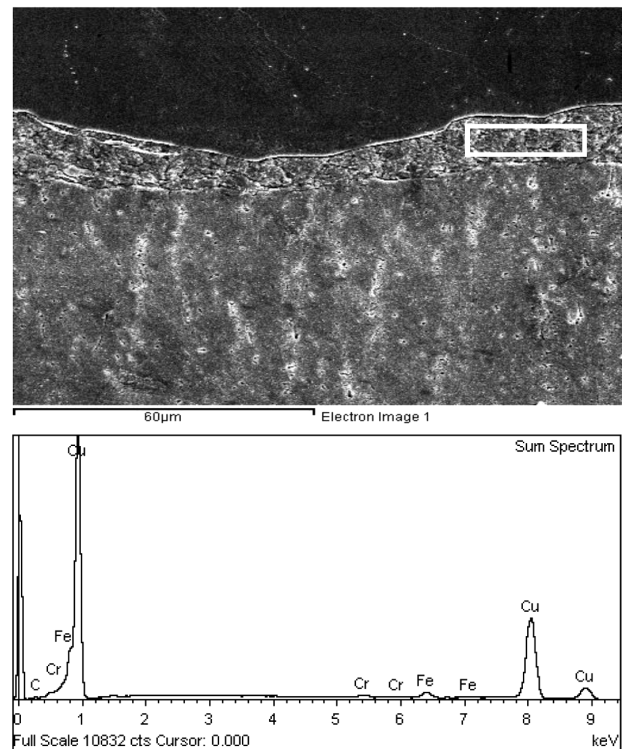


Figure 9: EDS analysis of the intermetallic-phase zone of a joint: a) SEM, b) EDS spectrum

Slika 9: EDS-analiza intermetalne faze na stiku: a) SEM, b) EDS spekter

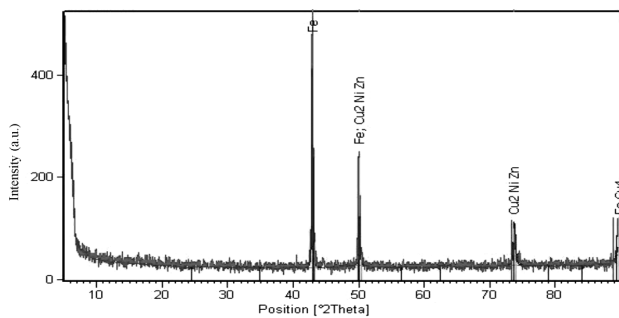


Figure 10: XRD results for the welding zone of a joint
Slika 10: Rezultati rentgenske analize (XRD) v zvaru stika

Table 7: EDS analysis of the defined zone at the interface
Tabela 7: EDS-analiza označenega področja na stiku

Element	(w/%)	(x/%)
C	2.70	12.72
Cr	0.98	1.07
Fe	2.96	3.00
Cu	93.36	83.21
Total	100.00	

than that of the steel side. There is no change in the grain size on the steel side. The presence of small particles on the copper side reveals hardening on this side. There are equiaxed α grains and Cu_2O particles on the copper side. The interface elements of both materials diffused along the interface and some intermetallic phases were formed at the interface as reported in^{20,21}.

The EDS analysis performed at a defined zone of the interface showed that the interface was formed of 2.70 % C, 0.98 % Cr, 2.96 % Fe and 93.36 % Cu (**Table 7**). Thus, the presence of intermetallic phases at the interface is obvious. Copper-oxide films were broken into pieces due to an excessive deformation at the interface caused by the rotation (**Figure 9**). According to **Figure 10**, the X-ray diffraction results for friction-welded stainless steel-copper joints indicated that FeCu_4 and

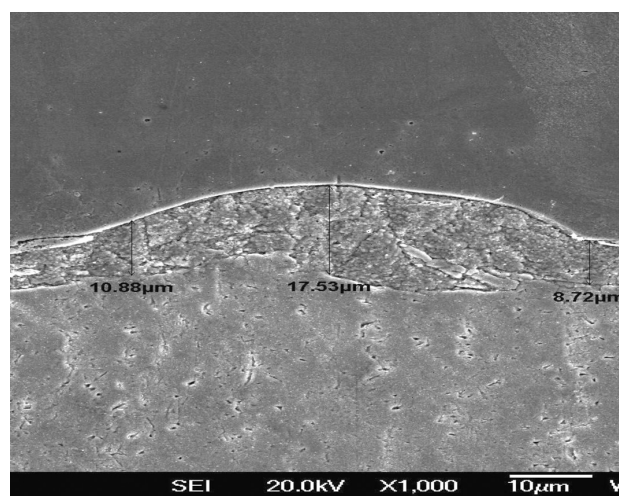


Figure 11: Thicknesses of the intermetallic phases at the interface
Slika 11: Debelina intermetalnih faz na stiku

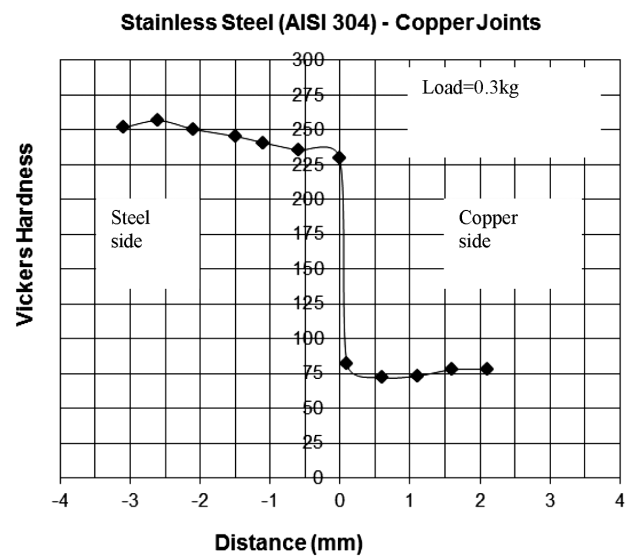


Figure 12: Microhardness variation across the joint
Slika 12: Spreminjanje mikrotvrdote preko spoja

Cu_2NiZn intermetallics were formed in the welding zone. The thickness of the layer containing the intermetallic phases varied between 8.72 μm and 17.53 μm (**Figure 11**).

3.3 Microhardness measurement

The microhardness of a joint was measured across the weld region and the values were plotted as shown in **Figure 12**. The microhardness is maximum at the interface; this may be due to the formation of brittle intermetallics, and it is one of the reasons for a lower tensile strength of dissimilar joints.

4 CONCLUSIONS

Stainless-steel and copper parts were successfully friction joined in this work. The following important conclusions were obtained from this investigation:

- Empirical relationships were developed to predict the tensile strength of the friction-welded stainless-steel and copper parts incorporating process parameters at a 95 % confidence level. The friction-welding parameters were optimized with the response-surface methodology to attain the maximum tensile strength.
- The maximum tensile strength of 223 MPa was attained in the friction-welded joints under the following welding conditions: a friction pressure/time relation of 8.82 MPa/s, an upset pressure/time relation of 8 MPa/s and a rotational speed of 23.5 s^{-1} .
- The friction pressure/friction time relation was found to have the greatest influence on the tensile strength of the joints, followed by the rotational speed.
- Various intermetallic phases such as FeCu_4 and Cu_2NiZn occurred at the interface. The formation of intermetallics at the interface is responsible for the

higher hardness and lower tensile strength of the friction-welded stainless steel-copper joints.

- The intermetallic phases at the interface are also expected to play a role in the hardness variations.

Acknowledgement

The author would like to thank Trakya University/Edirne-Turkey, Hema Industry/Çerkezköy-Turkey and TUBITAK MRC/Gebze-Turkey for the help in the experimental part of the study.

5 REFERENCES

- ¹ V. I. Vill, Friction Welding of Metals, AWS, New York 1962
- ² W. Kinley, Inertia welding: simple in principle and application, Welding and Metal Fabrication, (1979), 585–589
- ³ N. I. Fomichev, The friction welding of new high speed tool steels to structural steels, Weld. Prod., (1980), 35–38
- ⁴ C. R. G. Ellis, Friction Welding; some recent applications of friction welding, Welding and Metal Fabrication, (1977), 207–213
- ⁵ K. P. Imshennik, Heating in friction welding, Weld. Prod., (1973), 76–79
- ⁶ T. Rich, R. Roberts, Thermal analysis for basic friction welding, Met. Const. and British Weld. J., (1971), 93–98
- ⁷ A. Sluzalec, International Journal of Mechanical Sciences, 32 (1990) 6, 467–478, doi:10.1016/0020-7403(90)90153-A
- ⁸ M. Sahin, H. E. Akata, Journal of Materials Processing Technology, 142 (2003) 1, 239–246, doi:10.1016/S0924-0136(03)00589-2
- ⁹ M. Sahin, H. E. Akata, Industrial Lubrication & Tribology, 56 (2004) 2, 122–129, doi:10.1108/00368790410524074
- ¹⁰ M. Sahin, Assembly Automation, 25 (2005) 2, 140–145, doi:10.1108/01445150510590505
- ¹¹ M. Sahin, Materials and Design, 28 (2007) 7, 2244–2250, doi:10.1016/j.matdes.2006.05.031
- ¹² A. W. E. Nentwig, Friction welding of cross section of different sizes, Schweissen und Schneiden/Welding & Cutting, 48 (1996) 12, 236–237
- ¹³ B. S. Yılbaş, A. Z. Şahin, N. Kahraman, A. Z. Al-Garni, Journal of Materials Processing Technology, 49 (1995) 3–4, 431–443, doi:10.1016/0924-0136(94)01349-6
- ¹⁴ A. Z. Şahin, B. S. Yılbaş, M. Ahmed, J. Nickel, Journal of Materials Processing Technology, 82 (1998) 1–3, 127–136, doi:10.1016/S0924-0136(98)00032-6
- ¹⁵ W. B. Lee, S. B. Jung, Zeitschrift für Metallkunde, 94 (1993) 12, 1300–1306, doi:10.3139/146.031300
- ¹⁶ S. A. Fabritsiev, A. S. Pokrovsky, M. Nakamichi et al., Journal of Nuclear Materials, 258 (1998) 2, 2030–2035, doi:10.1016/S0022-3115(98)00126-3
- ¹⁷ L. Fu, S. G. Du, Journal of Materials Science, 41 (2006) 13, 4137–4142, doi:10.1007/s10853-006-6224-5
- ¹⁸ K. Jayabharath, M. Ashfaq, P. Venugopal et al., Materials Science and Engineering A: Structural Materials: Properties, Microstructure and Processing, 454–455 (2007), 114–123, doi:10.1016/j.msea.2006.11.026
- ¹⁹ M. Maalekian, Science and Technology of Welding & Joining, 12 (2007) 8, 738–759, doi:10.1179/174329307X249333
- ²⁰ M. Sahin, Industrial Lubrication and Tribology, 61 (2009) 6, 319–324, doi:10.1108/00368790910988435
- ²¹ M. Sahin, E. Çil, C. Misirli, Journal of Materials Engineering & Performance, 22 (2013) 3, 840–847, doi:10.1007/s11665-012-0310-4
- ²² K. G. K. Murti, S. Sundaresan, Parameter optimisation in friction welding dissimilar materials, Metal Construction, 15 (1983) 6, 331–335
- ²³ R. Karthikeyan, V. Balasubramanian, International Journal of Advanced Manufacturing Technology, 51 (2010) 1–4, 173–183, doi:10.1007/s00170-010-2618-2
- ²⁴ S. T. Selvamani, K. Palanikumar, Measurement: Journal of the International Measurement Confederation, 53 (2014), 10–21, doi:10.1016/j.measurement.2014.03.008
- ²⁵ C. W. Wegst, Stahlschlüssel, Verlag Stahlschlüssel Wegst GmbH, Marbach 1995
- ²⁶ G. E. P. Box, W. H. Hunter, J. S. Hunter, Statistics for experiment, John Wiley Publications, New York 1978
- ²⁷ A. I. Khuri, J. Cornell, Response Surfaces, Design and Analysis, Marcel Dekker, New York 1996

WEDM CUTTING OF INCONEL 718 NICKEL-BASED SUPERALLOY: EFFECTS OF CUTTING PARAMETERS ON THE CUTTING QUALITY

WEDM REZANJE NIKLJEVE SUPERZLITINE INCONEL 718: VPLIV PARAMETROV REZANJA NA KVALITETO REZANJA

Ulaş Çaydaş, Mustafa Ay

University of Firat, Technology Faculty, Department of Mechanical Engineering, 23119 Elazığ, Turkey
ucaydas@firat.edu.tr, ucaydas@gmail.com

Prejem rokopisa – received: 2015-01-26; sprejem za objavo – accepted for publication: 2015-02-19

doi:10.17222/mit.2015.026

Investigations of the effects of machining parameters on the cutting quality of wire-electrical-discharge-machining (WEDM) cutting of an annealed Inconel 718 nickel-based superalloy are described in this paper. The cutting-quality characteristics considered are the kerf width, the recast-layer thickness and the surface roughness of the cut specimens. The essential process input parameters were identified as the pulse-on time, the pulse-peak current, and the injection pressure. The analysis of variance (ANOVA) technique was used to find the parameters affecting the cut quality. The regression analysis was used for the development of empirical models able to describe the effects of the process parameters on the quality of the WEDM cutting. The ANOVA results show that the pulse-on time and the pulse-peak current are significant variables affecting the surface roughness of wire-EDMed Inconel 718. The surface roughness, the kerf width and the recast layer of the test specimens increased as these two variables increased. The measured and modelled results were in good agreement with respect to the correlation coefficients R_a , RLT and K_{II} .

Keywords: wire-electrical-discharge machining (WEDM), Inconel 718, recast layer, surface morphology, analysis of variance

V članku je opisana raziskava vplivov parametrov obdelave na kvaliteto reza, z žično elektroerozijo (WEDM) rezane žarjene nikljeve superzlitine Inconel 718. Upoštevane so bile karakteristike reza, kot je širina reza, debelina nataljenega sloja in hrapavost površine odrezanega vzorca. Ugotovljeno je, da so bistveni vhodni parametri procesa impulzi v času, tok vrha impulza in tlak vbrizgavanja. Za iskanje parametrov, ki vplivajo na kvaliteto reza je bila uporabljena tehnika analiza variance (ANOVA). Regresijska analiza je bila uporabljena za razvoj empiričnega modela, ki lahko opiše vpliv procesnih parametrov na kvaliteto WEDM rezanja. Rezultati iz ANOVE kažejo, da sta impulz v času in tok vrha impulza pomembni spremenljivki pri rezanju Inconela 718 z žično elektroerozijo. Hrapavost površine, širina zareze in debelina pretaljene plasti so naraščali pri preizkusnih vzorcih, če sta naraščali ti dve spremenljivki. Izmerjeni in modelirani rezultati so se dobro ujemali s korelacijskimi koeficienti R_a , RLT in K_{II} .

Ključne besede: žična elektroerozija (WEDM), Inconel 718, pretaljena plast, morfologija površine, analiza variance

1 INTRODUCTION

Among nickel-based alloys, the superalloy Inconel 718 is one of the most important ones. Due to its high corrosion and high temperature resistance, it is commonly used in the space industry, in particular for the hot parts of plane, marine and industrial gas-turbine engines, rocket engines, nuclear reactors, submarines, pressure tanks, steam-turbine generators and other high-temperature applications.¹⁻⁵ Despite this widespread use, it is classified as a difficult-to-machine material due to its unique characteristics such as low thermal conductivity, hardness, work hardening and the presence of abrasive carbide particles in its microstructure.^{3,6}

Due to its thermal machining ability, wire-electrical-discharge machining (WEDM) has been an important manufacturing method as it provides effective solutions for machining difficult-to-machine materials, such as zirconium, nimonic, titanium, nickel, etc., that cannot be machined with traditional methods.⁷ Nonetheless, there are problems that remain to be solved such as the

stresses that occur on the top layer where the material solidifies and in the formation of the heat-affected zone, micro-cracks, porosity, local hardness/softness, grain growth and small alloys that get transferred via dielectric fluids or the tool.^{8,9} For a complete and efficient WEDM, the machining parameters should be selected in accordance with the nature of the material.

Effects of the EDM-process parameters have been investigated. Kanlayasiri and Boonmung¹⁰ studied the effects of the pulse-on time, pulse-off time, pulse-peak current and wire tension (a wire electrode made of Cu-35 % of mass fractions of Zn; the wire was KH Sodick with 0.25 mm in diameter, tolerating a tension of up to 900 MPa) on the surface roughness of the DC53 die steel. Kuriakose and Shunmugam¹¹ investigated the characteristics of a WEDMed Ti6Al4V surface. Gökler and Ozanözgü¹² experimentally investigated the effects of the cutting parameters on the surface roughness in the WEDM process for the 1040, 2379 and 2738 steels. Miller et al.¹³ investigated the effects of the EDM process parameters, particularly the spark cycle time and

spark-on time on thin cross-section cuts of the Nd-Fe-B magnetic material. Ramakrishnan and Karunamoorthy¹⁴ developed a neural-network model in order to predict process outputs and to establish the optimum process parameters. Kang and Kim¹⁵ investigated the EDM characteristics of nickel-based heat resistant alloys; Hastelloy-X. Bai et al.¹⁶ developed electrical discharge surface alloying of superalloy Haynes 230 with Al and Mo. Aspinwall et al.¹⁷ developed 3D topographic maps of workpiece surfaces, microstructural and microhardness depth-profile data of Inconel 718.

So far, the most common workpiece materials used in the research of WEDM have been tool or die steels. Very little research was done to investigate the machinability of Inconel 718 with respect to WEDM. As a result, the effects of the machining parameters on the formation of the recast layer and the surface integrity during the WEDM of Inconel 718 remain to be elucidated in detail.

2 EXPERIMENTAL WORK

In this study, an annealed Inconel 718 nickel alloy with the AMS 5596 standard number was used. The chemical composition of this material is given in **Table 1**. WEDM cutting experiments were performed using an Accutex CNC WEDM machine. In the conducted experiments, a CuZn₃₇ wire with a tensile strength of 900 N/m² and a diameter of 0.25 mm was used. In the experimental

Table 1: Chemical composition of Inconel 718

Tabela 1: Kemijska sestava Inconel 718

Element	Composition (wt%)
Ni	53.60
Cr	18.20
Nb	5.06
Mo	3.04
Ti	0.97
Al	0.44
C	0.052
B	0.003
Si	0.10
S	<0.002
P	<0.005
Fe	Balance

Table 2: Machining parameters of WEDM in this study

Tabela 2: Parametri obdelave z WEDM v tej študiji

Cutting conditions	Settings		
	Level 1	Level 2	Level 3
Pulsed current (A)	8	10	12
Gap voltage (V)	39	–	–
Pulse-on duration (µs)	5	7	9
Pulse-off duration (µs)	9	–	–
Wire tension (N)	10	–	–
Wire speed (mm/s)	15	–	–
Flushing-circulation pressure (MPa)	1.27	1.47	1.76
Table-feed ratio (mm/min)	10		

studies, the pulse current (A), pulse duration (µs) and dielectric flushing circulation pressure (MPa) were chosen as variable parameters. With these cutting parameters and their levels, the Taguchi L9 experimental-design method was chosen as the basis and a total of 9 experiments were performed. The experimental parameters and their levels are provided in **Table 2** and the sequence of the experiments is provided in **Table 3**.

Table 3: Experimental layout using an L9 orthogonal array

Tabela 3: Eksperimentalna postavitev z uporabo L9 ortogonalne matrike

Exp. No	Pulsed current (A)	Pulse-on duration (µs)	Flushing pressure (MPa)
1	8	5	1.27
2	8	7	1.47
3	8	9	1.76
4	10	5	1.47
5	10	7	1.76
6	10	9	1.27
7	12	5	1.76
8	12	7	1.27
9	12	9	1.47

At the end of the experiments, the width of each cut was measured at five points along the cutting channel in order to determine the kerf widths. The measurements were performed using a profile-measuring microscope with a sensitivity of 0.002 mm (Model 98-0001, SCHERR-TUMICO, USA). In order to obtain the surface images, determining the microstructures of the surfaces and the heat-affected zones, the surface that was perpendicular and adjacent to the surface that was being machined was chosen and these surfaces were polished using 200–1200 mesh abrasive paper and a 3-µm diamond paste. The polished surfaces were etched with the electrolytic-etching method in a 50 % HCl and 50 % methanol solution and at a 4.5 V voltage.¹ The microstructural analysis of the specimens was done with a scanning electron microscope (SEM) and a three-dimensional atomic-force microscope (AFM). In order to determine the elements and phases on the machined surfaces, EDS (energy dispersive spectrograph) and XRD (X-ray diffraction) analyses were performed. Microhardness tests were conducted with a Leica Q500/L hardness tester using the Vickers scale. The surface roughness was obtained using a Mitutoyo SurfTest SJ-201 portable device.

3 RESULTS AND DISCUSSION

3.1 Effect of the cutting parameters on the surface structure

In **Figure 1**, an image obtained after the cutting of the Inconel 718 nickel alloy with WEDM is shown. The surface is composed of spherical grains detached from the material that cannot be removed from the plain space with the liquid pressure, debris that melt and stick to the

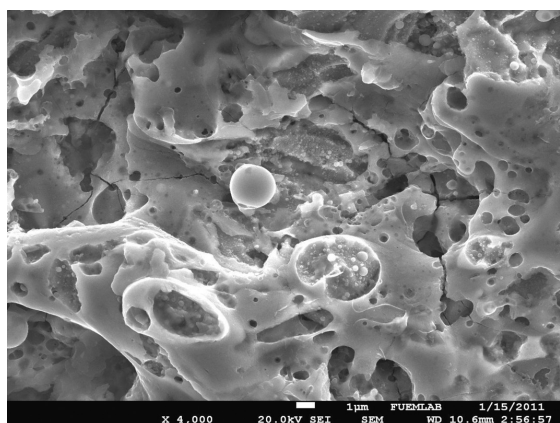


Figure 1: SEM micrograph of a WEDM-cut surface of Inconel 718
Slika 1: SEM-posnetek površine reza Inconel 718 po rezanju z WEDM

surface in drops, cracks, residues and randomly dispersed craters of various sizes. These craters are characterized as cavities formed by the spherical chips detached from the surface due to the effect of the sparks between the wire and the workpiece during the machining. In terms of the surface appearance, it was determined that the densities of the machined surfaces are similar, whereas the densities of the craters and hills on the surface are different, depending on the variations in the current and pulse duration.

Surface images of the specimens cut under different currents, pulse durations and fluid-circulation pressures are seen on **Figure 2**. As can be seen, when the strength of the current is constant, the surface gets rougher as the pulse duration increases. The pulse duration is the time

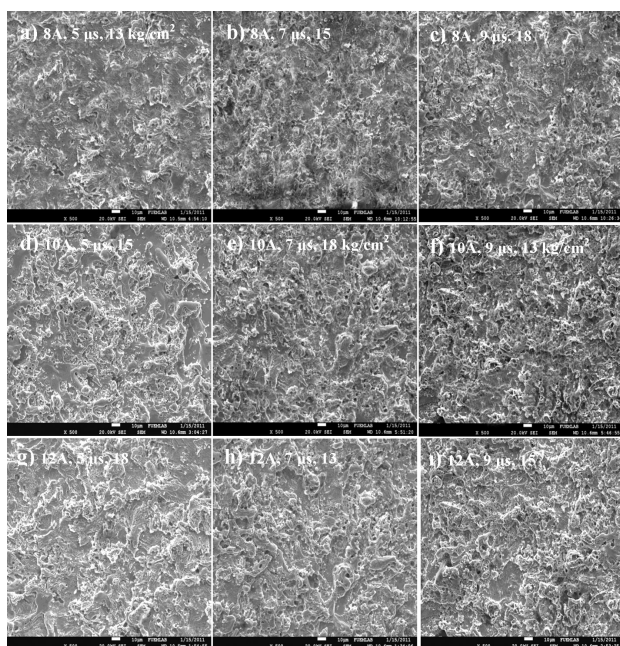


Figure 2: SEM micrographs of a surface WEDM-processed under different machining conditions

Slika 2: SEM-posnetki z WEDM obdelane površine pri različnih pogojih obdelave

duration of the discharge applied to the wire electrode. In other words, it is the time of the spark discharge that forms between the wire and the workpiece. Therefore, an increase in the pulse duration leads to an increased transfer of heat onto the surface of the workpiece and a formation of larger craters on the surface of the workpiece. Similarly, the surface was observed to deteriorate also with an increased current.

An increase in the current intensity leads to a more intense energy discharge to the workpiece surface; thus, more chips detach from the surface. The increase in the amount of detached chips from the surface, at the same time, deteriorates the surface roughness.¹⁸ The results of the experiments show that the liquid-circulation pressure had little effect on the surface structure. Similarly, previous studies indicate that while the surface roughness increases with the increasing current and pulse duration, and wire fractures are prevented using an appropriate liquid-circulation pressure, the effect of the liquid-circulation pressure on the surface roughness, the thickness of the recast layer and the microstructure is very low.^{9,19}

3.2 Effect of the cutting parameters on the recast-layer thicknesses

The basic metallurgical effects that occur during the cutting with WEDM are the formation and width of the recast layer and/or the heat-affected region. **Figure 3** shows a SEM photo obtained from the surface adjacent to a machined surface. When the image is examined, it is seen that three different regions formed after the cutting operation. At the very top, there is the recast layer. This layer developed because of the rapid cooling and re-solidification of the molten material with an auxiliary liquid-circulation pressure, without being removed from the cutting channel during the cutting with WEDM. The heat-affected region is the region where no melting occurs during the cutting, but the base metal undergoes microstructural changes under the influence of the resulting heat. At the very bottom, there is the base material.

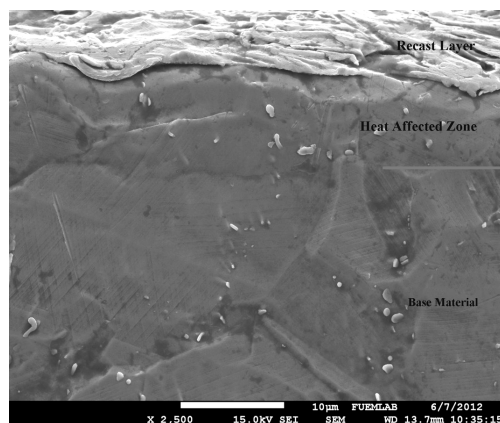


Figure 3: SEM of a kerf cross-section showing the RLT and HAZ
Slika 3: SEM-prikaz prečnega preseka zareze, ki kaže RLT in HAZ

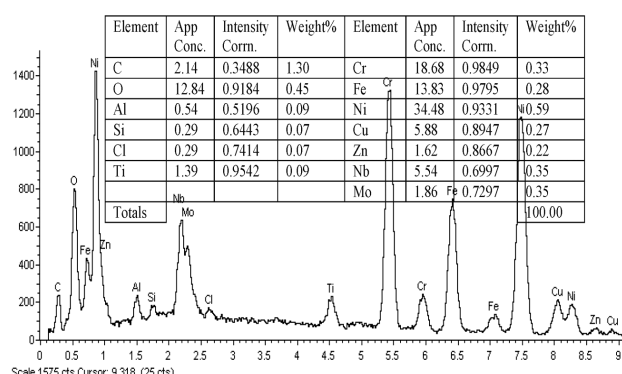


Figure 4: EDS analysis of the recast layer

Slika 4: EDS-analiza pretaljene plasti

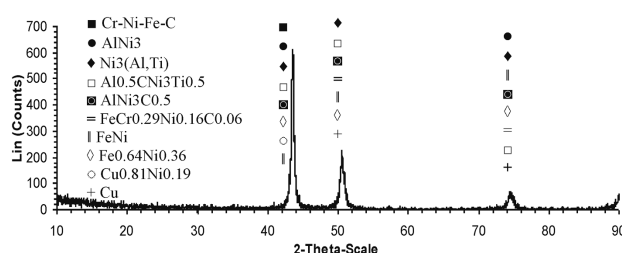


Figure 5: X-ray analysis of the recast layer

Slika 5: Rentgenska analiza pretaljene plasti

EDS and XRD results for the recast layer are provided in **Figures 4** and **5**. When the analyses are evaluated, the results show that the recast layer is enriched with oxygen and carbon. This phenomenon was explained by T. R. Newton et al.²⁰ to be the result of the electrolysis taking place in the dielectric liquid. In addition, the presence of copper and zinc compounds in the recast layer is evident. While Inconel 718 contains 0.08 % of mass fractions of Cu, the EDS results for the recast layer indicate that the density of Cu increases. Even though there is no Zn in the structure, the presence of this element in the recast layer indicates that these elements diffuse from the wire electrode into the workpiece, as reported in the previous studies.²¹

Table 4: Microhardness distribution through the cut surface section

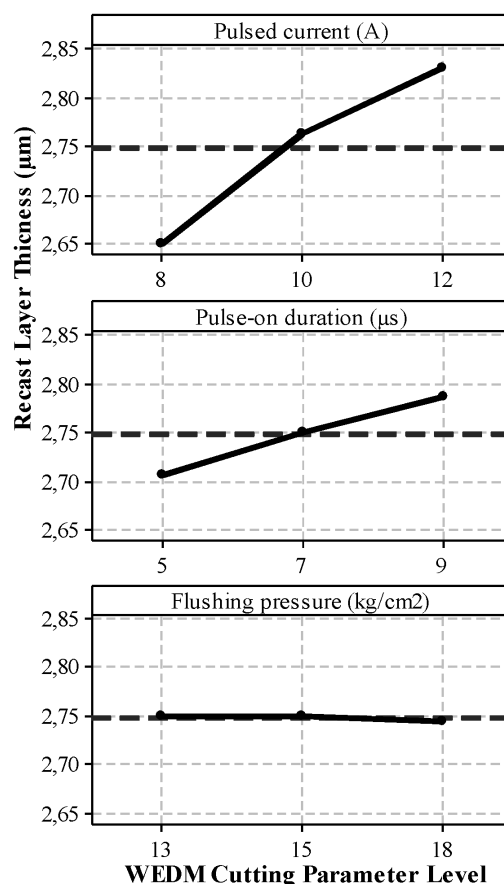
Tabela 4: Razporeditev mikrotvrdote skozi prerezano področje na površini

Measurement region	Experiment number								
	1	2	3	4	5	6	7	8	9
Base material	418	410	408	416	420	416	413	406	410
Recast layer	387	392	400	375	402	402	396	400	402
Heat-affected zone	415	474	422	424	426	412	418	410	418

Table 4 gives the average microhardness values for the three regions defined. While the hardness of the heat-affected region shows similarity to the base material, the microhardness of the recast layer shows a slight decrease when compared to the base material. The reason for this is assumed to be a decrease in the hardness of the recast layer, being a result of the dissolution

of the γ' (N_3Al,Ti) secondary phases and carbides back into the main matrix, after the heat treatment of the specimens. In their study, T. R. Newton et al.²⁰ indicated that the hardness of the recast layer reduces due to the wire-electrical-discharge machining of the age-hardened Inconel 718 alloy. In their study, a reduced chromium density in the recast layer and the existence of Cu and Zn in this region cause the properties of the region to change.

Since the outermost recast layer is in direct contact with the environment, the determination of the thickness of this layer plays an important role when assessing the finish cut. **Figure 6** shows the effects of the cutting parameters on the recast-layer thickness (*RLT*). In addition, in **Figure 7**, SEM images show a variation in the *RLT* depending on the experimental parameters. When these figures are analyzed, it is seen that while the effect of the circulation pressure on the recast layer is small, the effects of the current and the pulse duration are large. Under constant current conditions, the average *RLT* increases with the increasing pulse duration. Since the amount of heat transferred onto the surface of the work-piece increases with the increasing pulse duration, the amount of the material to be melted from the surface increases as well.

Figure 6: Main-effect plots of WEDM cutting factors for the *RLT*Slika 6: Diagrami glavnih vplivnih faktorjev pri WEDM rezanju na *RLT*

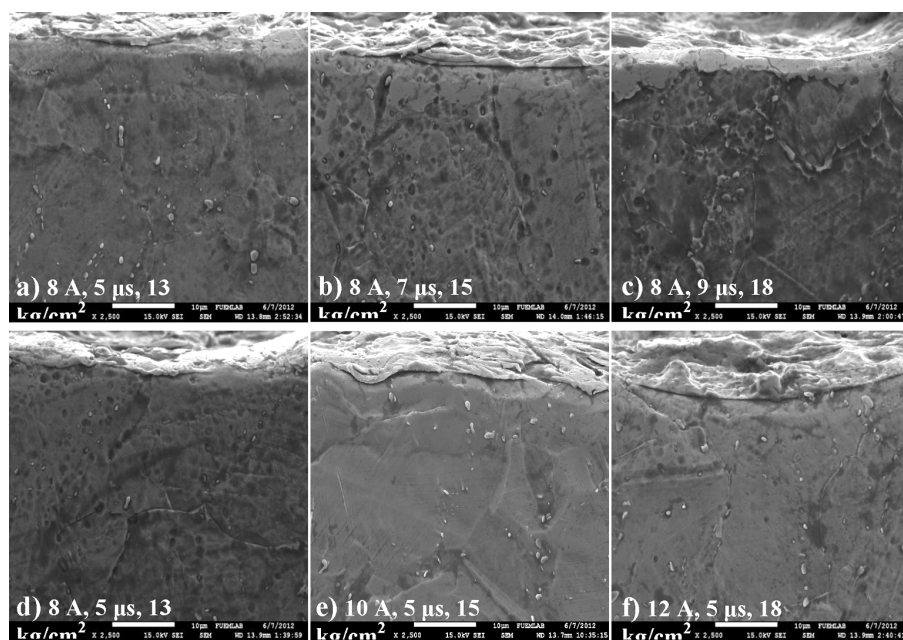


Figure 7: Cross-sectional SEM micrographs of a surface WEDM-processed under different machining conditions

Slika 7: SEM-posnetki presekov z WEDM obdelane površine pri različnih pogojih obdelave

As the pulse duration increases, the isothermal curves of the material spread more into the sublayers and the amount of the heat spreading under the surface covers a large area. This, in turn, causes a large region to be influenced by the heat and the *RLT* to increase.²² Moreover, the average *RLT* increases considerably with increased current values under constant pulse-duration conditions. As the current increases, the discharge energy gets more intense. High discharge energy causes more material to melt. In parallel with the thickness of the melted material, the *RLT* increases as well. In their study, Kanlayasiri and Boonmung¹⁰ mentioned that in the cases where the current and pulse duration were high, the machined surface was rougher and thermal damages were deeper since the discharge energy acting on the workpiece surface was more intense. For this reason, they indicated that the current and pulse duration should be kept at low levels, but also that in the cases where these two parameters are kept at low levels, the duration and cost of the machining process increase.

3.3 Effect of the cutting parameters on the surface roughness

During wire-electrical-discharge machining, the discharge energy released with each discharge produces a very high amount of heat at the point where the spark hits the workpiece. This heat causes small pieces on the surface to melt and detach via vaporization. Spherical chips removed from the surface with each discharge change the machined surface into a crater structure. The surface morphology depends on the sizes of the craters that form due to the contact between the sparks and the surface. Therefore, the surface profile is a function of the

current and pulse duration, determining the intensity of the applied sparks.²³

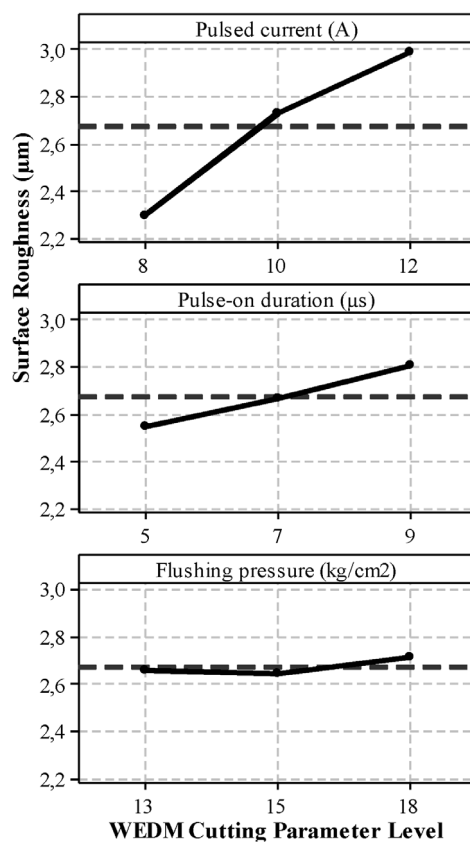


Figure 8: Main-effect plots of WEDM cutting factors for the surface roughness

Slika 8: Diagrami glavnih vplivnih faktorjev pri WEDM rezanju na hrapavost površine

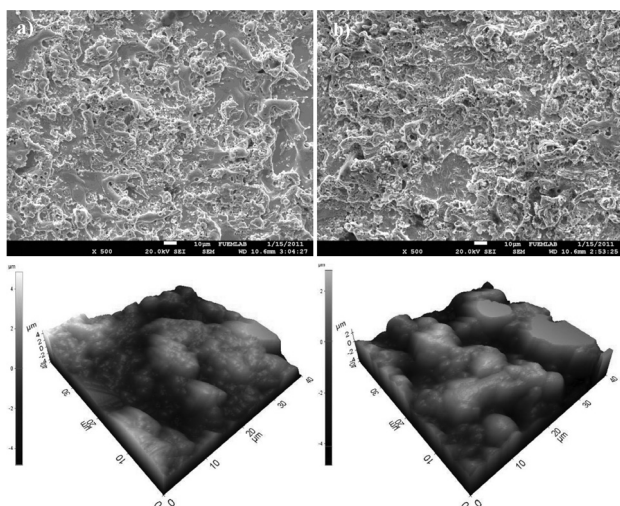


Figure 9: SEM and three-dimensional AFM images of the first and ninth experiments

Slika 9: SEM- in tridimenzionalni AFM-sliki prvega in devetega preizkusa

Figure 8 demonstrates the effects of the variables such as the current intensity, the pulse duration and the dielectric flushing pressure on the surface roughness, R_a . The fact that the current intensity and pulse duration have large effects on the surface roughness is clearly seen on the graphs. If the current is low, the intensity of the sparks that hit the surface of the piece with each discharge is also lower. This leads to a smoother surface due to a better erosion effect. Additionally, the amount of heat transferred to the surface of a piece decreases with a shortening pulse duration; therefore, less metal is melted. Thus, with the craters being more superficial, the surface roughness decreases.^{23,24}

The lowest surface roughness of $2.08 \mu\text{m}$ was measured at the end of experiment no. 1, while the highest surface roughness of $3.01 \mu\text{m}$ was measured at the end of experiment no. 9. In **Figure 9**, SEM and 3D AFM images of specimens 1 and 9 are shown. On the

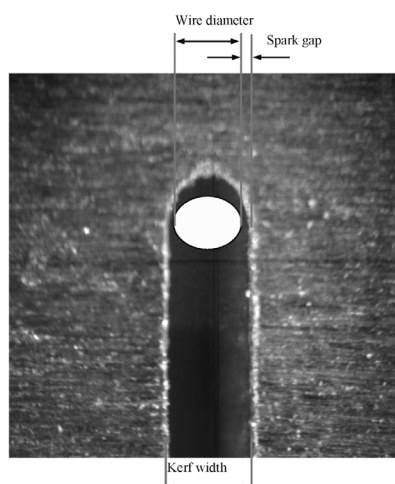


Figure 10: Schematic representation of the kerf width
Slika 10: Shematičen prikaz širine zareze

AFM image, it is possible to see the maximum and minimum heights of the surface profile and hillocks and valleys. A higher roughness can be assessed on the basis of the values for the Z depth of the AFM profile. When both figures are taken into account, it is observed that the surface-roughness values of the specimens show a tendency to decrease while all the cutting parameters decrease.

3.4 Effect of the WEDM parameters on the kerf width

Figure 10 shows a schematic representation of a kerf formed during wire-electrical-discharging. During wire-electrical-discharge machining, pieces are removed from the workpiece via melting as a result of the high temperature caused by spark discharges, occurring between the wire and the workpiece and the kerf occurs when these pieces are removed from the intermediate region with the liquid-circulation pressure. The kerf width varies depending on the parameters used during the machining. Alias et al.²⁵ proved that as the feed ratio increases, the kerf width decreases and, as a result of the experiments, low feed ratios increased the kerf width. Somashekhar and Ramachandran²⁶ did not recommend machining at high feed ratios as high feed rates increase the distortions in the kerf width. Tosun et al.²⁷ demon-

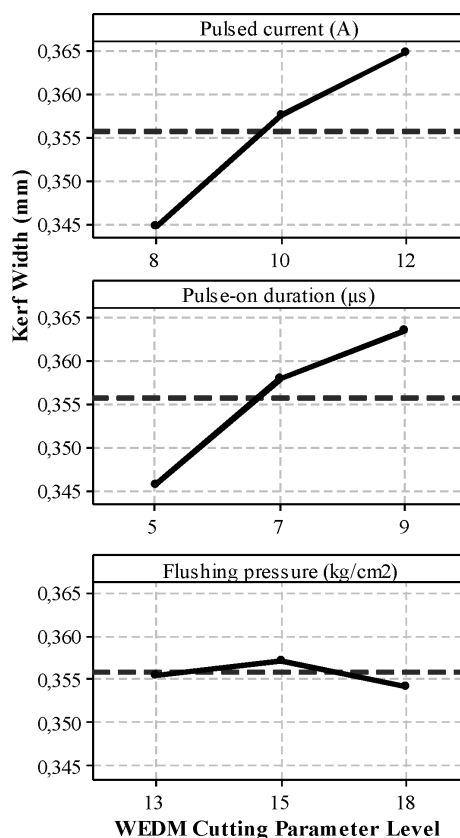


Figure 11: Main-effect plots of WEDM cutting factors for the kerf width

Slika 11: Diagrami glavnih vplivnih faktorjev pri WEDM rezanju na širino zareze

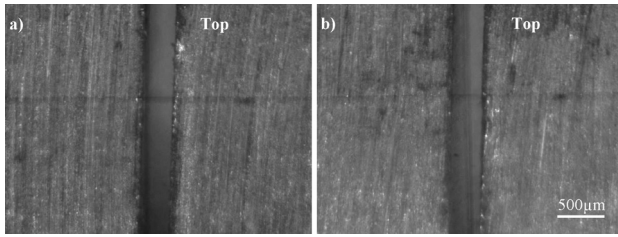


Figure 12: Light micrographs of the kerf width obtained at different cutting conditions: a) pulsed current = 8 A, pulse-on duration = 5 μ s, flushing pressure (kg/cm^2) = 13, b) pulsed current = 12 A, pulse-on duration = 9 μ s, flushing pressure (kg/cm^2) = 15

Slika 12: Svetlobna posnetka širine zareze, dobljena pri različnih pogojih rezanja: a) tok pulza = 8 A, trajanje pulza = 5 μ s, tlak splakovanja (kg/cm^2) = 13, b) tok pulza = 12 A, trajanje pulza = 9 μ s, tlak splakovanja (kg/cm^2) = 15

strated experimentally and mathematically that the open-circuit voltage and the pulse duration have a high influence on the kerf width and the material-lift ratio. They indicated that, for the kerf-width control, the voltage is three times more effective than the pulse duration.

Graphs showing the effects of the experimental parameters on the kerf width are given in **Figure 11**. As it can be seen, the average top kerf width varies dramatically, depending on the variations in the current intensity and pulse duration. An increase in the pulse duration causes a longer-term spark shock and, accordingly, the removal of more chips from the surface. As a result, depending on the amount of the chips removed from the cutting zone, the kerf width increases. Similarly, an

increase in the kerf width was observed with the increasing current intensity. If the current is low, the intensity of the sparks that hit the surface of the piece with each discharge is also low. High-intensity sparks lead to the widening of the kerf by creating a deeper corrosion effect on the surface.

Figure 12 gives images of specimens 1 and 9 where the lowest and highest kerf widths were obtained, respectively. Under the conditions of experiment 1 where the current intensity (8 A), pulse duration and liquid-circulation pressure (5 μ s, 1.27 MPa) were at their lowest values, the kerf width was measured as 0.335 mm. Under the conditions of experiment 9 where the current intensity, pulse duration and liquid-circulation pressure (12 A, 9 μ s, 1.47 MPa) were at their highest values, the kerf width was measured as 0.375 mm.

4 STATISTICAL ANALYSIS OF THE EXPERIMENTAL RESULTS

In this study, an analysis of the WEDM experimental results was performed using the analysis of variance (ANOVA) method. This method is used to statistically examine the impacts of the machining parameters on the operational performance. The experiment numbers and the measurements obtained at the end of the experiments are collectively presented in **Table 5**. The ANOVA results for the *RLT*, surface roughness and kerf width in the case of WEDM can be seen in **Tables 6 to 8**, respectively. According to the results in **Table 6**, the current intensity has a major effect of as much as 84 % on the

Table 5: Experimental results

Tabela 5: Rezultati eksperimentov

Exp. No	<i>RLT</i> (μ m)	Surface roughness (μ m)	Kerf width (mm)
1	2.61	2.08	0.335
2	2.65	2.31	0.348
3	2.69	2.51	0.351
4	2.73	2.61	0.349
5	2.76	2.69	0.359
6	2.80	2.89	0.365
7	2.78	2.95	0.353
8	2.84	3.00	0.367
9	2.87	3.01	0.375

Table 6: Results of ANOVA for the recast-layer thickness

Tabela 6: Rezultati ANOVA za debelino pretaljene plasti

WEDM cutting parameter	Degree of freedom (df)	Sum of square (SS_A)	Mean square	<i>F</i>	<i>P</i> (%)
Pulsed current (A)	2	0.04969	0.02484	15.11	83.65
Pulse-on duration (μ s)	2	0.00962	0.00481	0.58	16.16
Flushing pressure (MPa)	2	0.00008	0.00004	0.00	0.15
Error	–	–	–	–	0.04
Total	6	0.05939	–	–	100

Table 7: Results of ANOVA for the surface roughness

Tabela 7: Rezultati ANOVA za hrapavost površine

WEDM cutting parameter	Degree of freedom (df)	Sum of square (SS_A)	Mean square	<i>F</i>	<i>P</i> (%)
Pulsed current (A)	2	8.154	4.077	13.83	82.17
Pulse-on duration (μ s)	2	1.21	0.60	0.42	12.18
Flushing pressure (MPa)	2	0.16	0.08	0.05	1.57
Error	–	–	–	–	4.08
Total	6	9.524	–	–	100

Table 8: Results of ANOVA for the kerf width

Tabela 8: Rezultati ANOVA za širino reza

WEDM cutting parameter	Degree of freedom (df)	Sum of square (SS_A)	Mean square	<i>F</i>	<i>P</i> (%)
Pulsed current (A)	2	0.000636	0.000318	3.65	54.87
Pulse-on duration (μ s)	2	0.000508	0.000254	2.34	43.83
Flushing pressure (MPa)	2	0.000014	0.0000074	0.04	1.17
Error	–	–	–	–	0.13
Total	6	0.05939	–	–	100

RLT. The effect of the pulse duration on the *RLT* is 16 %, whereas the liquid-circulation pressure has no effect on the *RLT*. Similarly, **Tables 7 and 8** clearly show that the current intensity has a much larger effect on the surface roughness and kerf width than the pulse duration.

5 MATHEMATICAL MODELING OF THE EXPERIMENTAL RESULTS

In this study, mathematical modeling of the *RLT*, surface roughness and kerf width were performed by employing the multiple-linear-regression method on the results of the cutting experiments with WEDM. In addition, the appropriateness of the models obtained with the method of regression was investigated with ANOVA. Regression models with dependent parameters of the current intensity (I_p), pulse duration (T_{on}) and liquid-circulation pressure (P_s), and control parameters of the recast-layer thickness (*RLT*), surface roughness (R_a) and kerf width (K_w) are expressed as follows:

Recast-layer thickness

$$RLT = a_0 + a_1 \times I_p + a_2 \times T_{on} - a_3 \times P_s \quad (1)$$

Surface roughness

$$R_a = a_0 + a_1 \times I_p + a_2 \times T_{on} + a_3 \times P_s \quad (2)$$

Kerf width

$$K_w = a_0 + a_1 \times I_p + a_2 \times T_{on} - a_3 \times P_s \quad (3)$$

The regression and correlation coefficients obtained are presented collectively in **Table 9**. When these coefficients are substituted into the equations, the mathematical models of the recast-layer thickness (*RLT*), surface roughness (R_a) and kerf width (K_w) are obtained as:

$$RLT = 2.18 + 0.0450 \times I_p + 0.0200 \times T_{on} - 0.00140 \times P_s \quad (4)$$

$$R_a = 0.307 + 0.172 \times I_p + 0.0642 \times T_{on} + 0.0130 \times P_s \quad (5)$$

$$K_w = 0.278 + 0.00508 \times I_p + 0.00450 \times T_{on} - 0.000325 \times P_s \quad (6)$$

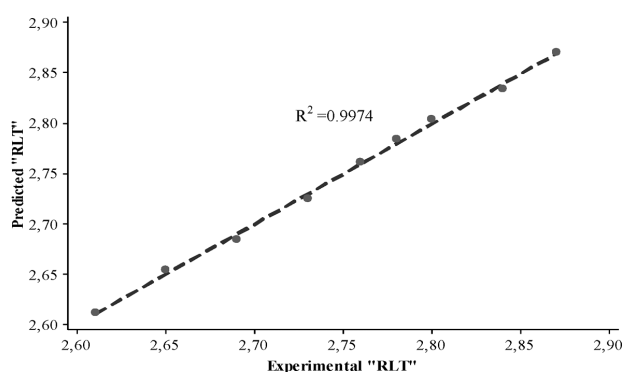


Figure 13: Comparison of experimental and predicted recast-layer thickness values

Slika 13: Primerjava eksperimentalno določene in napovedane debeline pretaljenega sloja

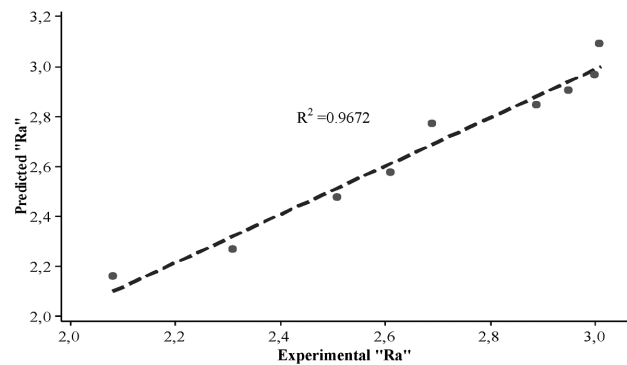


Figure 14: Comparison of experimental and predicted surface-roughness values

Slika 14: Primerjava eksperimentalno določene in napovedane hrpa-vosti površine

The correlation coefficients of the models from **Table 9** show that the models that are quite appropriate. Experimental values of the recast-layer thickness (*RLT*), surface roughness (R_a) and kerf width (K_w) are given in **Table 10** along with their predicted values calculated with the obtained mathematical models.

Table 9: Regression and correlation coefficients

Tabela 9: Regresijski in korelacijski koeficienti

	Regression coefficients	Correlation coefficients (r)			
		a_0	a_1	a_2	a_3
Recast-layer thickness	2.18	0.0450	0.0200	0.00140	98.1 %
Surface roughness	0.307	0.172	0.0642	0.0130	97.8 %
Kerf width	0.278	0.00508	0.00450	0.000325	95.9 %

Figures 13 to 15 show graphs of these values in their respective order. As it is seen on the figures, the experimental and numerical values show distributions quite close to the regression lines.

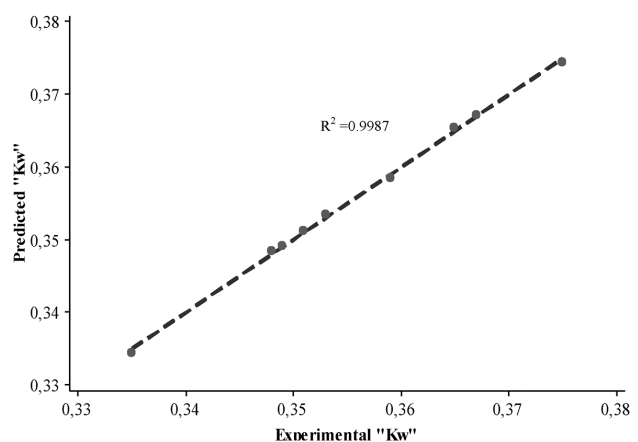


Figure 15: Comparison of experimental and predicted kerf-width values

Slika 15: Primerjava eksperimentalno določene in napovedane širine zareze

Table 10: Estimated values and calculations obtained with mathematical models**Tabela 10:** Določene in z dobljenim matematičnim modelom izračunane vrednosti

Exp. No	Recast-layer thickness	Surface roughness	Kerf width			
	Experimental RLT	Estimated RLT	Experimental R_a	Estimated R_a	Experimental K_t	Estimated K_t
1	2.61	2.61111	2.08	2.15889	0.335	0.334444
2	2.65	2.65444	2.31	2.26556	0.348	0.348444
3	2.69	2.68444	2.51	2.47556	0.351	0.351111
4	2.73	2.72444	2.61	2.57556	0.349	0.349111
5	2.76	2.76111	2.69	2.76889	0.359	0.358444
6	2.80	2.80444	2.89	2.84556	0.365	0.365444
7	2.78	2.78444	2.95	2.90556	0.353	0.353444
8	2.84	2.83444	3.00	2.96556	0.367	0.367111
9	2.87	2.87111	3.01	3.08889	0.375	0.374444

6 CONCLUSIONS

Based on the conducted research and investigations, the following conclusions can be drawn:

1. In the WEDM cutting process, the liquid-circulation pressure has little effect on the recast-layer thickness, surface roughness and kerf width, whereas the current and pulse duration are the most important parameters determining the quality of a cut. The highest quality cut was obtained with experiment 1 where the current and pulse duration were at their lowest values.
2. Considering the results of ANOVA, the intensity of the current was statistically found to have a larger effect on the surface roughness, kerf width and RLT than the pulse duration.
3. Taking the correlation coefficients into account, the obtained linear-regression models yield estimates with appropriate error rates. These results, in turn, show that the obtained models are appropriate.

7 REFERENCES

- ¹ A. Sharman, R. C. Dewes, D. K. Aspinwall, Journal of Materials Processing Technology, 118 (2001), 29–35, doi:10.1016/S0924-0136(01)00855-X
- ² A. Haşçalik, M. Ay, Optics & Laser Technology, 48 (2013), 554–564, doi:10.1016/j.optlastec.2012.11.003
- ³ M. Ay, U. Çaydaş, A. Haşçalik, Materials and Manufacturing Processes, 25 (2010), 1–6, doi:10.1080/10426914.2010.502953
- ⁴ E. O. Ezugwu, International Journal of Machine Tools & Manufacture, 45 (2005), 1353–1367, doi:10.1016/j.ijmachtools.2005.02.003
- ⁵ D. Dudzinski, A. Devillez, A. Moufki, D. Larrouquežre, V. Zerrouki, J. Vigneau, International Journal of Machine Tools & Manufacture, 44 (2004), 439–456, doi:10.1016/S0890-6955(03)00159-7
- ⁶ M. Ay, U. Çaydaş, A. Haşçalik, International Journal of Advanced Manufacturing Technology, 44 (2012), 439–456, doi:10.1007/s00170-012-4385-8
- ⁷ D. Scot, S. Boyina, K. P. Rajurkar, Int. J. Prod. Res., 29 (1991), 2189–2207, doi:10.1080/00207549108948078
- ⁸ P. Bley, J. P. Kruth, B. Lauwers, B. Schacht, V. Balasubramanian, L. Froyen, J. Van Humbeeck, Advanced Engineering Materials, 8 (2006), 15–25, doi:10.1002/adem.200500211
- ⁹ A. Haşçalik, U. Çaydaş, Journal of Materials Processing Technology, 148 (2004), 362–367, doi:10.1016/j.jmatprotec.2004.02.048
- ¹⁰ K. Kanlayasiri, S. Boonmung, Journal of Materials Processing Technology, 187–188 (2007), 26–29, doi:10.1016/j.jmatprotec.2006.11.220
- ¹¹ S. Kuriakose, M. S. Shunmugam, Materials Letters, 58 (2004), 2231–2237, doi:10.1016/j.matlet.2004.01.037
- ¹² M. İ. Gökler, A. M. Ozanözgü, International Journal of Machine Tools & Manufacture, 40 (2000), 1831–1848, doi:10.1016/S0890-6955(00)00035-3
- ¹³ S. F. Miller, C. C. Kao, A. J. Shih, J. Qu, International Journal of Machine Tools & Manufacture, 45 (2005), 1717–1725, doi:10.1016/j.ijmachtools.2005.03.003
- ¹⁴ R. Ramakrishnan, L. Karunamoorthy, Journal of Materials Processing Technology, 207 (2008), 343–349, doi:10.1016/j.jmatprotec.2008.06.040
- ¹⁵ S. H. Kang, D. E. Kim, KSME International Journal, 17 (2003), 1475–1484, doi:10.1007/BF02982327
- ¹⁶ C. Y. Bai, C. H. Koo, C. C. Wang, Materials Transactions, 45 (2004), 2878–2885, doi:10.2320/matertrans.45.2878
- ¹⁷ D. K. Aspinwall, S. L. Soo, A. E. Berrisford, G. Walder, CIRP Annals, 57 (2008) 1, 187–190, doi:10.1016/j.cirp.2008.03.054
- ¹⁸ M. S. Hewidy, T. A. El-Taweel, M. F. El-Safty, Journal of Materials Processing Technology, 169 (2005), 328–336, doi:10.1016/j.jmatprotec.2005.04.078
- ¹⁹ Y. S. Liao, J. T. Huang, H. C. Su, Journal of Materials Processing Technology, 71 (1997), 487–493, doi:10.1016/S0924-0136(97)00117-9
- ²⁰ T. R. Newton, S. N. Melkote, T. R. Watkins, R. M. Trejo, L. Reister, Materials Science and Engineering A, 513–514 (2009), 208–215, doi:10.1016/j.msea.2009.01.061
- ²¹ J. T. Huang, Y. S. Liao, W. J. Hsue, Journal of Materials Processing Technology, 87 (1999), 69–81, doi:10.1016/S0924-0136(98)00334-3
- ²² U. Çaydaş, Investigation of the Machinability of Ti6Al4V alloy by electrical discharge and electrochemical machining processes, PhD Thesis, Firat University Graduate School of Natural and Applied Sciences, 2008, 95–98
- ²³ Y. H. Guu, K. Hou, Materials Science and Engineering A, 466 (2007), 61–67, doi:10.1016/j.msea.2007.02.035
- ²⁴ H. Ramasawmy, L. Blunt, K. P. Rajurkar, Precision Engineering, 29 (2005), 479–490, doi:10.1016/j.precisioneng.2005.02.001
- ²⁵ A. Alias, B. Abdullah, N. M. Abbas, Procedia Engineering, 41 (2012), 1806–1811, doi:10.1016/j.proeng.2012.07.387
- ²⁶ K. P. Somashekhar, N. Ramachandran, J. Mathew, Int. J. Adv. Manuf. Technol., 51 (2010), 611–626, doi:10.1007/s00170-010-2645-z
- ²⁷ N. Tosun, C. Cogun, A. Gnan, Machining Science and Technology, 7 (2003), 209–219, doi:10.1081/MST-120022778

INFLUENCE OF DREDGED SEDIMENT ON THE SHRINKAGE BEHAVIOR OF SELF-COMPACTING CONCRETE

VPLIV IZKOPANIH SEDIMENTOV NA KRČENJE SAMOZGOŠČEVALNEGA BETONA

**Nasr-Eddine Bouhamou, Fouzia Mostefa, Abdelkader Mebrouki, Karim Bendani,
Nadia Belas**

LCTPE Laboratory, Civil Engineering Department, Mostaganem University, Route de Belahcel BP 227, 27000 Mostaganem, Algeria
bendani@yahoo.fr

Prejem rokopisa – received: 2013-10-16; sprejem za objavo – accepted for publication: 2015-02-10

doi:10.17222/mit.2013.252

Every year, millions of cubic meters of dams and restraints are dredged as part of the management and prevention procedures all over the world. These dredged sediments are considered as natural waste leading to environmental, ecological and even economic problems associated with their processing and depositing. Nevertheless, in the context of a sustainable development policy, a way of their management is open aiming at assessing the sediments as a building material and, particularly, as a new binder that can be industrially exploited and that can improve the physical, chemical and mechanical characteristics of the concrete. This study is a part of the research made at the Civil Engineering Department at the University of Mostaganem (Algeria) on the impact of the mud dredged from the Fergoug Dam on the behavior of self-consolidating concrete (SCC) in the fresh and hardened states, such as the mechanical performance and its impact on different deformations (shrinkage). The work aims to assess this mud in the SCC and to show possible interactions between the constituents. The obtained results provide the details needed for producing the SCC based on calcined mud.

Keywords: sediment, calcined mud, self-consolidating concrete, fresh state, hard state, shrinkage

Vsako leto po vsem svetu kot varovalni ukrep izkopljejo milijone kubičnih metrov sedimentov iz jezov in zadrževalnikov. Ti izkopani sedimenti so obravnavani kot naravni odpadki, ki povzročajo okoljske, ekološke in celo ekonomske težave pri njihovi predelavi ali odlaganju. Vseeno, v kontekstu politike trajnostnega razvoja je postavljena pot za njihovo obdelavo, za oceno teh sedimentov kot gradbenega materiala in še posebej kot novega veziva, ki ga je mogoče industrijsko izkoristiti in ki lahko izboljša fizikalne, kemijske in mehanske lastnosti betona. Ta študija je del raziskovalnega dela, opravljenega na oddelku za gradbeništvo Univerze v Mostaganemu (Alžirija), o vplivu izkopane mulje iz jezua Fergoug na vedenje samozgoščevalnega betona (SCC) v svežem in v strjenem stanju, na mehanske lastnosti in na različne deformacije (krčenje). Namen je oceniti to blato v SCC in pokazati morebitne interakcije med sestavinami. Prikazani rezultati so dobra možnost za izdelavo SCC na osnovi kalciniranega blata.

Ključne besede: sediment, kalcinirano blato, samozgoščevalni beton, sveže stanje, trdo stanje, krčenje

1 INTRODUCTION

This work addresses general problems associated with durable development. The search for new building materials indicates that the research is focused on the possibilities of reusing industrial and natural waste as an alternative to the currently used materials that will become scarce in the near future.

River sediments in dams can be seen as an environmental and economic threat. The big quantities generated by the silting phenomena make the authorities perplexed about their depositions.

An assessment of these sediments made in the area of civil engineering proved that they could be used as building materials (bricks, aggregates and cementitious materials).

As these studies are in their first step, the reuse of sediments in concrete is poorly documented, particularly for self-compacting concrete.

It is known that SCC contains a very high amount of a paste that requires a large quantity of cement; so, its

partial substitution with sediments can be a solution, reducing the use of cement.

2 IDENTIFICATION OF FERGOUG DAM

Regarded as one of the most silted dams in Algeria, the Dam of Fergoug (**Figure 1**) gave rise to the interest of several Algerian researchers who contributed various studies towards highlighting the causes, making it a disastrous dam.

These studies were primarily focused on explaining the phenomenon of silting, trying to find solutions for it and assessing the possibility of using the dredged sediments.^{1,2}

During its existence, the dam underwent several operations of dredging; the first one was carried out in 1984 and 1986 when more than 10 million m³ of mud were removed. The second operation of dredging was carried out in 1992 when 6.5 million m³ of mud was evacuated. The last operation was launched in 2005, at a cost of 800 million DA, which is 130 DA/m³, and carried out by the National Agency for Dams.

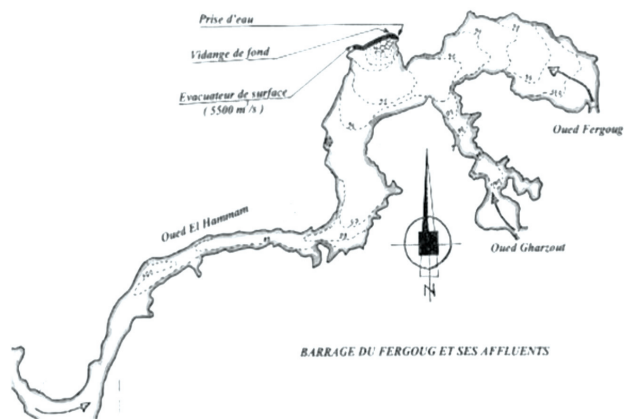


Figure 1: Fergoug Dam and its effluents

Slika 1: Jez Fergoug s pritoki

In spite of these various attempts, the rate of the current silting is estimated to be 97.77 % according to the bulletin published by the Agency for the Chergui Hydro Channel [ABHC]³.

3 MATERIALS AND METHODS

3.1 Used materials

3.1.1 Cement

The cement used was CEM I 42.5, made at the Zahana Factory (west of Algeria). The average physical and chemical characteristics of this cement are given in **Table 1**.

Table 1: Physical properties and chemical analysis of the cement
Tabela 1: Fizikalne lastnosti in kemijska analiza cementa

Physical properties of cement	
Bulk density (g/cm ³)	1.18
Specific gravity (g/cm ³)	3.13
Fineness (Blaine) (cm ² /g)	3180
Chemical analysis of cement, w/%	
SiO ₂	20.90
CaO	63.93
MgO	1.45
Fe ₂ O ₃	5.93
Al ₂ O ₃	5.10
SO ₃	0.86
Na ₂ O	0.17
K ₂ O	1.34
Loss on ignition	0.86
Carbonates	—
CO ₂	—
H ₂ O	0.6

3.1.2 Mud

The mud was taken downstream of the dam (**Figure 2a**) and activated thermally by burning it in a slow oven at a temperature of (750 ± 5) °C at a rate of 5 °C/min for 5 h, followed by steaming, crushing and sieving to 80 µm (**Figure 2b**). The calcined mud (**Figure 2c**) was obtained and stored away from the air and any moisture. The

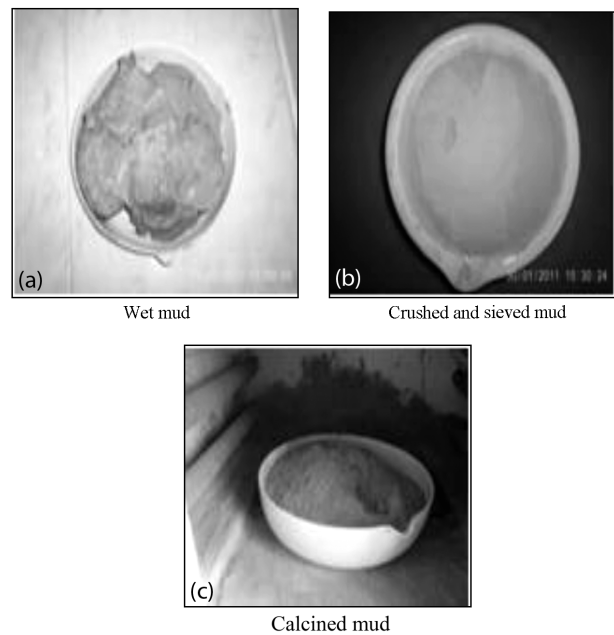


Figure 2: Mud-preparation stages

Slika 2: Stopnje priprave blata

Table 2: Physical characteristics of the calcined mud

Tabela 2: Fizikalne značilnosti kalciniranega blata

Test	Values
Bulk density (g/cm ³)	0.53
Specific gravity (g/cm ³)	2.62
Fineness (Blaine) (cm ² /g)	7964.00

Table 3: Chemical composition of the calcined mud

Tabela 3: Kemijska sestava kalciniranega blata

Component	Content, w/%
SiO ₂	54.69
CaO	14.25
MgO	3.08
Al ₂ O ₃	15.49
Fe ₂ O ₃	7.50
SO ₄	—
Loss on ignition	1.87

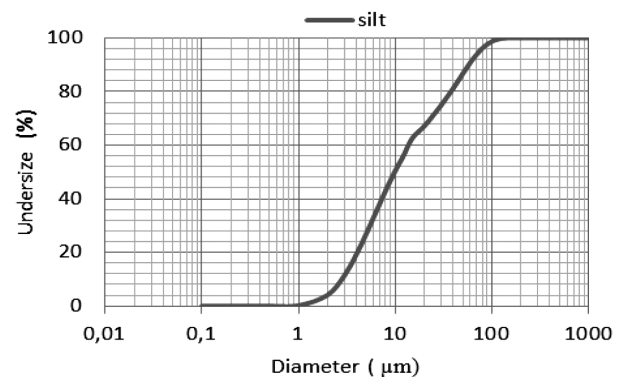


Figure 3: Fergoug-mud grain-size distribution (SIBELCO Laboratory, France, 2011)

Slika 3: Razporeditev velikosti zrn iz blata Fergoug (SIBELCO Laboratory, France, 2011)

physical and chemical characteristics of the calcined mud are presented in **Tables 2** and **3**.

The grain-size analysis of the mud was carried out at the SIBELCO Laboratory (France). The results of the analysis of this mud are shown with a grading curve in **Figure 3**.

3.1.3 Aggregates

The aggregates used in this work consist of broken particles of limestone with a well graded distribution, obtained from the quarry of Kristel (the Oran area) and the sand from the siliceous sea, from the quarry of Sidi Lakhdar (the area of Mostaganem). **Table 4** gives the characteristics of the aggregates for the whole of the concrete compositions.

Table 4: Physical characteristics of different aggregates

Tabela 4: Fizikalne značilnosti različnih agregatov

	Sea sand (Ss)	Quarry sand (Sc)	Gravel (G)	
Class	0/2	0/3	3/8	8/15
Nature	Silicious	Limestone	Limestone	Limestone
Specific gravity (g/cm ³)	2.56	2.68	2.66	2.66
Absorption (%)	–	–	0.86	0.40
Fineness modulus	1.64	2.63	–	–
Sand equivalent (ES)	83.18	88.96		

3.1.4 Admixture

The admixture employed is a superplasticizer provided by the GRANITEX Society, a high water reducer, containing synthesized polymers combined according to the NF EN 934-2 standard. The MEDAFLOW113 allows obtaining concretes and mortars of a very high quality, maintaining the workability and avoiding the segregation. Its density is 1.12 g/cm³ and its proportioning can vary from 0.8 % to 2.5 % of the binder mass.

3.2 Concrete mixtures

Four self-consolidating concretes were made to study the substitution effect of the cement with the calcined mud on the behavior in the fresh and hard states of the SCC. The concretes were made by adopting the method of the volume of the paste. The admixture proportioning is calculated in order to limit the segregation and bleeding and to obtain a distribution ranging between 60 cm and 75 cm.

The aggregate proportioning (*G/S*), the water/binder ratio (*W/B*) and the volume of the paste were kept constant for all the compositions of the SCCs. Tests were carried out on the concretes containing various percentages of the substitution mud with respect to the volume of cement, i.e., (10, 15 and 20) %. The compositions of various mixtures are presented in **Table 5**.

Table 5: Mix proportions of concretes

Tabela 5: Razmerje mešanic v betonih

Mix proportion (kg/m ³)	Concrete mixes			
	SCCR	SCCM10	SCCM15	SCCM20
Cement	450	420	408	395
Calcined mud	–	35	52	66
Water	225	218	216	213
Admixture	5.7	7.5	8.3	9.8
<i>W/B</i>	0.5	0.5	0.5	0.5
<i>Ss</i>	560	560	560	560
<i>Sc</i>	251	251	251	251
Gravel (3/8)	333	333	333	333
Gravel (8/15)	499	499	499	499

SCCR: Reference Concrete (0 % calcined mud)

SCCM10: Concrete with 10 % of calcined mud

SCCM15: Concrete with 15 % of calcined mud

SCCM20: Concrete with 20 % of calcined mud

3.2.1 Tests of the fresh concrete

The characterization made in the fresh state of the concretes was limited to the tests recommended by AFGC⁴ including the slump flow, L-box, sieve stability and bleeding.

3.2.2 Tests of the hardened concrete

3.2.2.1 Mechanical strength

The mechanical compressive strength is an essential characteristic of a concrete material and a fundamental parameter of our study. Consequently, its evolution was measured for all the formulations of concrete studied within this work.

The samples used to determine the mechanical compressive strength of various studied concretes are cylindrical test tubes with a diameter of 11 cm and a height of 22 cm. Once removed from the mold, they are preserved in water for a certain period (1, 7, 28 and 90) d. To measure the average tensile strength, three samples (7 cm × 7 cm × 28 cm) were broken at various ages by means of three-point-bending tensile tests.

3.2.2.2 Shrinkage deformation

It is interesting here to observe the deformations of the hardened material (after 24 h). For this purpose, two series of samples were produced and preserved in two different environments with and without a hydrous exchange with the external medium. The tests were performed to measure the total and endogenous shrinkage deformations. The shrinkage deformations were measured with a refractometer used on the prismatic test tubes with the size of 7 cm × 7 cm × 28 cm, placed in an air-conditioned room with a relative humidity of (20 ± 1) °C or (50 ± 5) %, according to the following two conditions:

- A hydrous exchange of the material with the environment: the total shrinkage is obtained and it represents the sum of the endogenous and drying shrinkages.
- No hydrous exchange with the environment because the test tubes are covered with one or two sheets of

self-adhesive aluminum paper: the endogenous shrinkage is identified.

The drying-shrinkage deformation is obtained from the difference between the total and endogenous shrinkage deformations.

Once removed from the mold, six test tubes relative to each concrete (three for the total shrinkage and three for the endogenous shrinkage) were tested over a very short period: first at its beginning, later the periodicity of the measurement increased with the time.

4 RESULTS AND DISCUSSIONS

4.1 Index and the activity coefficient of the calcined mud

The index of the activity noted, I_p , is defined as the ratio between compressive strengths $f_p(t)$ and $f_0(t)$ (Equation (1)) with respect to the strength of the standardized mortar containing 25 % of the calcined mud as the cement substitution p and the reference-mortar strength (with cement only) (Table 6):

$$I(p) = \frac{f_p(t)}{f_0(t)} \quad (1)$$

Table 6: Results of the compressive-crushing tests

Tabela 6: Rezultati tlačnih porušnih preizkusov

Age	$f_0(t)/\text{MPa}$	$f_p(t)/\text{MPa}$	$I(p)$
28 d	47.4	39.20	0.83
90 d	52.30	45.08	0.86

4.2 Fresh states

The characterization results carried out on the concretes are presented in Table 7.

Table 7: Workability test results

Tabela 7: Rezultati preizkusov obdelavnosti

Concrete	SCCR	SCCM10	SCCM15	SCCM20
Slump flow R/cm	66.5	65.4	63.6	63.3
$T_{50 \text{ cm/s}}$, slump flow	3.5	3.3	3.1	3.2
$(H_2/H_1)/\%$ (L-Box)	0.85	0.83	0.82	0.80
$T_{40/\text{s}}$ (L-Box)	3.4	3.5	3.7	3.6
$(H_2/H_1)/\%$ (L-Box)	8.47	7.55	6.90	4.55
Bleeding, ‰	1.25	1.18	1.12	1.15

4.3 Workability (slump-flow test)

It can be noted that all of the SCCs comply with the criterion of the flow spread where specified values lie between 63.3 cm and 66.5 cm (Figure 4), causing a lower viscosity. Although no limit is given for the times of the flow spread, the time needed to reach a 50 cm diameter (T_{50}) is close to the values usually noted, i.e., 3 s.

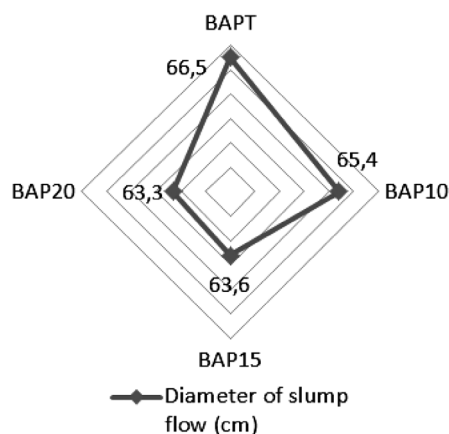


Figure 4: Diagram of the diameter of the slump flow

Slika 4: Diagram primera pri preizkusu razleza

4.4 Flowability (L-box test)

The L-box test is used to assess the filling and passing ability of SCC. This is a widely used test suitable for a laboratory as well as site use. A concrete can be accepted if the fill ratio (H_2/H_1) of the L-box is higher than 0.8⁴; the flowing times can be measured in order to assess the viscosity. The obtained results clearly show that the concrete present satisfies the ratio of 0.80–0.85.

4.5 Sieve-stability test

For this test, the results in Table 7 show that all the SCCs have a segregation rate lower than 15 %, indicating a good stability.⁴ When determined as $0 \leq \Pi \leq 5$ %, the resistance to the segregation is maintained to be "too significant" which is true in the case of SCCM20 where the paste is too viscous to run out through the sieve.⁵

4.6 Bleeding test

The results in Table 7 indicate that all the concretes meet the recommended value. The values obtained vary between 1.12 ‰ and 1.25 ‰.

4.7 Hardened state

4.7.1 Evolution of the mechanical compressive strength

According to the obtained results and curves represented in Figure 5, it is clear that the SCCR displays a good compressive performance at various testing stages compared to the concretes with the substitute material (SCCM). It is observed that over short periods the concretes have similar amplitudes; on the other hand, over long periods, their amplitudes start to move away from that of the SCC, except for the SCCM10, which displays a trend close enough to the SCCR observed between the 28th and 90th day.

The evolution of the compressive strength with respect to time shows that during a short-term period the

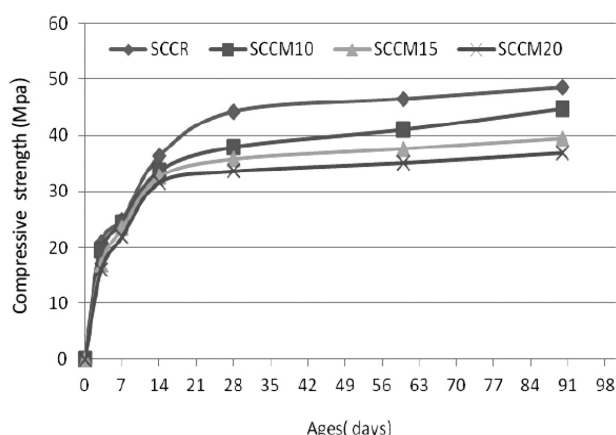


Figure 5: Compressive strength of concretes versus time

Slika 5: Tlačna trdnost betona v odvisnosti od časa

evolution rate of the strength of the SCCMs is developing more slowly than that of the SCCR; nevertheless, it can be noted that the variation between the measured values is slightly different, especially for the SCCM10.

The measured values indicate that the SCCR reached (48, 60 and 82) % of its compressive strength after 28 d for the testing ages of (3, 7 and 14) d, respectively. However, the SCCM10, SCCM15 and SCCM20 reached between 48–51 % after 3 d, 64–65 % after 7 d and 89–92 % after 14 d, which can only be explained with the densification effect. The calcined mud acted as the filler, filling in the pores and increasing the compactness of the cementitious matrix.

On the other hand, between the 28th and 90th day, it is the SCCM10 that evolves distinctly among the SCCMs. For these testing ages, the effect of the pozzolanic activity on the concretes can be distinguished. The evolution of this compressive strength can also be clearly noticed on the histogram presented in **Figure 6**, which also shows the effect of the variation of the *M/C* ratio (the proportioning of the mud to cement) on the strength evolution.

However, it is interesting to note that even with the 20 % substitution, the compressive strength remains

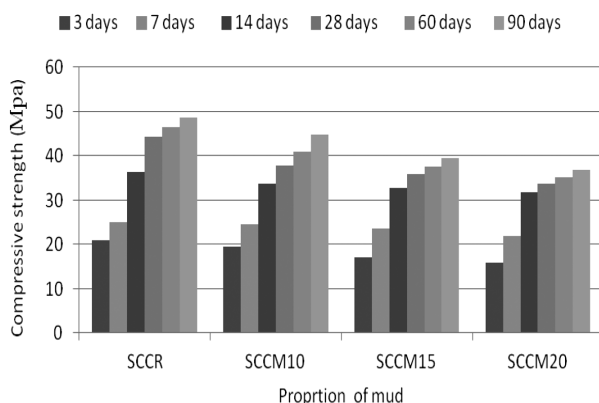


Figure 6: Histogram of evolution of the compressive strength with respect to the mud proportion

Slika 6: Histogram razvoja tlačne trdnosti glede na delež blata

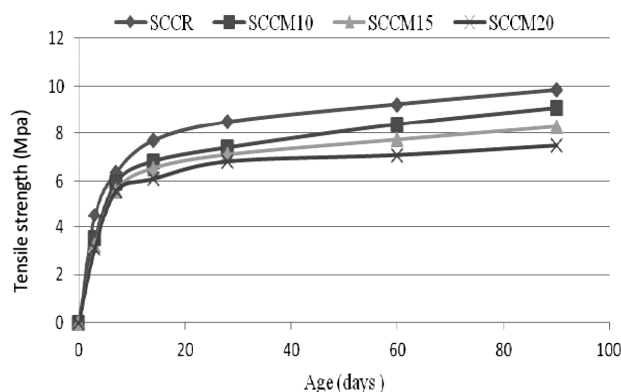


Figure 7: Evolution of the tensile strength at different ages

Slika 7: Razvoj natezne trdnosti pri različni starosti

within the reasonable limit of 30 MPa recommended by various construction specifications for building concretes.

4.7.2 Evolution of the mechanical tensile strength

It is known that the factors influencing the evolution of the compressive strength also influence the evolution of the tensile strength of concrete. The obtained results show that SCCMs developed a low tensile strength compared to the reference SCCR.

On **Figure 7**, we can see that the development of the tensile strengths follows the trend of the compressive strength and the evolutions of the strengths in the early period are identical, confirming the hypothesis that the mud acts as the filler.

It can also be noticed on **Figure 7** that the tensile strength of the SCCM10 displays a convergence towards that of the SCCR as of the 28th day with respect to the two other concretes, indicating a sufficiently attenuated amplitude.

Figure 8 clearly shows that the reference concrete exhibits the best performances followed by the SCCM10. In general, the loss of the resistance to compression or traction does not exceed the mean value of 25 % compared to the reference concretes irrespective of the age and the rate of substitution.

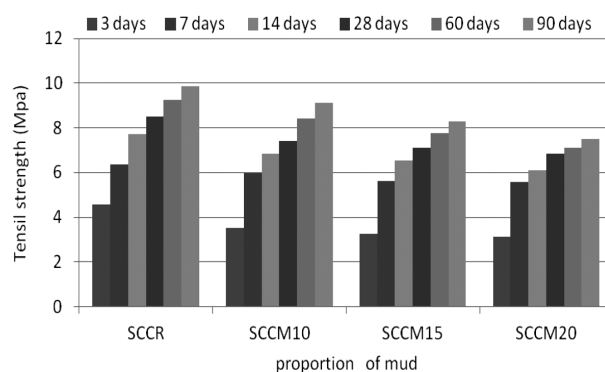


Figure 8: Histogram of the evolution of the tensile strengths with respect to the mud proportion

Slika 8: Histogram razvoja natezne trdnosti glede na delež blata

4.8 Different deformations

It is known that the factor with the highest influence on the shrinkage is the quantity of the water used. For this reason and in order to better determine the problem, the *W/B* ratio is kept equal to 0.5. The compositions of the tested SCCs only differ in the proportion of the calcined mud substituting the cement, so all the differences in the behavior of the concretes are related only to this parameter.

4.8.1 Endogenous shrinkage

The endogenous deformations measured from the first day onwards are displayed on **Figure 9**. The types of the kinetics of the endogenous-shrinkage deformations of the concretes are rather similar; at the beginning they take similar and almost identical forms and start to differ with time.

Since this shrinkage is a consequence of the hydration phase^{6,7}, it gives evidence of its kinetics and the quantity of formed hydrates. It can be observed that during the period from the 28th to 90th day, the orders of the magnitudes of the SCCMs approach that of the SCCR in comparison with the values displayed at the early age. At the 28th day, the SCCMs display reduced values, varying between 5.5 % and 15.5 % compared to the SCCR; on the other hand, between the 60 and 90th day, they are reduced by 4.6 % to 12.45 % compared to the SCCR, which shows that the deformations evolve in the same spindle, whereas the coming together of the values is a proof of the pozzolanic activity of the mud, which begins, a priori, after the 28th day.

The reduction in the endogenous shrinkage in the presence of the calcined mud can be explained with the fact that some hydrates (calcium aluminate) obtained via the pozzolanic reaction between the silica and the portlandite, are slightly expansive⁸, compensating for the dimensional variations due to the shrinkage.⁹ The shrinkages show the same development according to the mechanical compressive strength¹⁰, the auto-desiccation

known as the principal phenomenon, which governs the endogenous shrinkage growing under the influence of a high strength.

4.8.2 Drying shrinkage

This shrinkage develops from the surfaces exposed to the external environment; it is determined by calculating the difference between the total shrinkage and the endogenous shrinkage and it is presented with respect to time and mass loss. **Figure 10** shows that the curves obtained for the SCC appear in a spindle, indicating that, due to drying, the component is not modified by the *M/C* ratio. During the first phase, the values of the shrinkage of the SCCMs decrease compared to the SCCR, by the percentages varying between 21 % and 52 % on the 7th and 28th day. On the other hand, during the second phase, the evolution starts to slow down until becoming almost constant up to the 90 day. Thus, it can be noted that the difference between the measured values decreases compared to the first phase, as it varies between 16 % and 30 %, which proves that the amplitude of the shrinkage starts to stabilize.

Nevertheless, whatever the age, the SCCR always shows the highest values, contrary to the SCCMs as their values decrease with the increase in the rate of the calcined-mud substitution.

4.8.3 Mass loss

In order to try to improve the drying shrinkage, we also carried out follow-up tests of the test-tube mass shrinkage in order to quantify the hydrous exchanges.

The curves from **Figure 11** show that the mass losses are in agreement with the evolution of the drying shrinkage; the values of the mass loss are very high and almost identical as of the first day for all the concretes; all the curves start with a linear part whose slope seems to decrease slightly with the time. In the intermediate zone, the curves are strongly nonlinear, which explains the reduction to low values due to the evaporation. After 60 d, the mass losses start to decrease very slightly; they

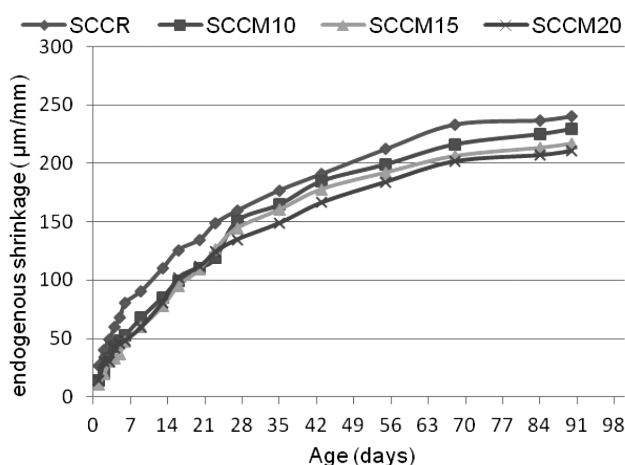


Figure 9: Evolution of the endogenous shrinkage versus time
Slika 9: Razvoj notranjega krčenja v odvisnosti od časa

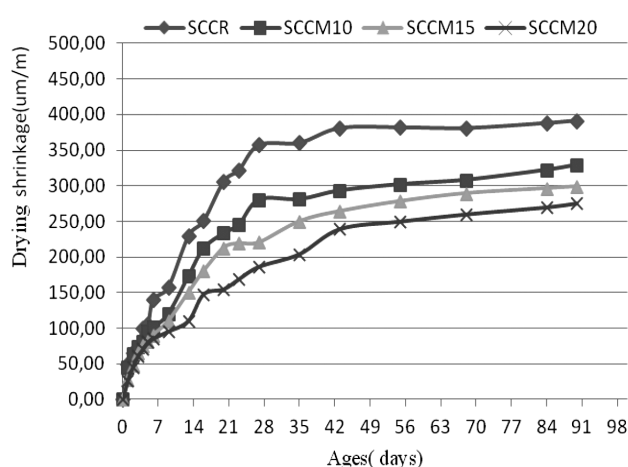


Figure 10: Evolution of the drying shrinkage versus time
Slika 10: Razvoj krčenja zaradi sušenja v odvisnosti od časa

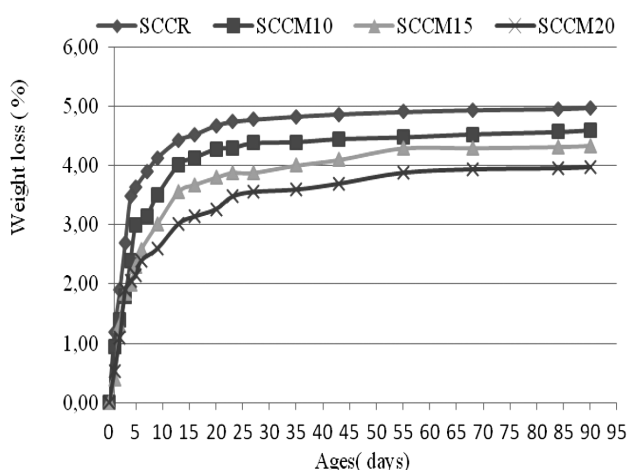


Figure 11: Evolution of the loss of mass versus time
Slika 11: Razvoj izgube mase v odvisnosti od časa

are weaker for the concrete with the mud-cement combination than for the reference concrete. Finally, the effect of the M/C ratio undoubtedly changes the hydrous-pressure development of the curves with respect to the degree of saturation.¹¹

Figure 12 also shows that various drying-shrinkage evolution curves for the mass loss are presented in two phases; the first schematizes the first water departure without any consequence for the shrinkage, while the second one schematizes the evolution of the shrinkage with the water loss. The explanation is based on the type of water and two families of pores: the water contained in the large pores leaves the material without causing a shrinkage, whereas the water contained in the small pores generates contractions of the material.¹²

4.8.4 Total shrinkage

It evolves very quickly for all the types of the test tubes kept in the air because of their sizes that make the desiccation more favorable. At the early stage, the shrinkage is almost independent of the composition of

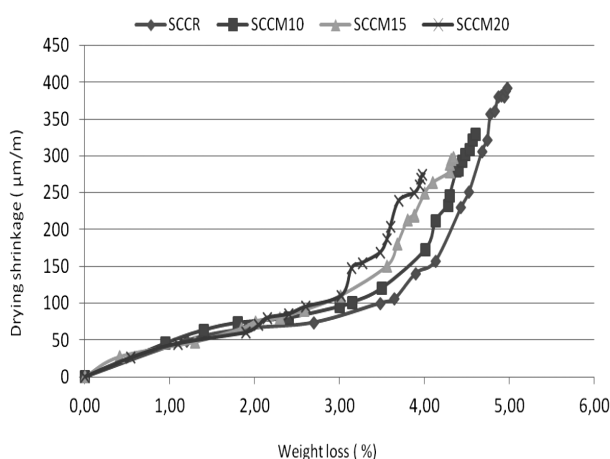


Figure 12: Drying shrinkage versus the loss of mass
Slika 12: Krčenje pri sušenju v odvisnosti od izgube mase

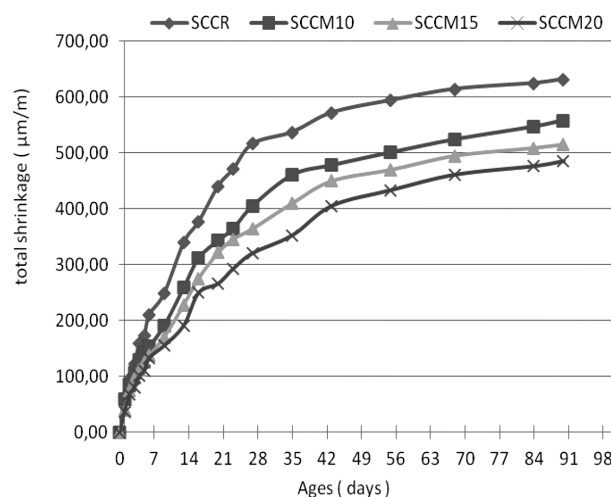


Figure 13: Evolution of the total shrinkage versus time
Slika 13: Razvoj skupnega skrčka v odvisnosti od časa

the concrete. The values of the shrinkage are concentrated in the same spindle and the effect of the addition takes place only after the first week, with a slight superiority for the SCCR. After a long period, the presence of the mud decreases the final shrinkage with respect to the proportion of the substitute material.

Figure 13 shows a similar evolution of deformation for all the SCCs. This is the reason why at the very early stage we find it difficult to distinguish between the representative graphs for each concrete. The order of the magnitude on the 7th day presents reductions, which vary from 14 % to 36 % for the SCCMs compared to the SCCR. After the 7th day, the shrinkage of the reference SCC evolves much more quickly and it is distinguished from the others up to the 90th day, having a similar amplitude.

It is also observed that for this shrinkage the reference SCC shows the highest values at all stages.

On **Figure 14**, the total shrinkage is plotted with respect to the $\lg(t)$ scale, rather than the drying shrinkage,

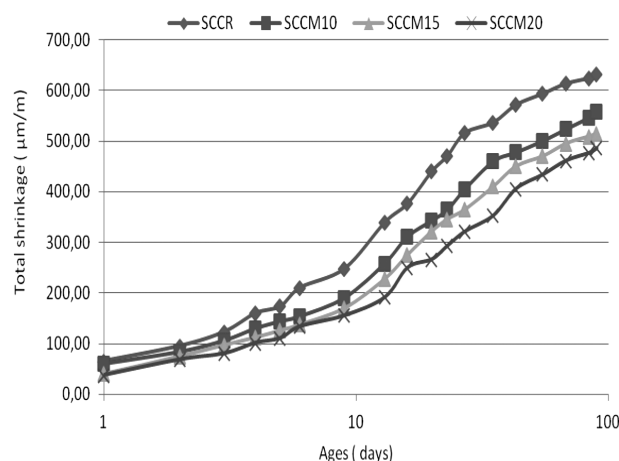


Figure 14: Total shrinkage according to the logarithmic scale
Slika 14: Skupen skrček prikazan v logaritmski skali

which is only a low estimate. Three phases appear; during the first one, the shrinkage gradually increases, during the second one, it evolves linearly with the logarithm of time and during the third one, the curve of the shrinkage inflects towards an asymptotic value.

5 CONCLUSIONS

Our study made it possible to confirm the possibility of using the mud from the Fergoug Dam as a partial substitute material for cement.

The principal conclusions obtained are as follows:

1. The study of the behavior of the SCC in the fresh state, with respect to the proportioning of the calcined mud, allows us to make the following observations:
 - The results indicate that the SCCs containing calcined mud are more viscous and less workable compared to the reference concrete because, beyond the critical proportioning, the viscosity of the concrete increases with the increased amount of the substitute material.
 - Only the SCCM20 presented too large a segregation according to the sieve test.
 - In addition to the bleeding test, the values obtained with the tests of the simple flow, the L-box and the sieve stability decrease when the proportion of the calcined mud increases.
 - A densification of the microstructure had a favorable effect by decreasing the bleeding, thus providing us with an idea on the improvement of the paste/aggregate interface.
2. In the hardened state, the mechanical tests of the compressive and tensile strengths carried out on the test tubes made of self-consolidating concrete with various amounts of the mud, in comparison with the reference concrete made of cement alone, gave the following results:
 - The evolution of the strength is influenced by the M/C ratio (the rate of the substitution of cement with the calcined mud); the results indicate that the compressive and tensile strengths decrease with the increase in the calcined-mud content; these values are very tolerable for the concretes employed for buildings constructions.
 - The best values of the SCCM compressive and tensile strengths are obtained with the SCCM10, but the SCCR always exhibits the highest values. However, the use of a mineral addition involves the formation of a new CSH, which fills in the pores of the hardened cement paste and densifies the structure of the paste, leading to a reduction in the porosity. These effects lead to an improvement of the mechanical strength.
3. With the tests of different deformations, carried out on the same concretes, we followed the evolution of free deformations in endogenous and drying conditions. The obtained results show that the calcined mud tends to slightly decrease the variety of deformations and it can be concluded that their kinetics is associated with the physicochemical mechanism, so:
 - The endogenous shrinkage decreases with the increase in the proportioning of the substitute calcined mud.
 - The compactness of the microstructure and the refinement of the pores lead to a fall in the permeability and prevent the diffusivity of water, consequently, decreasing the drying shrinkage and the mass loss.
 - The total shrinkage follows the same principle, being influenced by the endogenous shrinkage more than by the drying shrinkage; it also decreases in accordance with the M/C ratio, exhibiting a trend whereby the total shrinkage is an intrinsic phenomenon of the concrete.
 - The analysis of the phenomenon of shrinkage in the presence of calcined mud indicates that this addition contributes to a decrease in the shrinkage amplitudes compared to the reference concrete. The 20 % substitution seems to be the best option with respect to its contribution to the improvement of the microstructure and, finally, to the decrease in the shrinkage effects.
4. Finally, it is deduced that the calcined mud, due to its reactivity and fineness, influences the mechanical and other properties of the concretes:
 - The pozzolanic reaction starts to be perceptible over a long period by improving the compressive and tensile strengths.
 - The 10 % substitution of cement is the optimum content to give the best mechanical performances, followed by the 15 % and 20 % substitutions.
 - The 20 % substitution is the optimum solution for a reduction in the shrinkage and mass loss due to an improvement in the microstructure, making the matrix more compact and minimizing the diffusivity, followed by the 15 % and 10 % substitutions.
 - In conclusion, it can be deduced that the substitution of 15 % of cement by the mud is the most interesting option that proves to be optimal since it is the average proportion that satisfies the two criteria: the strength improvement and the shrinkage reduction.

6 REFERENCES

- ¹ B. Remini, Qualification du transport solide dans le bassin versant de l'oued Isser, Application à l'envasement du barrage de Béni Amrane, 2^{ème} CMEC Alger, 2002
- ² A. Semcha, Valorisation des sédiments de dragage: Applications dans le BTP, cas du barrage de Fergoug, Doctoral Thesis, University of Reims, Champagne-Ardenne, France, 2006
- ³ ABHC, Agence du bassin hydrographique Chott-Chergui de l'ouest, 2007
- ⁴ AFGC, Bétons Auto-Plaçants Recommandations provisoires, Association française de Génie Civil, 2008

- ⁵ F. Cussigh, M. Sonebi, G. Schutter, Project testing SCC-segregation test method, Proceedings of the Third international RILEM conference on self-compacting concrete, 2003, 311–322, http://www.rilem.org/gene/main.php?base=500218&id_publication=38
- ⁶ Andra, Référentiel géologique du site de Meuse/Haute-Marne sur le stockage géologique des déchets radioactifs à haute activité et à vie longue, Tome 2: matériaux cimentaires, 2005
- ⁷ I. Yurtdas, Couplage comportement mécanique et dessiccation des matériaux à cimentaire: étude expérimentale sur mortiers, Doctoral Thesis, Université des sciences et technologie de Lille, 2003
- ⁸ L. Courard, A. Darimont, M. Sschouterden, F. Ferauche, X. Willem, R. Degeimbre, Durability of mortars modified with metakaolin, Cement and Concrete Research, 33 (2003) 9, 1473–1479, doi:10.1016/S0008-8846(03)00090-5
- ⁹ J. J. Brook, M. A. Megat Johar, Effect of metakaolin on creep and shrinkage of concrete, Cement and Concrete Research Composite, 23 (2001), 495–502, doi:10.1016/S0958-9465(00)00095-0
- ¹⁰ B. Persson, Self-desiccation and its importance in concrete technology, Materials and Structures, 30 (1997) 5, 293–305, doi:10.1007/BF02486354
- ¹¹ P. Turcry, Retrait et fissuration des bétons autoplaçants: influence de la formulation, Doctoral Thesis, Ecole Centrale de Nantes, France, 2004
- ¹² A. Neville, Properties of Concrete, 4th Edition, John Wiley and Sons, 1996

STUDY OF THE PROPERTIES AND HYGROTHERMAL BEHAVIOUR OF ALTERNATIVE INSULATION MATERIALS BASED ON NATURAL FIBRES

ŠTUDIJ LASTNOSTI IN HIGROTHERMALNO OBNAŠANJE ALTERNATIVNIH IZOLACIJSKIH MATERIALOV NA OSNOVI NARAVNIH VLAKEN

Jiří Zach, Martina Reif, Jitka Hroudová

Brno University of Technology, Faculty of Civil Engineering, Veveří 331/95, 602 00 Brno, Czech Republic
zach.j@fce.vutbr.cz, reif.m@fce.vutbr.cz, hroudova.j@fce.vutbr.cz

Prejem rokopisa – received: 2014-08-01; sprejem za objavo – accepted for publication: 2015-03-02

doi:10.17222/mit.2014.169

The paper describes the results of a research focused on the development of natural thermal and acoustic insulation materials. They are mainly materials based on locally available agricultural waste (mainly in the third-world countries). In particular, this waste includes stems of rice and other plants. The paper describes the behaviour of these materials under different humidity conditions and the possibility to influence their properties by varying the ratio between organic and inorganic binders. Using the results, general conditions for the suitability of the application of these materials in building constructions were defined.

Keywords: natural fibres, moisture content, thermal conductivity, rice stems, cotton stems, thermal insulation

Članek opisuje rezultate raziskav usmerjenih v razvoj naravnih materialov za toplotno in akustično izolacijo. To so pretežno materiali, ki predstavljajo lokalno dosegljive kmetijske odpadke (večinoma v tretjem svetu). To so zlasti stebila riža in drugih rastlin. Članek opisuje obnašanje teh materialov pri različnih pogojih vlažnosti in možnosti za vplivanje na njihove lastnosti pri različnih razmerjih organskih in anorganskih veziv. Na podlagi rezultatov so bili določeni splošni pogoji za primernost in uporabnost teh materialov v gradbeništvu.

Ključne besede: naravna vlakna, vsebnost vlage, toplotna prevodnost, stebila riža, stebila bombaža, toplotna izolacija

1 INTRODUCTION

Considering the ever-increasing demand for insulation materials, the general need for a sustainable development and an effort to limit the exploitation of raw-material sources, fibrous insulation materials based on organic fibres from agriculture (hemp, flax, waste textile fibres, rice and cotton-plant stems, sheep wool, etc.) have been developed at Brno University of Technology, Faculty of Civil Engineering, for many years. The development of these materials was also carried out with regard to the findings of foreign experts recorded in the literature in specialized databases (Thomson Reuters, Scopus). We considered the research of the scientific teams from Europe and Asia.¹⁻⁸

These materials represent highly progressive building materials with a low carbon footprint and a low primary-energy input. They are locally available and easily renewable raw materials that can substitute non-renewable materials used in the production of insulation materials (e.g., foam plastic materials). In addition, the production of these materials has lower energy costs compared to the production of many modern synthetic insulators (e.g., mineral wool). The experiments performed during the previous research revealed that these materials show properties comparable with the synthetic

insulation materials available on the market.⁹ However, in terms of the thermal-insulation properties, these natural fibre-based materials exhibit a different hygrothermal behaviour due to different structures of the insulations and also a low thermal conductivity of the natural fibres compared to the glass or mineral ones.

2 INPUT RAW MATERIALS AND TEST MIXTURES

For the production of specimens, alkali-activated blast-furnace slag containing SiO₂ (42.24 %), CaO (44.87 %), Al₂O₃ (2.73 %) and MgO (5 %) was used with Fe₂O₃, MnO, TiO₂, P₂O₅, Na₂O, K₂O and sodium water glass. Rice and cotton-plant stems were used as the organic binders. The specific quantities of the raw materials are listed in **Table 1**.

Table 1: Overview of the specimen compositions

Tabela 1: Pregled sestave vzorcev

Mixture No.	Rice stems (kg m ⁻³)	Cotton stems (kg m ⁻³)	Slag (kg m ⁻³)	Water glass (kg m ⁻³)
1	100	–	300	200
2	120	–	250	190
3	–	100	300	200

3 METHODOLOGY

After removing the formwork, the specimens were stored under laboratory conditions at 23 ± 2 °C and a relative humidity of 50 ± 5 %. After 28 d, the specimens were dried and their bulk density was determined according to EN 1602.¹⁰ Subsequently, hygroscopicity was determined for the specimens stored at +23 °C and different relative-humidity conditions. The equal-sorption humidity as well as the thermal conductivity depending on the humidity were determined. The thermal conductivity was determined at the stable state in accordance with EN 12667¹¹ and ISO 8301.¹² Acoustic properties were also determined for the specimens. Specifically, the dynamic stiffness of the material was determined in accordance with ISO 9052-1¹³ and the sound-absorption coefficient was determined in accordance with EN ISO 11654¹⁴ and ISO 10534-1.¹⁵

4 RESULTS AND DISCUSSION

The bulk density was determined for the samples in the dried state in accordance with EN 1602¹⁰ and the specific values are shown in **Table 2**.

Table 2: Summary of individual bulk densities ρ_v of the specimens
Tabela 2: Pregled posameznih gostot ρ_v vzorcev

Mixture No.	1	2	3
ρ_v (kg m ⁻³)	440	430	430

The average bulk density ranged from 430 kg m⁻³ to 440 kg m⁻³ and its values for different fillers in mixtures 1 and 3 were also comparable. Next, the moisture content under laboratory conditions was determined. The samples were stored in the laboratory, at the temperature of 23 °C and the relative humidity of 50 % and were subsequently dried at a temperature of 105 °C. Afterwards, the natural-moisture content prior to drying was measured using the gravimetric method. The resulting values are shown in **Figure 1**.

The natural-water content of a material depends on the amount of the pores present in the material, their

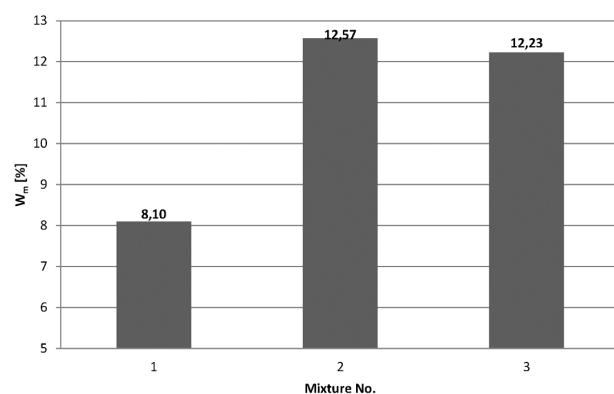


Figure 1: Natural-moisture content (w_m [%])

Slika 1: Vsebnost naravne vlage (w_m [%])

size, openness and the degree to which they are interconnected. The pore system depends on the compaction during the production, the amount of inorganic binders and the choice of organic fillers. It is clear from the graph that the cotton-stem sample has a higher natural moisture than the specimen with the same amount of rice stems. Increasing their amounts also increases the natural moisture. In addition, hygroscopicity of the specimens was determined. The specimens were stored in the environments with the following parameters:

- in laboratory conditions – a relative humidity of 50 % and a temperature of 23 °C
- in humid conditions – a relative humidity of 95 % and a temperature of 23 °C

The amounts of the moisture absorbed by the specimens into their structures are listed in **Table 3**.

Table 3: Summary of measured moistures w_m at varied relative humidity φ and temperature of +23 °C

Tabela 3: Povzetek izmerjenih vlažnosti w_m pri spreminjanju relativne vlažnosti φ in temperaturi +23 °C

φ [%]	Mixture No. 1	Mixture No. 2	Mixture No. 3
	w_m [%]		
0	0	0	0
50	8.10	12.57	12.23
95	33.04	47.00	42.11

A sorption curve was constructed from the obtained data. The determination of the sorption isotherm was carried out at 23 °C. The moisture content of the specimens was measured at the relative-humidity levels of 50 and 95 %. The results of the measurement are shown in **Figure 2**.

The amount of the absorbed moisture depends on the structure of the given material, the temperature and the relative humidity of the environment, to which the material is exposed. With its growing value, the moisture content in the material rises nonlinearly.

In the next stage, the thermal conductivity in dependence on the specimen moisture was determined in

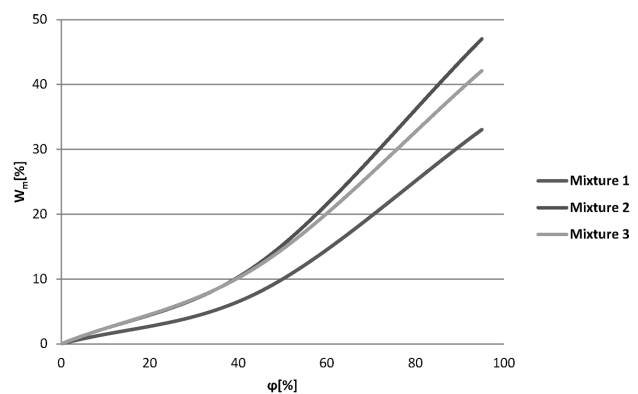


Figure 2: Moisture content w_m for the samples depending on relative humidity φ at the temperature of 23 °C

Slika 2: Vsebnost vlage w_m v vzorcih, v odvisnosti od relativne vlažnosti φ pri temperaturi 23 °C

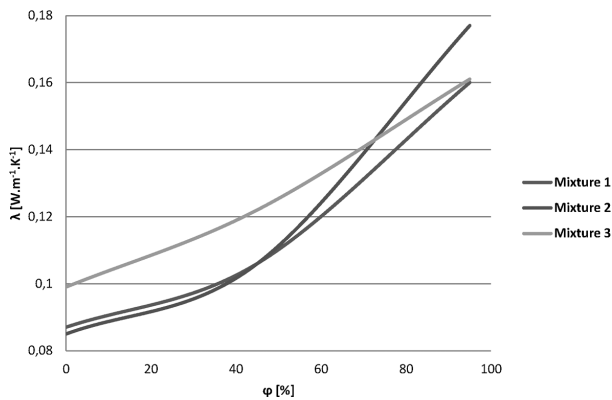


Figure 3: Dependence of thermal conductivity λ on relative humidity φ
Slika 3: Odvisnost toplotne prevodnosti λ od relativne vlažnosti φ

accordance with EN 12667¹¹ and ISO 8301.¹² The measurement was carried out at the natural weight moisture content state, at dry and at moist state. The results are listed in **Table 4** and **Figure 3**.

Table 4: Thermal conductivity λ in dependence on relative humidity φ
Tabela 4: Toplotna prevodnost λ v odvisnosti od relativne vlažnosti φ

Mixture No.	$\varphi/\%$	0	50	95
1	$w_m/\%$	0	8.10	33.04
	λ (W m ⁻¹ K ⁻¹)	0.087	0.106	0.160
2	$w_m/\%$	0	12.57	47.00
	λ (W m ⁻¹ K ⁻¹)	0.085	0.106	0.177
3	$w_m/\%$	0	12.23	42.11
	λ (W m ⁻¹ K ⁻¹)	0.099	0.122	0.161

As **Figure 3** indicates, the thermal conductivity depends on the relative humidity; as its value increases, the value of the thermal conductivity increases as well. This is most apparent for the specimens containing the organic cotton-plant filler. Among the specimens containing rice stems, the thermal conductivity in the damp condition significantly increased for specimen 2 with a lower content of binder and a higher porosity (it is possible to see it in the area where the relative humidity was above 50 %). Next, the dynamic stiffness of the material was tested using the resonance method in accordance with ISO 9052-1.¹³ The measured values are listed in **Table 5**, including the category pad and acoustic-material group.¹⁶

Table 5: Summary of dynamic stiffness s'

Tabela 5: Povzetek dinamične togosti s'

Mixture No.	s' (MPa m ⁻¹)	Category pad*	Acoustic-insulation properties*
1	10.91	Category I	Dynamically soft
2	13.15	Category I	Dynamically soft
3	12.47	Category I	Dynamically soft

* according to CSN 730532¹⁶

It can be assumed from the obtained values that all the specimens have good acoustic-insulation properties

in terms of the impact sound and can be classified as the group of dynamically soft acoustic-insulation materials for which $s' \leq 30$ MPa m⁻¹ applies. Considering the dynamic-stiffness values, the materials can be used as impact-sound insulators. Finally, the sound-absorption coefficient was determined. The measurement was carried out using an acoustic resonator in accordance with ISO 10534-1¹⁵ and from the obtained values the weighted sound-absorption coefficient α_w was calculated in line with EN ISO 11654.¹⁴ The resulting values are in **Table 6**, listing different sound-absorption categories.

Table 6: Weighted sound-absorption coefficient α_w for the frequency of 500 Hz

Tabela 6: Izmerjeni koeficient vpijanja zvoka α_w pri frekvenci 500 Hz

Mixture No.	α_w (-)	Class of sound absorption
1	0.75	C
2	0.80	B
3	0.90	A

It is clear from **Table 6** that the highest value of the weighted sound absorption was found for specimen 3, with the cotton-plant stems. Among the samples containing the rice-plant stems, specimen 2, with a higher amount of organic fillers and a reduced binder amount, has higher values.

5 CONCLUSION

The research into the possibility of using agricultural waste from the rice and cotton production brought interesting findings for the production of thermal and acoustic-insulation materials. The structure of the specimens was very porous as the coarse fractions of cotton and rice stems form an open porous system. The developed materials reached good values of the thermal conductivity, which can be influenced by increasing or reducing the amounts of the fillers or the binders. The amount of water glass must be chosen according to the need for activating the slag used. The thermal-conductivity value is also influenced by the sensitivity of the material to the relative humidity. In terms of the acoustic properties, the materials acted as good sound absorbers. Especially the porous structure created by cotton stems exhibited high values of the sound-absorption coefficient. To find the optimum formula for the lowest possible values of the thermal conductivity and good acoustic properties while maintaining a sufficient material consistency is the task for further research. The specimens also exhibited very good properties from the point of view of dynamic stiffness. All the samples can be classified as dynamic soft insulation materials.

With respect to the hygrothermal transport, it was found that these materials are sensitive to humidity; under normal conditions, they exhibit sorptive moisture comparable with wood. With a higher moisture content, the thermal insulating properties of these materials

degrade; however, a more significant degradation occurs in the environments with a higher humidity. It can, therefore, be stated that as long as these insulators (e.g., in the form of ETICS) are not exposed to a very high humidity or direct weather actions, they are able to function within the structure and can be successfully applied in many developing countries where they can provide protection not only from the negative effects of cold but also from the high temperatures during the summer (Central Asia, for instance). The research confirmed that binding by means of a slag-based alkali-activated binder could result in a very good ratio between the thermal insulation and mechanical properties. On the contrary, for instance, alkali-bound insulators obtained simply by being pressed or bound by means of bicomponent fibres, can be used in the structures with a lower mechanical load, putting relatively low demands on the production technology and for this reason, they can find use also in industrially less developed countries.^{2,9}

Acknowledgements

This paper was elaborated with the financial support of the projects GA 13-21791S and project No. LO1408 "AdMaS UP – Advanced Materials, Structures and Technologies", supported by Ministry of Education, Youth and Sports under the "National Sustainability Programme I".

6 REFERENCES

- ¹ K. W. Corscadden, J. N. Biggs, D. K. Stiles, Sheep's wool insulation: A sustainable alternative use for a renewable resource?, *Resources, Conservation and Recycling*, 86 (2014), 9–15, doi:10.1016/j.resconrec.2014.01.004
- ² K. Wei, C. Lv, M. Chen, X. Zhou, Z. Dai, D. Shen, Development and performance evaluation of a new thermal insulation material from rice straw using high frequency hot-pressing, *Energy and Buildings*, 87 (2015) 1, 116–122, doi:10.1016/j.enbuild.2014.11.026
- ³ D. P. L. Murphy, H. Behring, Arable crop materials for insulation in buildings, *Biomass for Energy and Industry*, 10th European Conference and Technology Exhibition on Biomass for Energy and Industry, Würzburg, 1998, 176–179
- ⁴ W. D. Brouwer, Natural fibre composites: Where can flax compete with glass?, *Sample Journal*, 36 (2000) 6, 18–23
- ⁵ S. A. Ibraheem, A. Ali, A. Khalina, Development of Green Insulation Boards from Kenaf Fibres, Part 2: Characterizations of Thermal and Water Absorption, *Key Engineering Materials*, 462–463 (2011), 1331–1336, doi:10.4028/www.scientific.net/KEM.462-463.1331
- ⁶ S. A. Ibraheem, A. Ali, A. Khalina, Development of Green Insulation Boards from Kenaf Fibres, Part 1: Development and Characterizations of Mechanical Properties, *Key Engineering Materials*, 462–463 (2011), 1343–1348, doi:10.4028/www.scientific.net/KEM.462-463.1343
- ⁷ S. Mukhopadhyay, D. Annamalai, R. Srikanta, Coir Fiber for Heat Insulation, *Journal of Natural Fibers*, 8 (2011) 1, 48–58, doi:10.1080/15440478.2010.551001
- ⁸ S. A. Ibraheem, A. Ali, A. Khalina, Development of Green Insulation Boards from Kenaf Fibres and Polyurethane, *Polymer-Plastics Technology and Engineering*, 50 (2011) 6, 613–621, doi:10.1080/03602559.2010.551379
- ⁹ A. Korjenic, V. Petráněk, J. Zach, J. Hroudová, Development and performance evaluation of natural thermal-insulation materials composed of renewable resources, *Energy and Buildings*, 43 (2011) 9, 2518–2523, doi:10.1016/j.enbuild.2011.06.012
- ¹⁰ EN 1602 Thermal insulating products for building applications – Determination of the apparent density, 2013
- ¹¹ EN 12667 Thermal performance of building materials and products – Determination of thermal resistance by means of guarded hot plate and heat flow meter methods – Products of high and medium thermal resistance, 2001
- ¹² ISO 8301 Thermal insulation – Determination of steady-state thermal resistance and related properties – Heat flow meter apparatus, 2010
- ¹³ ISO 9052-1 Acoustics – Determination of dynamic stiffness – Part 1: Materials used under floating floors in dwellings, 1989, reviewed in 2011
- ¹⁴ EN ISO 11654 Acoustics – Sound absorbers for use in buildings – Rating of sound absorption, 1997
- ¹⁵ ISO 10534-1 Acoustics – Determination of sound absorption coefficient and impedance in impedance tubes – Part 1: Method using standing wave ratio, 1996, reviewed in 2011
- ¹⁶ ČSN 730532 Acoustics – Protection against noise in buildings and evaluation of acoustic properties of building elements – Requirements, 2010

PREDICTION OF THE ELASTIC MODULI OF CHICKEN-FEATHER-REINFORCED PLA AND A COMPARISON WITH EXPERIMENTAL RESULTS

NAPOVEDOVANJE MODULOV ELASTIČNOSTI PLA, OJAČANEGA S PIŠČANČJIM PERJEM IN PRIMERJAVA Z EKSPERIMENTALNIMI REZULTATI

Uğur Özmen, Buket Okutan Baba

Celal Bayar University, Engineering Faculty, Mechanical Engineering Department, 45140 Muradiye/Manisa, Turkey
u.ozmen@hotmail.com

Prejem rokopisa – received: 2014-08-07; sprejem za objavo – accepted for publication: 2015-03-04

doi:10.17222/mit.2014.182

The purpose of this study is to obtain the elastic moduli, the key material property, of random discontinuous fiber composites with experiments and micromechanical models and to compare them. The proposed study makes it possible to assess the elastic moduli of chicken-feather fiber (CFF)/PLA green composites with different CFF mass fractions and to determine the feasibility of the micromechanical models for the CFF/PLA composites. For this purpose, initially, CFF/PLA composites including 2, 5 or 10 % chicken-feather mass fractions were extruded and standard tensile specimens for ISO 527 were formed with the injection-molding method. Tensile tests were carried out in accordance with the standards and the elastic moduli were calculated using the stress-strain curve. Then, using six different micromechanical models, the elastic moduli of the CFF/PLA composites with different mass fractions were calculated and compared with the experimental results. The results of the experiments and the models indicated that the presence of chicken feather increased the elastic moduli of all the composites in comparison with the pure PLA. According to the experimental data, the maximum increase in the elastic moduli of the composites with the presence of CFF was found to be 5.4 %. The maximum error in the prediction is about 16.8 % for the composite with a chicken-feather rate of 10 % when Manera's model is used. Among the micromechanical models, the ones that gave more converging results for the prediction of the elastic moduli of the CFF/PLA composites are Pan's 2-D, IROM (the inverse rule of mixtures), Nielsen-Chen and Halpin-Tsai models. A comparison of the results of these six models shows that the maximum deviation (the percentage error in prediction) is the smallest (1.4 %) for the Nielsen-Chen model. Therefore, the Nielsen-Chen model is the most appropriate model for the prediction of the elastic moduli of the CFF/PLA composites.

Keywords: chicken feather, PLA, green composite, micromechanical models

Namen te študije je dobiti module elastičnosti kot glavne lastnosti materiala, kompozitov z naključnimi vlakni, z eksperimenti in z mikromehanskimi modeli ter njihova primerjava. Predlagana študija bo omogočila določitev modula elastičnosti kompozita iz vlaken piščančjega perja (CFF)/PLA, z različnim masnim deležem CFF in ugotoviti izvedljivost mikromehanskih modelov za CFF/PLA kompozite. V ta namen so bili najprej kompoziti CFF/PLA z 2 %, 5 % in 10 % piščančjih peres, ekstrudirani in izdelani so bili standardni natezni preizkušanci po ISO 527, z metodo brizganja v formo. Natezni preizkusi so bili izvršeni v skladu s standardom in modul elastičnosti je bil izračunan iz krivulje napetost-raztezek. Nato so bili izračunani moduli elastičnosti kompozita CFF/PLA, z uporabo šestih različnih mikromehanskih modelov in primerjani z rezultati preizkusov. Rezultati preizkusov in modelov so pokazali, da prisotnost piščančjih peres poveča modul elastičnosti vseh kompozitov, v primerjavi s čistim PLA. Eksperimentalni podatki so pokazali, da je največje povečanje modula elastičnosti kompozita s CFF za 5,4 %. Pri uporabi Manera modela je bila največja napovedana napaka okrog 16,8 % pri kompozitu z 10 % deležem piščančjega perja. Med mikromehanskimi modeli, ki imajo največji raztros rezultatov pri napovedovanju modula elastičnosti CFF/PLA kompozitov so Pan's 2-D, IROM (Inverse Rule of Mixtures), Nielsen-Chen in Halpin-Tsai model. Primerjava rezultatov teh šestih modelov kaže, da je največje odstopanje (odstotek pri napovedi) najmanjše (1,4 %) pri Nielsen-Chen modelu. Torej je Nielsen-Chen model najbolj primeren za napovedovanje modula elastičnosti CFF/PLA kompozitov.

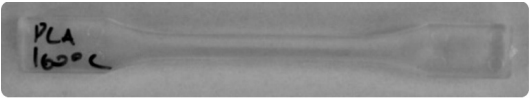
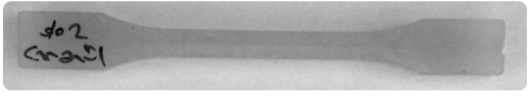
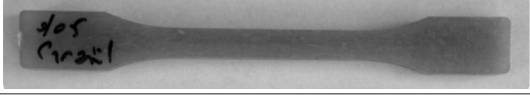
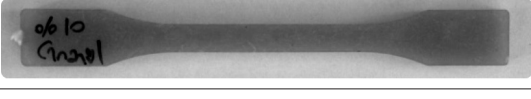
Ključne besede: piščančje perje, PLA, zelen kompozit, mikromehanski modeli

1 INTRODUCTION

Since the straw-reinforced cement in the antique ages, random discontinuous short-fiber-reinforced composites have always existed.¹ A lot of experimental studies have been done on this subject. Many are about natural-fiber-reinforced ones because of the structure of natural fibers that cannot be converted into long fibers. Waste-based,² synthetic-based,³ plant-based⁴⁻⁷ and animal-based⁸⁻¹² fibers have been studied by many researchers. Experimental studies are substantially important to get the highest efficiency from the random

discontinuous short-fiber-reinforced composites. Experimental studies are still hard to perform, as time-consuming and costly tests need to be done to characterize the composite materials.¹³ Therefore, researchers developed certain micromechanical models for calculating the properties of the composites to avoid a great number of tests. Modelling of the random discontinuous short-fiber-reinforced composites is quite hard compared to the long and oriented ones. For the situations where the well-known method named the rule of mixtures for predicting the elastic moduli of composite materials could not provide proper predictions,

Table 1: Tensile-test specimens of composites with different chicken-feather mass fractions**Tabela 1:** Natezni preizkušanci kompozitov z različnim masnim deležem piščančjega perja

Pure PLA	
Tensile specimens containing 2 % of chicken feather	
Tensile specimens containing 5 % of chicken feather	
Tensile specimens containing 10 % of chicken feather	

Christensen and Waals,¹⁴ Pan,¹⁵ Manera,¹⁶ Nielsen-Chen¹⁷ and Halpin-Tsai^{18,19} proposed new models based on the rule of mixtures. While for some models the range of validity is limited to specific mass fractions, other models are different. Although each of these models was developed for all the random discontinuous short-fiber-reinforced composites, they may give unexpected results for some of the composites.

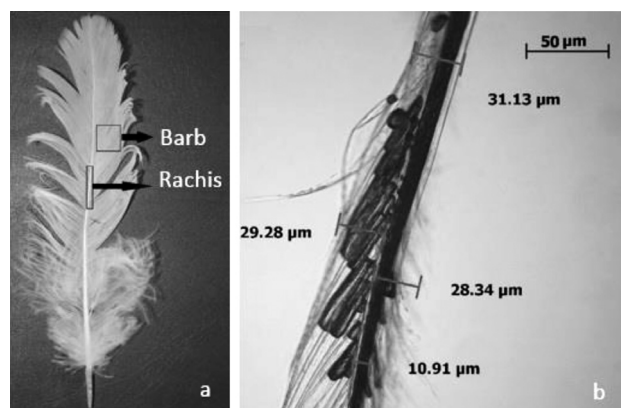
The purpose of this study is to predict the elastic moduli of the composites with different chicken-feather mass content via the models developed for random discontinuous short-fiber-reinforced composites. The volume fractions, with which these models express their sensitive results, were investigated and the volume-fraction range for these composite materials was determined.

2 EXPERIMENTAL WORK

Two materials were used for the composites, poly lactic acid (PLA) as the matrix and chicken-feather fibers (CFFs) as the reinforcement. The CFFs were procured from a local company in Manisa/Turkey. The

CFFs (or barbs) were separated from the rachis (**Figure 1a**). They were washed with hot water for sterilization and kept in water for 24 h. Then, the CFFs were kept in an oven at 60 °C for 6 h in order to dehumidify them. The lengths of the CFFs varied from 10 mm to 30 mm. Their diameters were measured to be approximately 20–40 µm using a light microscope (**Figure 1b**). The PLA was purchased from Resinex BMY AS in Istanbul/Turkey. The type of the PLA was NatureWorks 3052D with a density of 1.24 g/cm³.

The CFF/PLA composites with CFF mass fractions of (2, 5 and 10) % were manufactured by extrusion. Initially, the PLA granules and the CFFs were mixed with a mechanical mixer. The mixtures were extruded using a

**Figure 1:** a) Parts of a chicken feather, b) light-microscope image of the barb**Slika 1:** a) Deli piščančjega peresa, b) svetlobni posnetek stržena peresa in perja**Figure 2:** Specimen during the tensile test**Slika 2:** Vzorec med nateznim preizkusom

ThermoFisher Scientific EuroLab 16 XL twin-screw extruder. The barrel temperature-zone profile and the screw speed were 165/175/185/195/205 °C and 150 min⁻¹, respectively. Following the extrusion process, the composites were chopped, with a pelletizer, into pieces with a length of 0.3 cm. Then, the granules were manufactured as the tensile specimens in line with the ISO 527 standards, with a PERMAK injection-molding machine. The barrel temperatures and pressure were 154/160/154 °C and 147 bar, respectively. The tensile specimens are shown in **Table 1**.

The length of the tensile specimens was 88 mm, the width of the narrow and wide sections was 5 and 10 mm, respectively. The thickness of the specimens was 4 mm and the gage length was 40 mm. The tensile test was conducted to determine the elastic moduli of the composites. Each specimen was tested at a speed of 1 mm/min, using a 100 kN Shimadzu Autograph testing machine (**Figure 2**). At least five identical specimens were tested per specimen type.

3 MICROMECHANICAL MODELS

The micromechanical models that can predict the elastic moduli of random discontinuous fiber composites are presented below.

The fiber volume fraction (V_f) used in the equations is calculated as follows:¹³

$$V_f = \frac{\frac{M_f}{\rho_f}}{\frac{M_f}{\rho_f} + \frac{M_c - M_f}{\rho_m}} \quad (1)$$

where M_f and ρ_f indicate the mass and the density of the fiber material. M_c indicates the mass of the composite material and ρ_m indicates the density of the matrix.

3.1 Christensen-Waals model

Christensen and Waals¹⁴ investigated a composite-material system whose random fiber orientation has three dimensional directions. They considered both the fiber orientation and the fiber/matrix interaction. They calculated the elastic moduli of the composite materials with low fiber fractions for the plane stress using the formula below:

$$E = \frac{c}{3} E_f + (1+c) E_m \quad c < 0.2 \quad (2)$$

where E indicates the elastic modulus of the composite material, E_f indicates the elastic modulus of the fiber material, E_m indicates the elastic modulus of the matrix material and c indicates the fiber volume fraction.

3.2 Pan's model

Pan¹⁵ put forward a new approach for the prediction of the elastic moduli of the randomly oriented fiber composites. First, he used the rule of mixtures for the parts where the fibers were not unidirectional; he used the relationship between the fiber volume fraction and the fiber-area ratio. He obtained the equations below for 2- and 3-dimensional cases:

$$E^{2D} = E_f V_f \frac{1}{\pi} + E_m \left(1 - \frac{1}{\pi} V_f \right) \quad (3)$$

$$E^{3D} = E_f V_f \frac{1}{2\pi} + E_m \left(1 - \frac{1}{2\pi} V_f \right) \quad (4)$$

where, E indicates the elastic modulus of the composite material, E_f indicates the elastic modulus of the fiber material, E_m indicates the elastic modulus of the matrix material and V_f indicates the fiber volume fraction.

3.3 Inverse rule of mixtures (IROM)

The rule-of-mixtures model is frequently used to predict the elastic moduli of the composite materials with continuous and unidirectional fibers. Since the inverse rule of mixtures indicates that the loading is perpendicular to the fibers, it is used to predict the elastic moduli of the random discontinuous short-fiber-reinforced composites in this study.¹³ The inverse rule of mixtures is expressed as:

$$E = \left(\frac{V_f}{E_f} + \frac{1-V_f}{E_m} \right)^{-1} \quad (5)$$

where E indicates the elastic modulus of the composite material, E_f indicates the elastic modulus of the fiber material, E_m indicates the elastic modulus of the matrix material and V_f indicates the fiber volume fraction.

3.4 Manera's model

Manera¹⁶ developed a new equation by making some assumptions on Puck's micromechanical model and simplifying it. These assumptions include a high fiber orientation ratio, two-dimensional random-fiber range, and he also considered the randomly oriented discontinuous fibers as the laminate of an unlimited number of layers. Manera's equation is as follows:

$$E = V_f \left(\frac{16}{45} E_f + 2 E_m \right) + \frac{8}{9} E_m \quad (6)$$

where E indicates the elastic modulus of the composite material, E_f indicates the elastic modulus of the fiber material, E_m indicates the elastic modulus of the matrix material and V_f indicates the fiber volume fraction.

3.5 Nielsen-Chen model

Nielsen and Chen built a new model for the prediction of the elastic moduli of the composite materials using the rule of mixtures and the inverse rule of mixtures.¹⁷

$$E = \frac{3}{8} E_{\parallel} + \frac{5}{8} E_{\perp} \quad (7)$$

where;

$$E_{\parallel} = E_f V_f + E_m (1 - V_f) \quad (8)$$

$$E_{\perp} = \frac{E_f E_m}{E_f (1 - V_f) + V_f E_m} \quad (9)$$

and E indicates the elastic modulus of the composite material, E_f indicates the elastic modulus of the fiber material, E_m indicates the elastic modulus of the matrix material and V_f indicates the fiber volume fraction.

3.6 Halpin-Tsai model

The Halpin-Tsai model is quite complicated in comparison with the other micromechanical models.^{18,19} Its consideration of the aspect ratio is the most important advantage of this model. Therefore, the Halpin-Tsai model converges better to the experimental results. The Halpin-Tsai model is as follows:

$$E = E_m \frac{1 + \xi \eta V_f}{1 - \eta V_f} \quad (10)$$

where η and ξ are:

$$\eta = \frac{\frac{E_f}{E_m} - 1}{\frac{E_f}{E_m} + \xi} \quad (11)$$

$$\xi = \frac{2L}{D} \quad (12)$$

and E indicates the elastic modulus of the composite material, E_f indicates the elastic modulus of the fiber material, E_m indicates the elastic modulus of the matrix material and V_f indicates the fiber volume fraction. L and D indicate the fiber length and diameter, respectively.

4 RESULTS AND DISCUSSION

The elastic moduli of PLA and CFF/PLA composites were obtained with tensile testing and the results are shown in **Table 2**. The elastic modulus of PLA was

Table 2: Experimental data for the elastic moduli of CFF/PLA composites

Tabela 2: Eksperimentalni podatki za module elastičnosti CFF/PLA kompozita

Chicken-feather mass fractions, (w/%)	Chicken-feather volume fractions, (V_f /%)	Elastic modulus (E /MPa)
0	0	3004 (255)
2	2.76	3083 (83)
5	6.83	3076 (309)
10	13.4	3166 (132)

*The values given in the parentheses are standard deviations.

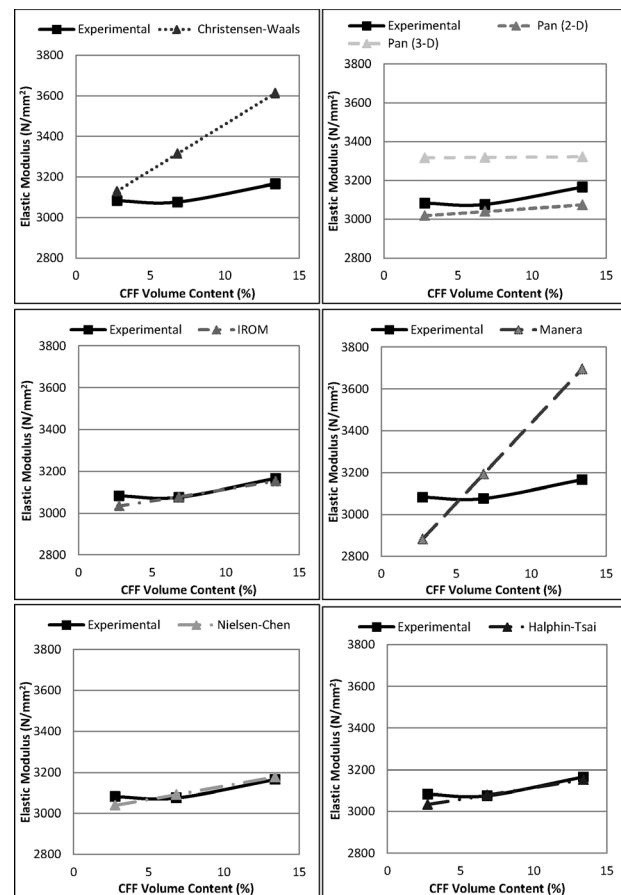


Figure 3: Comparison of the elastic moduli of the composite materials obtained with different micromechanical models

Slika 3: Primerjava modulov elastičnosti kompozitnih materialov, dobljenih iz različnih mikromehanskih modelov

Table 3: Elastic moduli of composite materials obtained with micro-mechanical models

Tabela 3: Moduli elastičnosti kompozitnih materialov iz mikromehanskih modelov

Chicken-feather mass fractions (w/%)	Christensen-Waals Model	IROM	Pan's Model (2-D)	Pan's Model (3-D)	Manera's Model	Nielsen-Chen Model	Halpin-Tsai Model
2	3130 (1.7)	3034 (1.6)	3019 (2.1)	3317 (7.6)	2882 (6.3)	3040 (1.4)	3034 (1.6)
5	3315 (7.8)	3079 (0.1)	3040 (1.2)	3319 (7.9)	3194 (3.8)	3092 (0.5)	3079 (0.1)
10	3614 (14.1)	3153 (0.4)	3074 (2.9)	3322 (4.9)	3697 (16.8)	3179 (0.4)	3153 (0.4)

*The values given in the parentheses are percentage differences between the elastic moduli obtained with the micromechanical models and experiments.

experimentally measured as 3004 MPa. The chicken-feather addition increased the elastic modulus by approximately 2.6 % for the mass fraction of 2 %, while increasing the elastic modulus by 2.4 % for the mass

fraction of 5 %. Similarly, its increase for the composite materials with a chicken-feather mass fraction of 10 % was 5.4 %. The increasing CFF content raised the elastic modulus as expected. This increase in the elastic modulus validated the predictions made with the micro-mechanical models.

A comparison of the elastic moduli obtained with the models and tests for the composite materials including the chicken-feather mass fractions of (2, 5 and 10) % is shown in **Table 3**. To show the differences between the results of the models and the tests, the elastic moduli from **Table 3** are plotted as shown in **Figure 3**. According to the literature, the Christensen-Waals model gives accurate results for some composite materials containing a mass fraction of up to 20 %. In this study, the CFF/PLA composites having a mass fraction of 2 % show a deviation of 1.7 %, which is a close to the experimental results, as mentioned above. The materials including mass fractions of 5 and 10 % show deviations of 7.8 % and 14.1 %, respectively, which means that the results diverge from the experimental data when the mass fraction of the material increases. Consequently, the Christensen-Waals model does not predict the elastic modulus very well for a fiber mass fraction of more than 2 %.

IROM shows a deviation of 1.6 % from the prediction of the elastic modulus of the composites including a 2 % chicken-feather content when compared with the experimental results. IROM produces accurate values converging by more than 99 % to the prediction of the elastic moduli of the composites having mass fractions of 5 and 10 %. Pan's 2-D model shows the results close to the experimental elastic-modulus values of the composites including (2, 5 and 10) % of CFF. Their deviations are (2.1, 1.2 and 2.9) %, respectively. On the other hand, the elastic modulus found with Pan's 3-D model is higher than the test data even at low fiber mass fractions.

Manera's model fails to give good predictions of the elastic modulus for high fiber mass fractions. Therefore, it is not possible to use Manera's model for the prediction of the elastic moduli of the composites including high fiber contents. However, the model gives reasonable predictions for the fiber mass fractions of about 5 %. Manera's model exhibits a deviation of 3.8 % for the composite including a mass fraction of 5 %.

Another elastic-modulus-prediction model is the Nielsen-Chen model. The predictions of this model are close to the test data. It exhibits deviations of (1.4, 0.5 and 0.4) % for the elastic moduli of the composites including (2, 5 and 10) % of the CFF content, respectively, when compared with the experimental results. Hence, the Nielsen-Chen model is the best model producing the closest and most reliable results among the models investigated in this study. As seen in **Figure 2**, the Halpin-Tsai model exhibits the results similar to IROM and its deviations are very close to the ones found with IROM. The Halpin-Tsai model is also one of the

most appropriate models to predict the elastic moduli of the CFF/PLA composites.

5 CONCLUSION

In this study, the elastic moduli of the composites including mass fractions of (2, 5 and 10) % of chicken-feather fibers were predicted using six different micro-mechanical models and the results were compared with the experimental data. The results are given below:

Although the Christensen-Waals model gives good predictions for low fiber mass fractions, it does not fit well the test data for high fiber mass fractions. Pan's 3-D model and Manera's model do not produce reliable results when used to predict the elastic moduli of the CFF/PLA composites.

The comparison with the experimental results shows that Pan's 2-D model, the inverse rule of mixtures and the Halpin-Tsai model can be used to predict the elastic moduli of the CFF/PLA composites.

From the comparison, it can be seen that the Nielsen-Chen model gives the best predictions of the elastic modulus of the CFF/PLA composites. Consequently, the most appropriate model to predict the elastic moduli of the CFF/PLA composites is the Nielsen-Chen model.

Acknowledgements

This project was supported by the Celal Bayar University Research Funds 2013/35.

6 REFERENCES

- ¹ F. P. La Mantia, M. Morreale, Green composites: A brief review, *Composites: Part A*, 42 (2011), 579–588, doi:10.1016/j.compositesa.2011.01.017
- ² M. S. Huda, L. T. Drzal, A. K. Mohanty, M. Misra, Chopped glass and recycled newspaper as reinforcement fibers in injection molded poly(lactic acid) (PLA) composites: A comparative study, *Composites Science and Technology*, 66 (2006), 1813–1824, doi:10.1016/j.compscitech.2005.10.015
- ³ K. Oksman, M. Skrifvars, J. F. Selin, Natural fibres as reinforcement in polylactic acid (PLA) composites, *Composites Science and Technology*, 63 (2003), 1317–1324, doi:10.1016/S0266-3538(03)00103-9
- ⁴ N. Graupner, A. S. Herrmann, J. Müssig, Natural and man-made cellulose fibre-reinforced poly(lactic acid) (PLA) composites: An overview about mechanical characteristics and application areas, *Composites: Part A*, 40 (2009), 810–821, doi:10.1016/j.compositesa.2009.04.003
- ⁵ A. K. Bledzki, A. Jaszkiwicz, D. Scherzer, Mechanical properties of PLA composites with man-made cellulose and abaca fibres, *Composites: Part A*, 40 (2009), 404–412, doi:10.1016/j.compositesa.2009.01.002
- ⁶ S. Ochi, Mechanical properties of kenaf fibers and kenaf/PLA composites, *Mechanics of Materials*, 40 (2008), 446–452, doi:10.1016/j.mechmat.2007.10.006
- ⁷ B. Bax, J. Müssig, Impact and tensile properties of PLA/Cordenka and PLA/flax composites, *Composites Science and Technology*, 68 (2008), 1601–1607, doi:10.1016/j.compscitech.2008.01.004

- ⁸ M. P. Ho, K. T. Lau, H. Wang, D. Bhattacharyya, Characteristics of a silk fibre reinforced biodegradable plastic, *Composites: Part B*, 42 (2011), 117–122, doi:10.1016/j.compositesb.2010.10.007
- ⁹ H. Y. Cheung, K. T. Lau, X. M. Tao, D. Hui, A potential material for tissue engineering Silkworm silk/PLA biocomposite, *Composites: Part B*, 39 (2008), 1026–1033, doi:10.1016/j.compositesb.2007.11.009
- ¹⁰ H. Y. Cheung, K. T. Lau, Y. F. Pow, Y. Q. Zhao, D. Hui, Biodegradation of a silkworm silk/PLA composite, *Composites: Part B*, 41 (2010), 223–228, doi:10.1016/j.compositesb.2009.09.004
- ¹¹ S. Huda, Y. Yang, Composites from ground chicken quill and polypropylene, *Composites Science and Technology*, 68 (2008), 790–798, doi:10.1016/j.compscitech.2007.08.015
- ¹² M. Zhan, R. P. Wool, J. Q. Xiao, Electrical properties of chicken feather fiber reinforced epoxy composites, *Composites: Part A*, 42 (2011), 229–233, doi:10.1016/j.compositesa.2010.11.007
- ¹³ A. K. Kaw, *Mechanics of Composite Materials*, 2nd ed., Taylor & Francis Group, New York 2006, 457
- ¹⁴ R. M. Christensen, F. M. Waals, Effective Stiffness of Randomly Oriented Fiber Composites, *Journal of Composite Materials*, 6 (1972), 518–532, doi:10.1177/002199837200600307
- ¹⁵ N. Pan, The elastic constants of randomly oriented fiber composite: A new approach to prediction, *Science and Engineering of Composite Materials*, 5 (1996) 2, 63–72, doi:10.1515/SECM.1996.5.2.63
- ¹⁶ M. Manera, Elastic properties of randomly oriented short fiber-glass composites, *Journal of Composite Materials*, 11 (1977), 235–247, doi:10.1177/002199837701100208
- ¹⁷ E. Vannan, P. Vizhia, Prediction of the Elastic Properties of Short Basalt Fiber Reinforced Al Alloy Metal Matrix Composites, *Journal of Minerals and Materials Characterization and Engineering*, 2 (2014), 61–69, doi:10.4236/jmmce.2014.21010
- ¹⁸ J. E. Ashton, J. C. Halpin, P. H. Petit, *Primer on Composite Materials: Analysis*, Technomic, Stamford, Conn. 1969
- ¹⁹ J. C. Halpin, Stiffness and Expansion Estimates for Oriented Short Fiber Composites, *Journal of Composite Materials*, 3 (1969), 732–734, doi:10.1177/002199836900300419

COMPOSITES BASED ON INORGANIC MATRICES FOR EXTREME EXPOSURE CONDITIONS

KOMPOZITI Z ANORGANSKO OSNOVO ZA IZPOSTAVITEV EKSTREMNI RAZMERAM

Amos Dufka, Tomáš Melichar

Brno University of Technology, Faculty of Civil Engineering, Institute of Building Materials and Components, Veveří 95, 602 00 Brno, Czech Republic
dufka.a@fce.vutbr.cz, melichar.t@fce.vutbr.cz

Prejem rokopisa – received: 2014-08-18; sprejem za objavo – accepted for publication: 2015-01-06

doi:10.17222/mit.2014.205

The vast majority of reinforced-concrete structures are exposed to aggressive substances from the environment during their exploitation. The consequence is the degradation of the materials and reduction in the lifetime of the structures. Therefore, it is natural to make an effort to develop and apply the materials that are maximally resistant to such conditions. Materials based on alkali-activated matrices show a high resistance against chemically aggressive environments. The article is focused on the use of the materials based on alkali-activated substances as repair materials for the structures exposed to aggressive groundwater.

Keywords: alkali-activated substances, aggressive surrounding, durability of structures

Velika večina betonskih konstrukcij je med uporabo izpostavljena agresivnim snovem iz okolja. Posledica je razpadanje materiala in skrajšanje trajnostne dobe konstrukcije. Zato je naravno, da si prizadevamo razviti in uporabiti materiale, ki so najbolj zdržljivi v danih razmerah. Materiali, ki imajo z alkalijami aktivirano osnovo, izkazujejo veliko odpornost pri izpostavitvi kemijsko agresivnemu okolju. Članek obravnava uporabo materialov, ki temeljijo na snoveh, aktiviranih z alkalijami, kot materialih za popravilo konstrukcij, ki so izpostavljene agresivni talni vodi.

Ključne besede: z alkalijami aktivirane snovi, agresivno okolje, zdržljivost konstrukcij

1 INTRODUCTION

A lot of structures are exposed to the environments that are, due to their chemistry, quite aggressive to reinforced concrete. The material's resistance against the aggressive substances from the external environment is mainly determined by the features of its matrix.¹ Compared to concrete stone, the materials with the matrices based on alkali-activated substances have a significantly higher resistance to chemical substances. The article deals with the development and, especially, the application of the repair materials based on alkali-activated materials used for the repair of the reinforced-concrete lining of an underground collector used in a chemically aggressive environment.

2 SPECIFICATIONS OF THE COLLECTOR AND THE CONDITIONS OF ITS EXPLOITATION

The excavation of the underground collector was done using the machine-excavation technology, while the final scraping of the excavation area was carried out with the classical, manual excavation method. The excavation area is from 13 m² to 14 m² (by stationing). The length of the underground part of the collector is 7.87 km; the lining and casing of the tunnels are made of shotcrete, whose strength within this project is determined to be 20 MPa. The lining of the tunnels is reinforced with welded

mesh panels (Ø 6–100/100 mm) and a rigid mine casing. The thickness of the shotcrete is 100 mm. Dry shotcrete was applied.

Already one year after the construction, significant defects began to occur. These were mainly the penetration of water through the lining, new formations of solid carbonate on the surface of the lining, the formation of waste products associated with the reinforcement corrosion, etc. A typical state of the damaged lining after one year of operation is shown in **Figures 1 and 2**.



Figure 1: View of the location, in which a massive penetration of moisture occurred: new solid-carbonate formations are visible on the surface of the lining

Slika 1: Prikaz področja, kjer se je pojavila močna penetracija vlage; viden je nastanek trdnega karbonata na površini podlage



Figure 2: Collection of core bores from the lining. Significant carbonate efflorescence is visible on the surface of the wall.

Slika 2: Zbiranje jeder iz izvrtine v podlagi. Na površini stene je viden močan razcvet karbonatov.

The state of the structure continued to deteriorate very quickly and, therefore, it was necessary to take corrective measures. It was found that before the construction of the collector no hydrogeological survey was performed, or it was performed unprofessionally and insufficiently.

To properly assess the causes of the failures, a detailed construction and technical investigation was carried out in the places where the state of the concrete was being evaluated, and an analysis of the chemical composition of the groundwater in various locations of the collector was performed. The results of the chemical analysis of the groundwater are given in **Table 1**.

The foregoing shows that in terms of the durability of the concrete the amount of sulphate ions in the water is essential. The aggressiveness of the environment in different parts of the collector can be classified as relevant in accordance with EN 206-1 (**Table 2**).

Table 1: Results of the chemical analysis of groundwater

Tabela 1: Kemijska analiza talnice

Chemical composition	Stationing 0.57 km – tertiary sediments	Stationing 1.56 km – quaternary sediments	Stationing 2.68 km – tertiary sediments
Alkalinity	7.68	7.50	7.70
Sulphates	3450 mg L ⁻¹	148 mg L ⁻¹	1369 mg L ⁻¹
Chlorides	170 mg L ⁻¹	152 mg L ⁻¹	260 mg L ⁻¹
Nitrates	146 mg L ⁻¹	124 mg L ⁻¹	180 mg L ⁻¹
Ammonia ions	0.17 mg L ⁻¹	0.13 mg L ⁻¹	0.08 mg L ⁻¹
Chemical composition	Stationing 4.42 km – tertiary sediments	Stationing 5.93 km – tertiary sediments	Stationing 6.67 km – quaternary sediments
Alkalinity	7.15	7.25	7.38
Sulphates	3825 mg L ⁻¹	1740 mg L ⁻¹	193 mg L ⁻¹
Chlorides	156 mg L ⁻¹	78 mg L ⁻¹	178 mg L ⁻¹
Nitrates	160 mg L ⁻¹	112 mg L ⁻¹	134 mg L ⁻¹
Ammonia ions	4.12 mg L ⁻¹	0.17 mg L ⁻¹	16. mg L ⁻¹

Table 2: Evaluation of groundwater aggression

Tabela 2: Ocena poškodb zaradi talne vode

Stationing 0.57 km – tertiary sediments	Highly aggressive environment
Stationing 1.56 km – quaternary sediments	No aggression
Stationing 2.68 km – tertiary sediments	Moderately aggressive chemical environment
Stationing 4.42 km – tertiary sediments	Highly aggressive environment
Stationing 5.93 km – tertiary sediments	Moderately aggressive chemical environment
Stationing 6.67 km – quaternary sediments	No aggression

On the basis of the results of the chemical analysis of the water samples it was possible to conclude that the water that passes through quaternary sediments does not cause the sulphate corrosion of the concrete. A completely different situation occurs when the water passes through tertiary sediments. These waters show moderate and, in some areas, even high sulphate aggressiveness. The results of the chemical analysis clearly demonstrated a high level of aggressiveness of the groundwater affecting the collector. Underestimating this fact or failing to carry out a hydrogeological research before the construction of a collector is, therefore, shown to be a serious deficiency.

To assess the actual state after two years of the operation of the collector, a construction and technical research was performed, aimed especially to:

- assess the state of the concrete, in terms of both physical and mechanical parameters (i.e., particularly in terms of compressive strength) and in terms of its chemical and mineralogical compositions;
- assess the state of the reinforcement and the degree of its corrosion, especially in connection to the concrete's ability to passivate the reinforcement corrosion with its natural alkalinity.

The process of the construction and technical research was carried out in accordance with the provisions of the Technical Conditions for Reinforced Concrete Structure Reinstalment¹ and the relevant technical stan-

Table 3: Concrete's compressive strength depending on the aggressiveness of groundwater in different parts of the collector

Tabela 3: Trdnost betona v odvisnosti od poškodb zaradi talne vode na različnih pozicijah kolektorja

Stationing 0.57 km – tertiary sediments	8 MPa
Stationing 1.56 km – quaternary sediments	25 MPa
Stationing 2.68 km – tertiary sediments	14 MPa
Stationing 4.42 km – tertiary sediments	10 MPa
Stationing 5.93 km – tertiary sediments	16 MPa
Stationing 6.67 km – quaternary sediments	27 MPa

dards. The sampling for testing the compressive strength and for the physico-chemical analysis was carried out with core bores.

Within the project, the strength class of the concrete was defined as 20 MPa. The results for the compressive strength determined on the samples and collected within the research are summarized in **Table 3**.

The mineralogical composition of the concrete was evaluated with an X-ray diffraction analysis, its results are presented in **Table 4**.

Table 4: Results of the mineralogical analysis of the concrete

Tabela 4: Rezultati mineraloške sestave betona

Sampling point	Identified minerals
Stationing 0.57 km – tertiary sediments	Calcite, ettringite, gypsum, quartz, feldspar
Stationing 1.56 km – quaternary sediments	Calcite, portlandite, calcium silicate hydrate II, monosulphate, quartz, feldspar
Stationing 2.68 km – tertiary sediments	Calcite, portlandite, monosulphate, quartz, feldspar
Stationing 4.42 km – tertiary sediments	Calcite, ettringite, gypsum, monosulphate, quartz, feldspar
Stationing 5.93 km – tertiary sediments	Calcite, portlandite, calcium silicate hydrate II, monosulphate, quartz, feldspar
Stationing 6.67 km – quaternary sediments	Calcite, portlandite, calcium silicate hydrate II, carbonate complex, monosulphate, quartz, feldspar

It is clear that in certain locations, already after two years of the groundwater penetration, a massive degradation of the concrete occurred. The concrete's compressive strength in the affected areas is only about half of its original value. This finding corresponds completely with the results of the physical and chemical analyses showing massive corrosion formations (gypsum, secondary ettringite) in the microstructure of the affected concrete. In addition, the physical and chemical analyses showed that in some areas the water penetrating the lining caused quite an intense decomposition ("a washout") of the cement matrix. This, of course, resulted in a decrease in the strength of the concrete.

So, massive and negative symptoms occurred after two years of the operation of the collector. On the basis of the experience with similar types of structures, supported by a mathematical simulation, an assumption was formulated, according to which in approximately two years, in some parts of the collector the rate of degradation of the lining will be so high that the static load of the collector will be affected.

Therefore, it was necessary to repair the structure. The first phase of the repair work related to the most affected areas. In these locations, the entire layer of the concrete along the lining was removed and the reinforcement affected by extreme corrosion was replaced. The removed concrete was then replaced with the repair material. Due to the highly aggressive environment, a mate-

rial with a matrix based on alkali-activated substances was used.

3 REPAIR MATERIAL BASED ON ALKALI-ACTIVATED MATERIALS

When developing a formula based on alkali-activated materials, we used the results from earlier researches.²⁻⁷

In terms of the properties of the resulting mixture, the compositions of individual components are important. The basic characteristics of the materials used for producing the mixtures with alkali-activated matrices are summarized in the following tables (**Tables 5 to 7**).

Table 5: Chemical composition of metakaolin

Tabela 5: Kemijska sestava metakaolina

Component	Representation (%)
Al ₂ O ₃	41.90
SiO ₂	52.90
K ₂ O	0.77
Fe ₂ O ₃	1.08
TiO ₂	1.80
MgO	0.18
CaO	0.13

Table 6: Chemical composition of slag

Tabela 6: Kemijska sestava žlindre

Component	Representation (%)
Al ₂ O ₃	7.42
SiO ₂	38.51
CaO	36.26
MgO	10.11
K ₂ O	0.43
Fe ₂ O ₃	0.74
TiO ₂	0.026

Table 7: Chemical composition of sodium-silica water glass

Tabela 7: Kemijska sestava vodnega stekla Na-Si

Component	Representation (%)
SiO ₂	50.82
Na ₂ O	26.25
Water	22.12
Silicate module	1.92

Table 8: Formula of the repair mixture based on alkali-activated materials

Tabela 8: Sestava reparaturne mešanice na osnovi z alkalijo aktiviranega materiala

Ingredient	Ingredient dosage of concrete, kg/m ³
Slag	430
Sodium-silica glass	95
Metakaolin	50
Water	180
Aggregates	1750

Aggregates with fractions of 0–4 mm and 4–8 mm were used as the filler. The particle-size distribution

curve was optimized according to the Empa II procedure.⁵

The mixture composition is given in **Table 8**.

This mixture was applied in the locations of the lining, where it was necessary to remove the original concrete. The effectiveness of this measure was then evaluated using the procedure described in the following section.

4 PERFORMANCE ANALYSIS OF THE NEW MATERIAL

The efficiency, or durability, of the repair material was evaluated as follows: One year after the repairs, control samples were taken from the localities in which the repair mixture in question was applied. A set of physico-mechanical and physico-chemical parameters of these samples was determined. Attention was focused especially on the following parameters:

- the tensile strength of the surface layers;
- the compressive strength;
- the microstructure, analysed with physico-chemical methods. The X-ray diffraction analysis and the scanning electron microscopy were used.

The tensile-strength test of the surface layers was made "in situ", the sampling for testing the compressive

strength and for the physico-chemical analysis was carried out with core bores.

These analyses were performed with the procedures that are in accordance with the provisions of the relevant technical standards. The samples representing the repair material were then subjected to the same set of experiments after being stored for about 28 d and 360 d in standard laboratory conditions (i.e., $t = (20 \pm 2) ^\circ\text{C}$, $\varphi = (60 \pm 5) \%$). These values were considered as the references. The comparison of the values recorded on the reference bodies and the samples of the repair materials exposed to the environment of the collector for one year was the essential criterion in the evaluation of the effectiveness of the repairs carried out. The data found with the set of experiments are shown below (**Tables 9 and 10**).

Table 9: Results of the strength-parameter tests of the repair material
Tabela 9: Rezultati preizkusa trdnosti reparaturnega materiala

sample identification	Bulk density (kg/m ³)	Tensile strength of surface layers (MPa)	Compressive strength (MPa)
Reference set – stored for 28 d in standard laboratory conditions	2450	2.1	35.6
Reference set – stored for one year in standard laboratory conditions	2400	2.3	36.2
Stationing 0.57 km – significant sulphate aggressiveness, annual exposure	2420	1.9	34.3
Stationing 4.42 km – tertiary sediments, annual exposure	2380	2.0	34.0

Table 10: Results for the mineralogical composition of the repair material

Tabela 10: Mineraloška sestava reparaturnega materiala

Sample identification	Identified minerals
Reference set – stored for 28 d in standard laboratory conditions	Calcium silicate hydrate II, goethit, quartz, feldspar
Reference set – stored for one year in standard laboratory conditions	Calcium silicate hydrate II, goethit, quartz, feldspar
Stationing 0.57 km – significant sulphate aggressiveness, annual exposure	Calcium silicate hydrate II, goethit, quartz, feldspar
Stationing 4.42 km – tertiary sediments, annual exposure	Calcium silicate hydrate II, goethit, quartz, feldspar

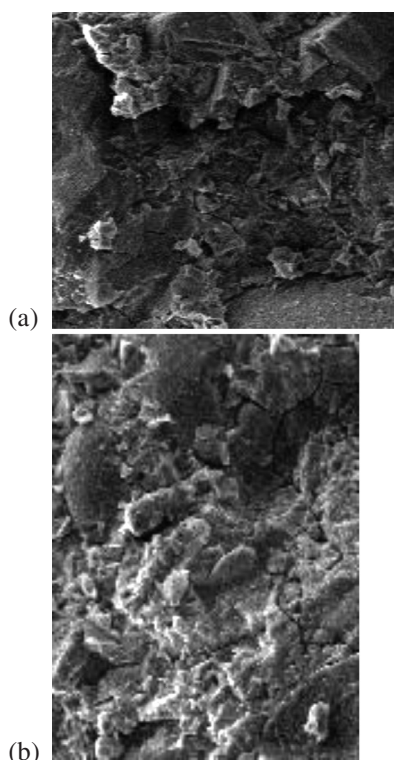


Figure 3: Detailed analysis of the microstructure showed a: a) de-facto amorphous phase of the matrix for both the reference material and b) the exposed material of the collector

Slika 3: Podrobnejša analiza mikrostrukture pokaže: a) amorfno osnovo tako v primerjalnem materialu kot tudi v b) izpostavljenem materialu v kolektorju

The microstructure of the material was also analysed using the scanning electron microscopy (**Figure 3**).

On the basis of the above findings we can say that in terms of both the strength parameters and mineralogy, the parameters of the repair material exposed to the highly corrosive environment are quite comparable with the reference parameters.

5 CONCLUSIONS

The article deals with the way of repairing an underground collector affected, in some areas, by underground waters with a highly aggressive chemical effect. Already in one or two years of the collector's operation these waters caused distinct disorders. In the affected areas there was a significant reduction in the mechanical properties of the concrete, and its ability to protect the reinforcement against the corrosion was significantly reduced. Thus, local repairs were carried out, whereby a material with its matrix based on alkali-activated materials was used as the repair material.

The matrix of the repair material was composed of a mixture of blast-furnace slag and metakaolin. Water glass was used as the activator. The metakaolin added to the mixture was to reduce the negative effects associated with the autogenous shrinkage that usually accompanies the aging of the materials with pure-slag matrices.^{3,6}

The control tests that were conducted one year after the repair work demonstrated that the aggressive effects of the water did not result in a decrease in the strength of the repair material. Neither were negative changes found in its microstructure. It was also established that the reinforcement was very well protected against the corrosion due to the repair material.

It is clear that the period (one year of application) is short in terms of the durability of the structures, and for a precise verification of our findings, we will need to continue with the monitoring of the concerned construction. However, despite this fact, it can be noted that so far the results have indicated a high potential of the material with a matrix based on alkali-activated materials in the repair of the reinforced concrete structures exposed to chemically aggressive environments.

Acknowledgements

This research was done with the financial help of project GAČR 14-25504S, Research of Behaviour of Inorganic Matrix Composites Exposed to Extreme Conditions, and EU project The Research and Development for Innovation, reg. number CZ.1.05/2.1.00/03.0097, through the activities of regional centre AdMaS – Advanced Materials, Structures and Technologies.

6 REFERENCES

- ¹ R. Drochytka, J. Dohnálek, J. Bydžovský, V. Pumpr, A. Dufka, P. Dohnálek, *Technické podmínky pro sanace betonových konstrukcí TP SSBK III.*, 1. edition, Sdružení pro sanace betonových konstrukcí, (The specifications for the reinstalment of concrete structures TP SSBK III, 1st edition, Association of Concrete Structure Reinstalment), Brno 2013, 262 pages
- ² M. Palacios, F. Puertas, Effect of shrinkage reducing admixtures on properties of alkali-activated slags, mortars and pastes, *Cement and Concrete Research*, 37 (2007) 5, 691–702, doi:10.1016/j.cemconres.2006.11.021
- ³ P. Rovnaník, *Vliv působení vysokých teplot na stavební materiály na bázi alkalicky aktivovaných pojiv*, habilitační práce (The influence of high temperatures on building materials based on alkali-activated binders, habilitation thesis), University of Technology in Brno, 2012
- ⁴ W. Brylicki, J. Malolepszy, S. Stryczek, Alkali activated cementitious material for drilling operation, 9th International Congress on the Chemistry of Cement, New Delhi, India, 3 (1992), 312–318
- ⁵ D. Wu, Y. Pei, B. Huang, Slag-mug mixtures improve cementing operations in China, *Oil and Gas Journal*, (1996), 95–100
- ⁶ X. Chen, N. Yang, Influence of polymeric structure of granulated blast furnace slag on their hydraulic activities, 2nd Beijing International Symposium on Cement and Concrete, Beijing, 1989, 346–351
- ⁷ J. Malolepszy, J. Deja, W. Brylicki, Industrial application of slag alkaline in concretes, 9th international conference on alkaline cements and concretes, Kiev, 2 (1994), 989–1001

THE EFFECT OF EO AND STEAM STERILIZATION ON THE MECHANICAL AND ELECTROCHEMICAL PROPERTIES OF TITANIUM GRADE 4

VPLIV EO IN STERILIZACIJE S PARO NA MEHANSKE IN ELEKTROKEMIJSKE LASTNOSTI TITANA GRADE 4

Marcin Basiaga, Witold Walke, Zbigniew Paszenda, Anita Kajzer

Silesian University of Technology, Faculty of Biomedical Engineering, Zabrze, Poland
marcin.basiaga@polsl.pl

Prejem rokopisa – received: 2014-09-23; sprejem za objavo – accepted for publication: 2015-03-09

doi:10.17222/mit.2014.241

Currently, various modifications to surfaces are made more and more frequently in order to improve implants' haemocompatibility. The main criterion determining the applicability of the respective surface-modification method is obtaining a product featuring suitable functional properties. These properties depend to a great extent on the corrosion resistance in the environment of human blood. Subject-matter literature does not devote much attention to the sterilisation process for titanium and cpTi alloys with surface modifications. A problem that still remains unsolved is the selection of a proper test showing the full characteristics of their behaviour contact with a blood environment during the time that the implant is used. Therefore, the authors of this study made an attempt to evaluate the impact of medical sterilisation methods, i.e., the ethylene oxide anodic oxide and SiO₂ layer, by means of the sol-gel method. The efficiency of the suggested technology for oxide layer application was evaluated on the basis of mechanical and electrochemical tests. Sterilisation in ethylene oxide and steam had a favourable influence on the electrochemical and mechanical properties of cpTi, irrespective of the method of surface preparation. In order to simulate real conditions, the tests were performed in artificial plasma at a temperature of $T = 37 \pm 1$ °C and pH = 7.0 ± 0.2 . The results proved the diversification of electrochemical properties of the oxide layers, depending on the technological parameters of its application. The suggestion of proper variants of the surface modification with the application of electrochemical and chemical methods is of long-range importance and will contribute to the development of technological conditions with specific parameters for the creation of oxide layers on metallic implants made of cpTi.

Keywords: cpTi (Grade 4), SiO₂, TiO₂, mechanical properties, electrochemical properties

Vedno pogostejše se opravljajo različne modifikacije površine, da bi se izboljšala hemokompatibilnost vsadkov. Glavni kriterij, ki določa uporabnost metode za modifikacijo površine je, da proizvod pokaže primerne funkcionalne lastnosti. Te lastnosti so v veliki meri odvisne od korozijske odpornosti v človeški krvi. Obstoječa literatura ne posveča velike pozornosti postopku sterilizacije titana in cpTi zlitin z modificirano površino. Problem, ki še ni rešen, je izbira primerne preizkusa, ki bi pokazal vse značilnosti o obnašanju stika s krvjo med uporabo vsadka. Zato so avtorji v tej študiji poizkusili oceniti vpliv medicinskih metod sterilizacije, kot je etilen oksid anodni oksid in SiO₂ plast izdelano s pomočjo metode sol-gel. Predlagana tehnologija uporabe oksidnega sloja je bila ocenjena z mehanskimi in elektrokemijskimi preizkusi. Sterilizacija v etilen oksidu in pari je imela ugodne vplive na elektrokemijske in mehanske lastnosti cpTi, ne glede na način priprave površine. Za simulacijo realnih pogojev so bili preizkusi izvršeni v umetni plazmi pri temperaturi $T = 37 \pm 1$ °C in pH = $7,0 \pm 0,2$. Dobljeni rezultati so potrdili različnost v elektrokemijskih lastnostih oksidnih plasti, odvisno od tehnoloških parametrov njene uporabe. Predlog ustreznega načina spremembe površine z uporabo elektrokemijskih in kemijskih metod je dolgoročno pomemben in bo prispeval k razvoju tehnoloških pogojev s specifičnimi parametri nastajanja plasti oksidov na kovinskem implantatu iz cpTi.

Ključne besede: cpTi (Grade 4), SiO₂, TiO₂, mehanske lastnosti, elektrokemijske lastnosti

1 INTRODUCTION

Literature does not devote much attention to the sterilisation process for titanium and cpTi alloys with surface modification.^{1,2} In recent years there has been a dynamic development in pure titanium coating methods, aimed at improving the hemocompatibility.^{3,4} Surface-layer modification methods must be selected in a way that does not cause phase or structural transitions, or precipitation processes in the base material. It has a particular significance for the geometry of implants having small cross-sectional areas or small-radii edges (stents or heart valves). For this reason, surface-layer modification for titanium and its alloys uses low-temperature methods, and especially anodic oxidation coating and the sol-gel method. The properties of TiO₂ layers obtained through

the process of anodic oxidation and SiO₂ layers obtained with the sol-gel method depend on the properties of the titanium surface and the process parameters. The development and verification of conditions for coating cpTi with layers of TiO₂ and SiO₂ characterized by high hemocompatibility was the topic of previous papers published by the authors.⁵⁻⁷ The safety of a medical device involving contact with blood is also related to the necessity of observing the appropriate procedures, preventing the transfer of pathogenic microorganisms into the human body. Such procedures are aimed at the removal and efficient elimination of microorganisms and the obtaining of sterile medical devices complying with certain specified quality requirements. A medical device is considered sterile when it achieves a Sterility Assur-

ance Level (SAL) of 10^{-6} . Therefore, in order to determine the impact of the procedure on the properties of the proposed surface layers, the authors subjected cpTi samples to steam sterilization and ethylene oxide sterilization. These two methods of medical sterilization are currently the most frequently used for devices having contact with blood. Taking the sterilization process into consideration will allow the characterization of the physical and chemical properties of the proposed surface layers in a more complete way, which has a significant influence on reducing the incidence of failures in the treatment of cardiovascular diseases.

2 MATERIALS AND METHODS

The study material was Grade 4 cpTi in the form of disks of the following dimensions: diameter, $d = 14$ mm, thickness, $g = 2$ mm. The samples were subjected to metal finishing consisting of mechanical grinding and electrolytic polishing, and then coating with layers of SiO_2 and TiO_2 based on two methods. The SiO_2 layer was applied using the sol-gel method with the following process parameters: $v = 3.0$ cm/min, $T = 430$ °C, $t = 60$ min. The silica precursors were: tetraethyl orthosilicate (TEOS), $\text{Si}(\text{OC}_2\text{H}_5)_4$ and tetramethyl orthosilicate (TMOS), $\text{Si}(\text{OCH}_3)_4$. Other reagents included ethyl alcohol (EtOH) and water. On the other hand, the TiO_2 layer was applied with the use of anodic oxidation at a potential of 100 V in an electrolyte based on phosphoric and sulphuric acids. Later, the prepared samples were subjected to ethylene oxide sterilization and steam sterilization. Ethylene oxide sterilization was conducted during a 12-hour cycle of exposure to ethylene oxide at 30 °C. After the process, the samples were ventilated for 2 h with the use of an EOGas series sterilizer from Andersen Products. The cycle yielded a Sterility Assurance Level SAL of 10^{-6} . The process was controlled by means of a chemical indicator, a biological indicator and an ethylene oxide exposure indicator. The steam sterilization was performed in a Basic Plus autoclave at temperature, $T = 134$ °C, pressure, $p = 2.1$ bar, and time, $t = 12$ min.

The tests were performed on samples coated with SiO_2 and TiO_2 (cpTi+ SiO_2 and cpTi+ TiO_2), coated with SiO_2 and TiO_2 and subjected to steam sterilization (cpTi+ SiO_2 +steam and cpTi+ TiO_2 +steam), and coated with SiO_2 and TiO_2 and subjected to ethylene oxide sterilization (cpTi+ SiO_2 +EO and cpTi+ TiO_2 +EO). In order to assess the impact of a given type of medical sterilization on the mechanical and electrochemical properties of the proposed cpTi surface modifications, the authors selected electrochemical potentiodynamic and impedance tests. The assessment of the mechanical properties, in turn, consisted of a measurement of the layer adhesion to the base and a measurement of the hardness.

The investigation of the electrochemical properties began with potentiodynamic tests and registration of the

polarization curves. The measurement facility consisted of a potentiostat with a PGP-201 generator, an electrochemical cell with a set of electrodes (platinum PtP-201 electrode the auxiliary and calomel electrode as the reference), and a solution (250 mL) functioning as artificial plasma ($\text{pH} = 7.0 \pm 0.2$). The artificial plasma during the test had a temperature $T = 37.0 \pm 1$ °C. Corrosion tests started by determining the open-circuit potential E_{OCP} for no current flowing. Anodic polarization curves were registered from the initial potential value, $E_{\text{start}} = E_{\text{OCP}} - 100$ mV. The potential change took place in the anodic direction at a speed of 0.16 mV/s.^{8–10} After obtaining an anodic current density of 1 mA/cm² or the measurement range +4000 mV, the polarization direction was changed in order to register the formation of any hysteresis loop. Further, electrochemical impedance spectroscopy (EIS) tests were conducted using an AutoLab PGSTAT 302N system equipped with an FRA2 module. The measurement system was used in the frequency range 10^4 – 10^{-3} Hz, with a sinusoidal voltage amplitude of the stimulating signal of 10 mV. The impedance spectra were determined and the measurements matched to an equivalent circuit by means of the least-squares method. The impedance spectra of the studied system were presented in the form of Nyquist plots for various frequencies and Bode plots.¹¹

The mechanical properties were then tested, with the properties of interest being the adhesion of the layers to the base and their hardness. The adhesion of the layers to the base was tested using the scratch-test method on an open platform equipped with a CSM Micro-Combi-Tester in compliance with the standard.¹² The test involved generating a scratch with an indenter (Rockwell-type diamond cone), gradually increasing the load on the indenter. The assessment of the critical load, L_c , was made on the basis of registered acoustic emission changes, friction force and coefficient, as well as observations from the light microscope integrated into the platform. The tests were performed at increasing loads in the range 0.03–20 N and for the following parameters: load rate 10 N/min, table speed 1.5 mm/min, scratch length ≈ 3 mm. The instrumental hardness measurement was performed using the Oliver-Pharr method, with the use of a Berkovich indenter on the open platform Micro-Combi-Tester by CSM Instruments. The loading and unloading rate amounted to 0.40 mN/min, while the loading force exerted on the indenter was 0.20 mN.¹³

3 RESULTS

Polarization curves registered during the potentiodynamic tests were the basis for a determination of the characteristic quantities describing the pitting-corrosion resistance of cpTi with a modified surface layer before and after sterilization (steam and EO) (**Figure 1** and **Table 1**).

The corrosive potential registered for the samples before sterilization assumed the following values: $\text{cpTi}+\text{TiO}_2 - E_{\text{corr}} = -235 \text{ mV}$ and $\text{cpTi}+\text{SiO}_2 - E_{\text{corr}} = -178 \text{ mV}$. In the case of the samples subjected to anodic oxidation and sterilization, the corrosive potential was: $\text{cpTi}+\text{TiO}_2+\text{steam} - E_{\text{corr}} = -142 \text{ mV}$ and $\text{cpTi}+\text{TiO}_2+\text{EO} - E_{\text{corr}} = -170 \text{ mV}$, while for the samples coated with silica and sterilized it was: $\text{cpTi}+\text{SiO}_2+\text{steam} - E_{\text{corr}} = -121 \text{ mV}$ and $\text{cpTi}+\text{SiO}_2+\text{EO} - E_{\text{corr}} = -121 \text{ mV}$. Regardless of the surface-modification method and the medical sterilization method, no hysteresis loop was observed, which shows that the analysed samples polarized up to potential value of +4000 mV are fully resistant to pitting corrosion (**Figure 1** and **Table 1**).

Table 1: Results of potentiodynamic test (mean measurement values)

Tabela 1: Rezultati potenciodinamičnega preizkusa (srednje izmerjene vrednosti)

Surface	E_{corr} , mV	R_p , $\text{M}\Omega \text{ cm}^2$
cpTi+TiO₂		
inital state	-235	4.02
EO	-170	43.70
steam	-142	30.58
cpTi+SiO₂		
inital state	-178	0.47
EO	-121	9.20
steam	-121	1.30

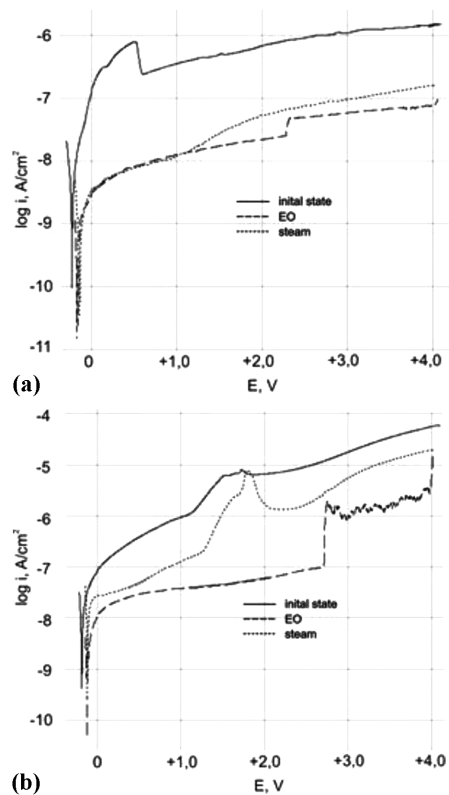


Figure 1: Anodic polarisation curves of sample: a) cpTi(TiO₂), b) cpTi(SiO₂)

Slika 1: Krivulje anodne polarizacije vzorcev: a) cpTi(TiO₂), b) cpTi(SiO₂)

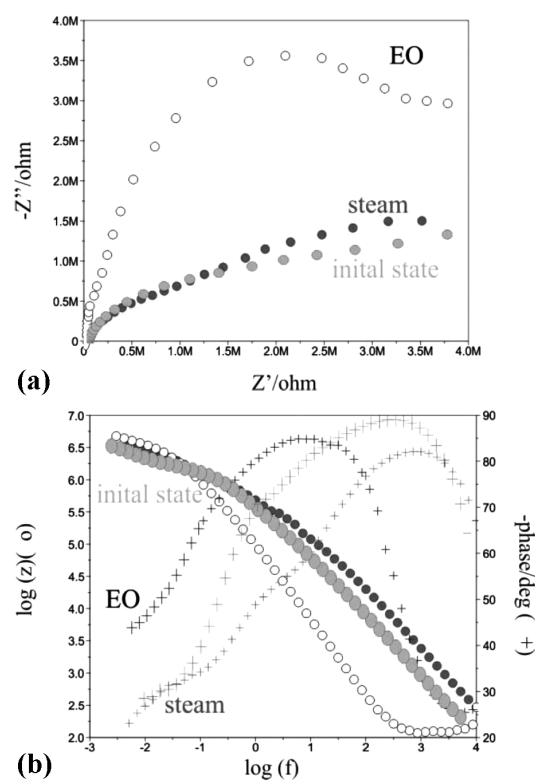


Figure 2: Impedance spectra for the sample cpTi(TiO₂): a) Nyquist plot, b) Bode diagram

Slika 2: Spekter impedance za vzorec cpTi(TiO₂): a) Nyquist diagram, b) Bode diagram

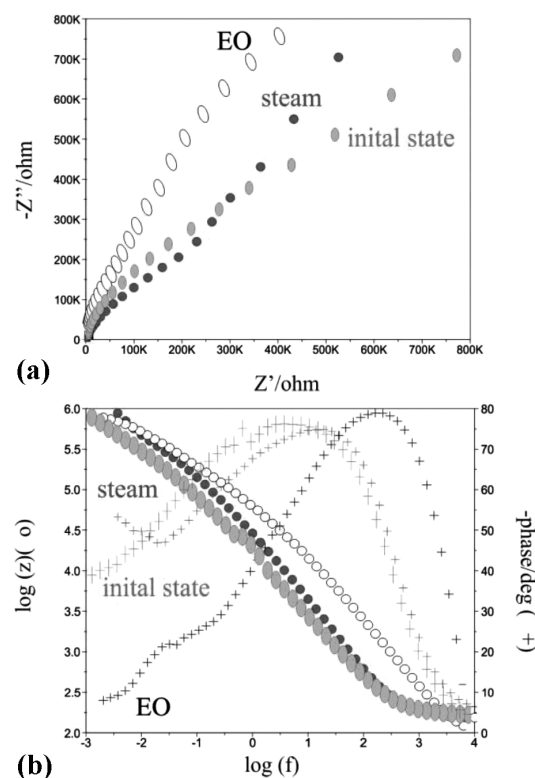
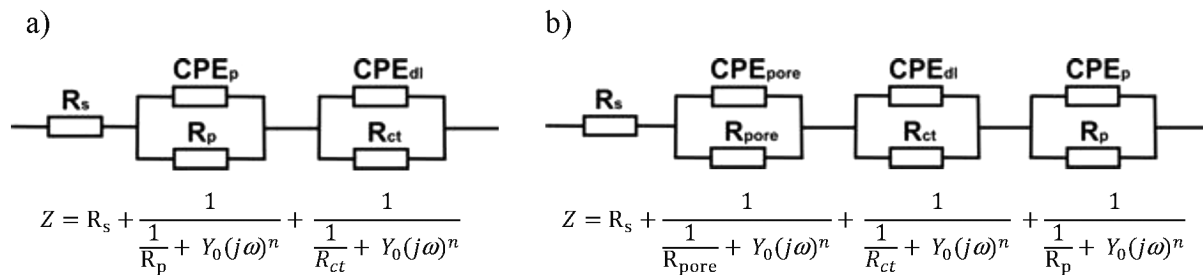


Figure 3: Impedance spectra for the sample cpTi(SiO₂): a) Nyquist plot, b) Bode diagram

Slika 3: Spekter impedance za vzorec cpTi(SiO₂): a) Nyquist diagram, b) Bode diagram

**Figure 4:** Physical models of an electrical equivalent system for a corrosion system: metal – solution^{5,6,11}**Slika 4:** Fizikalni modeli ekvivalentnega električnega sistema za korozijski sistem: kovina – raztopina^{5,6,11}**Table 2:** EIS analysis results**Tabela 2:** Rezultati EIS-analize

Surface	$R_s/\Omega\text{cm}^2$	$R_{\text{pore}}/\Omega\text{cm}^2$	CPE_{pore}		$R_p/\text{k}\Omega\text{cm}^2$	CPE_p		$R_{ct}/\text{M}\Omega\text{cm}^2$	CPE_{dl}	
			$Y_0/\Omega^{-1}\text{cm}^{-2}\text{s}^{-n}$	n		$Y_0/\Omega^{-1}\text{cm}^{-2}\text{s}^{-n}$	n		$Y_0/\Omega^{-1}\text{cm}^{-2}\text{s}^{-n}$	n
cpTi+TiO ₂										
inital state	19	—	—	—	968	0.2083E-6	0.89	4.26	0.1852E-5	0.81
EO	18	—	—	—	700	0.1460E-6	0.96	4.40	0.1901E-6	0.93
steam	18	112	0.2092E-6	0.94	817	0.5091E-6	0.90	3.66	0.2417E-5	0.82
cpTi+SiO ₂										
inital state	18	—	—	—	188	0.6605E-5	0.93	1.59	0.2065E-4	0.88
EO	19	—	—	—	224	0.1730E-5	0.83	3.00	0.6317E-5	0.75
steam	17	—	—	—	160	0.9806E-5	0.85	2.40	0.2664E-4	0.85

The impedance spectra determined during the EIS tests indicate diversified kinetics during the process taking place in the surface layers formed on the cpTi base before and after medical sterilization (**Figures 2 and 3**). The impedance spectra were analysed with the use of equivalent circuits, and their resultant impedances described (**Figure 4 and Table 2**). The best conformity between the model spectra and the experimental spectra obtained from the artificial plasma was achieved in the following circuits:^{5,6,11}

- circuit indicating the existence of a double layer, where R_s is the resistance of the artificial plasma, CPE_p is a constant phase element modelling the capacity of the surface zone of the material, with a highly developed surface, R_p – an element modelling the solution resistance in this zone, R_{ct} and CPE_{dl} –

resistance and capacity of the oxide layer (**Figure 4a**),

- circuit including also CPE_{pore} – an element representing the capacity of a double (porous) layer and an R_{pore} resistor representing the electrolytic resistance in the pores (**Figure 4b**).

In the case of the cpTi+TiO₂+steam sample, the layer was triple. This was a result of the penetration of the artificial plasma into the surface layer, resulting from the fact that the oxide layer created during anodic oxidation was destroyed by the steam, and recreated deeper inside, up to the layer adjacent to the base. In the remaining samples, the presence of a layer with high surface development was observed. The layer functioned as an additional barrier protecting the material against the corrosive environment.

Table 3: The results of adhesion of the layer on the cpTi substrate**Tabela 3:** Rezultati adhezije plasti na podlago iz cpTi

	Failure of the layer	The value of registered indenter load F_n/N					
		cpTi+SiO ₂			cpTi+TiO ₂		
		initial state	steam	EO	initial state	steam	EO
Measurment 1	Delamination Lc_1	2.59	2.89	2.79	2.71	1.66	1.87
	Complete break Lc_2	7.58	4.32	4.05	5.35	2.67	2.58
Measurement 2	Delamination Lc_1	3.78	3.26	1.95	2.96	1.67	1.65
	Complete break Lc_2	5.76	4.55	2.59	4.95	2.56	2.37
Measurement 3	Delamination Lc_1	3.38	2.41	2.01	3.33	1.82	1.78
	Complete break Lc_2	6.16	4.88	2.89	5.08	2.89	2.12
Average	Delamination Lc_1	3.25	2.85	2.25	3.00	1.71	1.76
	Complete break Lc_2	6.50	4.58	3.08	5.12	2.70	2.35
Standard deviation	Delamination Lc_1	±0.60	±0.42	±0.46	±0.31	±0.09	±0.11
	Complete break Lc_2	±0.95	±0.28	±0.77	±0.20	±0.16	±0.23

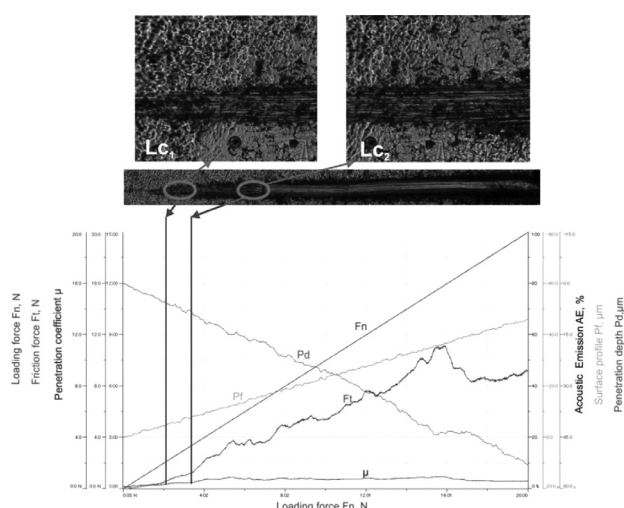


Figure 5: Results of the adhesion tests of the sample cpTi+TiO₂+EO
Slika 5: Rezultati preizkusa adhezije vzorca cpTi+TiO₂+EO

The results of the tests of adhesion of the analysed layers to the base material are presented in **Table 3** and **Figures 5** and **6**. Regardless of the sterilization method, the results indicate the impairment of adhesion of the layers coated by both anodic oxidation and the sol-gel method in comparison to the baseline samples. This can be seen from the values of the parameters determined on the basis of the measurements (**Table 3**). It was observed that for the samples not subjected to sterilization, the critical load causing layer delamination inwards and outwards was $Lc_2 = 6.50$ N (cpTi+SiO₂ – sol-gel method) and $Lc_2 = 5.12$ N (cpTi+TiO₂ – anodic oxidation). After sterilization (both steam and EO sterilization), the critical load value decreased to: $Lc_2 = 4.58$ N (cpTi+SiO₂+Steam), $Lc_2 = 3.08$ N (cpTi+SiO₂+EO) for the sol-gel method, and $Lc_2 = 2.70$ N (cpTi+TiO₂+Steam), $Lc_2 = 2.35$ N (cpTi+TiO₂+EO) for the anodic oxidation. Regardless of the type of sample, no acoustic emission signal was registered, which indicated that the bond

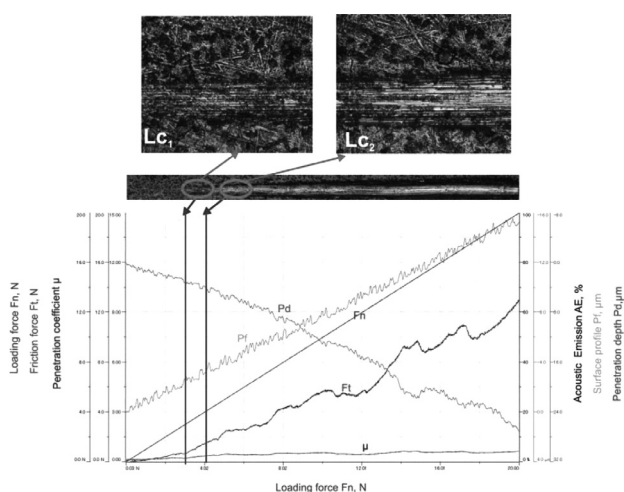


Figure 6: Results of the adhesion tests of the sample cpTi+SiO₂+EO
Slika 6: Rezultati preizkusa adhezije vzorca cpTi+SiO₂+EO

energy between the base and the coating was too low. No significant changes between steam and EO sterilization were observed.

The next step involved the hardness testing of the layers. The results of the measurements are shown in **Table 4**. The results do not show any significant differences between the samples after steam and ethylene oxide sterilization and the baseline samples.

Table 4: The results of nanohardness of the layers

Tabela 4: Rezultati meritve mikrotvrdote plasti

i.c.	Nanohardness H_{IT} , MPa					
	cpTi+SiO ₂			cpTi+TiO ₂		
	initial state	steam	EO	initial state	steam	EO
Measurement 1	1181	1304	1082	1236	1434	1171
Measurement 2	1236	1278	923	913	1247	1241
Measurement 3	1021	1189	1120	1021	1156	1089
Average	1146	1257	1041	1056	1279	1167
Standard deviation	±152	±60	±104	±164	±141	±76

4 CONCLUSIONS

The correct selection of physical and chemical properties is a significant issue in the process of adjusting the functionalities of cardiac implants,¹⁴ and has a direct impact on the final quality of medical devices. Physical and chemical devices are shaped by means of various types of metal finishing.^{14,15} The influence of various types of titanium alloy finishing on orthopaedic implants has been demonstrated by Szweczenko et al.¹⁶ He has shown that the method of base preparation has a crucial influence on the physical and chemical properties of the anodic oxide coating. Paszenda has proposed chemical surface modifications of the Cr-Ni-Mo steel intended for cardiac implants in order to achieve a higher hemo-compatibility.¹⁷ The literature review indicates that there are no comprehensive works devoted to a possible change of properties during medical sterilization.^{18–20} Therefore, the authors of this paper focused on an assessment of the possible changes to the mechanical and electrochemical properties of a coating subjected to pressurized steam sterilization and ethylene oxide sterilization. The tests on the samples following medical sterilization processes have shown differences in relation to those samples that did not undergo sterilization. Pressurized-steam sterilization caused a change in the corrosive potential value towards positive values and increased the polarization resistance, regardless of the surface-modification method. For the TiO₂-coated samples, it stopped the diffusion processes stemming from the anodic oxidation and caused the formation of an additional layer with a highly developed surface, which functioned as an additional barrier protecting the material against the corrosive environment and increasing the ion-transfer resistance. In the case of the SiO₂ layer, this type of sterilization did not cause significant changes to

the corrosive resistance of cpTi. The mechanical properties, on the other hand, remained unchanged, regardless of the type of metal finishing. However, the adhesion to the base was weaker in comparison to those samples not subjected to sterilization, which may be caused by the restructuring of the surface oxides under the influence of a sterilizing agent, which has a direct impact on the strength of the bonds between the chemical compounds, such as between $\text{TiO}_2/\text{Ti}_2\text{O}_3$ and the base. Ethylene oxide sterilization of the samples with a modified surface also caused changes to their electrochemical and mechanical properties. As in the case of pressurized-steam sterilization, the samples coated with TiO_2 and SiO_2 had a better resistance to corrosion in contact with the artificial plasma. On the surface of the samples coated with TiO_2 , the presence of an additional porous layer has been observed. This is the result of the partial degradation of the oxide layer and an increase in its porosity, which, as a consequence, leads to much weaker adhesion to the base. In the scratch test, a decrease in the critical load causing delamination of the layer towards the base was observed.

In conclusion, the study has shown the significant influence of medical sterilization on the physical and chemical properties of the TiO_2 and SiO_2 layers. It has been proved that, regardless of the surface layer type, the choice of the sterilizing method is an important issue. A SiO_2 layer applied with the sol-gel method exhibited a higher electrochemical stability. In the future, the authors plan further work to help identify the chemical composition and chemical compounds formed as a result of the sterilization processes and possible changes to the layer thickness.

Acknowledgements

The project was funded by the National Science Centre allocated on the basis of the decision No. 2011/03/B/ST8/06499.

5 REFERENCES

- ¹ P. Karasiński, *Opt. Appl.*, 35 (2005), 117–128
- ² J. Szewczenko, J. Jaglarz, M. Basiaga, J. Kurzyk, E. Skoczek, *Prz. Elektrot.*, 88 (2012) 12B, 228–231
- ³ A. Sadeq, Z. Cai, R. D. Woody, A. W. Miller, J. Prosth. Dent., 90 (2003) 1, 10–17, doi:10.1016/S0022-3913(03)00263-4
- ⁴ B. Surowska, J. Bienias, M. Walczak, K. Sangwal, A. Stoch, *Appl. Surf. Sci.*, 238 (2004), 288–294, doi:10.1016/j.apsusc.2004.05.219
- ⁵ M. Basiaga, W. Walke, Z. Paszenda, P. Karasiński, J. Szewczenko, *Biomatt.*, 4 (2014), 1–6, doi:10.4161/biom.28535
- ⁶ M. Basiaga, Z. Paszenda, W. Walke, P. Karasiński, J. Marciniak, *Inf. Technol. Biomed.*, 284 (2014), 411–420, doi:10.1007/978-3-319-06596-0_39
- ⁷ W. Walke, Z. Paszenda, M. Basiaga, P. Karasiński, M. Kaczmarek, *Inf. Technol. Biomed.*, 284 (2014), 403–410, doi:10.1007/978-3-319-06596-0_38
- ⁸ ASTM F2129-08 Standard Test Method for Conducting Cyclic Potentiodynamic Polarization Measurements to Determine the Corrosion Susceptibility of Small Implant Devices, 2008, doi:10.1520/F2129-08
- ⁹ W. Kajzer, A. Kajzer, *Prz. Elektrot.*, 12 (2013), 275–279
- ¹⁰ A. Kajzer, W. Kajzer, J. Semenowicz, A. Mroczka, *Sol. St. Phen.*, 227 (2015), 523–526, doi:10.4028/www.scientific.net/SSP.227.523
- ¹¹ M. Kaczmarek, W. Walke, Z. Paszenda, *Prze. Elektrot.*, 12b (2011), 74–77
- ¹² PN-EN 1071-3. Advanced technical ceramics. Determination of adhesion and other mechanical failure modes by a scratch test, 2007
- ¹³ EN ISO 14577-1 Metallic materials-Instrumented indentation test for hardness and materials parameters-Part1: Test method, 2015
- ¹⁴ J. Głuszek, *Inż. Mat.*, 5 (2002), 351–354
- ¹⁵ L. Gan, J. Wang, A. Tache, N. Valiquette, D. Deporter, R. Pilliar, *Biomat.*, 25 (2004), 5313–5321, doi:10.1016/j.biomaterials.2003.12.039
- ¹⁶ J. Szewczenko J. Jaglarz, M. Basiaga, J. Kurzyk, Z. Paszenda, *Optica Applicata*, 43 (2013) 1, 173–180, doi:10.5277/oa130121
- ¹⁷ Z. Paszenda, *Inf. Tech. Biomed., Adv. Soft Comp.*, 47 (2008), 15–27, doi:10.1007/978-3-540-68168-7_2
- ¹⁸ N. Kuromoto, R. Simao, G. Soares, *Materials Characterization*, 58 (2007), 114–121, doi:10.1016/j.matchar.2006.03.020
- ¹⁹ B. Yang, M. Uchida, H. M. Kim, X. Zhang, T. Kokubo, *Biomat*, 25 (2004), 1003–1010, doi:10.1016/S0142-9612(03)00626-4
- ²⁰ H. Song, S. Park, S. Jeong, Y. Park, *Journal of Mater. Proc. Techn.*, 209 (2009), 864–870, doi:10.1016/j.jmatprotec.2008.02.055

INFLUENCE OF THE CARBIDE-PARTICLE SPHEROIDISATION PROCESS ON THE MICROSTRUCTURE AFTER THE QUENCHING AND ANNEALING OF 100CrMnSi6-4 BEARING STEEL

VPLIV PROCESA SFEROIDIZACIJE KARBIDNIH DELCEV NA MIKROSTRUKTURO JEKLA 100CrMnSi6-4 ZA LEŽAJE PO KALJENJU IN POPUŠČANJU

Jaromir Dlouhy, Daniela Hauserova, Zbysek Novy

COMTES FHT, Prumyslova 995, 334 41 Dobruška, Czech Republic
jdlohy@comtesfht.cz

Prejem rokopisa – received: 2014-12-12; sprejem za objavo – accepted for publication: 2015-01-21

doi:10.17222/mit.2014.303

Bearings are used mostly in the quenched and tempered state, e.g., steel 100CrMnSi6-4 with a microstructure of low-tempered martensite and carbide particles undissolved during the quenching austenitization. The size and density of the particles depend on the spheroidisation annealing which is the standard operation at the beginning of the bearing manufacturing. The particles decrease the grain growth of the austenite and determine the grain size after the quenching. The process of accelerated carbide spheroidisation and refinement (ASR) was developed and is used as a replacement of the conventional spheroidisation soft annealing. The ASR process produces the structure of a ferritic matrix and fine globular carbides. The carbide size is several times smaller in comparison with the conventional soft annealing. This microstructure is better for quenching and tempering and ensures a better bearing performance. The article compares the structures and properties of the quenched and tempered 100CrMnSi6-4 steel pre-treated with the conventional soft annealing and ASR. The smaller ASR particle size allows the use of lower quenching temperatures, ensuring the desired final hardness. Samples in the hardened state were compared, considering the prior-austenite grain size, the carbide-particle size and distribution as well as the hardness.

Keywords: accelerated spheroidisation, carbide-particle morphology, hardening, bearing steel

Ležaji se običajno uporabljajo v kaljenem in popuščnem stanju, na primer jeklo 100CrMnSi6-4 z mikrostrukturo nizko popuščnega martenzita in s karbidnimi delci, ki se ne raztopijo pri avstenitizaciji pred kaljenjem. Velikost in pogostost delcev je odvisna od sferoidizacijskega žarjenja, ki je standardna operacija na začetku izdelovanja ležaja. Delci zavirajo rast avstenitnih zrn in določajo velikost zrn po kaljenju. Razvit je bil postopek pospešene sferoidizacije in udrobnjenja karbidov (ASR), ki je bil uporabljen namesto običajnega sferoidizacijskega mehkega žarjenja. Pri ASR procesu nastane feritna osnovna mikrostruktura in drobni globularni karbidi. Velikost karbidov je nekajkrat manjša v primerjavi z običajnim mehkim žarjenjem. Taka mikrostruktura je boljša za kaljenje in popuščanje in zagotavlja boljše lastnosti ležaja. V članku so primerjane mikrostrukture in lastnosti kaljenega in popuščanega jekla 100CrMnSi6-4 predhodno mehko žarjenega in ASR. Manjša velikost delcev pri ASR omogoča uporabo nižje temperature kaljenja za doseganje željene trdote. Vzorci v utrjenem stanju so bili primerjani z upoštevanjem velikosti prvotnih avstenitnih zrn, velikosti in razporeditve karbidnih delcev, kot tudi trdote.

Ključne besede: pospešena sferoidizacija, morfologija karbidnih zrn, kaljivost, jeklo za ležaje

1 INTRODUCTION

Bearing steels are well studied in terms of the effect of the technological parameter on the final microstructural properties.¹ The final properties of a hardened product depend on the parameters of hardening, e.g., the austenitization temperature and or the tempering temperature. Their influence on the hardness and prior-austenite grain size was studied properly. Much less attention was paid to the influence of the initial material microstructure on the final material properties. The soft

annealed microstructure, used as the standard material state for hardening, consists of globular carbide particles with a size mostly from 0.5 μm to 1 μm dispersed in the ferritic matrix. Two initial states were used for the hardening – the conventional soft-annealed state and the state after accelerated carbide spheroidisation and refinement (ASR).² The ASR state exhibits the same microstructural morphology, but the globular carbides are about 3-times smaller than after the soft annealing and are also more densely spread in the ferritic matrix.^{3,4} Such a significantly finer structure provides for a faster

Table 1: Chemical composition of the 100CrMnSi6-4 bearing steel in mass fractions (w/%)

Tabela 1: Kemijska sestava 100CrMnSi6-4 jekla za ležaje v masnih deležih (w/%)

C	Si	Mn	P	S	Cr	Mo	Ni	Al	Cu	Fe
0.98	0.54	1.14	0.011	0.011	1.50	0.006	0.02	0.018	0.017	bal.

carbide-particle dissolution during the austenitization at the quenching temperature³ and a stronger pinning of the grain boundaries, thus leading to a smaller austenite grain size due to the pinning effect and a martensitic structure after the quenching. These microstructural features can lead to a higher hardness and toughness with the same hardening parameters. Another possibility is to reduce the quenching temperature or austenitization time, but still with good final mechanical properties.^{5,6}

2 EXPERIMENTAL WORK

2.1 Material

The experimental material was the 100CrMnSi6-4 bearing steel grade with the chemical composition shown in **Table 1**. The material was supplied as hot-rolled 21 mm-diameter bars, with a microstructure of pearlite and a small amount of secondary cementite along the austenite boundaries and a hardness of 383 HV10. The samples were cut in the form of 30 mm long cylinders.

2.2 Spheroidisation annealing

The initial pearlitic microstructure was spheroidised and samples with fine and coarse globular pearlite were prepared. The coarse structure was obtained with the conventional soft annealing in an atmospheric furnace at a temperature of 805 °C for 11 h and air cooling. Fully spheroidised pearlite consisted of cementite globules with diameters of 0.3–1 µm in the ferritic matrix. The fine structure was obtained with the ASR heat treatment consisting of three temperature cycles. Each cycle consisted of the induction heating to 780 °C, a 15-second dwell period at this temperature and cooling in air to a temperature of 650 °C. The overall annealing duration was 5 min. The structure after the ASR process consisted of globular carbides with a size of 0.1–0.3 µm dispersed in the ferritic matrix.

2.3 Quenching and tempering

The heating to the quenching temperature was performed in an electric atmospheric furnace. The samples were held at the austenitization temperature for 30 min. Austenitization temperatures of (800, 820, 840 and 860) °C were used. The quenching was performed in an oil bath, immediately followed by tempering. All the samples were tempered for 4 h at a temperature of 240 °C.

2.4 Sample analyses

All the samples were cut longitudinally and metallographic specimens were prepared by mechanical grinding, polishing and Nital etching. The microstructure was examined with SEM JEOL 7400F. The prior-austenite grain size (PAGS) was assessed on the samples etched in a picric-acid-saturated aqueous solution at a

temperature of 80 °C and the average grain diameter was determined with a linear intercept procedure. The hardness was measured with the Vickers method at a load of HV10.

3 RESULTS AND DISCUSSION

3.1 Microstructure analyses

The microstructures after the soft annealing and ASR treatment are shown in **Figures 1** and **2**. Much finer carbide globules were formed during the ASR treatment. **Figures 3** and **4** show quenched-sample microstructures (quenched from 800 °C). There is a clear difference in the carbide density between the samples. This difference is pronounced with higher austenitizing temperatures.

The ASR-treated samples retained a much denser carbide distribution even after the quenching from 860 °C (**Figures 5** and **6**). A higher dispersion strengthening could cause a hardness increase in comparison with the conventionally soft-annealed samples. Apparently, a denser carbide distribution causes a pronounced pinning effect on the prior-austenite grain boundaries. There were coarse carbides retained in the soft-annealed samples after the quenching from higher temperatures

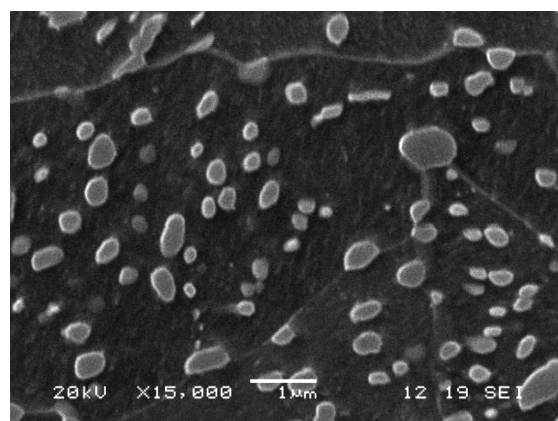


Figure 1: Conventionally soft-annealed sample
Slika 1: Običajno mehko žarjen vzorec

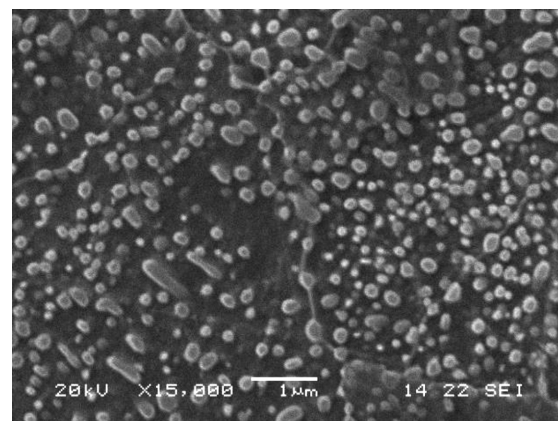


Figure 2: ASR-treated sample with finer carbides
Slika 2: ASR-obdelan vzorec z drobnimi karbidi

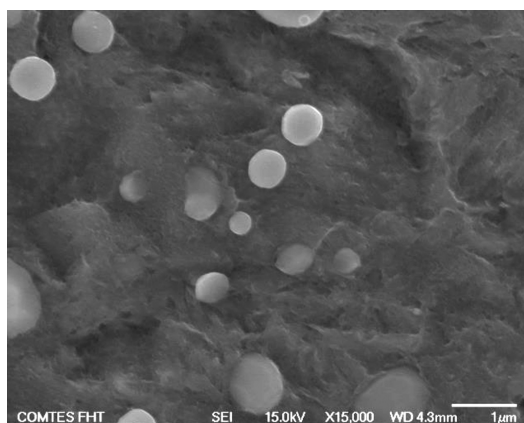


Figure 3: Soft-annealed sample quenched from 800 °C
Slika 3: Mehko žarjen vzorec po kaljenju iz 800 °C

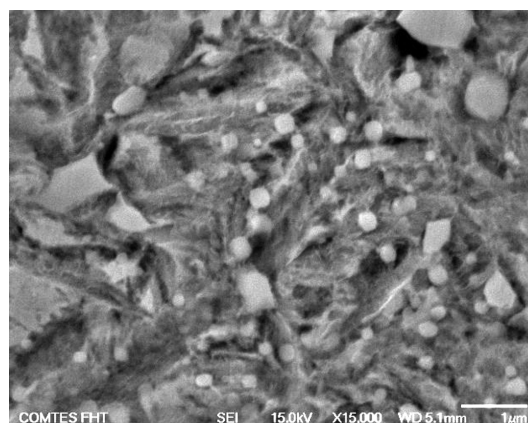


Figure 6: ASR-treated sample quenched from 800 °C
Slika 6: ASR-obdelan vzorec po kaljenju iz 800 °C

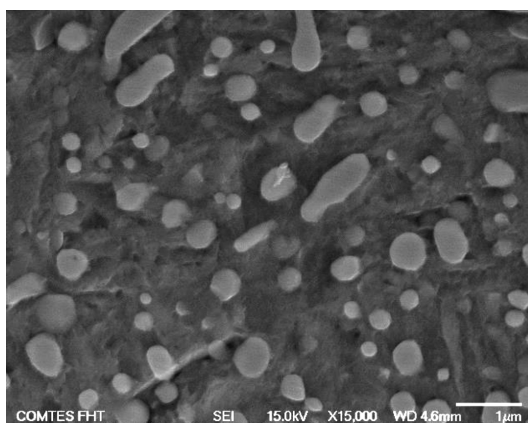


Figure 4: ASR-treated sample quenched from 800 °C
Slika 4: ASR-obdelan vzorec po kaljenju iz 800 °C

(840 and 860 °C). Smaller carbides with a size of up to 0.5 µm were almost completely dissolved.

3.2 Hardness and PAGS

Different austenitization temperatures resulted in different hardness values found after the quenching and

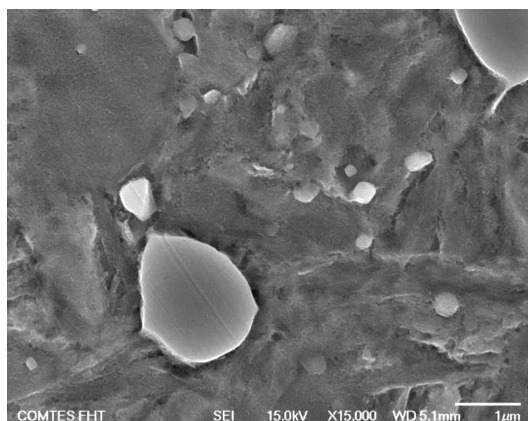


Figure 5: Soft-annealed sample quenched from 800 °C
Slika 5: Mehko žarjen vzorec po kaljenju iz 800 °C

tempering and also in different *PAGS* values. There were significant differences between the samples with coarse and fine structures as shown in **Figure 7**.

There is a clear trend in the hardness value in the case of the conventionally soft-annealed samples with coarse carbides in the microstructure. A higher austenitization temperature caused a hardness increase due to the dissolution of a larger amount of carbon. On the other hand, there is no clear trend in the case of the hardness of the quenched ASR samples. The hardness after the tempering increased with the quenching temperature and was significantly higher with all the quenching temperatures in comparison with the conventionally soft-annealed samples.

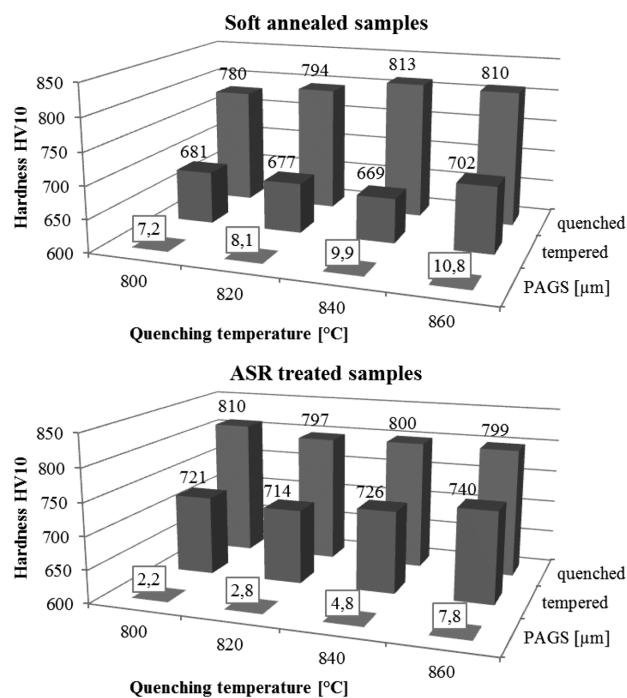


Figure 7: Hardness and *PAGS* of samples after quenching and tempering

Slika 7: Trdota in *PAGS* vzorcev po kaljenju in po popuščanju

The *PAGS* is much smaller in the case of the ASR-treated samples. Its values grew with the increasing quenching temperature for both sample types – the ASR-treated and conventionally soft-annealed samples. The finer-structured ASR-treated samples exhibited a more pronounced *PAGS* increase. Finer carbides dissolved at higher quenching temperatures and thus their pinning effect on the austenite grain boundaries was diminished. The difference between the *PAGS* values of the ASR and soft-annealed samples decreased with the rising quenching temperatures.

4 CONCLUSION

The microstructures and hardness values of hardened samples with different initial microstructures were compared. The influence of the carbide-particle density is clearly visible in terms of the prior-austenite grain size and hardness. The samples with fine carbides after the ASR process had higher hardness values after the quenching and tempering for the whole range of examined quenching temperatures from 800 to 860 °C. The hardness increase was about 40 HV10 in comparison with the conventionally soft-annealed samples with coarser carbide particles and was probably caused by the dispersion strengthening and a possible

higher dissolution of the fine carbides during the austenitization.

Acknowledgment

This paper was created by project Development of West-Bohemian Centre of Materials and Metallurgy No.: LO1412, financed by the MEYS of the Czech Republic.

5 REFERENCES

- ¹ H. K. D. H. Bhadeshia, Steels for bearings, *Progress in Materials Science*, 57 (2012), 268–435, doi:10.1016/j.pmatsci.2011.06.002
- ² D. Hauserova, J. Dlouhy, Z. Novy, Microstructure Development of Bearing Steel during Accelerated Carbide Spheroidisation, *Materials Science Forum*, 782 (2014), 123–128, doi:10.4028/www.scientific.net/MSF.782.123
- ³ J. H. Kang, P. E. J. Rivera-Díaz-del-Castillo, Carbide dissolution in bearing steels, *Computational Materials Science*, 67 (2012), 364–372, doi:10.1016/j.commatsci.2012.09.022
- ⁴ D. Hauserova, J. Dlouhy, Z. Novy, J. Zrník, Accelerated carbide spheroidization and refinement (ASR) of the C45 steel during induction heating, *Mater. Tehnol.*, 47 (2013) 6, 701–705
- ⁵ H. Jirkova, D. Hauserova, L. Kucerovala, B. Masek, Energy- and time-saving low-temperature thermomechanical treatment of low-carbon plain steel, *Mater. Tehnol.*, 47 (2013) 3, 335–339
- ⁶ A. I. Katsamas, A computational study of austenite formation kinetics in rapidly heated steels, *Surface & Coatings Technology*, 201 (2007), 6414–6422, doi:10.1016/j.surfcoat.2006.12.014